vlaams nederlandse Schelde commissie

departement Mobiliteit en Openbare Werken

Rijkswaterstaat
Ministerie van Infrastructuur en Milieu

Instandhouding vaarpassen Schelde Milieuvergunningen terugstorten baggerspecie

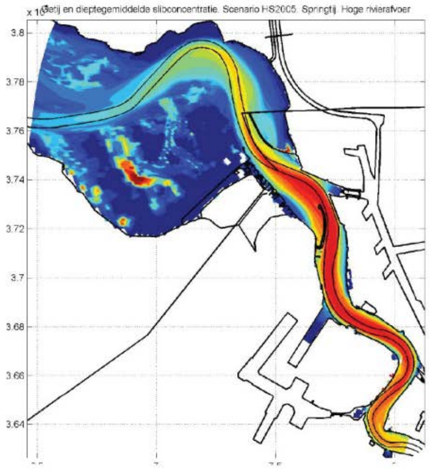

LTV – Veiligheid en Toegankelijkheid

Response of tidal rivers to deepening and narrowing

Basisrapport grootschalige ontwikkeling G-14

01 oktober 2013

IMDC International Marine & Dredging Consultants
Deltares Enabling Delta Life
SVASEK HYDRAULICS COASTAL, HARBOUR AND RIVER CONSULTANTS
ARCADIS Infrastructuur · Water · Milieu · Gebouwen

Colofon

International Marine & Dredging Consultants

Adres: Coveliersstraat 15, 2600 Antwerpen, België

☎: + 32 3 270 92 95

🗐: + 32 3 235 67 11

Email: info@imdc.be

Website: www.imdc.be

Deltares

Adres: Rotterdamseweg 185, 2600 MH Delft, Nederland

☎: + 31 (0)88 335 8273

🗐: +31 (0)88 335 8582

Email: info@deltares.nl

Website: www.deltares.nl

Svašek Hydraulics BV

Adres: Schiehaven 13G, 3024 EC Rotterdam, Nederland

☎: +31 10 467 13 61

🗐: +31 10 467 45 59

Email: info@svasek.com

Website: www.svasek.com

ARCADIS Nederland BV

Adres: Nieuwe Stationsstraat 10, 6811 KS Arnhem, Nederland

☎: +31 (0)26 377 89 11

🗐: +31 (0)26 377 85 60

Email: info@arcadis.nl

Website: www.arcadis.nl

Document Identificatie

Titel	Response of tidal rivers to deepening and narrowing
Project	Instandhouding vaarpassen Schelde Milieuvergunningen terugstorten baggerspecie
Opdrachtgever	Afdeling Maritieme Toegang - Tavernierkaai 3 - 2000 Antwerpen
Bestek nummer	16EF/2010/14
Documentref	I/RA/11387/12.292/GVH
Documentnaam	K:\PROJECTS\11\11387 - Instandhouding Vaarpassen Schelde\10-Rap\Op te leveren rapporten\Oplevering 2013.10.01\G-14 - Response of tidal rivers to deepening and narrowing_v2.0.docx

Revisies / Goedkeuring

Versie	Datum	Omschrijving	Auteur	Nazicht	Goedgekeurd
1.0	28/11/2012	Finaal	J.C. Winterwerp	GVH	MSA
1.1	31/03/2013	Klaar voor revisie	J.C. Winterwerp	GVH	MSA
2.0	01/10/2013	Finaal	J.C. Winterwerp	GVH	MSA

Verdeellijst

1	Analoog	Youri Meersschaut
1	Digitaal	Youri Meersschaut

Deltares

Title

On the response of tidal rivers to deepening and narrowing

Client	Project	Reference	Pages
Rijkswaterstaat, Water, Verkeer en Leefomgeving & Vlaamse Overheid, Afdeling Maritieme Toegang	1207720-000	1207720-000-ZKS-0009	94

Keywords
tidal amplification, hydraulic drag, dispersion equation, regime shift, Elbe, Ems, Loire, Scheldt

Summary

This report discusses man-induced regime shifts in small, narrow and converging estuaries, with focus on the interaction between effective hydraulic drag, fine sediment import and tidal amplification, induced by river engineering works, e.g. narrowing and deepening. In this report, a simple linear analytical model is derived, solving the linearized shallow water equations in exponentially converging tidal rivers. Distinguishing reflecting and non-reflecting conditions, a non-dimensional dispersion equation is derived which yields the real and imaginary wave numbers as a function of the estuarine convergence number and effective hydraulic drag. The estuarine convergence number describes the major geometrical features of a tidal river, e.g. intertidal area, convergence length and water depth. We present a conceptual model on the response of tidal rivers to narrowing and deepening. It is argued that, upon the loss of intertidal area, flood-dominant conditions prevail, upon which fine sediments are pumped into the river, reducing its effective hydraulic drag. Then a snowball effect may be initiated, bringing the river into a hyper-turbid state. This state is self-maintaining because of entrainment processes, and favourable from an energetic point of view, and therefore highly stable. We may refer to an alternative steady state.

Next, the historic development in tidal range in four rivers is analysed, e.g. the Elbe, Ems, Loire and Scheldt, all in North-West Europe; data are available for many decades, up to a century. We use the analytical model, showing that the effective hydraulic drag in the Ems and Loire have decreased considerably over time, as anticipated. We did not find evidence that the Upper Sea Scheldt is close to its tipping point towards hyper-turbid conditions, but risks have been identified. In the Elbe, tidal reflections against the profound step in bed level around Hamburg seem to have affected the tidal evolution in the last decades.

It is emphasized that the conceptual picture sketched here is still hypothetical, and needs to be validated, for instance through hind-cast modelling of the evolution of these rivers. This will not be an easy task, as historical data for a proper calibration of the models required are scarce.

Version	Date	Author	Initials	Review	Initials	Approval	Initials
	July 2013	J.C. Winterwerp		M.Taal		T. Schilperoort	

State
final

Contents

Samenvatting voor beheerders Schelde estuarium

Het is zeer ongewenst dat de Boven-Zeeschelde hetzelfde gedrag gaat vertonen als de Loire en de Eems, waar hypertroebele systemen met hoge slibconcentraties en zuurstofloosheid ontstonden. Vanwege de samenwerking met andere beheerders in het INTERREG-project TIDE is gevraagd een analyse op te zetten met behulp van een vergelijking van meerdere Noordwest-Europese estuaria.

Het onderzoek omvatte theorievorming (om principes achter het ontstaan van hypertroebele systemen in kaart te brengen). Hierna zijn data van estuaria verzameld en geïnterpreteerd. Met de data is de theorie getoetst, is een vergelijking tussen de estuaria uitgevoerd en zijn de risico's voor het Schelde-estuarium beschreven.

Conclusies op basis theorievorming

Wat in de Loire en de Eems is gebeurd, is een 'systeemomslag'. Het estuarium is zich geheel anders gaan gedragen (met andere fysische wetten). Door een samenspel van vergroting van de getijslag en de vorm van het getij wordt slib de rivier ingepompt. Dit slib verlaagt, in tegenstelling tot de normale situatie, waarin de slibconcentratie de waterbeweging niet beïnvloedt, de weerstand voor de waterbeweging ingrijpend. Dit vergroot de getijslag (verder) en doet nog meer slib naar binnen komen. Er is een zichzelf versterkende kringloop ontstaan, een sneeuwbaleffect. Als gevolg daarvan is een dikke sliblaag (fluid mud) op de bodem ontstaan. Deze kringloop staat centraal getekend in figuur 1. De condities waaronder dit plaatsvindt zijn een samenspel van (i) het vergroten van de getijslag, (ii) slib-importerend gedrag, want stroomsnelheden tijdens vloed zijn groter dan tijdens eb, (iii) de afname in hydraulische weerstand, en (iv) de beschikbaarheid van slib in de waterkolom.

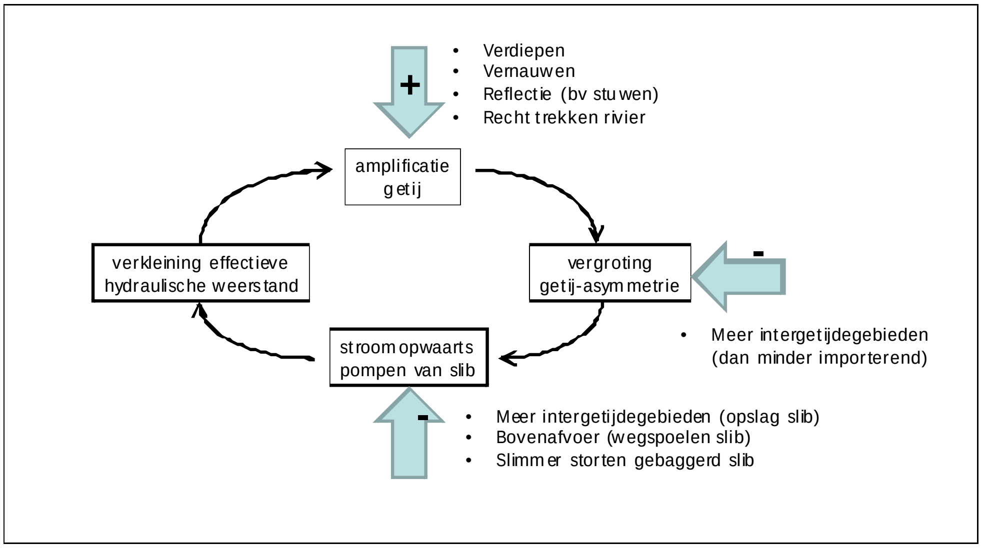

Fig. 1: Het sneeuwbaleffect dat hypertroebele systemen doet ontstaan. De factoren die de kringloop beïnvloeden zijn met + (versterking) of – (mitigatie) aangeduid, bij het aspect waarop ze aangrijpen.

De figuur toont ook dat intergetijdengebieden de veerkracht van het estuarium (tegen het optreden van een systeemomslag) op twee manieren beïnvloeden:

1. Verlies aan intergetijdegebied vergroot de getij-amplificatie bij verdiepen en induceert een vloed-dominant systeem (het laatste effect is het belangrijkste).
2. Intergetijdengebieden en andere plaatsen waar slib kan bezinken, geven ‘accommodatieruimte’. Hier kan slib (tijdelijk) opgeborgen worden. Dit verlaagt de slibconcentraties in de waterkolom. Het rollen van de sneeuwbal begint wanneer de slibconcentraties in het water daarvoor groot genoeg zijn, en kan al gebeuren bij enkele honderden mg/l, mits over een significante lengte van de rivier (vele km’s).

Conclusies op basis data-analyse voor alle estuaria

Het blijkt dat in veel Noordwest-Europese estuaria er een aanzienlijke toename van de getijslag heeft plaatsgevonden (figuur 2). Voor de Loire en de Eems is dit inderdaad gepaard gegaan met een afname van de ruwheid (figuur 3). De data bevestigen de hiervoor uiteengezette theorie over het ontstaan van hypertroebele systemen.

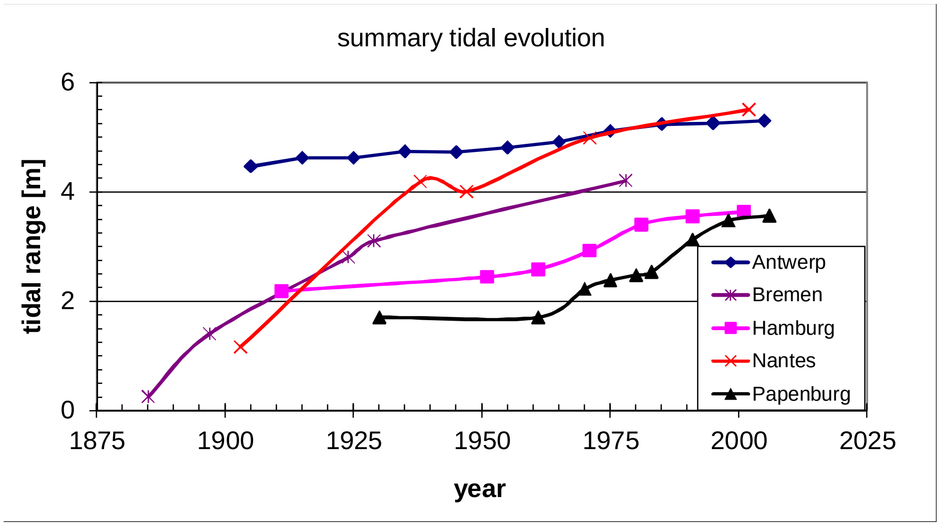

Fig. 2: Versterking getijslag in de afgelopen eeuw in vijf Europese havens.

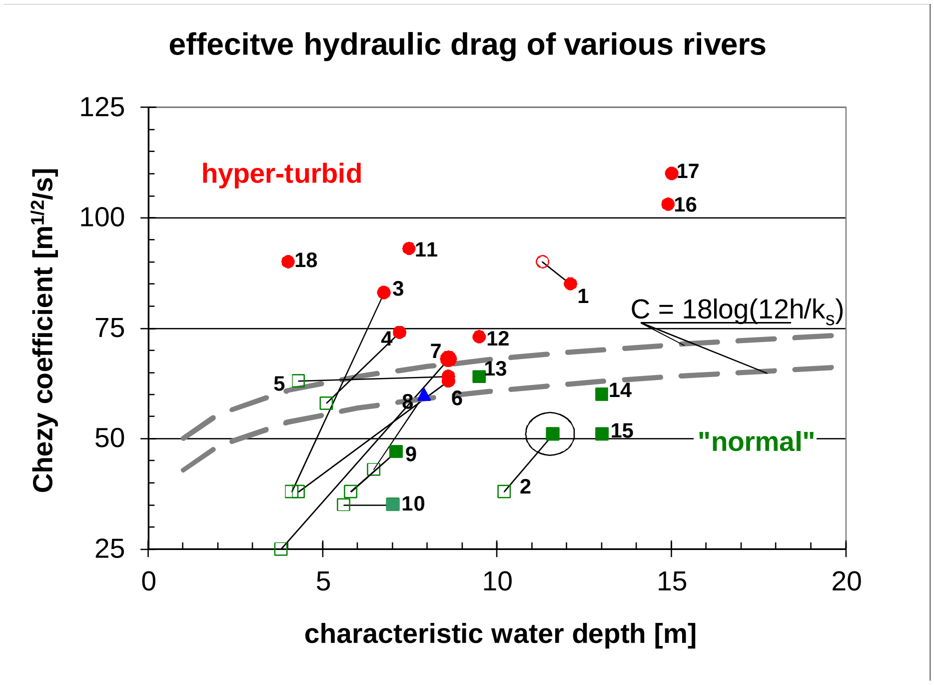

Fig. 3: Vergelijking effectieve hydraulische weerstand als functie van de waterdiepte. The C-h relatie is gebaseerd op arbitraire waardes, k_s = 2 en 5 cm. Rode symbolen representeren hypertroebele condities, en groene symbolen "normale" estuaria, en blauw mogelijk overgangscondities. Historische data zijn met open symbolen weergegeven. 1: Elbe-outer; 2: Elbe-inner; 3: Ems/E-L; 4: Ems/L-P; 5: Loire/P-C; 6: Loire/C-laM; 7: Loire/LaM-N; 8: Scheldt/S-T;9: Scheldt/T-StA; 10: Scheldt/StA-D; 11: Thames; 12: Severn-inner; 13: Severn-outer; 14: Western Scheldt; 15: Gironde-outer; 16: Gironde-inner (Villaret et al., 2011); 17: Yangtze estuary; 18: Vilaine (Vested et al., 2013).

Conclusies op basis data-analyse voor Boven-Zeeschelde

In de afgelopen eeuw is het getij sterker de Boven-Zeeschelde ingekomen. Rond de jaren 70 van de vorige eeuw is deze toename versneld, mede door een forse verdieping van de Boven-Zeeschelde. De oorzaak van deze verdieping is niet bekend, maar is mogelijk veroorzaakt door een morfologische responsie op verdiepingen/verwijdingen en zandwinning benedenstrooms. De mate waarin het getij gedempt wordt is over veel trajecten afgenomen. Deze (niet-gewenste) historische toename van de getijslag in de Boven-Zeeschelde komt voor 2/3 door lokale veranderingen en voor 1/3 door de veranderingen in het getij benedenstrooms (Westerschelde en Beneden-Zeeschelde). Het gehele Schelde-estuarium is vloed-dominant (duur stijgend water is korter dan die van het dalend water). Deze vloeddominantie neemt toe in stroomopwaartse richting en is niet veel veranderd sinds 1900.

Met de beschikbare data en het analytisch model kan geen eenduidig antwoord gegeven worden op de vraag of de Boven Zeeschelde zich aan het ontwikkelen is in de richting van een hyper-troebel systeem. Er is enige, maar nog geen grote afname van de ruwheid te zien (figuur 3). De veerkracht van de Boven Zeeschelde is zeker fors afgenomen:

1. Er is vrijwel geen intergetijdegebied meer, en de rivier is over haar gehele lengte vloed-dominant.

2. De accommodatieruimte voor slibafzettingen is fors afgenomen, zodat slibgehaltes in de waterkolom zullen toenemen indien slib de Boven Zeeschelde wordt ingepompt.

Deze conclusies kunnen robuuster gemaakt worden door ook de ontwikkelingen in de slibbalans van de (Boven) Zeeschelde erbij te betrekken en door de reflectie (bijvoorbeeld via een numeriek 1-D model) verder te bestuderen.

Aanbevelingen voor beheer van estuaria en Boven-Zeeschelde in het bijzonder

De volgende richtlijnen voor het beheer van estuaria, die het risico van systeemomslag verkleinen, kunnen worden afgeleid:

- Met een grotere rivierafvoer kan slib naar buiten worden gespoeld,
- Vergroot de accommodatieruimte, zodat de slibconcentratie in de waterkolom niet te veel stijgt,
- Vergroot het intergetijdegebied om het getij minder vloed-dominant te maken,
- Vergroot de hydraulische weerstand in het systeem (bijvoorbeeld herstel van afgesneden bochten – door het herstellen van afgesneden bochten wordt de rivier ook langer, en daarmee de convergentielengte)
- Wegbaggeren van bestaande slibafzettingen, wat accommodatieruimte vergroot.

Deze maatregelen zijn gebaseerd op kwalitatieve gronden, en nog op generlei wijze gekwantificeerd, dus de efficiëntie is onbekend.

Meer specifiek adviezen voor de Boven-Zeeschelde zijn:

- Het ontwikkelen van overstroombare gebieden, met een inrichting die een vergroting inhoudt van de accommodatieruimte, is in elk scenario een verstandige maatregel, want ze verkleint de kansen op een systeemomslag.
- Betrek de mogelijkheden voor het bezinken van slib uit de waterkolom bij de planning van slibstortingen.

Daar 2/3 van de toename van de getijslag in de Boven-Zeeschelde lokale oorzaken heeft is het verstandig om daar eerst te zoeken naar getij-reducerende maatregelen, en te onderzoeken wat de oorzaak is van de forse verdiepingen in de zeventiger jaren van de vorige eeuw.

1 Introduction

This report describes the results of the Task M research on the integrity of the Scheldt fairways, with focus on the risks of changes in the large-scale behavior of fine sediments (regime shift) in the Upper Sea Scheldt (Boven Zeeschelde). This work is (partly) based on a comparison with other estuaries.

The relevant management question for this part of the study reads: How can the balance of fine sediment in the turbidity maximum in the Scheldt estuary be controlled and affected by human interventions, decreasing the supply of fine sediments in zones characterized by too high siltation rates in relation to nautical and/or ecological aspects, or increasing the supply to zones with too little fine sediments in relation to ecological aspects.

This management question is driven by the Accessibility of the Port of Antwerp and dredging costs, and by Nature 2000 regulations.

The Scheldt-estuary is renowned for its long lasting human interventions, such as deepening, narrowing by embankments (land reclamations, and loss of intertidal area), sand mining and large-scale sediment displacements by dredging and dumping. However, the Scheldt is not the only river with such a history, rather it is characteristic for many estuaries in Europe, and elsewhere in the world. One of the consequences of these human interventions is an increase in tidal range, which also affects natural sediment movements in the estuary. In some of these estuaries, changes have been so large, that they led to a regime shift: the Ems and Loire Rivers are typical examples, developing into hyper-turbid systems with large amounts of fluid mud and serious water quality problems (depletion of oxygen).

Worldwide, managers are seeking for measures to minimize or compensate the effects of human interventions, and many ideas have been proposed, and many measures have been tried. These ideas and trials provide inspiration for the management of the Scheldt estuary.

The current Task M project focuses on the behavior of fine sediments in and around the Upper Sea Scheldt (Boven Zeeschelde). The behavior of non-cohesive sediments, in particular in the Western Scheldt is subject of studies in another framework. Also the behavior of fine, cohesive sediments in the Western Scheldt is treated elsewhere, as far as the fine sediment dynamics in the Upper Sea Scheldt are not affected.

An evaluation and mutual comparison of estuarine systems can provide useful information only when these systems and their response to human interventions are properly understood. The first research question therefore is:

1. What is the response of the tidal range, and through that of the tidal flow velocities, to various interventions in general, and in the Scheldt estuary in particular, and can this response be compensated and/or minimized?

The gross and net transports of fine sediment are not only controlled by the absolute values of the tidal flow velocities, but also by tidal asymmetry, salinity distribution, etc. Therefore, the second research question is:

2. What is the response of net and gross fine sediment transports to human interventions, both more directly (e.g. changes in tidal range), and more indirectly (e.g. changes in intertidal area, etc.).

These questions will be addressed in Chapter 5 of this report, based on the analyses presented in the three preceding chapters. The strategy of this study is that we compare a variety of tidal rivers with respect to their physical properties and behavior on the basis of a number of dimensionless parameters – only the use of dimensionless parameters allows comparison of rivers of various dimensions and hydraulic regimes. These dimensionless parameters are obtained from an analytical solution of the linearized water movement equations, as presented in Chapter 2.1. This analytical solution also provides analytical relations on the response of the tidal range and tidal asymmetry to riverine geometry, necessary to address research question 1. In Chapter 2.2, we present the analytical results in graphical form to get a feeling of their behavior. From earlier studies (Winterwerp, 2001, 2009, 2011) we found a profound effect of fine suspended sediment on the effective hydraulic drag in open channel flow. This effect may induce a positive feed-back between tidal properties and suspended sediment concentrations. Therefore, we pay ample attention to the effect of the effective hydraulic drag, realizing though that this drag is difficult to measure directly.

In Chapter 3 we analyze the mass balance in one-dimensional longitudinal direction, identifying the various terms contributing to the net and gross sediment transport (research question 2). We distinguish between processes which induce a net up-estuary transport, and processes which induce a net down-estuary transport. The latter is governed by riverine flushing (we argue to ignore the rectification of the Stokes drift). Chapter 3 also contains a brief summary on the effects of fine suspended sediment on the effective hydraulic drag and processes initiating a regime shift towards hyper-concentrated conditions.

The historical evolution of the tidal dynamics and fine sediment behavior in four rivers are evaluated in Chapter 4 – these rivers are the Ems estuary, the Loire estuary, the Elbe River, and the Upper Sea Scheldt (we have some data on the Weser River as well, but insufficient for a full analysis). Currently, we have too few data to analyze other rivers. A comparison of the behavior of these rivers and the implications for the Upper Sea Scheldt are discussed in Chapter 5, and a summary of recommendations is presented in Chapter 6.

2 Tidal evolution in a converging estuary with intertidal area

2.1 Derivation of the relevant equations

the equations

In this section, we derive the dispersion equation for tidal propagation in a converging estuary with a compound cross section, e.g. Fig. 2.1.

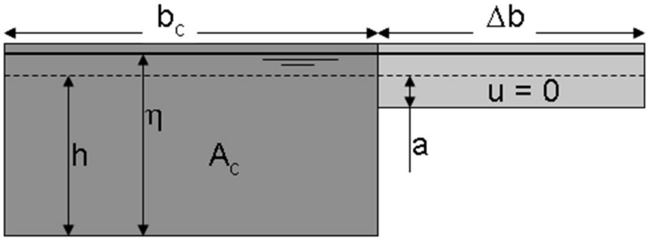

Fig. 2.1: Compound channel and definitions.

We follow Friedrichs (2010) and Dronkers (2005), but make no a priori assumptions on the contribution of the various terms in the equations, except for a linearization of the friction term, and we neglect the advection term in the momentum equation:

$$
\begin{aligned}
&\left(b_c+\Delta b\right)\frac{\partial \eta}{\partial t}+\frac{\partial A_c u}{\partial x}=0\\
&\frac{\partial u}{\partial t}+g\frac{\partial \eta}{\partial x}+\frac{ru}{h}=0
\end{aligned}
\tag{1}
$$

We refer to Dronkers (1964) for a complete analysis of these equations in a straight channel. Here we focus on a converging estuary, as almost all natural, alluvial estuaries are characterized by a so-called trumpet shaped plan form (e.g. Prandle, 2004). If we assume $A_c \approx hb_c$, equ. (1) can be re-written as:

$$\frac{\partial \eta}{\partial t}+\frac{A_c}{b_c+\Delta b}\frac{\partial u}{\partial x}+\left[\frac{1}{b_c}\frac{\partial b_c}{\partial x}+\frac{1}{h}\frac{\partial h}{\partial x}\right]\frac{A_c}{b_c+\Delta b}u=0 \tag{2a}$$

$$\frac{\partial u}{\partial t}+g\frac{\partial \eta}{\partial x}+\frac{ru}{h}=0 \tag{2b}$$

where η = instantaneous water level, u = cross-sectionally averaged flow velocity, h = tidal-mean water depth, b_c = width flow-carrying cross section, Δb = width intertidal area (over which the flow velocity is zero), A_c = surface area flow-carrying cross section $\left(A_c \approx hb_c\right)$, assuming $\left|\eta-h\right| << h$, r = linear friction term $r=8c_D U/3\pi$ [m/s], c_D = drag coefficient, U = characteristic (maximal) velocity, and x and t are longitudinal co-ordinate and time (x = 0 at the estuaries mouth, and x > 0 up-estuary). We focus on exponentially converging estuaries, e.g.

$b_c = b_0 \exp\{-x/L_b\}$, where b_0 = width flow-carrying cross section in the mouth of the estuary and L_b = convergence length (typical values between ~20 and ~40 km). The drag coefficient c_D attains values of 0.001 to 0.003 m/s (corresponding Chézy values of 100 – 60 $\mathrm{m}^{1/2}$/s, as $r \approx gU/C^2$), hence r also varies from around 0.001 to 0.003. In the following, we assume that the river flow is so small that its effects can be neglected. Finally, further to our linear approach, we also assume that parameters may vary along the estuary, such as the tidal amplitude, but that these variations are relatively small, and that the tidal amplitude is small compared to the water depth.

If we neglect longitudinal gradients in tidal-mean water depth $(\partial h/\partial x)$, the continuity and mass balance equation read[1]:

$$\frac{\partial \eta}{\partial t} + \frac{A_c}{b_c + \Delta b}\frac{\partial u}{\partial x} - \frac{A_c}{b_c + \Delta b}\frac{u}{L_b} = 0 \tag{3a}$$

$$\frac{\partial u}{\partial t} + g\frac{\partial \eta}{\partial x} + \frac{ru}{h} = 0 \tag{3b}$$

the dispersion relation and wave numbers

We assume that the solution to (3) follows a harmonic function:

$$\eta(x,t) = h + a_0 \exp\{i(\omega t - kx)\} \quad \text{and} \quad u(x,t) = U_0 \exp\{i(\omega t - kx - \phi)\} \tag{4a}$$

where a_0 = tidal amplitude at x = 0, U_0 = amplitude flow velocity at x = 0, ω = tidal frequency; $\omega = 2\pi/T$; T = tidal period, k = complex wave number; $k = k_r + ik_i$, k_r = real wave number ($k_r = 2\pi/\lambda$), λ = tidal wave length, k_i = imaginary wave number, and ϕ = phase angle between tide and velocity. Note that the three unknowns a_0, U_0 and ϕ are real. Next, we substitute (4a) into (3a) and (3b):

$$i\omega a_0 - \left(\frac{A_c}{b_c + \Delta b} ik + \frac{A_c}{b_c + \Delta b}\frac{1}{L_b}\right) U_0 \exp\{-i\phi\} = 0 \tag{5a}$$

$$igka_0 - \left(i\omega + \frac{r}{h}\right) U_0 \exp\{-i\phi\} = 0 \tag{5b}$$

From equ. (5b) we can derive the velocity amplitude U_0 as a function of a_0:

$$U_0 = \mathrm{mod}\left[\frac{igka_0}{(i + r_*)\,\omega \exp\{-i\phi\}}\right] = \frac{ga_0}{\omega}\sqrt{\frac{k_r^2 + k_i^2}{r_*^2 + 1}} \tag{5c}$$

---

[1] *Note that a more general derivation is obtained by assuming an exponentially converging cross section; however, it is difficult to account for spatially varying water depth. To account for longitudinal variations in water depth as good as possible, the rivers are sub-divided into sub-sections with constant depth in our analyses below (see f.i. Jay, 1991).*

equ's (5a) and (5b) can be written in matrix form:

$$\begin{bmatrix} i\omega & -\left(\dfrac{A_c}{b_c+\Delta b}ik+\dfrac{A_c}{b_c+\Delta b}\dfrac{1}{L_b}\right)\exp\left\{-\phi i\right\} \\ igk & -\left(i\omega+\dfrac{r}{h}\right)\exp\left\{-\phi i\right\} \end{bmatrix}\begin{bmatrix} a_0 \\ U_0 \end{bmatrix}=0 \tag{6}$$

Requiring the existence of non-trivial solutions yields a dispersion equation implicit in the wave number k:

$$-i\omega\left(i\omega+\frac{r}{h}\right)+igk\left(\frac{A_c}{b_c+\Delta b}ik+\frac{A_c}{b_c+\Delta b}\frac{1}{L_b}\right)=0$$

$$\text{or}\quad \kappa^2-2i\kappa-\Lambda_e\left(1-ir_*\right)=0 \tag{7}$$

$$L_b k^2-ik-\frac{b_c+\Delta b}{ghb_c}L_b\omega^2\left(1-i\frac{r}{\omega h}\right)=0$$

in which the following dimensionless parameters have been defined:

$$\begin{aligned}
&\kappa=\kappa_r+i\kappa_i=2\left(k_r+ik_i\right)L_b=2kL_b \\
&L_*=\frac{2L_b\omega}{\sqrt{gh}}=\frac{2L_b}{L_g},\quad \text{where}\quad L_g\equiv\frac{\sqrt{gh}}{\omega} \\
&r_*=\frac{r}{\omega h}=\frac{gU}{\omega hC^2} \\
&b_*=\frac{b_c+\Delta b}{b_c} \\
&\Lambda_e=b_*L_*^2=\frac{b_c+\Delta b}{b_c}\frac{4L_b^2\omega^2}{gh}=\frac{4L_b^2\omega^2}{gA_c/b_{tot}}
\end{aligned} \tag{8}$$

Here we introduce the estuarine convergence number Λ_e, through which all geometrical and bathymetrical features of the rivers are accounted for. Note that Λ_e decreases with increasing water depth, increasing convergence of the river's plan form, and decreasing intertidal area. Next, from (7) k is resolved:

$$k_{1,2}=i\frac{1\pm\sqrt{1-4\dfrac{b_c+\Delta b}{gA_c}L_b^2\omega^2+4\dfrac{b_c+\Delta b}{gA_c}L_b^2 i\omega\dfrac{r}{h}}}{2L_b}=i\frac{1\pm\sqrt{1-\Lambda_e+i\Lambda_e r_*}}{2L_b} \tag{9}$$

Using MAPLE, the real and imaginary part of (9) are determined:

$$k_r = \pm\frac{1}{4L_b}\left[2\sqrt{\left(4\left(1+\Delta b/b_c\right)\frac{L_b^2\omega^2}{gh}-1\right)^2+\left(4\left(1+\Delta b/b_c\right)\frac{L_b^2\omega^2}{gh}\right)^2\left(\frac{r}{\omega h}\right)^2}+\right.$$
$$\left.+2\left(4\left(1+\Delta b/b_c\right)\frac{L_b^2\omega^2}{gh}-1\right)\right]^{1/2} \tag{10a}$$

$$k_i = \frac{1}{2L_b}\mp\frac{1}{4L_b}\left[2\sqrt{\left(4\left(1+\Delta b/b_c\right)\frac{L_b^2\omega^2}{gh}-1\right)^2+\left(4\left(1+\Delta b/b_c\right)\frac{L_b^2\omega^2}{gh}\right)^2\left(\frac{r}{\omega h}\right)^2}+\right.$$
$$\left.-2\left(4\left(1+\Delta b/b_c\right)\frac{L_b^2\omega^2}{gh}-1\right)\right]^{1/2} \tag{10b}$$

The positive and negative real wave numbers represent the up-estuary propagating tidal wave, and its reflection, if any. We note that the imaginary wave number for the up-estuary propagating wave differs from its reflection, which is to be attributed to the funnel shape of the estuary. This explains why κ_i^- is always positive, i.e. the reflected tidal wave is always damped. Indeed, when $L_b = \infty$, as in the case of a straight, prismatic channel, all wave numbers become symmetric again.

For a non-converging ($L_b = \infty$), frictionless channel ($r = 0$), equ. (10) converges to the well-known relations $k_r = \omega\sqrt{\left(b_c+\Delta b\right)/b_c gh}$ and $k_i = 0$. For a non-converging channel with friction, we obtain:

$$k_r = \pm\sqrt{\frac{b_*\omega^2}{2gh}}\left[\sqrt{1+r_*^2}+1\right]^{1/2} \quad \text{and} \quad k_i = \mp\sqrt{\frac{b_*\omega^2}{2gh}}\left[\sqrt{1+r_*^2}-1\right]^{1/2} \tag{10c}$$

In dimensionless form, the wave numbers (10) for the up-estuary propagating wave, and its reflection, represented by the superscripts $\blacksquare^+$ and $\blacksquare^-$, respectively, read:

$$\kappa_r^+ = \frac{1}{2}\left[2\sqrt{\left(\Lambda_e-1\right)^2+\left(\Lambda_e r_*\right)^2}+2\left(\Lambda_e-1\right)\right]^{1/2} \quad \text{and}$$
$$\kappa_r^- = -\frac{1}{2}\left[2\sqrt{\left(\Lambda_e-1\right)^2+\left(\Lambda_e r_*\right)^2}+2\left(\Lambda_e-1\right)\right]^{1/2} \tag{11a}$$

$$\kappa_i^+ = 1-\frac{1}{2}\left[2\sqrt{\left(\Lambda_e-1\right)^2+\left(\Lambda_e r_*\right)^2}-2\left(\Lambda_e-1\right)\right]^{1/2} \quad \text{and}$$
$$\kappa_i^- = 1+\frac{1}{2}\left[2\sqrt{\left(\Lambda_e-1\right)^2+\left(\Lambda_e r_*\right)^2}-2\left(\Lambda_e-1\right)\right]^{1/2} \tag{11b}$$

In the remainder, we will work with both the dimensionless and non-dimensionless equations. However, we will use the dimensionless parameters of equ. (8) comparing the various estuaries in Section 4 of this report.

limiting values of the wave numbers

Let us analyze these solutions for a converging estuary with a rough, frictionally-dominated bed ($r = \infty$) and for an estuary with a very smooth bed, formed by fluid mud ($r \approx 0$). In the first case the friction term dominates the expression below the square root-sign, in the second case, friction can be neglected. The real and imaginary wave number for a frictionless system read (assuming shallow water, i.e. h not too large)

$$\begin{aligned} &\kappa_r\big|_{r\downarrow 0} = \sqrt{\Lambda_e - 1} \quad \text{and} \quad \kappa_i\big|_{r\downarrow 0} = 1 \quad \text{for} \quad \Lambda_e \geq 1 \\ &\kappa_r\big|_{r\downarrow 0} = 0 \quad \text{and} \quad \kappa_i\big|_{r\downarrow 0} = 1 - \sqrt{1 - \Lambda_e} \quad \text{for} \quad \Lambda_e \leq 1 \end{aligned} \tag{12a}$$

Equ. (11b) shows that for a smooth bed and $\Lambda_e \geq 1$, the tidal wave is amplified with the convergence length $k_i = 1/2L_b$; this is therefore the maximum amplification of the tide according to linear theory; the estuary is said to be in synchronous mode (see below – weakly dissipative, Jay, 1991; Lanzoni and Seminara, 1998). In case of a rough bed ($r = \infty$), the real and imaginary wave number become:

$$\begin{aligned} &k_r\big|_{r\uparrow\infty} = \frac{1}{4L_b}\sqrt{2\Lambda_e r_*} \quad \text{or} \quad \kappa_r\big|_{r\uparrow\infty} = \sqrt{\Lambda_e r_*/2} \\ &k_i\big|_{r\uparrow\infty} = -\frac{1}{4L_b}\sqrt{2\Lambda_e r_*} \quad \text{or} \quad \kappa_i\big|_{r\uparrow\infty} = -\sqrt{\Lambda_e r_*/2} \end{aligned} \tag{12b}$$

The phase angle between tidal elevation and velocity follows from substitution of (4a) into (3a), elaborating the real part only:

$$i\omega a_0 - i\frac{A_c}{b_c + \Delta b}kU_0 \exp\{-i\phi\} - \frac{A_c}{b_c + \Delta b}\frac{1}{L_b}U_0 \exp\{-i\phi\} = 0 \tag{5a}$$

$$\tan\{\phi\} = \frac{L_b k_i - 1}{L_b k_r} = \frac{\kappa_i - 2}{\kappa_r} \tag{13a}$$

Note the similarity of (13a) with Van Rijn's Table 1 (2012). Substituting from (11b and 11c) yields the phase angle for a smooth and friction-dominated system (see also Dronkers, 2005 and Friedrichs, 2010):

$$\begin{aligned} &\tan\{\varphi\}\big|_{r\downarrow 0} = -\frac{1}{\sqrt{\Lambda_e - 1}} \quad \text{for } \Lambda_e \geq 1 \quad \text{and} \\ &\tan\{\varphi\}\big|_{r\downarrow 0} = \infty; \quad \varphi = 90^\circ \quad \text{for } \Lambda_e \leq 1 \\ &\tan\{\varphi\}\big|_{r\uparrow\infty} = -\frac{\sqrt{\Lambda_e r_*} + 2}{\sqrt{\Lambda_e r_*}} \approx -1 \quad \text{for all } \Lambda_e \end{aligned} \tag{13b}$$

The celerity c of the tidal wave into the estuary is given by:

$$c = \frac{\omega}{k_r} = \frac{2\omega L_b}{\kappa_r} \tag{14a}$$

Substituting from (11a) yields the celerity for a smooth and friction dominated system (e.g. Le Blond, 1978):

$$\begin{aligned} &c\big|_{r\downarrow 0} = \frac{2\omega L_b}{\sqrt{\Lambda_e - 1}} \quad \text{for} \quad \Lambda_e \ge 1 \text{ and } \quad c\big|_{r\downarrow 0} = \infty \quad \text{for} \quad \Lambda_e \le 1 \\ &c\big|_{r\uparrow\infty} = \frac{4\omega L_b}{\sqrt{2\Lambda_e r_*}} \quad \text{for all } \Lambda_e \end{aligned} \tag{14b}$$

The behavior of the tidal wave for frictionless conditions and small estuarine convergence number $\Lambda_e \le 1 \left(\text{i.e. } L_b \le L_g/2 \text{ for } \Delta b = 0\right)$ needs some further explanation. For these conditions, the wave length and celerity become infinite, whereas the phase angle between water level and velocity becomes 90$^{\text{o}}$. Though these conditions are identical to those of a standing wave, we have to realize we did not prescribe any wave reflections in our boundary conditions. Though this pathological behavior is referred to as super-critical by Toffolon and Saveneije (2011), and was also found by Friedrichs and Aubrey (1994), we do not really understand the physical meaning of these solutions to the equations.

the general solution

Next, we study the propagation and amplification/damping of the tide in an infinitely long estuary and/or an estuary of finite length ℓ (for instance by a weir at $x = \ell$). In dimensionless form, the length of the estuary then measures $\lambda_r = \ell/2L_b$. At the mouth of the estuary we prescribe a simple cosine tide:

$$\eta(0,t) = h + a_0 \cos\{\omega t\} \tag{15}$$

in which a_0 = amplitude of the tide. Next, we introduce its complex equivalent $\tilde{\eta}(x,t)$ and require that $\mathrm{Re}\{\tilde{\eta}(0,t)\} = a_0$. The harmonic solution to equ. (3) then reads:

$$\begin{aligned} &\tilde{\eta}(x,t) = h + a_0^+ \exp\left\{i\left(\omega t - k^+ x\right)\right\} + a_0^- \exp\left\{i\left(\omega t - k^- x\right)\right\} \quad \text{and} \\ &\quad \tilde{u}(x,t) = U_0^+ \exp\left\{i\left(\omega t - k^+ x - \phi\right)\right\} + U_0^- \exp\left\{i\left(\omega t - k^- x - \phi\right)\right\} \end{aligned} \tag{16a}$$

in which a^+ and a^- are the amplitudes of the incoming and reflecting tidal wave. In case of an infinitely long river, equ. (16a) reduces to:

$$\tilde{\eta}(x,t) = h + a_0 \exp\left\{i\left(\omega t - kx\right)\right\} \quad \text{and} \qquad \tilde{u}(x,t) = U_0 \exp\left\{i\left(\omega t - kx - \phi\right)\right\} \tag{16b}$$

as in equ. (4a). The boundary conditions to the solution of equ.'s (3) and (16a) are given by:

- $x = 0$: $a_0^+ + a_0^- = a_0$,
- $x = \ell$: $U = 0$, hence $U^+ = -U^-$.

Further to equ. (3b), the latter implies that

- $x = \ell$: $\partial a^+ / \partial x = -\partial a^- / \partial x$, so that $a_0^+ k^+ \exp\left\{-ik^+\ell\right\} + a_0^- k^- \exp\left\{-ik^-\ell\right\} = 0$.

Hence, we find for the two amplitudes a_0^+ and a_0^- from the modulus of a_0:

$$a_0^+ = \frac{k^- \exp\left\{-ik^-\ell\right\}}{k^- \exp\left\{-ik^-\ell\right\} - k^+ \exp\left\{-ik^+\ell\right\}} a_0; \quad a^+ = \frac{k^- \exp\left\{-ik^-\ell\right\} \exp\left\{-ik^+x\right\}}{k^- \exp\left\{-ik^-\ell\right\} - k^+ \exp\left\{-ik^+\ell\right\}} a_0 \tag{17a}$$

$$a_0^- = \frac{k^+ \exp\left\{-ik^+\ell\right\}}{k^+ \exp\left\{-ik^+\ell\right\} - k^- \exp\left\{-ik^-\ell\right\}} a_0; \quad a^- = \frac{k^- \exp\left\{-ik^+\ell\right\} \exp\left\{-ik^-x\right\}}{k^+ \exp\left\{-ik^+\ell\right\} - k^- \exp\left\{-ik^-\ell\right\}} a_0 \tag{17b}$$

resonance of the tidal wave

As $k^- = -k_r + ik_i^- = -k_r + i\left(p+q\right)$ and $k^+ = k_r + ik_i^+ = k_r + i\left(p-q\right)$, where p and q are dummy variables, we can re-write (17) as:

$$a_0^+ = \frac{k^- \exp\left\{ik_r\ell\right\}}{k^- \exp\left\{ik_r\ell\right\} - k^+ \exp\left\{-ik_r\ell\right\} \exp\left\{-2q\ell\right\}} a_0 \tag{18a}$$

$$a_0^- = \frac{k^+ \exp\left\{-ik_r\ell\right\} \exp\left\{-2q\ell\right\}}{k^+ \exp\left\{-ik_r\ell\right\} \exp\left\{-2q\ell\right\} - k^- \exp\left\{ik_r\ell\right\}} a_0 \tag{18b}$$

Hence, $\lim\limits_{\ell \to \infty}\left\{a_0^+\right\} = a_0$ and $\lim\limits_{\ell \to \infty}\left\{a_0^-\right\} = 0$, retrieving the simple propagating wave in an infinitely long converging estuary. Furthermore, equ. (17) shows that resonance can occur when:

$$\mathrm{Re}\left[k^{-}\exp\left\{-ik^{-}\ell\right\}-k^{+}\exp\left\{-ik^{+}\ell\right\}\right]=0 \quad \text{, i.e}$$

$$\tan\left\{k_r\ell\pm n\frac{\pi}{2}\right\}=-\frac{k_r\exp\left\{k_i^{-}\ell\right\}+k_r\exp\left\{k_i^{+}\ell\right\}}{k_i^{-}\exp\left\{k_i^{-}\ell\right\}+k_i^{+}\exp\left\{k_i^{+}\ell\right\}} \quad \text{or} \tag{19a}$$

$$\tan\left\{\kappa_r\lambda_r\pm n\frac{\pi}{2}\right\}=-\frac{\kappa_r\exp\left\{\kappa_i^{-}\lambda_r\right\}+\kappa_r\exp\left\{\kappa_i^{+}\lambda_r\right\}}{\kappa_i^{-}\exp\left\{\kappa_i^{-}\lambda_r\right\}+\kappa_i^{+}\exp\left\{\kappa_i^{+}\lambda_r\right\}}$$

As equ. (19) is implicit in ℓ, we cannot determine the conditions for resonance analytically. However, for a straight channel, $k_i^{-}=-k_i^{+}$ (e.g. equ. (11b), $\tan\left\{k_r\ell\right\}=\infty$, which is the case if $\ell=\lambda/4$, where λ = wave length in a straight frictionless channel, e.g. Dronkers (1964). For a very strong converging channel, e.g. $\lim_{L_b\to 0}k_r=\lim_{L_b\to 0}k_i^{+}=\lim_{L_b\to 0}k_i^{-}=1$, $\tan\left\{k_r\ell\right\}=1$, and $\ell=\lambda/8$. Of course, the wave length in a straight and very converging channel are very much different (in fact if L_b = 0, λ = 0).

The solution to equ. (19) is depicted graphically in Fig. 2.2. Note that typical values for Λ_e range from 1 to 2 (e.g. Chapter 4).

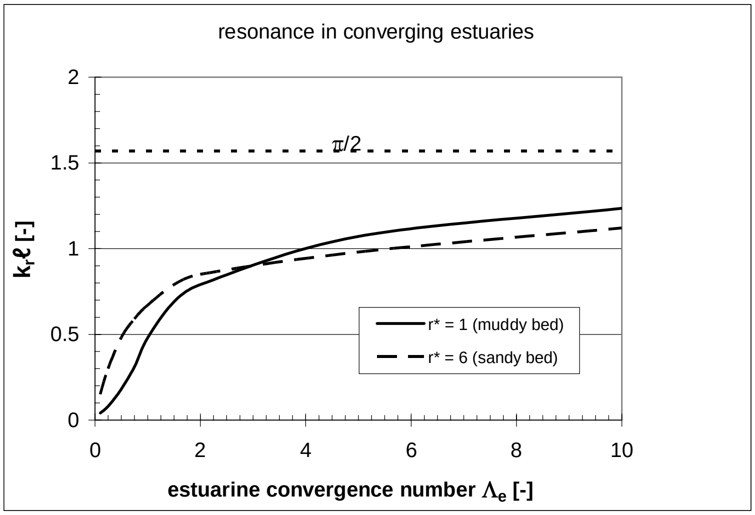

Fig. 2.2: Conditions for resonance (solution of equ. 19) for a converging estuary as a function of the estuarine convergence number.

Note that it is not really possible to re-write equ. (16a), in conjunction with equ. (17) in the form of a single, up-estuary progressing wave with real and imaginary wave numbers k_r and k_i:

$$\tilde{\eta}\left(x,t\right)=h+a_0^{\oplus}\exp\left\{i\left(\omega t-\left(k_r^{\oplus}+ik_i^{\oplus}\right)x\right)\right\} \tag{16c}$$

However, it is possible to determine the damping/amplification of the tide through an equivalent imaginary wave number from the ratio of the tidal amplitudes at two locations, using the definition

$a_2 = a_1 \exp\left\{k_i^{\oplus} x\right\}$, where $k_i^{\oplus}$ is the equivalent imaginary wave number – where relevant however, we have omitted the superscript. We will use this approach in Chapter 4 to establish the effect of reflections in the various estuaries.

tidal asymmetry

Next, we study the dependency of tidal asymmetry on the estuaries' bathymetry. Though we prescribe harmonic solutions (equ.'s (4) and (16) with one frequency only), we can derive a proxy for the internally generated tidal asymmetry by analyzing the celerity of the tidal wave. Further to Friedrichs (2010) and Dronkers (2005) we define an asymmetry parameter $\gamma = c_{\mathrm{HW}}/c_{\mathrm{LW}}$, where c_{HW} and c_{LW} are the celerity at high water (i.e. $h = h_0 + a$) and low water (i.e. $h = h_0 - a$), respectively:

$$\gamma = \frac{c_{HW}}{c_{LW}} = \frac{k_{r,LW}}{k_{r,HW}} = \left[\frac{\sqrt{\left(\Gamma_{LW} - 1\right)^2 + \Gamma_{LW}^2 \left(\frac{r}{\omega h \left(1 - a/h\right)} \right)^2} + \Gamma_{LW} - 1}{\sqrt{\left(\Gamma_{HW} - 1\right)^2 + \Gamma_{HW}^2 \left(\frac{r}{\omega h \left(1 + a/h\right)} \right)^2} + \Gamma_{HW} - 1} \right]^{1/2} \quad \text{with} \tag{20a}$$

$$\Gamma_{LW} = \frac{4}{gh\left(1 - a/h\right)} L_b^2 \omega^2 = \frac{L_*^2}{\left(1 - a/h\right)}$$

$$\Gamma_{HW} = 4 \frac{1 + \Delta b / b_c}{gh\left(1 + a/h\right)} L_b^2 \omega^2 = \frac{b_* L_*^2}{\left(1 + a/h\right)}$$

This proxy is relevant for progressive waves, and looses its meaning in case of a fully standing wave. Equ. (20a) can be written in dimensionless form:

$$\gamma = \frac{k_{r,LW}}{k_{r,HW}} = \left[\frac{\left(1 + a/h\right)}{\left(1 - a/h\right)} \right]^{1/2} \left[\frac{\left[\sqrt{\left(L_*^2 - \left(1 - a/h\right)\right)^2 + \left(\frac{L_*^2 r_*}{\left(1 - a/h\right)} \right)^2} + L_*^2 - \left(1 - a/h\right) \right]}{\left[\sqrt{\left(b_* L_*^2 - \left(1 + a/h\right)\right)^2 + \left(\frac{b_* L_*^2 r_*}{\left(1 + a/h\right)} \right)^2} + b_* L_*^2 - \left(1 + a/h\right) \right]} \right]^{1/2} \tag{20b}$$

Further, for a friction-dominated system we find:

$$\left.\gamma\right|_{r=\infty} = \left.\frac{k_{r,LW}}{k_{r,HW}}\right|_{r=\infty} \approx \left[\frac{\dfrac{1}{\left(1 - a/h\right)} \dfrac{1}{\left(1 - a/h\right)}}{\dfrac{1 + \Delta b / b_c}{\left(1 + a/h\right)} \dfrac{1}{\left(1 + a/h\right)}} \right]^{1/2} = \frac{1 + a/h}{1 - a/h} \sqrt{\frac{1}{b_*}} \approx \frac{\left(1 + a/h\right)^2}{\sqrt{b_*}} \tag{21a}$$

Note that this solution can be derived directly from the general formulation of wave celerity in a straight prismatic compound channel, e.g. $c = \sqrt{gA_c / b_t}$. For a frictionless system we find:

$$\gamma\big|_{r=0} = \left.\frac{k_{r,LW}}{k_{r,HW}}\right|_{r=0} = \left[\frac{\Gamma_{LW} - 1}{\Gamma_{HW} - 1}\right]^{1/2} \approx \left[\frac{\left(1 + a/h\right)^2 \Lambda_e / b_* - \left(1 + a/h\right)}{\Lambda_e - \left(1 + a/h\right)}\right]^{1/2} \qquad (21b)$$

In the next section, we study the behavior of these solutions graphically, analyzing the response of an estuary to deepening and narrowing (loosing intertidal area).

The γ-proxy for tidal asymmetry has been defined for a single up-estuary propagating wave. As long as the effects of reflection are not too large, this proxy is still useful. However, in the asymptotic case of a truly standing wave, the tide is entirely symmetrical, though γ would always be larger than unity.

2.2 The response of an estuary to deepening and narrowing

In this section, we study the behavior of the tidal evolution in a converging estuary graphically. In particular, we analyze the response of the tide to deepening and narrowing of the estuary, where the latter implies reduction/loss of intertidal area. Moreover, we elaborate on the effect of bed friction as one implication of a regime shift towards hyper-concentrated conditions is a dramatic decrease in effective hydraulic drag in the estuary. In the Fig.'s 2.3 and 2.4, we assume a convergence length of L_b = 25 km.

First, we evaluate the behavior of the combined solution of equ. (17, e.g. incoming and reflecting wave), as that solution is not easy to interpret owing to its complex character. Fig. 2.3 indeed shows resonant behavior in an almost straight channel when a weir is placed at a quarter wave length when friction is small. If friction is large enough, damping is predicted. This behavior was presented earlier by e.g. Dronkers (1964) and our results match his results.

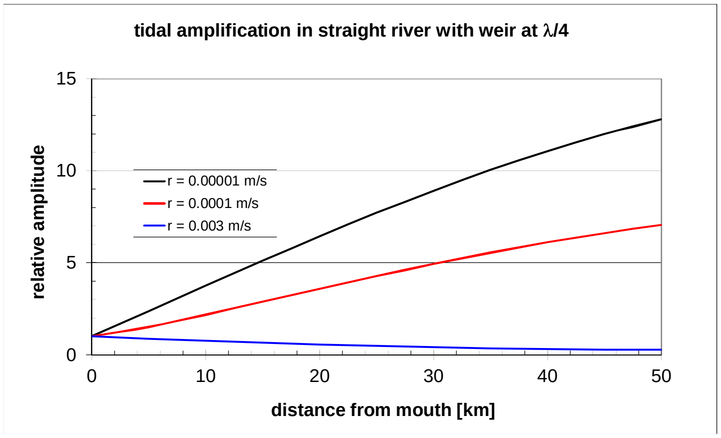

Fig. 2.3: Evolution of tidal wave in 5 m deep, almost straight estuary (λ = 315 km) and weir at 79 km; r = 0.000001 m/s yields $C \approx 1000\ m^{1/2}/s$; r = 0.0001 m/s yields $C \approx 300\ m^{1/2}/s$ and r = 0.003 yields $C \approx 60\ m^{1/2}/s$ (L_b = 50,000 km).

Fig. 2.4 presents computed tidal amplitudes in a 5 m deep converging river (L_b = 33 km, e.g. Ems-conditions) with and without a weir for two values of the friction coefficient, the smaller representative for high-concentration conditions and the larger for a sandy bed. We have also plotted the tidal amplitude computed with k_i^+ for an infinitely long estuary, using the definition $a(x) = a_0 \exp\{k_i^+ x\}$ - these results overlap the solution based on equ. (17) exactly. Fig. 2.4 suggests that the impact of reflections on the tidal amplitude increases with decreasing effective hydraulic drag.

Next, we focus on infinitely long estuaries ($\ell = \infty$), and we study the tidal propagation into the estuary. Fig. 2.5 presents the phase difference between the flow velocity and tidal elevation ϕ (e.g. equ. 13a) as a function of depth, width of intertidal area, and bed friction.

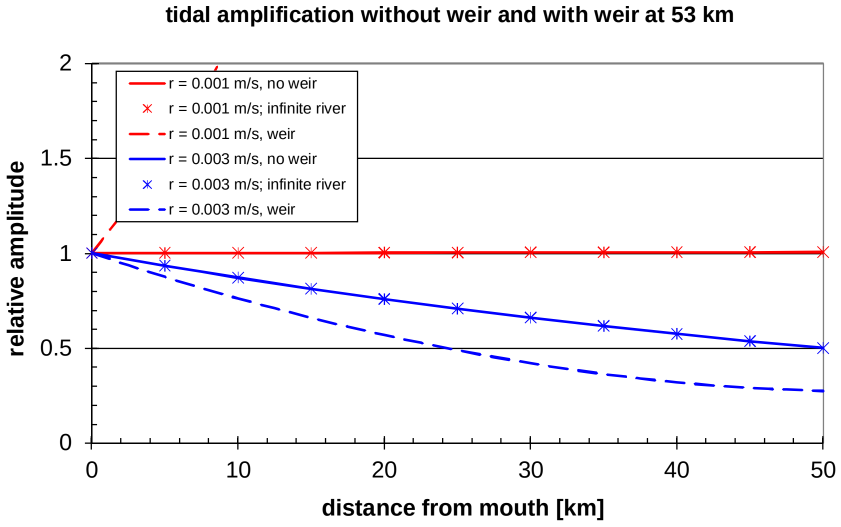

Fig. 2.4: Evolution of tidal wave in short converging estuary (ℓ = 53 km, L_b = 33 km); r = 0.00001 m/s yields C ≈ 300 $m^{1/2}/s$; r = 0.001 m/s yields C ≈ 100 $m^{1/2}/s$; r = 0.003 yields C ≈ 60 $m^{1/2}/s$.

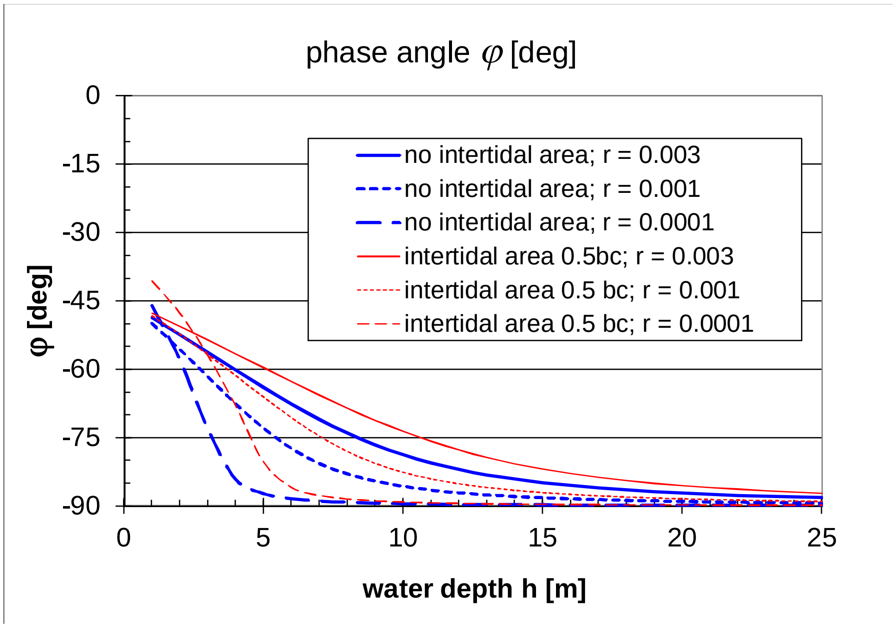

Fig.2.5: Phase angle ϕ between flow velocity and tidal elevation ($\ell = \infty$, L_b = 33 km).

Fig. 2.6 presents the celerity c of the tidal wave into the estuary, using equ. (14a). Because of the rapid increase in c with depth h and inverse friction $1/r$, we have used a logarithmic axis.

For $\phi = -90^o$ (e.g. Fig. 2.5), high water slack (HWS) occurs at high water (HW), as for standing waves. This condition is met at large water depths, but also at moderate water depths when the hydraulic drag becomes small – the tidal amplification is governed by convergence mainly. The latter is the case for instance in the presence of pronounced layers of fluid mud, as in the Ems and Loire Rivers. However, than the friction length increases, and the effects of reflections become more important. Fig. 2.6 shows that then c increases rapidly, and can become so large that high waters along the estuary occur almost simultaneously. For instance, for h = 7 m, and r = 0.001, we find c = 100 m/s (e.g. Fig. 2.6), and high water at 60 km from the river mouth would occur only 10 minutes after high water at that mouth. Note that a progressive wave approach $\left(c = \sqrt{gh}\right)$ would yield a travel time of almost 2 hours.

From equ.'s (3a) and (4a) we observe that $\phi = -90^o$ occurs when $\partial u / \partial x = 0$ (see also Dronkers, 2005 and Friedrichs, 2010), and from equ. (13a), we conclude that $\phi = -90^o$ implies $k_r = 0$. This explains the rapid increase in c. This also implies large flow velocities over the major part of the estuary. Then, owing to the harmonic solution prescribed (equ. 4a), also the tidal amplitude is more or less constant over a large part of the estuary. An estuary with such conditions is called synchronous (e.g. Dronkers, 2005). Examples are the current conditions in the Ems and Loire River (e.g. Chapter 4).

Note that the evolution towards a synchronous estuary is delayed in case of (some) intertidal area, e.g. Fig. 2.5. However, the celerity is not too sensitive to the intertidal area, though decreases with $\Delta b/b_c$ (results not shown).

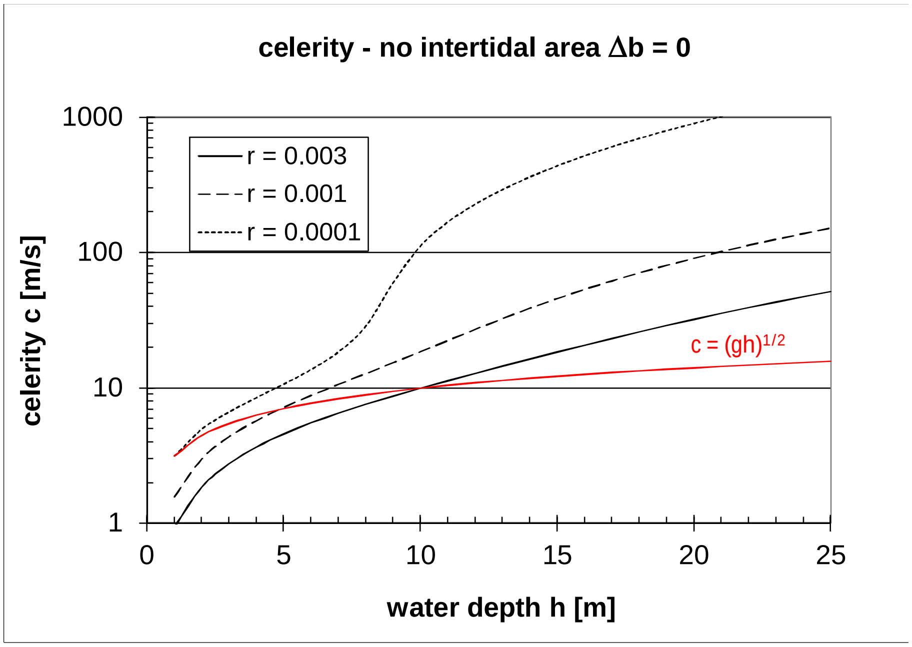

Fig. 2.6: Celerity of tidal wave ($\ell = \infty$, L_b = 33 km) with frictionless straight-channel value $c = \sqrt{gh}$ for reference.

At these resonant conditions for low hydraulic drag, amplification of the tide is governed solely by the convergence of the river's plan form (e.g. equ. 11b). This implies a local equilibrium between water movement and bathymetry. At such conditions, we may expect low sensitivity of the water movement to interventions in the river, in particular of interventions up-estuary. This has great implications for mitigating measures in estuaries at resonant conditions.

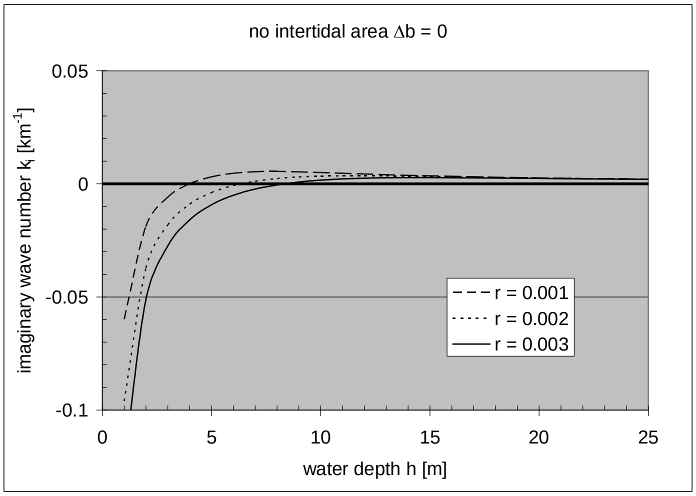

Fig. 2.7: Damping of tidal wave in converging estuary without intertidal area.

Next, we study the amplification of the tide along the estuary; note that $a(x)/a_0 = \exp\{k_i x\}$, e.g. $k_i > 0$ implies amplification of the tide into the estuary. Here we elaborate on the wave numbers directly, whereas in Chapter 5, we will present results in the form of tidal amplitudes facilitating discussion of the results. Fig.'s 2.7, 2.8 and 2.9 show the imaginary wave number as a function of water depth, for three values of the hydraulic roughness (from sandy to muddy conditions) and for three values of the intertidal area. These graphs suggest that a simultaneous deepening and canalization (loss of intertidal area) results in a very sensitive response of the tidal amplitude (e.g. Fig. 2.7). This is in particular the case at low hydraulic drag, which can be explained from the resonant character described above.

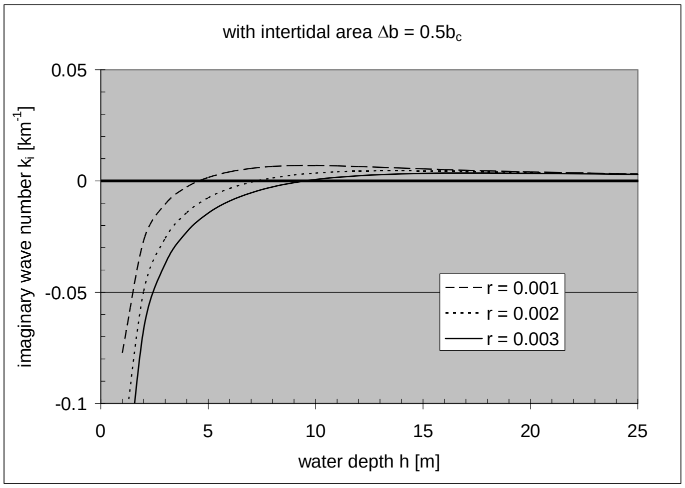

Fig. 2.8: Damping of tidal wave in converging estuary with small intertidal area.

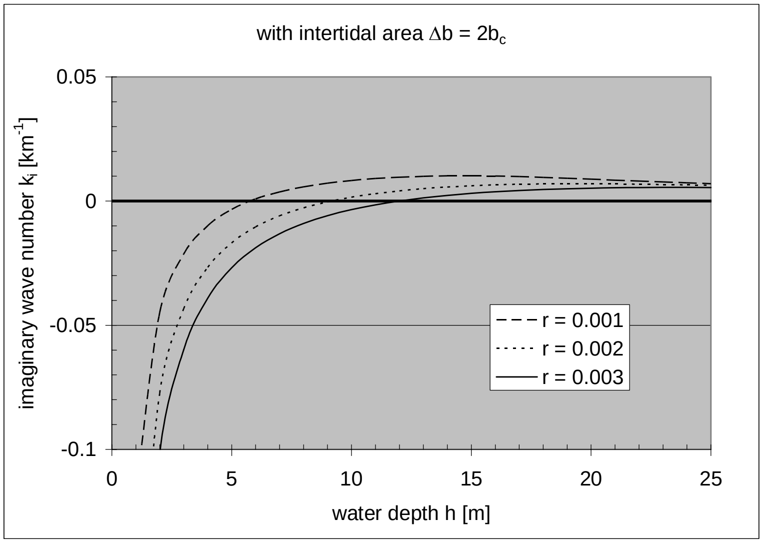

Fig. 2.9: Damping of tidal wave in converging estuary with large intertidal area.

Note that in case of more intertidal area, more water enters the estuary, implying higher water levels, i.e. apparent larger amplification with intertidal area. We conclude that loss of intertidal area has a major effect on the sensitivity of the estuary to further deepening and to a loss in overall hydraulic drag. One may conclude that the resilience of the estuary to human interferences reduces rapidly with the loss of intertidal area.

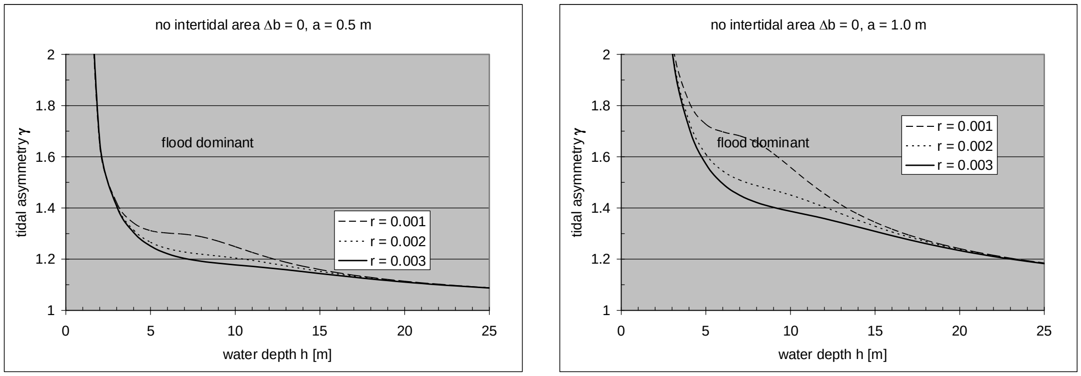

Fig. 2.10: Tidal asymmetry $\gamma\left(=c_{HW}/c_{LW}\right)$ *without intertidal area.*

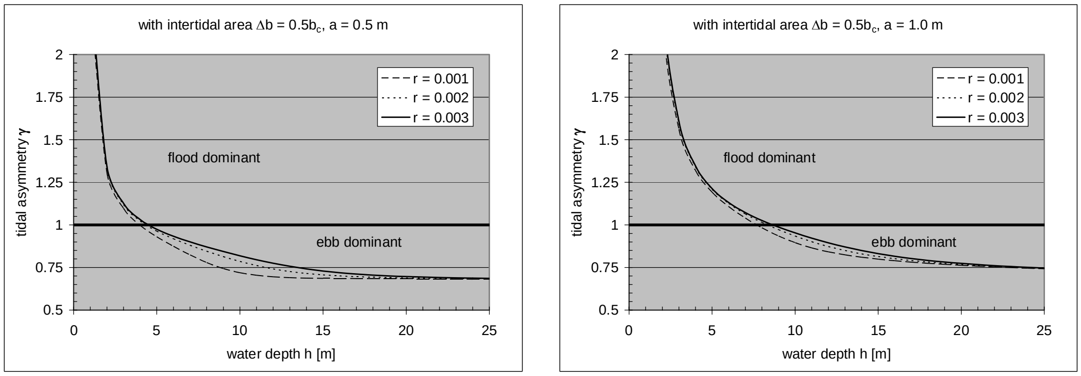

Fig. 2.11: Tidal asymmetry $\gamma\left(=c_{HW}/c_{LW}\right)$ *with some intertidal area.*

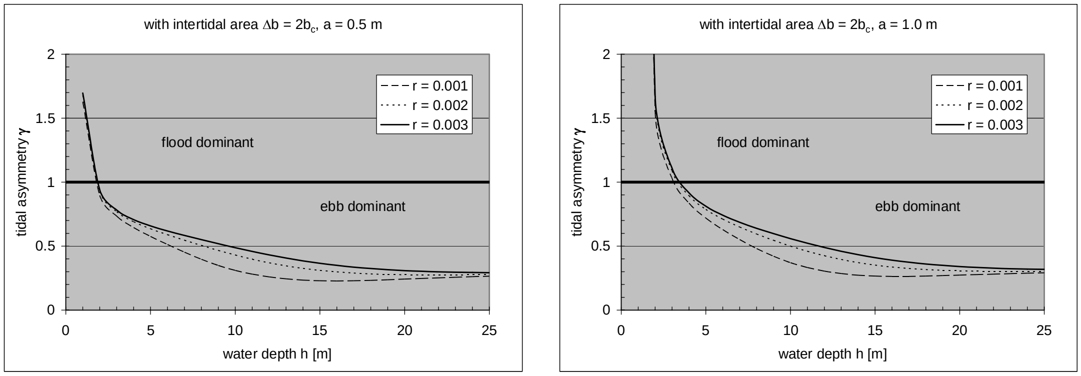

Fig. 2.12: Tidal asymmetry $\gamma\left(=c_{HW}/c_{LW}\right)$ *with large intertidal area.*

Our linear analysis also allows for an assessment of tidal asymmetry, analyzing the celerity at high and low water, e.g. equ. (20). This analysis requires information on the tidal amplitude, and we present results for a = 0.5 m and a = 1 m (kept constant along the river), bearing in mind that the amplitude should be small compared to water depth in our linear approach. The tidal asymmetry parameter γ is presented in the Fig.'s 2.10, 2.11 and 2.12 as a function of water depth for three values of hydraulic drag and three values of intertidal area. Remember that $\gamma > 1$ implies flood dominant conditions.

These graphs suggest a large sensitivity of the tidal asymmetry as a function of the size of the intertidal area. Without intertidal area, the estuary is always flood dominant. This dominance decreases with increasing depth and roughness, but is shown to increase rapidly with tidal amplitude. Small areas of intertidal area (represented by $\Delta b = 0.5b_c$) already have a major effect on the tidal asymmetry. However, Fig. 2.11 suggests that with increasing amplitude such transition can be obtained at larger depths only. Or, in other words, after deepening, restoration of the intertidal only is likely not sufficient to restore the original situation.

These results further suggest that in very shallow estuaries, with depths of a few meters only, flood dominant conditions will always prevail, even for very large intertidal areas.

Finally, the figures (especially Fig. 2.10) suggest a positive feed-back at high concentrations of fine sediment – at these conditions, the effective hydraulic drag reduces, and the system becomes even more flood-dominant, while at the same time the tidal amplification in the estuary increases.

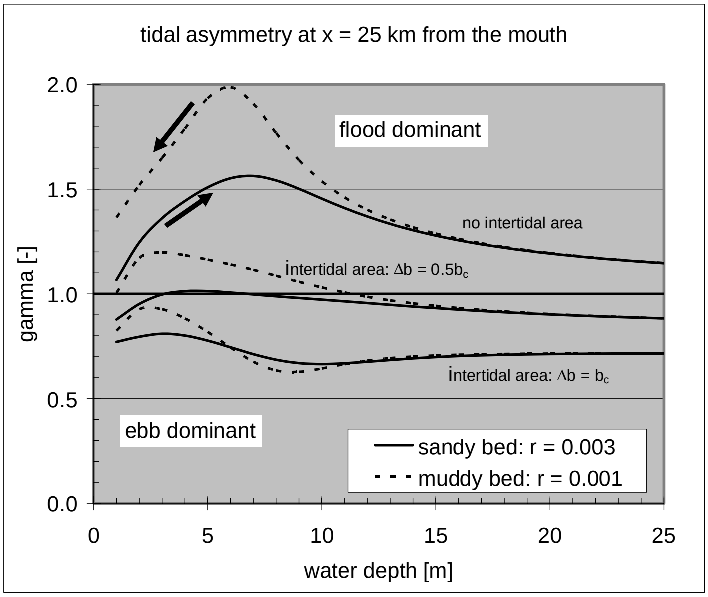

Fig. 2.13: Tidal asymmetry in converging tidal river as function of water depth and intertidal area ($\ell = \infty$, L_b = 33 km).

The results of the Fig.’s 2.7 – 2.9 and 2.10 – 2.12 are combined in Fig. 2.13, where we present the tidal asymmetry at x = 25 km, i.e. almost one converging length from the mouth. First, we have computed the tidal range at this location, accounting for tidal amplification as a function of water depth, hydraulic drag and intertidal area. The resulting amplitude was then substituted into equ. (20) computing the tidal asymmetry at x = 25 km.

Fig. 2.13 shows initially a rapid increase in tidal asymmetry with water depth at water depths between 3 and 7 m in the case without intertidal area. This is in particular true for cases of low hydraulic drag, as when fluid mud is present. This figure also suggests hysteresis in the response of a hyper-concentrated river in case of undeepening, as hyper-turbid conditions are likely to be maintained, owing to the energetically favorable conditions (Section 3.3.)

For the case with some intertidal area ($\Delta b = 0.5 b_c$) the tide is more or less symmetrical, except at low hydraulic drag. When the intertidal area is sufficiently large, ebb-dominant conditions always prevail, and the river is fairly resilient to deepening, as no feed-back occurs.

Fig. 2.13 suggests that in case of no or little intertidal area, deepening leads to progressive flood-dominant conditions, pumping mud into the estuary (or arresting river-borne sediments), as a result of which the hydraulic drag decreases and asymmetry increases further. This would yield a hysteresis in the response of the river to deepening – re-establishing the initial depth will not automatically lead to the pre-deepening conditions of the river.

3 Fine sediment transport in narrow estuaries

3.1 Transport components

In the previous section, we have discussed the development of the tide in a converging estuary. However, an assessment of the tidal evolution of the dynamics of fine sediment transport requires more information. In this section we derive the components for the transport of fine sediment in narrow estuaries, i.e. lateral gradients are small, an discuss components are affected by the tidal dynamics discussed in Chapter 2. We follow Uncles (1985), Fischer et al. (1979) and many others in the decomposition of fine sediments in narrow estuaries. The cross section of the estuary is schematized as before through the compound channel in Fig. 2.1, and we neglect all lateral variations in the flow-carrying cross section. Moreover, again we assume that the flow-carrying cross section A_c may be modeled as $A_c = hb_c$. The longitudinal transport of fine sediment is described with the advection-diffusion equation, in which the effects of exchange of fine sediment between main channel and intertidal area, and over the cross-section of the estuary are accounted for by a dispersion term D_x:

$$\frac{\partial\left(b_c+\Delta b\right)hc}{\partial t}+\frac{\partial b_c huc}{\partial x}-\frac{\partial}{\partial x}hb_c D_x\frac{\partial c}{\partial x}=\left[P\left(x,t\right)-S\left(x,t\right)\right]\left(b_c+\Delta b\right) \tag{22a}$$

in which huc is the fine sediment flux $f(x,t)$ per unit width through the flow-carrying cross section, and P and S are production (f.i. from erosion) and sink terms (in particular sedimentation on intertidal areas) per unit width. In the case of a dynamic equilibrium, we may cancel erosion and deposition in the channel itself, and only the sink term in (22a) is maintained. If we further neglect longitudinal turbulent diffusion, we can simplify equ. (22a) into

$$\frac{\partial hc}{\partial t}+\frac{b_c}{b_c+\Delta b}\frac{\partial huc}{\partial x}-\frac{b_c}{b_c+\Delta b}\frac{1}{L_b}huc=-\frac{\Delta b}{b_c+\Delta b}S\left(x,t\right)\text{ or} \tag{22b}$$

$$\frac{\partial hc}{\partial t}+\frac{b_c}{b_c+\Delta b}\left(\frac{\partial f}{\partial x}-\frac{f}{L_b}\right)=-\frac{\Delta b}{b_c+\Delta b}S\left(x,t\right) \tag{22c}$$

Further to its effects on the tidal movement in a converging estuary, the loss of intertidal area will reduce accommodation for deposition of fine sediment ($S \to 0$), and the mass of sediment in the estuary per unit width hc increases.

Next, we elaborate on the flux f addressing the various contributions by estuarine circulation, tidal asymmetry, etc. Therefore, water depth h, flow velocity u and suspended sediment concentration c are decomposed in depth-mean values, their variation over depth, tide-mean values, and variation over time[2)]:

[2)] *Note that in our schematization* b_c *and* Δb *are not a function of time, though at low water,* $b_{tot} = b_c$.

$$\begin{aligned} h &= \langle h \rangle + \tilde{h}(t) \\ u &= \langle \bar{u} \rangle + \tilde{\bar{u}}(t) + \langle u'(z) \rangle + \tilde{u}'(z,t) \\ c &= \langle \bar{c} \rangle + \tilde{\bar{c}}(t) + \langle c'(z) \rangle + \tilde{c}'(z,t) \quad \text{with} \\ \langle \tilde{x} \rangle &= \frac{1}{T}\int_T \tilde{x}\ \mathrm{d}t = 0, \qquad \overline{x'} = \frac{1}{h}\int_h x'\ \mathrm{d}z = 0 \end{aligned} \tag{23}$$

in which $\tilde{\bullet}$ and $\bullet'$ represent variation over time and depth, respectively, and triangular brackets and overbar averaging over the tidal period T and water depth h, respectively. Note that all parameters in equ. (23) are still a function of x. Substituting equ. (23) into the advection term of equ. (22a), yields for the longitudinal sediment flux per unit width F [kg/m], integrated over the depth first and next over the tidal period:

$$F = \int_T \left\{ \int_h (uc)\ \mathrm{d}z \right\} \mathrm{d}t = T \left\langle \bar{f} \right\rangle = T \left\langle h\overline{uc} \right\rangle =$$

$$\begin{aligned} &= T\Big[\langle h \rangle \langle \bar{u} \rangle \langle \bar{c} \rangle + \langle h \rangle \left\langle \tilde{\bar{u}} \cdot \tilde{\bar{c}} \right\rangle + \langle h \rangle \left\langle \overline{u'c'} \right\rangle + \langle h \rangle \left\langle \overline{\tilde{u}'\tilde{c}'} \right\rangle + \\ &\quad + \left\langle \tilde{h}\left(\langle \bar{u} \rangle \tilde{\bar{c}} + \tilde{\bar{u}} \langle \bar{c} \rangle + \tilde{\bar{u}} \cdot \tilde{\bar{c}} + \overline{u'c'} + \left\langle \overline{\tilde{u}'\tilde{c}'} \right\rangle + \left\langle \overline{u'\tilde{c}'} \right\rangle + \left\langle \overline{\tilde{u}'c'} \right\rangle \right) \right\rangle \Big] = \end{aligned} \tag{24}$$

$$\begin{aligned} &= T\Big[\langle \bar{u} \rangle \langle h \cdot \bar{c} \rangle + \left\langle \tilde{h} \cdot \tilde{\bar{u}} \right\rangle \langle \bar{c} \rangle + \left\langle h \cdot \tilde{\bar{u}} \cdot \tilde{\bar{c}} \right\rangle + \\ &\quad + \left\langle h \cdot \overline{u'c'} \right\rangle + \left\langle h \cdot \overline{\tilde{u}'\tilde{c}'} \right\rangle + \left\langle \tilde{h} \cdot \overline{u'\tilde{c}'} \right\rangle + \left\langle \tilde{h} \cdot \overline{\tilde{u}'c'} \right\rangle \Big] \equiv F_r + F_S + F_p\,(= F_a) + F_g + F_v + F_l \end{aligned}$$

Here we have defined the following six contributions to the longitudinal transport of fine sediment, ignoring the possible longitudinal transport by dispersion (D_x; even though this transport can be large):

F_r	Residual fine sediment transport as a result of net river flow and a net transport rectifying for Stokes drift, in which $\langle \bar{u} \rangle$ = residual flow velocity (river flow and rectifying Stokes drift). If the Stokes drift is zero, as for low-friction synchronous converging (short) estuaries, then $F_r = Tq_{riv} \langle h \cdot \bar{c} \rangle / h$, where q_{riv} = specific river discharge, i.e. per unit width.
F_S	This term is known as the Stokes drift. For a low-friction synchronous(short) estuary with exponentially converging river plan form. For fine sediments, which are reasonably well mixed over the water column, the Stokes drift F_s and its rectification are more or less equal, and we do not further discuss these terms.
F_p	This term is generally known as tidal pumping. Note that this term represents the important asymmetries in peak velocity and in slack water velocity (scour and settling lag), and is responsible for the net transport of (fine) sediment by tidal asymmetry. We

will therefore refer to this term as F_a, highlighting the tidal asymmetry contributions. The tidal analysis discussed in Chapter 2 focuses on this term.

F_g This term is generally referred to as the estuarine circulation, or gravitational circulation, induced by longitudinal salinity gradients – sometimes longitudinal gradients in temperature and/or suspended sediment may play a role as well, but these are not elaborated in this report.

F_v This term represents asymmetries in vertical mixing, sometimes referred to as internal tidal asymmetry (Jay and Musiak, 1996). Note that these asymmetries can be induced by vertical salinity gradients, and/or by vertical gradients in suspended sediment.

F_l The last two terms are triple correlations, and represent lag effects, such as around slack water, and settling and scour lag (e.g. Dronkers, 1986; Postma, 1961; and Van Straaten & Kuenen, 1957 & 1958). Note that these triple products are often ignored in literature on the decomposition of transport fluxes, though they can be very important, in particular for starved-bed conditions.

The decomposition of transport terms was first developed to study the salinity distribution in estuaries (e.g. Dyer, 1997 and Fischer et al., 1979). Later, for instance Uncles (1985) and others applied this technique analyzing sediment fluxes in estuaries. Note that different authors use various definitions for the transport components in equ. (24) – the various terms therefore may not always directly be compared with literature values.

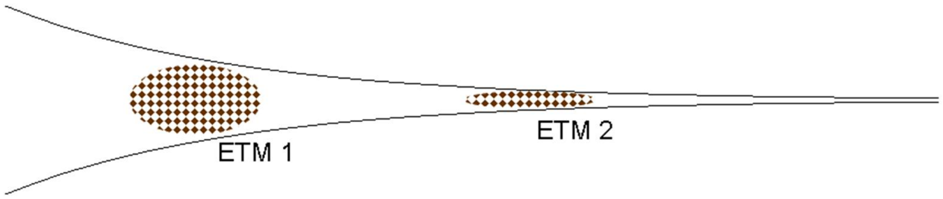

Fig. 3.1: Sketch of converging estuary with two ETM's (estuarine turbidity maximum).

The transport by asymmetries in tidal peak velocity (also referred to as tidal pumping) is important in particular for alluvial conditions, i.e. when abundant fine sediment is available. This is certainly the case in rivers such as the Ems River and Loire River, as explained below. When the river bed is predominantly sandy containing little fines (starved bed conditions), asymmetries in/around the slack water period are often more important.

In general, one finds a turbidity maximum near the mouth of the estuary near the head of salinity intrusion, referred to as ETM-1 in Fig. 3.1. Here, the sediment transport is governed by a balance between river-flow induced flushing, and import by estuarine circulation (possibly in conjunction with salinity-induced internal tidal asymmetry) and tidal asymmetry (slack water asymmetry) – the more important terms are given in bold:

$$\boldsymbol{F_r} + F_a + \boldsymbol{F_g} + F_v + F_l = 0 \tag{25a}$$

It may be argued that as long as the river flow is large enough to flush the turbidity maximum out of the river at times (once a year?), no fine sediments can accumulate in the river forming hyper-concentrated conditions. Our linear model is unsuitable to analyze such conditions in more detail, though a qualitative description is given in Section 3.2.

When suspended sediment concentrations within the river, and/or when sediment loads from the river are large, a second turbidity maximum may be formed (ETM2 in Fig. 3.1) through a balance by river-induced flushing and tidal asymmetry (peak velocities and internal asymmetry):

$$\boldsymbol{F_r} + \boldsymbol{F_a} + F_v + F_l = 0 \tag{25b}$$

Again, the most important processes are given in bold. Such a second ETM is found for instance in the Ems River (Fig. 3.2) where high suspended sediment concentrations are found in the fresh water region, well beyond the head of salinity intrusion. However, Fig. 3.2 suggests that within the Ems no localized ETM is found, but a large patch of highly turbid water that moves to and from with the tidal excursion. We anticipate that this is due to the slow remobilization of sediment from the bed, inducing a longitudinal dispersion of the sediment over the tidal excursion.

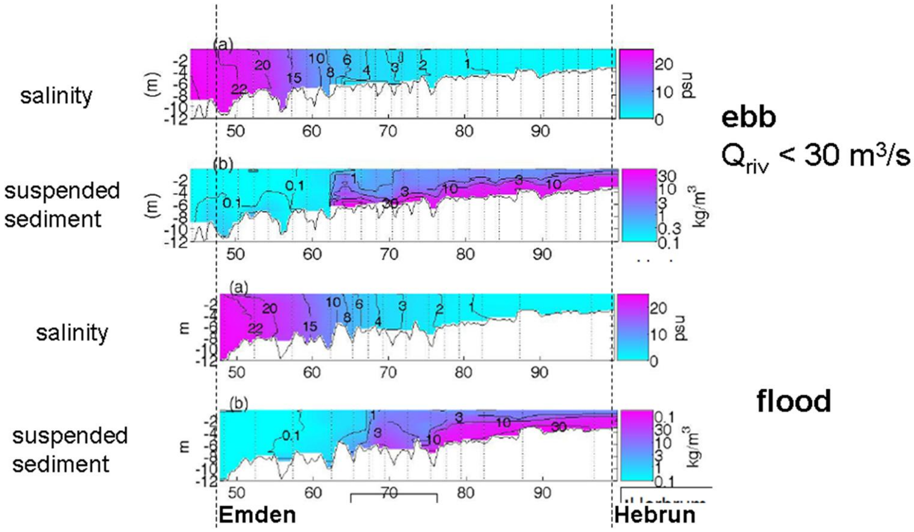

Fig. 3.2: Measured (August 2, 2006) salinity and SPM distributions in the Ems River during flood and ebb (after Talke et al., 2009) – note that the suspended sediment dynamics have become independent of the salinity dynamics.

In Section 3.4 we describe qualitatively the evolution from a "normal" estuary to a hyper-concentrated system, with the Ems River as an example. We argue that it is the change in dominant processes, e.g. from the balance of equ. (25a) to (25b) which characterizes this regime shift, and which is responsible for the persistence of this new regime with its second turbidity maximum (ETM 2).

3.2 Reduction in effective hydraulic drag

In Chapter 2 we have shown that the response of the tide in a converging estuary is sensitive to the effective hydraulic drag. In this section we present a simple formula to assess reductions in hydraulic drag as a function of suspended sediment concentration. Note that these formulae do not apply for very high concentrations, when fluid mud is formed (occasionally).

Winterwerp et al. (2009) derived a simple formula to quantify the reduction in hydraulic drag as a function of enhanced levels of suspended sediment concentration and longitudinal salinity gradients:

$$\frac{\overline{u}}{u_*} \equiv \frac{C_{eff}}{\sqrt{g}} = \frac{C_0}{\sqrt{g}} + \frac{C_{SPM}}{\sqrt{g}} = \frac{C_0}{\sqrt{g}} + 4\frac{h}{h_{ref}}\mathbf{Ri}_*\boldsymbol{\beta} \tag{26a}$$

or in terms of excess Chézy coefficient, where h_{ref} is set to unity:

$$\frac{\Delta C_{eff}}{\sqrt{g}} = 4h\mathbf{Ri}_*\boldsymbol{\beta} \tag{26b}$$

in which the Rouse number $\boldsymbol{\beta}$ and bulk Richardson number $\mathbf{Ri}_*$ are defined as:

$$\mathbf{Ri}_* \equiv \frac{(\rho_b - \rho_w)gh}{\rho_b u_*^2} = \frac{\varepsilon_\rho cgh}{(\rho_w + \varepsilon_\rho c)u_*^2} \quad \text{and} \quad \boldsymbol{\beta} \equiv \frac{\sigma_T W_s}{\kappa u_*} \tag{27}$$

in which σ_T is turbulent Prandtl-Schmidt number.

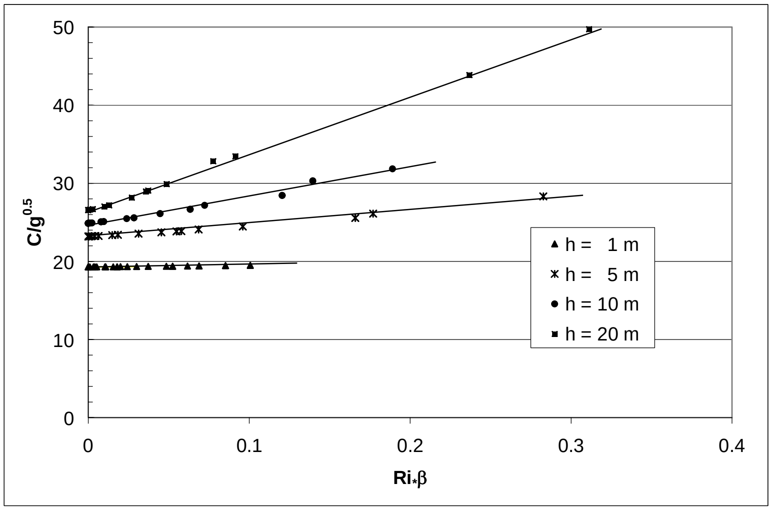

*Fig. 3.3: Effective hydraulic drag (*Chézy *coefficient) as function of the bulk Richardson and Rouse number.*

From the implicit equ. (27) we can draw the following conclusions on the effective Chézy number:

1. The effective Chézy coefficient increases, hence the hydraulic drag decreases with increasing water depth.
2. The effective Chézy coefficient increases with suspended sediment concentration c.
3. The effective Chézy coefficient increases with settling velocity, hence with flocculation.

Note that the reduction in effective hydraulic drag is essentially induced by vertical stratification, induced by vertical gradients in the suspended sediment (SPM) concentration. Because of hindered settling effects, the same vertical gradient in SPM concentration can exist at relatively low and relatively high concentrations. Or in other words, low- and high-concentrated mixtures can be kept in suspension with the same kinetic energy (e.g. Section 3.3).

Hence, the effective Chézy coefficient scales with the following dimensionless parameters:

$$\frac{C_{eff}}{\sqrt{g}} \propto \mathbf{Ri}_*, \boldsymbol{\beta} \tag{28}$$

The relation between the effective Chézy coefficient and suspended sediment concentrations (e.g. equ. (26)) is shown in Fig. 3.3. Note that the rivers discussed in this report have water depth of typically 5 – 10 m, hence we expect an increase in the effective Chézy coefficient by 15 – 30 m1/2/s. Only the Elbe is considerably deeper, and the excess Chézy value is therefore expected to be larger as well.

3.3 Hyper-concentrated conditions

The literature contains a variety of definitions on hyper-concentrated conditions. In this section, we present a definition which is relevant for the present study. Winterwerp (2011) argues that the Ems and Loire River are currently in these hyper-concentrated conditions.

In our definition, hyper-concentrated conditions are related to the concept of saturation (e.g. Winterwerp, 2001). Let us assume a straight, prismatic channel with a uniform flow at flow velocity U_1. First, we analyze the transport of sand in suspension. From all classical literature, and data on sand transport, we know that an equilibrium sand transport is established, with an equilibrium vertical profile in suspended sand concentration, which can be described with a classical Rouse profile. This profile describes a balance between vertical turbulent mixing and settling of the grains by gravity. If the flow velocity U_1 is reduced to U_2, then a new equilibrium is established immediately, at smaller suspended sand concentrations though. A new equilibrium between vertical turbulent mixing and settling is established, the suspended sand concentration being smaller because turbulent mixing is smaller owing to the decrease in flow velocity. Note that upon deposition from state 1, sand grains form a rigid bed immediately, allowing full turbulent production, at state 2 conditions, though.

In the case of fine suspended sediment, a different picture emerges, owing to the fact that fine sediment consists of flocs with high water content (up to 95%). When the flow velocity decreases from U_1 to U_2, the fine sediment flocs settle as well, owing to the decrease in turbulent mixing in response to the lower flow velocity. However, these flocs do not form a rigid bed immediately, but a layer of soft fluffy sediment. As a result, turbulence production decrease beyond the value expected at state 2 conditions over a rigid bottom, and more flocs settle, as turbulent mixing drops further. This snowball effect continues till virtually all flocs have settled on the bed: a layer of fluid mud has been formed. These conditions are referred to as saturation, and have been elaborated in detail in Winterwerp (2001).

A similar condition emerges when the flow velocity is kept constant, but the suspended fine sediment concentration slowly increases. At a certain level, referred to as the saturation concentration, vertical turbulent mixing is too small to keep the flocs in suspension, and a fluid mud layer is formed by the snowball effect described above. This is depicted in Fig. 3.4 (e.g. Winterwerp, 2011, 2006). The horizontal axis depicts the volumetric concentration ϕ of the suspended sediment, in case of fine sediment, the volume concentration of the flocs; the vertical axis depicts the flux Richardson number $\mathbf{Ri_f}$, a parameter describing that part of the kinetic energy of the flow available for mixing.

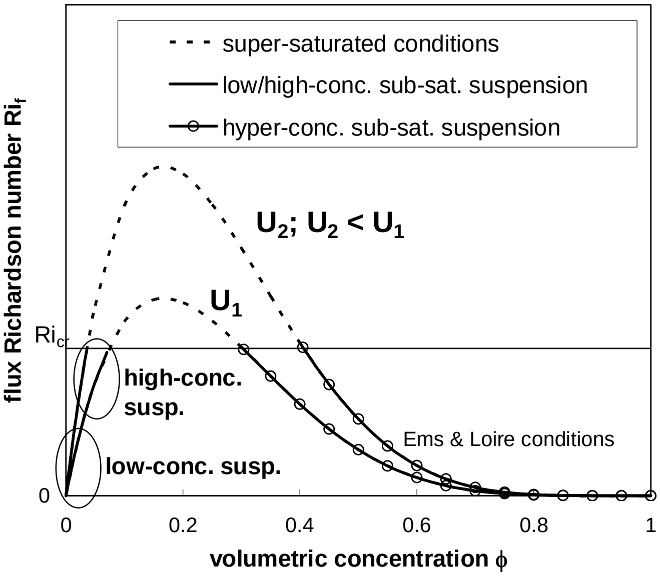

Fig. 3.4: Stability diagram showing saturation and super-saturated conditions (dotted line). At smaller concentrations rivers are in the left branch of the diagram, at higher concentrations, right-branch conditions prevail – these are referred to as hyper-concentrated conditions. The flux Richardson number $\mathrm{Ri_f}$ *yields a proxy for the (kinetic) energy required for vertical mixing, and this diagram shows that each value of* $\mathrm{Ri_f}$ *(at sub-critical conditions) can be obtained with two different volumetric concentrations.*

From the above, and from Fig. 3.4 we can conclude that at low suspended sediment concentrations (left branch of Fig. 3.4), an increase in suspended sediment concentration, for instance through erosion of the bed, will ultimately lead to a collapse of the concentration profile, the formation of fluid mud, hence super-saturated conditions. In terms of Fig. 3.4, we follow the stability curve to the right, and up to larger $\mathbf{Ri_f}$ values until a critical value is surpassed. In Section 3.2 we have shown that prior to these conditions, already a profound decrease in effective hydraulic drag may occur.

In the right-hand branch of the stability diagram, we refer to hyper-concentrated conditions. The suspended sediment concentration is so high, that the sediment's settling velocity decreases significantly (up to two orders of magnitude), so that very little turbulent energy/mixing is required to keep the sediment in suspension. Furthermore, we note that if the flow would erode sediment from the bed, we would follow the stability curve to the right, but now to lower $\mathbf{Ri_f}$ values, contrary to the low-concentrated conditions above. This implies that the suspension becomes more stable: "it likes" to erode the bed, reducing the energy to keep the sediment in suspension. This is one reason that hyper-concentrated conditions are so persistent, and that rivers, such as the Ems and the Loire, brought into these hyper-concentrated conditions, are difficult to train back into conditions more favorable from an environmental point of view. The reader is referred to Bruens et al. (2012) for a full analysis on the stability of these hyper-concentrated conditions, and why they do not consolidate, but remain fluid over such long periods of time.

3.4 A qualitative description of the regime shift in the Ems estuary

Winterwerp (2010) analyzed how the Ems River responded to ongoing deepening. We have no data on the transition of the Ems River from a “normal” turbid river into its current, hyper-concentrated state over time (Fig. 3.2). Therefore, we have developed a conceptual picture for the transition of the river as a result of deepening from its former equilibrium, using our observations described on the previous pages. This picture is summarized in Table 3.1. We start a long time ago from a long-term equilibrium, referred to as phase 0 in Table 3.1, at which up-river directed fine sediment transport induced by gravitational circulation and the various effects of tidal asymmetry balance the down-river transport induced by the river flow. The fine sediments in the Ems River are mainly marine-born, though some sediment may be delivered by the river. Over shorter time periods, accumulation or flushing may occur, as a result of e.g. varying river flows. Under these conditions, the formation of an estuarine turbidity maximum (ETM) is expected near the head of the saline intrusion. Over longer time scales, land formation initiated on vegetated mudflats, may reduce the river’s tidal volume, affecting the long-term morphodynamic equilibrium.

As a response to deepening, net accumulation is expected, restoring equilibrium, Phase 1, Table 3.1. The underlying processes are a decrease in river-induced flushing, as river flow velocities decrease in proportion to the river’s cross section, in conjunction with an augmented net transport by gravitational circulation, as water depth increase (scales with h^2). Deepening would also increase tidal asymmetry in case of reduced intertidal areas (e.g. Chapter 2). Possibly, reduced vertical mixing already starts to play a role, enhancing the trapping efficiency of the river (see below). As the accumulating fine sediments do not form a rigid bed immediately, also turbidity levels increase, as more sediments are available for remobilization, and suspended sediment concentrations in the ETM increase.

A further increase of the river’s depth would increase the amount of remobilizable sediments further, accompanied by a further increase in suspended sediment concentrations. When the riverbed becomes predominantly muddy, profound feed-backs between the various processes are expected through which the river evolves into its present hyper-concentrated state. In this regime, gravitational circulation still plays a role, but its effect is small compared to the dominant contributions of internal tidal asymmetry, with profound differences in vertical mixing during ebb and flood: during ebb, the river is highly stratified by sediment-induced buoyancy destruction.

Winterwerp (2010) suggests that this regime shift may be initiated in the Ems River at depth-averaged concentrations typically of the order of a few 100 mg/l. Then, the trapping efficiency of the river increases rapidly as a result of vertical stratification during ebb, and asymmetry in floc size. The rate at which the river really accumulates fine sediments is determined merely by the supply of these sediments from the Wadden Sea – Dollard estuary, than by internal hydro-sedimentological processes.

We anticipate a second regime shift in the estuary, Phase 3, Table 3.1, when the river starts to develop pronounced occurrences of fluid mud, as observed presently by Schrottke (2008). In that case, fine sediment transport rates are expected to be dominated by the tidal asymmetry of the peak currents themselves. Now re-entrainment of the fluid mud layers, which scales with U^3 as well, becomes a dominant mechanism (Bruens et al., 2012). Sediment is transported up-river towards the river’s head at Herbrum by the large tidal asymmetry, and the entire river becomes highly turbid. As the consolidation rate of fluid mud layers scales with their thickness squared, we expect that the properties of the fluid mud layer are fully determined by the velocities during flood conditions. Note that not much consolidation of the thick fluid mud layers during ebb is expected.

Table 3.1: Summary of Ems River response to its deepening – see text for further explanation; river depth in Phases 2 and 3 are not necessarily larger than in Phase 1. Phase 0 refers to “undisturbed” state of the river.

phase	**dominant transport processes**		**comments**
	flood-directed transport	**ebb directed transport**	
0	“normal” estuary with ETM; equilibrium[†)]		long-term balance between ebb and flood transport
	(slack water) tidal asymmetry; gravitational circulation[ɘ)]	river-induced flushing	
1	small disturbance; transient state		net import;
	(slack water) tidal asymmetry ? enhanced gravitational circ.	reduced river-induced flushing	weak feed back
2	large disturbance; transient state		large net import;
	internal tidal asymmetry: mixing & floc size; limited sediment load & determined by ebb conditions;		strong feed-back; large trapping
	fairly well-mixed flood; relative unimportant grav. circ.; sediment-induced grav. circ. ?	stratified ebb; fluid mud; small ebb transport	
3	hyper-concentrated estuary; new equilibrium[‡)]		large net import;
	asymmetry in tidal velocity; internal tidal asymmetry; pronounced fluid mud formation; capacity conditions; transport formula applicable		strong feed-back; large trapping

[ɘ)] Including possible effects of internal asymmetry, in particular when the salinity field is stratified,

[†)] Long-term equilibrium may be disturbed by land formation, reducing estuary’s tidal volume,

[‡)] Without maintenance, estuary may return towards its original state if a rigid bed can be formed.

In summary, we infer that in response to deepening of the Ems River, the sediment load in the river first increases through an increase in the up-river transport by gravitational circulation and a decrease in river-induced flushing. Then, in the second phase of the river’s transition towards its hyper-concentrated state, when the concentration in the river attains values of a few 100 mg/l, internal tidal asymmetry becomes dominant because of pronounced interactions between the sediment load, and the turbulent water movement and vertical mixing. We believe that the 1990-survey conditions (e.g. Van Leussen, 1994) fall within this second phase of development. Finally, the load of fine sediment becomes so large that in the final phase of the river’s evolution, thick fluid mud layers are formed, and the up-river fine sediment transport is dominated by tidal asymmetry of the current velocity. The second phase in transition is probably not stable: trapping is so large that a further development towards the final phase may be inevitable; the time scale of this intermediate phase depends mainly on the sediment supply, and may amount to a decade or so, as in the Ems River.

Finally, tidal reflections from the weir at Herbrum are expected to augment the tidal range by a few dm (e.g. Fig. 2.4), further increasing the tidal pumping of mud into the river.

4 Comparison of various estuaries

In this section, we compare properties and evolution of a number of estuaries and tidal rivers:

- Ems – Germany & The Netherlands
- Loire – France
- Elbe – Germany
- Weser – Germany
- Upper Sea Scheldt – Belgium

We have some data available for the Humber (Ouse) and Tamar, both in the UK, the Garonne and Vilaine, both in France, and the Passaic River in the USA. Note that Kuijper presented similar analyses for the Western Scheldt estuary.

In the following, the data of the various rivers are analyzed – a synthesis of this analysis is given in Chapter 5. In this phase of the study we ignore the effects of reflection by a weir, as this is not easily to be accounted for in an analytical approach. Based on the graphs of Fig. 2.4, it is anticipated that the tidal amplitude is under-estimated with the single-wave analytical model by a few decimeter. This implies that a lower friction coefficient (larger Chézy value) is required in calibrating the model to reproduce observed tidal elevations. However, we expect that the relative effect of deepening and fine sediments are still reasonably well predicted.

In a next phase of the study we will account for the effects of reflections on barriers/weirs in the river, but the in current study we discuss the effects of reflections only qualitatively.

The procedure of our data analysis is as follows:

1. We have collected and analysed all available data on historical interventions in the various rivers, starting from the time that the first tidal data are available.
2. The convergence length L_b of the river has been established by plotting the width of the flow-carrying cross-section against length. In some cases, L_b showed a profound kink mid-river, in which case we apply two different values of L_b. Apart for the Elbe and Loire, L_b remained more or less constant over the period over which tidal data are available.
3. When available, the width of the intertidal area was established. If not, an estimate was made on the basis of Google-Earth images – note that in those cases Δb is quite small, and does not contribute too much to the tidal dynamics, hence errors in these are not too important.
4. Water depths were provided in various formats, such as the depth of the river’s thalweg. Ideally, the hydraulic radius is to be used, but the mean depth $h = A_c/b_c$ is a good approximation in shallow rivers, which has been used throughout the study.
5. Water depths are generally given with respect to some reference level. The mean water depth had therefore to be corrected for the tidal range, assuming the mean slope is not too large. As a rule of the thumb, we presume that the mean water level is found midway high and low water.
6. The river is subdivided into subsections in between the tidal stations. For each subsection, a characteristic water depth and convergence length are determined.
7. The imaginary wave number k_i is determined from the data for each subsection by dividing the measured tidal ranges of two adjacent tidal stations being Δx apart: $\left(a_2 / a_1 = \exp\left\{k_i \Delta x\right\}\right)$.
8. When times of bathymetrical and tidal data do not synchronize, either of the two have been interpolated, obtaining a consistent set of synchronous data.

9. Imaginary wave number and bathymetrical data were made dimensionless, obtaining κ_i and Λ_e, as discussed in Chapter 2.
10. These data points are plotted in a $\kappa_i - \Lambda_e$ diagram; every pair of these parameters represents the measured bathymetry and tidal amplification/damping of one subsection of the river for one particular time period. Then, the analytical solution (equ. 10b of Part I) was fitted through these data points by tuning the friction parameter r_*. Note that we assume infinitely long rivers, and do not account for possible reflections against a weir, or otherwise, unless stated otherwise.
11. For some rivers, we studied the effects of tidal reflections in a schematic way; a more thorough approach requires a different model.
12. Step 10 yields the time evolution of r_*, e.g. the change in effective hydraulic drag over time. From r_*, the Chézy coefficient is established, for which the flow velocity is needed. For this, we use the analytical solution given by equ. (5c).
13. Finally, we determine the tidal asymmetry. In most cases, data on asymmetry are given, and we do not need to use the proxy γ, defined in Chapter 2.
14. For the Elbe and Scheldt rivers, an indicative assessment of the contributions of tidal reflections to the tidal amplifications is made.

Hence, the linear model discussed in Chapter 2 is merely used as a tool to analyze the historical data from the various rivers. By making tidal amplification/damping and river geometry/bathymetry dimensionless, we can compare the various rivers mutually (e.g. Chapter 5).

4.1 The Ems River

The Ems River is about 53 km long from the weir at Herbrum to Emden, flowing through Germany into the Ems-Dollard estuary (Fig. 4.1). This river is renowned for its large suspended sediment concentrations, with values up to 30 – 40 g/l over most of the upper part of the river (e.g. Talke et al., 2009). These high concentrations are found well beyond the region of salinity intrusion, and move to and fro with the tide. Also profound layers of fluid mud are found, in particular around slack water and neap tide (e.g. Schrottke, 2008). Currently, the total mass of suspended solids amounts to about 1 Mton, while yearly about 1.5 Mton of solids is removed from the Ems River by dredging. For further details on the river, the reader is referred to Krebs and Weilbeer (2005).

The Ems River is characterized by a profound tapering, as shown in Fig. 4.2. The overall convergence length of the river amounts to about 19 km, whereas for the stretches between Emden – Leeroort $L_b \approx 32$ km, Leeroort – Papenburg $L_b \approx 27$ km, and Papenburg – Herbrum $L_b \approx 33$ km. In the following, we refer to these three sections as E-L, L-P and P-H. The apparent discrepancy of the overall convergence length and those of three smaller stretches of the river is attributed to some jig-saw patterns in the b-x curve (e.g. Fig. 4.2). In our analysis, we used the larger values.

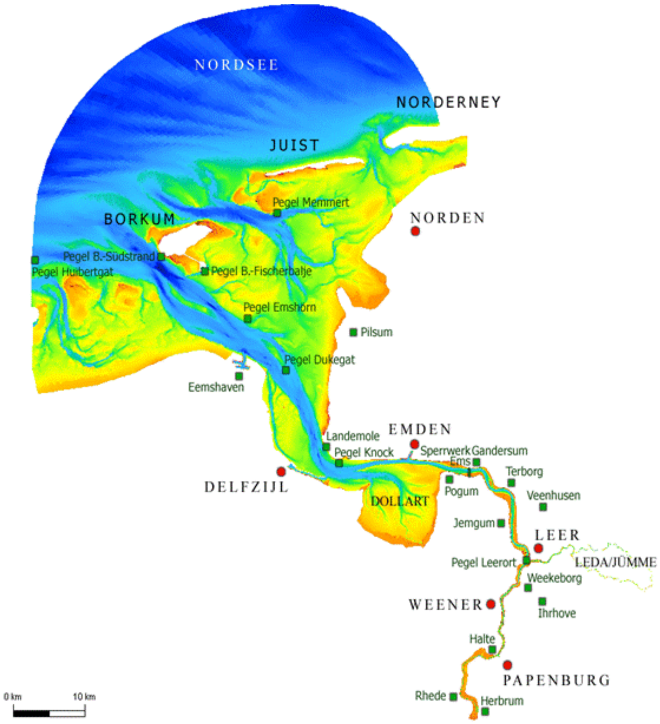

Fig. 4.1: Lay-out of Ems-Dollart estuary and Ems River.

An overview of the various interventions in the river was summarized in Vroom et al. (2012), based on information from Rijkswaterstaat and the Bundesanstalt fur Wasserbau. The evolution in design depths of the river for the three stretches E-L, L-P and P-H is presented in Fig. 4.3, where the depths have been averaged to obtain mean values for these stretches. The river is only deepened to these design depths when large cruise ships have to be conveyed down-estuary, which occurs on average once per year. Note that after 1940 no reclamation of intertidal area took place, though we anticipate that a large part of the remaining intertidal areas has been lost in due time owing to sedimentation on these areas (see discussion below). Around 1961, in the upper part of the river (P-H), groins have been constructed, narrowing the river locally.

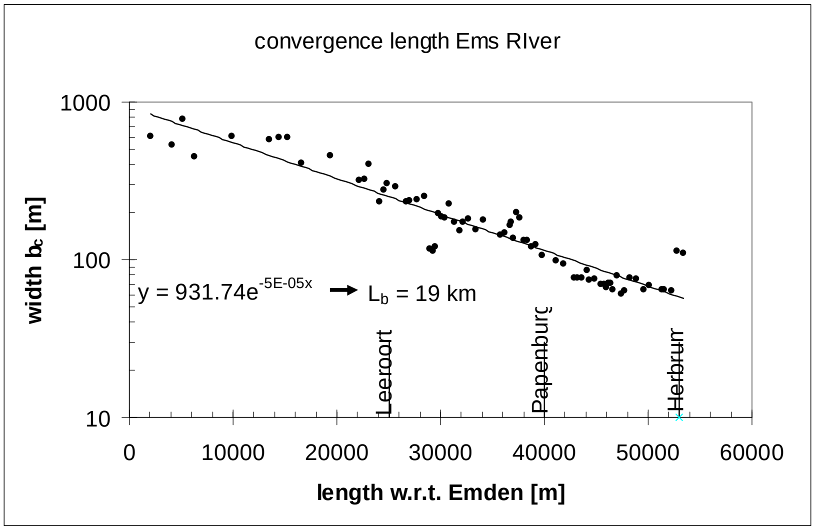

Fig. 4.2: Convergence length of Ems River.

The response of the tidal range to these interventions is presented in Fig. 4.4, in conjunction with an overview of the human interventions (Herrling, 2007). Fig. 4.4 suggests that the response of the tidal range to the various interventions is not instantaneous, but takes considerable time to attain equilibrium – Fig. 4.4 suggests a time scale of at least 20 years. We will address this further below. Finally, it is noted that the tidal range at Herbrum becomes highly irregular as a result of variations in the yearly river flow – this will be elaborated in another study.

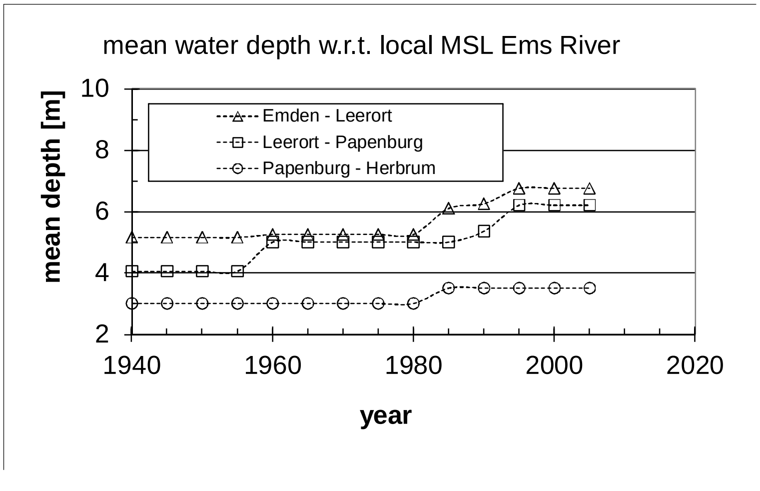

Fig. 4.3: Evolution of mean design water depths in Ems River for three trajectories (water depth with respect to mean sea level at Emden).

We note that more regular data are to be expected from harmonic analyses, including the effects of the 18.6 year cycle (see also Chapter 4.5 on the Scheldt data). However, the original data are not in our possession.

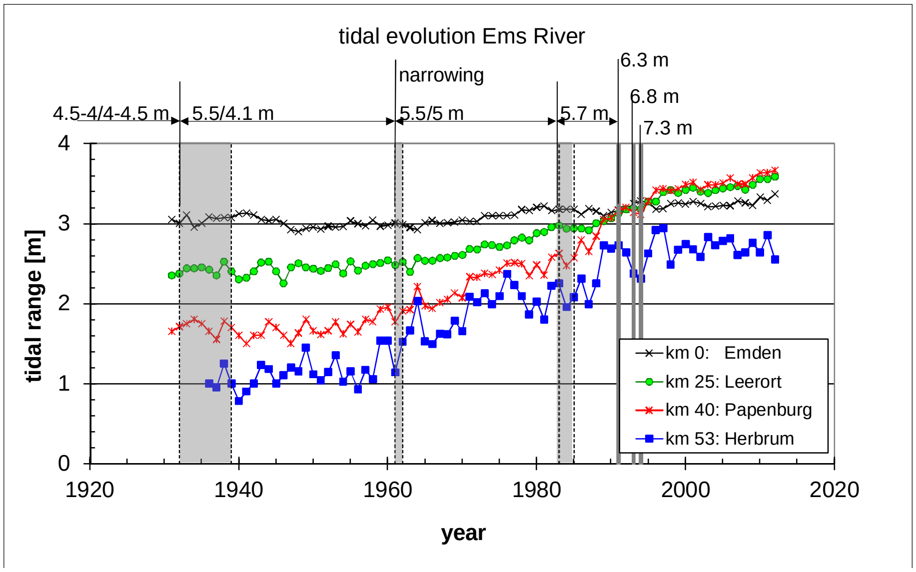

Fig. 4.4: Evolution of measured mean tidal range in Ems River and summary of interventions – 5.5/4.1 m indicates a design depth of 5.5. m over the Emden-Leeroort reach, and 4.5 m over the Leeroort-Papenburg reach; Design depth Papenburg-Herbum reach was 3 m till 1980, and then 3.5 m (data from BAW, and prior to 1950 by Herrling, 2007).

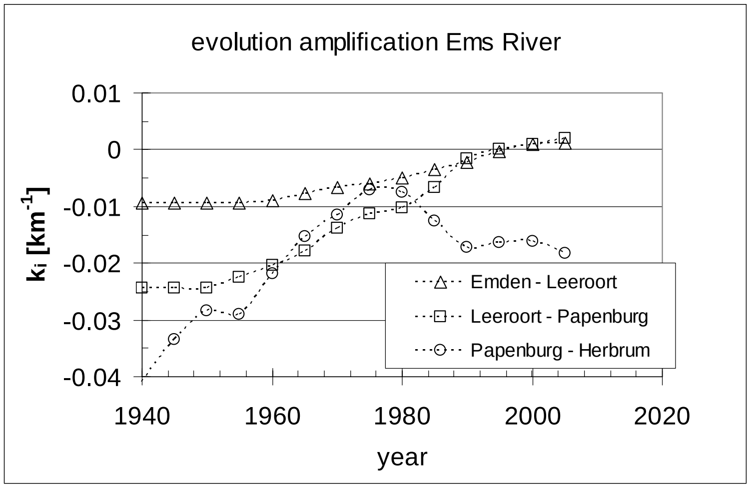

Fig. 4.5: Evolution of imaginary wave number in Ems River; note that in the remainder the data for the trajectory Papenburg – Herbrum have been ignored because of their irregularity.

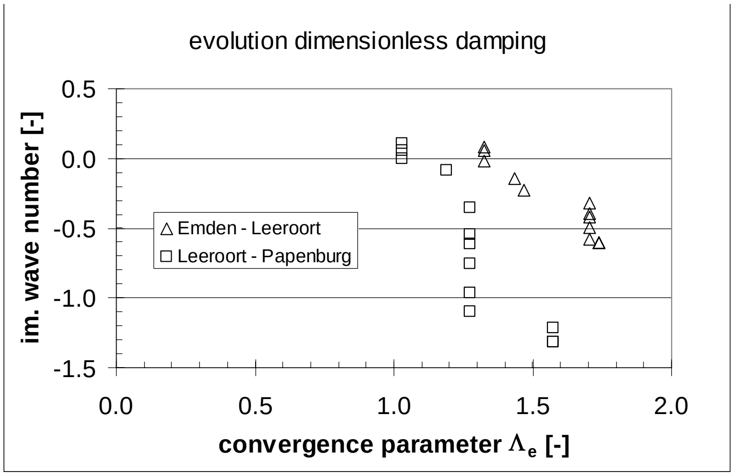

Fig. 4.6: Evolution of dimensionless imaginary wave number κ_i with variations in estuarine convergence number Λ_e.

From Fig. 4.4, the imaginary wave number k_i (amplification factor) was determined. For this purpose, mean values over a period of five subsequent years were determined from the Fig. 4.4-data, and then k_i was determined by dividing the tidal range at Leeroort by that at Emden, etc. The results are presented in Fig. 4.5, showing a regular increase in k_i for the trajectories E-L and L-P. However, for the trajectory P-H, a highly irregular behavior is found. The pattern of this behavior can be entirely changed by using another averaging procedure for the data of Fig. 4.4, or using the tops or troughs of the curve. At present, we are not sure which behavior is representative, and we therefore ignore the behavior of the tide along the trajectory Papenburg – Herbrum. We believe that only a detailed harmonic analysis of the tidal measurements (M2 component) can shed light on the irregular behavior of the Herbrum tidal curve.

Finally it is noted that for both trajectories E-L and L-P the data show that amplification of the tide is observed from 1995 on – before the tidal wave was still damped, though little only.

Next, the imaginary wave number is made dimensionless by the convergence length L_b (e.g. κ_i , equ. 8 & 11) and plotted against the estuarine convergence number Λ_e in Fig. 4.6. Then the linear solution (equ. 13b) is fitted to the data by tuning the roughness parameter r_*, appreciating that the assumptions to attain this linear solution are grossly violated (in particular the tidal range is not small compared to the water depth, and the water depth itself is not constant along the two trajectories under analyses. Yet, the linear solution should allow us to analyze the trends in the data observed in the Ems River.

The results of the calibration are shown in Fig. 4.7, in which the data, presented before in Fig. 4.6 have now been colored to mark the various intervention periods in the river. The 1960 data and earlier for L-P can be fitted with r_* = 7, whereas the 1980 data require r_* = 4. Note that interventions were carried out in 1960 and 1983 – the response to the 1960 intervention was apparently not yet at equilibrium in 1980.

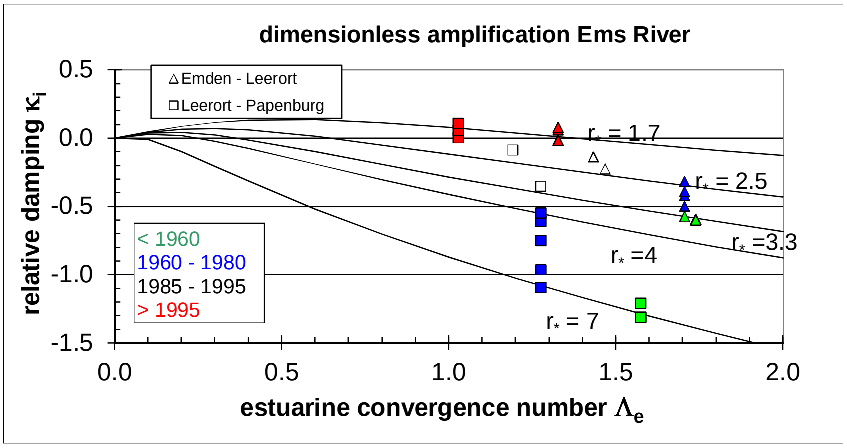

Fig. 4.7: Fits of linear solution to observed data through tuning of roughness parameter in κ_i – Λ_e diagram.

For a more physical interpretation, the roughness parameter r_* has to be converted; arbitrarily we choose to convert to the Chézy coefficient C. In this conversion we use the observed water depth for the various years, and use the imaginary wave number k_i to determine the flow velocity along the river, assuming that in the 1960s, the peak velocity at Emden was 1 m/s (e.g. equ. 4a). To obtain the variation of C with time, we have fitted the linear solution (as in Fig. 4.7) through all data points by tuning r_*, the results of which are presented in Fig. 4.8.

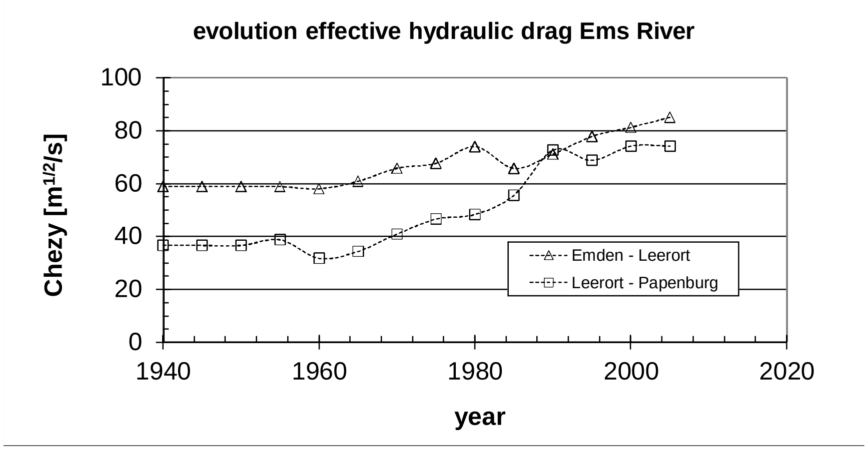

Fig. 4.8: Evolution of effective hydraulic drag (Chézy coefficient) with time.

Fig. 4.8 suggests that up to the 1960s the Ems River was quite rough, with Chézy values in the E-L reach of about 60 $m^{1/2}$/s, which is typical for a sandy river bed. Further upstream, in the L-P reach, Chézy values as low as 40 $m^{1/2}$/s are found. We are not certain that these are correct, but if so, they may be indicative for profound steep bed forms (dunes), such as observed for instance in the Elbe and Weser Rivers (e.g. Van Rijn, 1993). The gradual increase in Chézy coefficient between the 1960s and 1980s may then be attributed to a gradual decrease in dune heights and steepness owing to ongoing dredging. However, from the 1990's onward, the Ems River became more and more infamous for its very high suspended sediment concentrations with hyper-concentrated values after 2000. Today, suspended sediment concentrations measure several 10 g/l, e.g. Talke et al. (2009). The very large values of C = 80 – 90 $m^{1/2}$/s can be explained by the profound buoyancy-induced damping by the large suspended sediment concentrations. Note that Fig. 4.8 suggests an increase in Chézy values of 15 – 25 $m^{1/2}$/s for the conditions prevailing in the Ems River with water depths between 5 and 10 m.

As we have ignored the effects of tidal reflections against the weir at Herbrum we expect that the Chézy values, in particular for the trajectory Leeroort-Papenburg (e.g. Fig. 2.4) are a bit over-estimated, and should be lower by a value of 5 – 10 $m^{1/2}$/s.

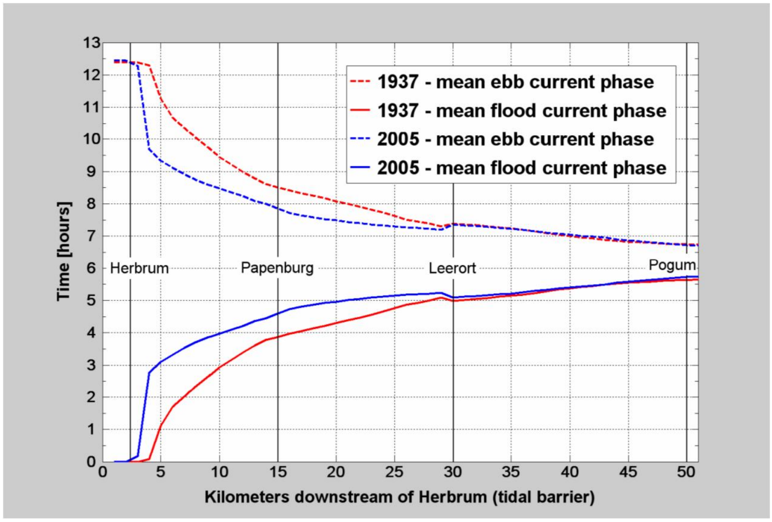

Fig. 4.9: Travel time tidal wave along Ems River computed with three-dimensional numerical hydraulic model (Herrling, 2007).

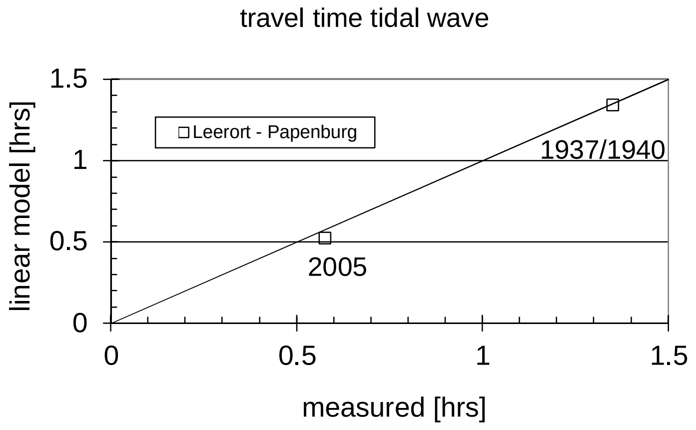

Fig. 4.10: “Measured” and computed travel time tidal wave along Ems River in 1940 and 2005.

Next the evolution in celerity along the Ems River is elaborated. We start from the data in Fig. 4.9, showing a significant decrease since 1937 in the travel time of the tide upstream of Leeroort. The travel times in Fig. 9 were obtained through simulations with a three-dimensional numerical model, referred to as “measured” values in Fig. 4.10.

Using the estuarine convergence number Λ_e, and the roughness parameter r_* obtained from calibration of the linear model against the "measured" evolution in tidal range, the celerity computed with the linear model (equ. 17) can be compared to the data. Fig. 4.10 shows that the linear model predicts the evolution in travel time very well, though only two points in time are available, of course. Fig. 4.9 suggests that this part of the river comes close to synchronous conditions.

Finally, the asymmetry parameter γ (e.g. equ. 18) is determined, using the measured values for water depth and tidal amplitude. The results are presented in Fig. 4.11, showing that over the entire data range, $\gamma > 1$, i.e. flood dominant conditions prevail, as anticipated in Section 2.1 for rivers with little or no intertidal area. The tidal asymmetry remains almost constant for the E-L trajectory of the river, but γ for the L-P trajectory grows continuously after the deepening of the 1960s, exceeding the asymmetry in the E-L range beyond the 1980s. Of course, the tidal asymmetry should be related to (changes) in river flow to get a complete picture of the sediment dynamics in the estuary.

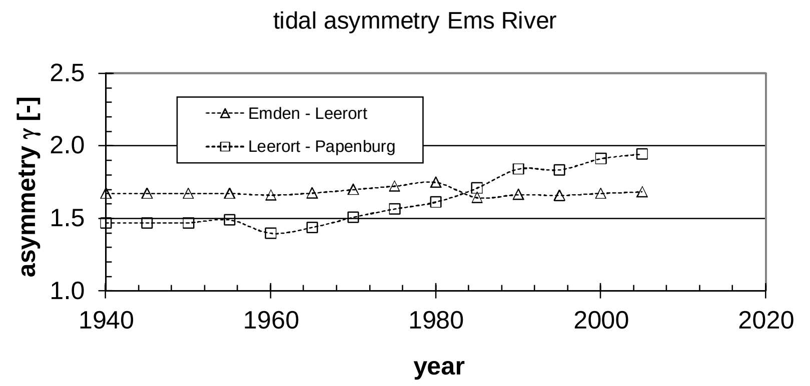

Fig. 4.11: Evolution of tidal asymmetry parameter with time.

4.2 The Loire River

The Loire estuary from St Nazaire to Nantes measures about 53 km. In this report we study the development of the tide in the Loire river from Paimboeuf (at km 14), which is located at the transition between the inner and outer estuary, where the estuary converges strongly, e.g. Fig. 4.12. Hence, we study a stretch of about 40 km. Mean fresh water flow rates range from 400 – 700 m^3/s, with maxima up to 5000 m^3/s.

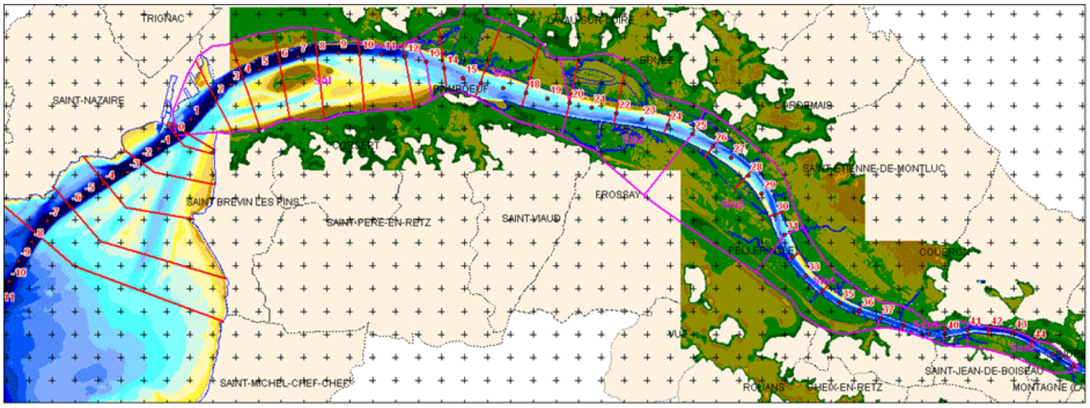

Fig. 4.12: Current plan view of the Loire River; St Nazaire at km 0, Paimboeuf at km 14, Cordemais at km 27, La Martiniere at km 37 and Nantes at km 53.

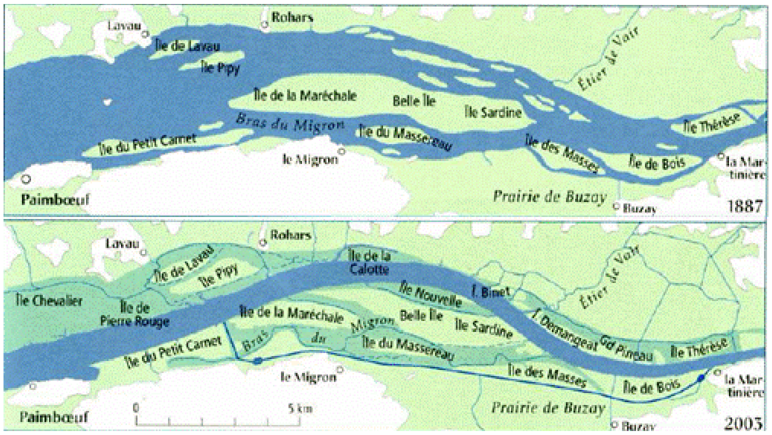

Fig. 4.13: Canalization of the Loire River in 1903 – 1910.

The data discussed below have been collected in a study by Deltares commissioned by GIP (Briere et al., 2012), summarizing reports by Sogreah (2006),in particular Sogreah's report on the historical development of the Loire River.

In the early decades of the 20th century, the Loire River was heavily modified. Fig. 4.13 shows the canalization of a major part of the river, realized in the first decade. Though Fig. 4.13 suggests that modifications were limited to the reaches down-estuary of La Martinière (km 37), canalization and embankments took place up to Nantes. A decade later, e.g. 1910 – 1920 the so-called Bassin Marée has been created by large-scale withdrawal of sand from the river. We were not able to find data on these withdrawals, but Fig. 4.14 suggests that the river bed was affected and lowered well beyond Nantes.

The width of the Loire is plotted against the river length in Fig. 4.15, showing an exponential narrowing with a convergence length of about L_b = 21 km. The relatively small width between km 32 and 36 should be attributed to the local presence of groins. Fig. 4.13 suggests that prior to the large scale narrowing of the river early 2000, the convergence length of the river may have been considerably different. As we have no data, we have not altered L_b in our analyses below, but accounted for this narrowing by reducing the relative intertidal area b_* from 2 to 1.1.

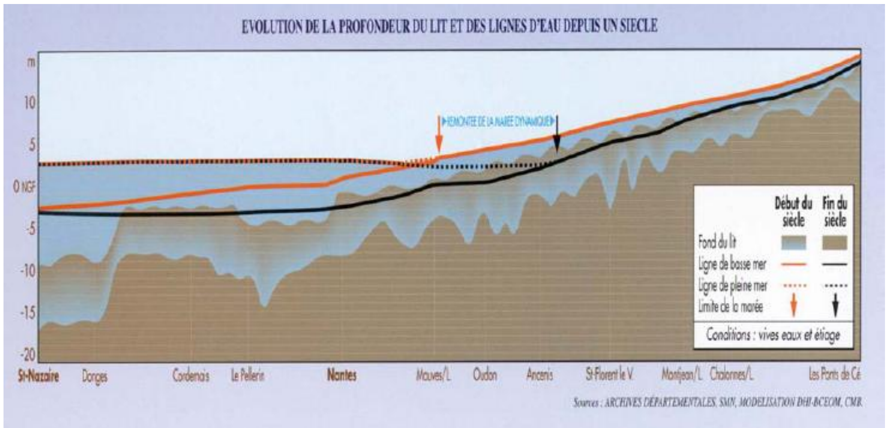

Fig. 4.14: Evolution of the river bed in the Loire River (after Sogreah, 2006).

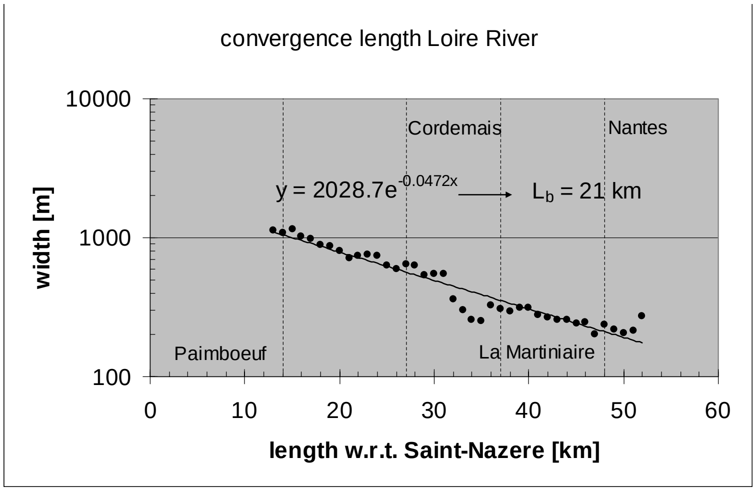

Fig. 4.15: Convergence length of Loire River; the small widths around x = 32 – 36 km are related to a series of groins in this stretch of the river.

The evolution in water depth is presented in Fig. 4.16, showing a profound deepening in the early 20th century, and then again in the 1960's (Sogreah, 2006). The early/mid 1900 deepening may have been the by-product of the significant narrowing of the river in the first decade of the 20th century (Fig. 4.13) and the subsequent formation of the Bassin Marée, increasing the river's tidal prism, and not created by dredging. However, we have no further data on these interventions and their implications.

The data received concern values of the thalweg with respect to chart datum CM96, which is about 3.6 m below mean sea level at the mouth of the estuary (St Nazaire). It is estimated that MSL is about 0.3 m higher at Nantes, and the subsequent slope in MSL along the river has been accounted for in Fig. 4.16. From an analysis of the data of the present bathymetry, it is estimated that the thalweg lies about 1 – 2 m below the mean water depth (cross section divided by river width), e.g. Deltares (2011). In the following we assume that the depth of Fig. 4.16 should be raised by 1 m for the years 1900 – 1947, and with 2 m for the years thereafter – this has been accounted for in the analyses below.

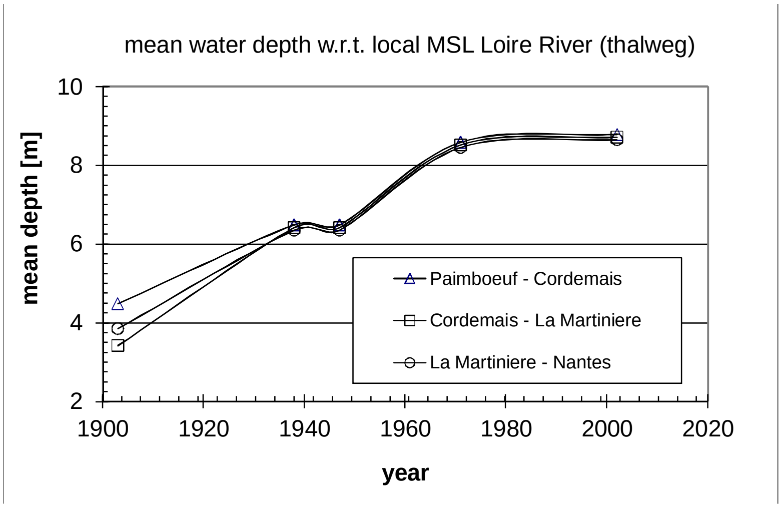

Fig. 4.16: Evolution of water depth (thalweg) with respect to local mean water level (data convergence: chart datum CM96 is 3.6 m below MSL at St Nazaire)..

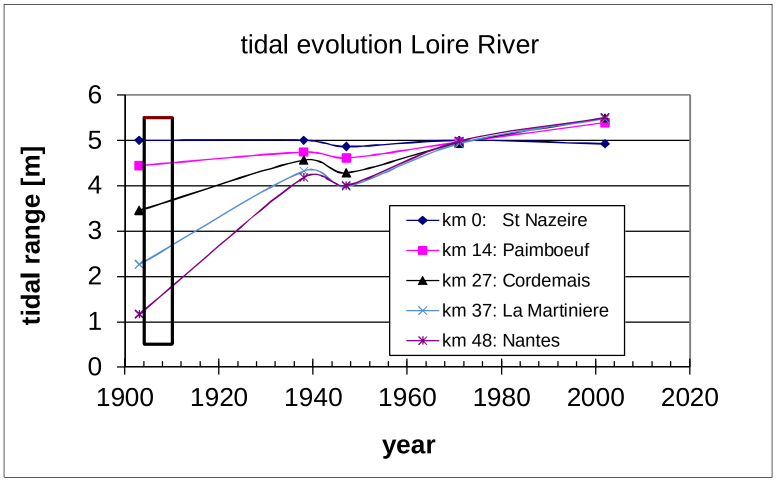

Fig. 4.17: Evolution of the tidal amplitude along the Loire River; the black box represents the period of river narrowing (e.g. Fig. 4.13).

Note that the data of Fig. 4.17 are not very accurate, nor complete, so the analysis in this section is not so accurate, in particular the developments later in the 20th century – more detailed data have been requested.

The measured evolution in tidal amplitude is presented in Fig. 4.17, showing huge amplifications of the tide in the first half of the 20th century. Though at a smaller rate, the tidal amplitude continues to increase after the 1950s; at Nantes for instance by 0.7 m. In the following we focus on the inner river (e.g. up-estuary of Paimboeuf) and subdivide the river further to the four tidal stations along the river (Paimboeuf – Cordemais; Cordemais – La Martiniere; La Martiniere – Nantes, e.g. stretches of 13, 10 and 11 km respectively).

From the data of Fig. 4.17 the evolution of the imaginary wave number can be established, the results of which are shown in Fig. 4.18. Huge changes occurred in the early 20th century, no doubt because of the canalization of the river in that period. From 1940 onwards, $k_i \approx 0$, i.e. the tide is no longer damped in the Loire river. Note that signal is very strong and therefore consistent in the early 20th century, but thereafter becomes a bit erratic. We believe that this is due to inaccuracies of the data in general, and to ignoring the effects of the 18.6 year cycle (e.g. section 4.5).

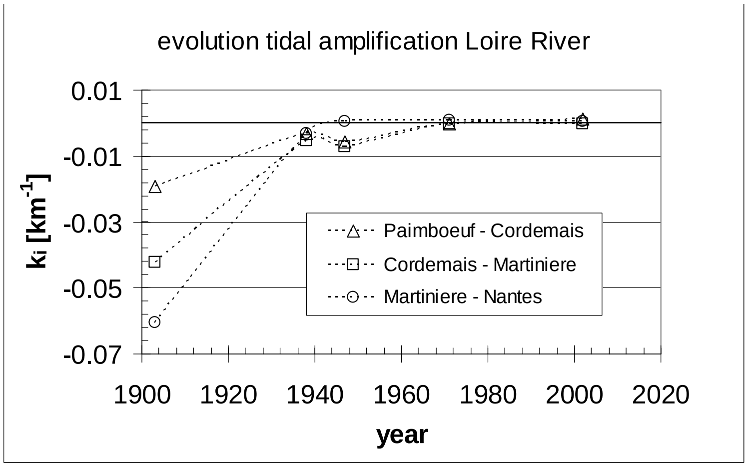

Fig. 4.18: Evolution of the imaginary wave number, based on the tidal data of Fig. 4.17.

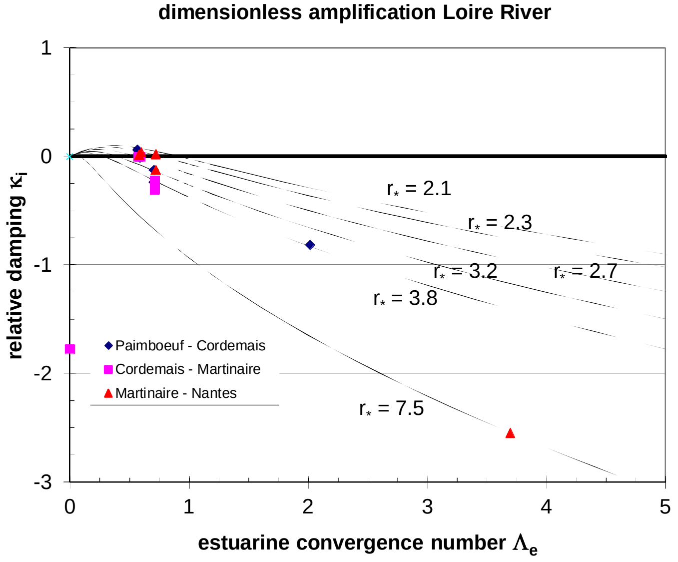

Fig. 4.19a: Tidal amplification as function of convergence number

Next, the imaginary wave numbers of Fig. 4.18 have been made dimensionless with the convergence length and plotted against the estuary convergence number Λ_e (equ. 8), the results of which are shown in Fig. 4.19a. Time evolution is diagonally from the left lower corner to the right upper corner of the figure. If we focus on the data beyond 1940 (omitting the three data points with $\Lambda_e > 2$), we obtain Fig. 4.19b.

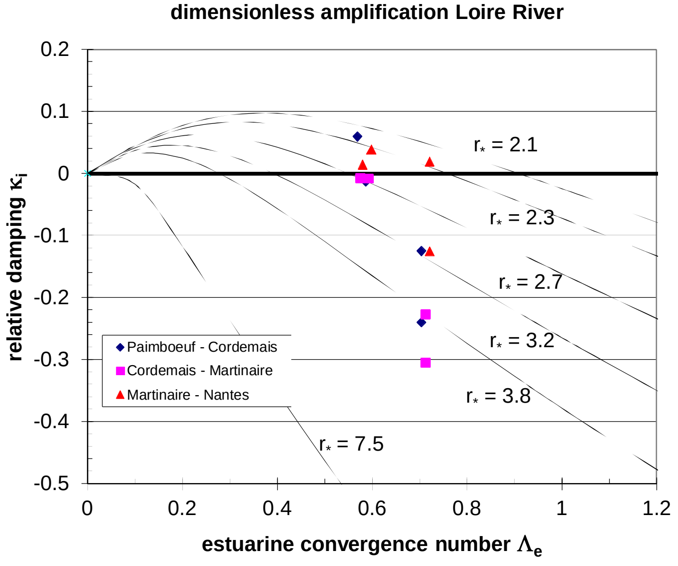

Fig. 4.19b: Tidal amplification as function of convergence number

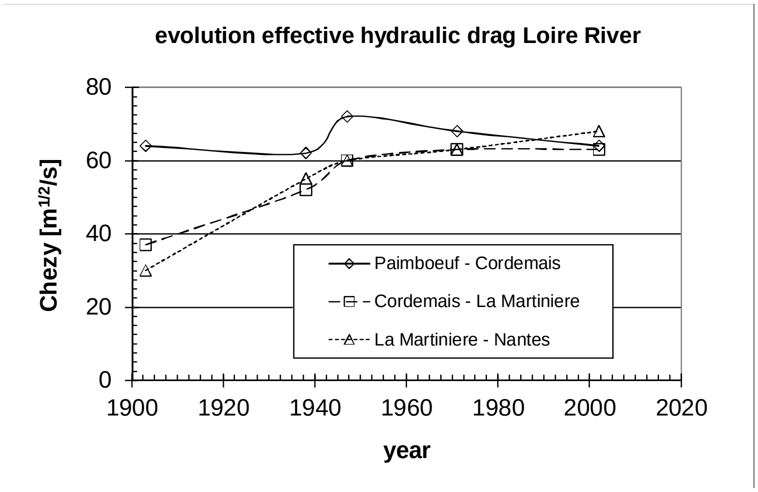

Fig. 4.20: Evolution of effective hydraulic drag Loire estuary – note that because of low accuracy of the tidal data, the error in this graph is relatively large.

Then, the linear model for an infinitely long tidal river (equ. 11) is fitted to the measured tidal damping by tuning the effective dimensionless roughness coefficient r_* to the data, e.g. Fig. 4.19a and 4.19b.

From the fitted r_*-values the effective Chézy coefficient can be obtained (equ. 8), using the observed (corrected) water depths and estimated flow velocities – for the latter, we assume that U = 1 m/s at the mouth of the river, and changes along the river in line with the imaginary wave number).

Fig. 4.20 shows the variation in Chézy coefficient throughout the 20th century for the three river stretches in the Loire. The Chézy coefficient in the first part of the estuary (Paimboeuf – Cordemais) has basically remained constant over time at a value between 60 and 70 $m^{1/2}/s$. However, in the upper two sections, the Chézy coefficient has increased from around 30 – 40 $m^{1/2}/s$ till 60 – 70 $m^{1/2}/s$. The major changes took place in the period before 1940, when the estuary was considerably narrowed. Note that the higher values are not very high, in particular not for a very muddy system as the Loire – fluid mud is general observed between Cordemais and Nantes (Sogreah, 2007). However, the historic data are too inaccurate to provide a better analysis of the historic development of the Loire River.

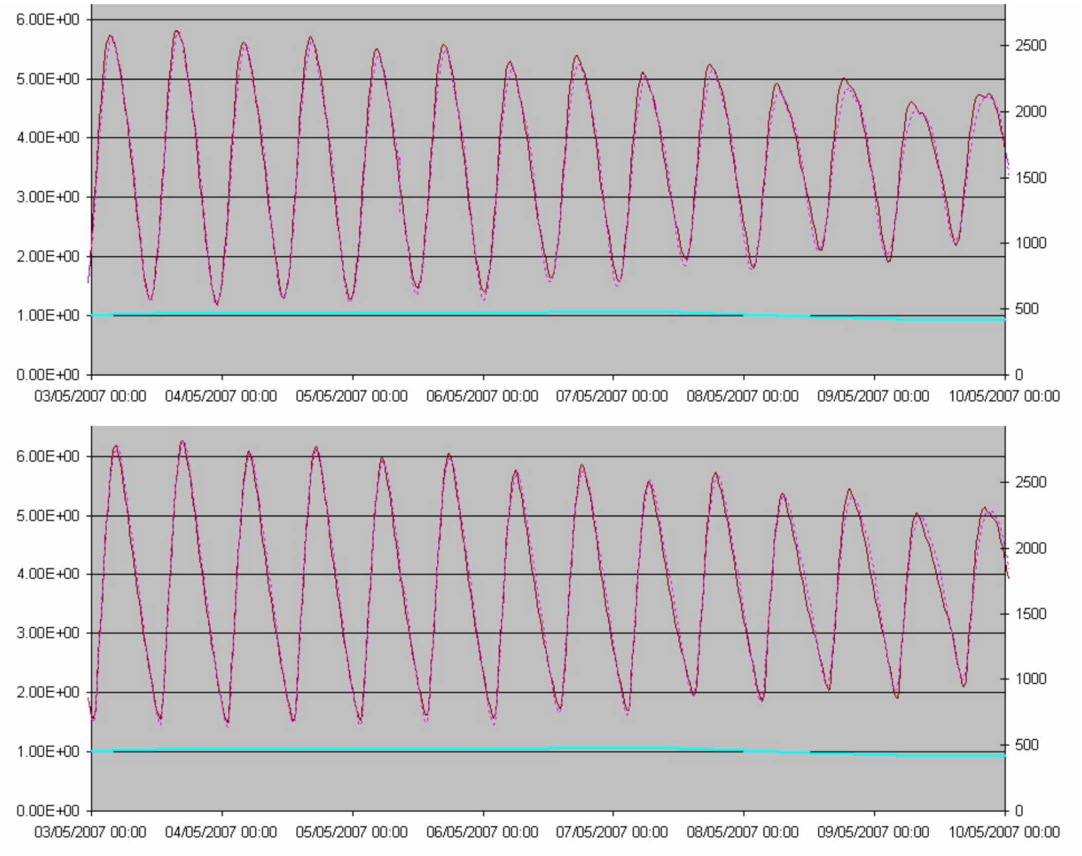

Fig. 4.21: Computed (Sogreah, 2006) tidal amplitude(vertical axis) at Donges (upper panel, km 11) and Chantenay (lower panel, km 51) showing development of steepening of the rising tide.

Because of inaccuracies in the available tidal data it is not possible to obtain proper trends in the γ-parameter with the analytical model. However, all information reveals that the tide in the Loire has become highly asymmetrical. Whereas the tide in the mouth of the Loire River (observations at Donge, e.g. Sogreah, 2006) is almost symmetrical, near Nantes rising tide takes place in about 4 hours, and falling tide is about 50% longer. These observations are corroborated by numerical simulations by Sogreah (2006), results of which are presented in Fig. 4.21.

Note that the asymmetry in flow velocity is largely affected by the fresh water river flow, which may be large. Hence, the effects of tidal asymmetry (both in peak velocity and internal mixing, e.g. section 3.1) may be overruled by the effects of the river flow, inducing ebb dominance, flushing mud from the system.

Sogreah, 2006) reports full flushing of the fluid mud from the river at prolonged (>12 days) high river flows, e.g. around 2000 m^3/s, conditions which may not occur each year.

4.3 The Elbe River

The Elbe River originates in the Karkonosze mountains of the Czech Republic and flows through Germany over 630 km passing the city of Hamburg (largest German seaport) at about 110 km from the mouth at Cuxhaven (North Sea). The mean annual fresh water discharge is about 700 m^3/s with a variation range of 200 to 3600 m^3/s. The mouth of the estuary is characterized by a narrow deep channel and a very wide tidal flood plain up to 2 m above LAT (Hakensand, Medem sand, Norder Grunde), see also Admiralty Chart No. 3261. The total width of the mouth is about 15 km. The width of the deep channel is in the range of 1500 to 3000 m. The area below LAT of the deep channel at the mouth is in the range of about 20000 to 40000 m^2. Fig. 4.22 shows a plan view of the river.

Fig. 4.23 presents the evolution of the tidal range along the Elbe River, as presented by Weilbeer and Klöpper (2011), showing a considerable amplification of the tide upstream of kmr ~670/680 after the 1970’s. Initially, i.e. in the beginning of the century, the tide was damped over the entire estuary.

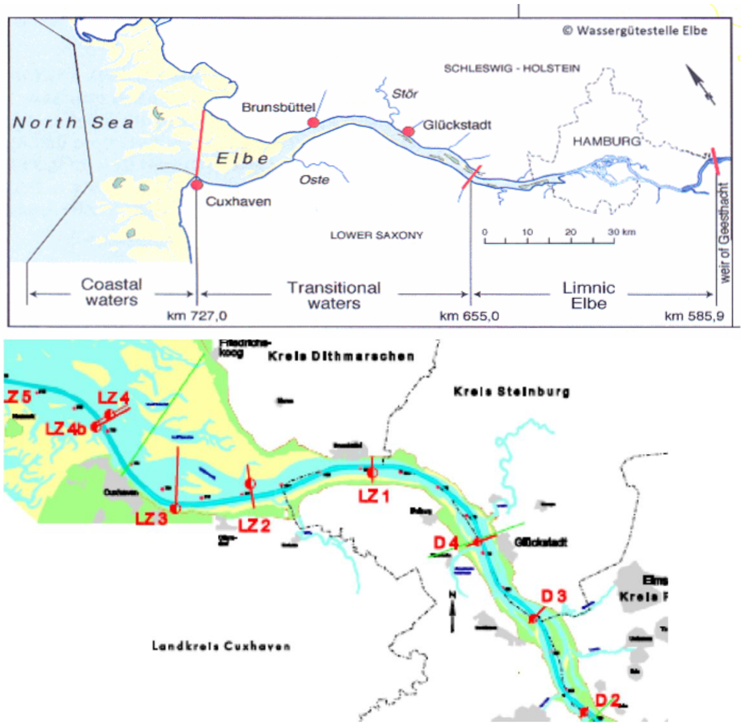

Fig. 4.22: Plan view of lower Elbe river from Hamburg (kmr ~620) to Cuxhafen (kmr 724) and kmr – co-ordinates along the river.

Fig. 4.23 suggests a discontinuity in tidal response around kmr 680. This is further substantiated by the longitudinal variation in flow carrying cross section, presented in Fig. 4.24, showing a substantial kink in this variation. In fact, the cross section in the outer part of the estuary is almost constant, whereas the inner part follows a more exponential distribution. It is postulated that this fairly uncommon distribution is the result of human interventions, in particular with respect to embanking and reclamation.

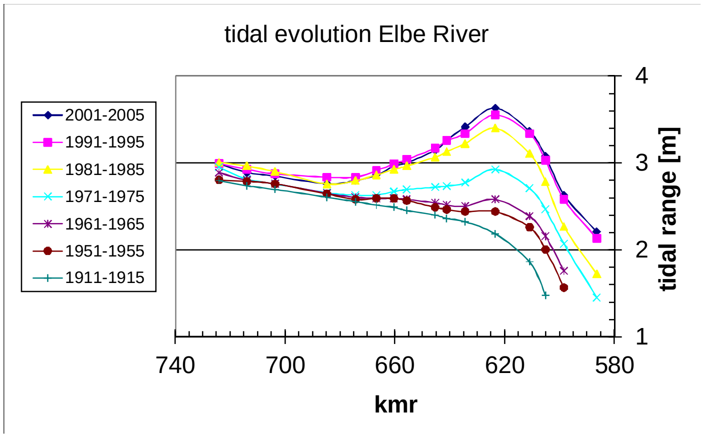

Fig. 4.23: Tidal amplification as function along Elbe River (after Weilbeer and Klöpper, 2011)

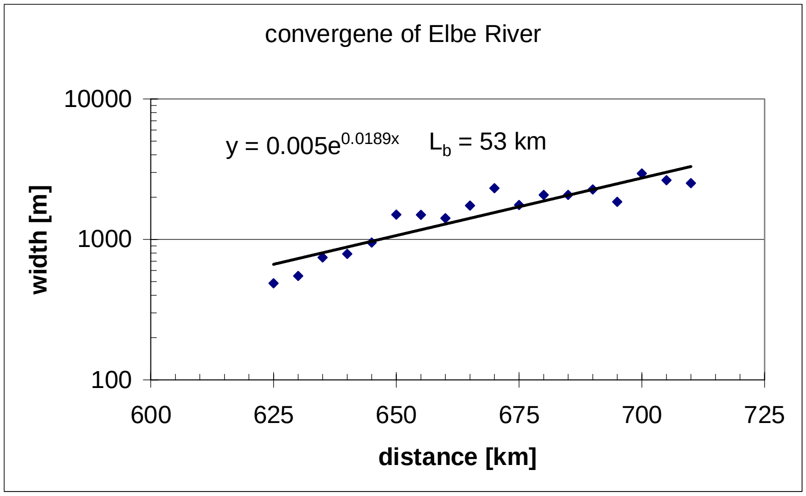

Fig. 4.24: Longitudinal variation of flow-carrying cross section with discontinuity at kmr 670 (after Portal Tideelbe, 1999). The overall convergence length measures 53 km.

In the following, we distinguish between the inner and outer estuary, with their transition around kmr 680. Because of a lack of sufficiently detailed data, we treat the outer and inner estuary as two different, but homogeneous parts of the river. Then, based on the data of Fig. 4.23, the variation in the imaginary wave number k_i can be assessed for the two river parts, as shown in Fig. 4.25. Fig. 4.25 also contains information on the design depth of the fairway in the Elbe River, and the years in which the deepenings were realized. Note that we do not have data before 1940, though the Portal Tideelbe (chapter 3.3 Veränderungen am Flusz) states that in 1859 the fairway was deepened to -5.9 m, whereas form 1910 a depth of 8 – 10 m have been maintained.

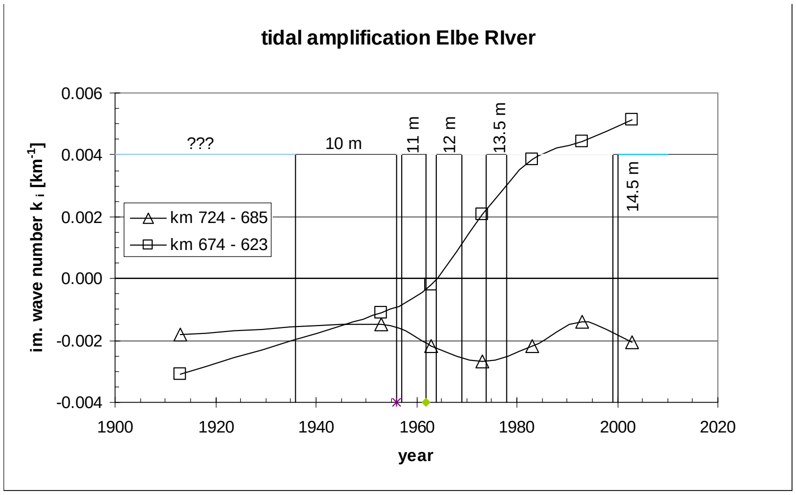

Fig. 4.25: Variation of imaginary wave number k_i $\left(a(x) = a_0 \exp\{k_i x\}\right)$ in outer and inner estuary and time windows with targeted fairway design depths.

In our analyses below, we use the design depths within the time windows as indicated in Fig. 4.25, and use k_i values within these windows by interpolation. Note that if all cross sections would have been available, our analyses could be carried out from tidal station to tidal station.

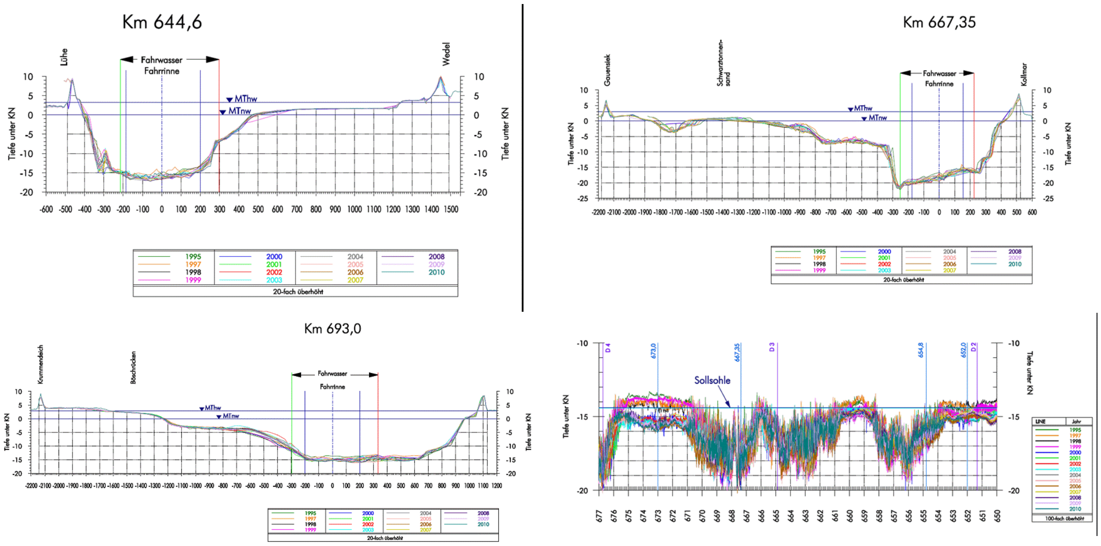

Fig. 4.26: Examples of cross sections in the Elbe River and one longitudinal section (between kmr 650 and 677) (after Portal Tideelbe, 1999)

Fig's 4.24 and 4.26 show that the river's cross section increases in seaward direction. Remember that in our analysis it is not the water depth itself that plays a role, but the flow-carrying cross section divided by the total width (e.g. A_c/b_{tot}) is important. Deepening of the fairway in the inner estuary therefore has a larger effect on the total cross section than in the outer estuary. We have used the available cross sections to compute changes in these cross sections in response to deepening of the fairway. Then, if we assume that the width of the flow-carrying cross section did not change over time, we can construct the evolution in mean depth for the outer and inner estuary, e.g. Fig. 4.27.

Fig. 4.27 also depicts the development of the depth of the fairway showing a profound step in depth near around Hamburg, in particular in later years (e.g. Kappenberg and Fanger, 2007).

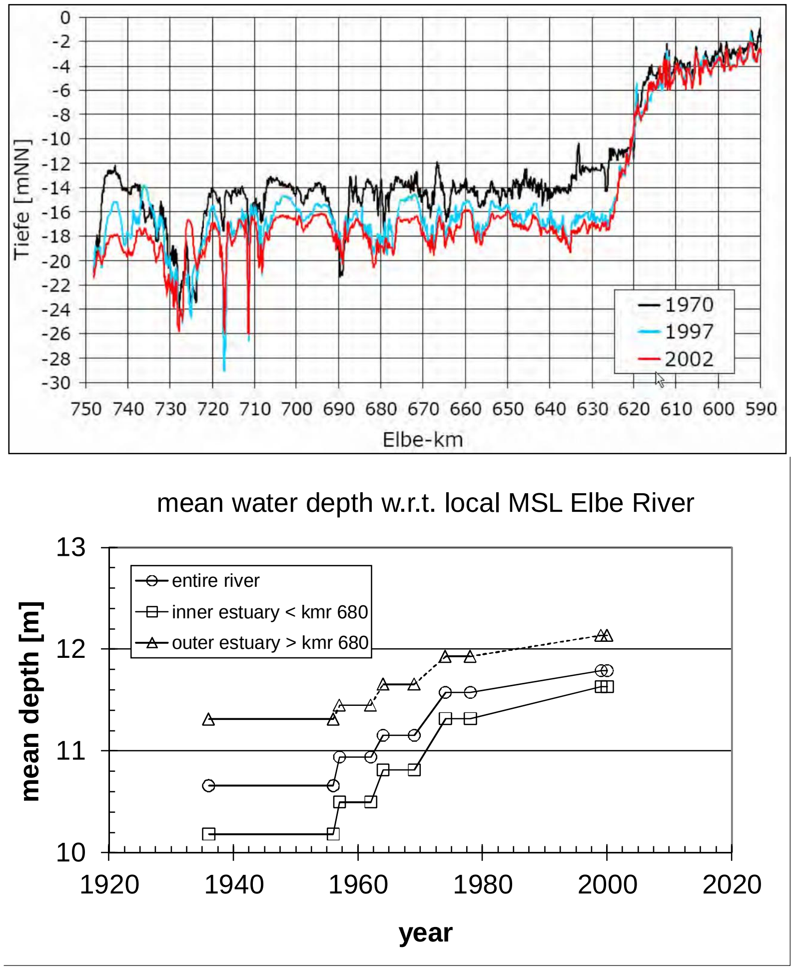

Fig. 4.27: Evolution of mean water depth along Elbe River. Fairway (upper panel) and mean depth in outer and inner estuary.

Fig. 4.28 shows the longitudinal variation in width of the flow-carrying cross section along the Elbe River, based on data provided by BAW (2012). The mean convergence length amounts to about 53 km (Fig. 4.24), though the data show large scatter. However, as suggested by Fig. 4.24, and the data of Fig. 4.28, the convergence length in the outer estuary is much larger than in the inner estuary – in the following we will use two different lengths, i.e. 93 and 30 km in the outer and inner estuary, respectively. In the inner estuary, the intertidal area seems to amount to about 20% and in the outer estuary about 60% of the width of the flow-carrying cross section (e.g. $b_* =$ 1.2 and 1.6, respectively). Note that from an inspection of Google Earth images, these numbers are likely to be on the high side. A detailed analysis of the river's hypsometry is required to obtain more accurate data. Moreover, we have no information on how the intertidal area changed over time.

Because of the large scatter in the data of Fig. 4.24, the convergence length of the inner and outer estuary are fairly sensitive to the location of the kind in L_b; a few km further up-estuary or down-estuary makes a considerable difference. However, L_b for inner and outer estuary are quite different, and the overall conclusions of the analysis in this section appear to be not too dependent on the choice of the location of L_b -kink (results of sensitivity analyses not presented here).

Using the various parameters, the time-variations in imaginary wave number k_i can be made dimensionless with the convergence length L_b, and plotted against time-variations in river bathymetry, i.e. the estuarine convergence number Λ_e. The results are shown in Fig. 4.29. Note that variations in the outer estuary are fairly small, owing to the limited interventions with respect to cross sectional area. The variations in the inner estuary are much larger, though, and in agreement with the evolution of the tide presented in Fig. 4.23.

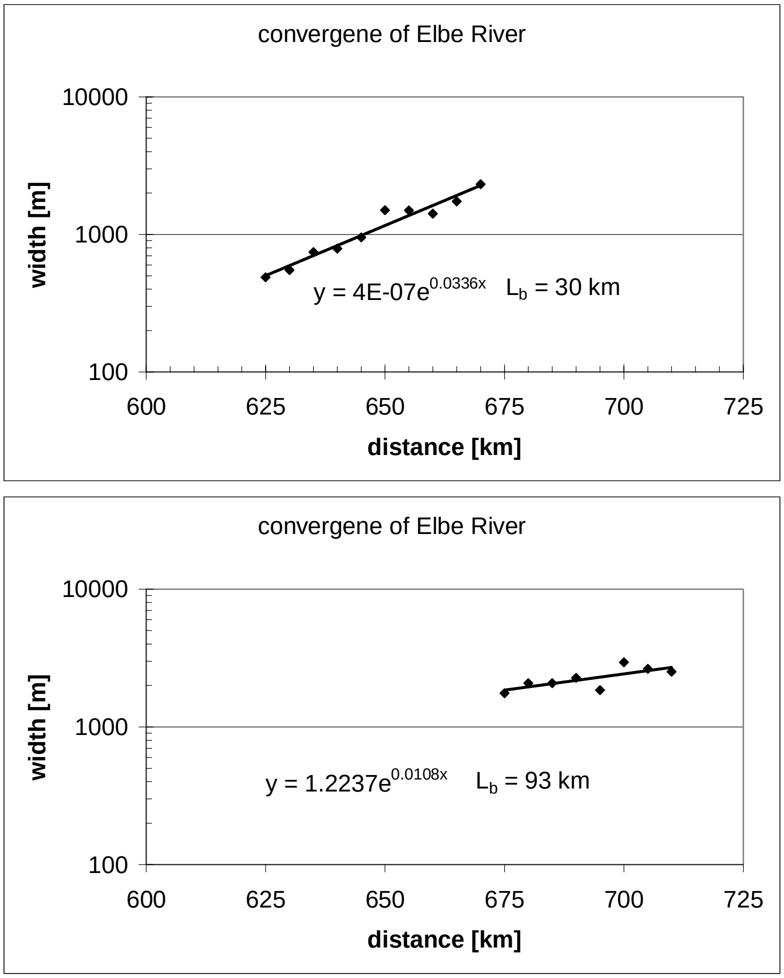

Fig. 4.28: Total width and width of flow-carrying cross section of Elbe River; the intertidal area in the outer estuary amounts to about 50% and in the inner estuary to about 30% (data BAW).

Next, the analytical solution to the linear tidal model has been added to Fig. 4.29, and again the dimensionless roughness parameter r_* is used as a calibration parameter. The results show that, for the given L_b and h values, the data in the inner estuary can be described with roughness values ranging from r_* = 2.8 for the pre-1950 situation to r_* = 0.9 for the post-2000 conditions. Data for the outer estuary can be described with roughness values close to r_* = 0.9.

Note that smaller variations over time in r_* for the inner estuary are possible only when we assume either one of the following possibilities, or a combination of these:

- much smaller values of L_b (half or so) – this is not a very likely assumption,
- profound changes over time in convergence length L_b
- profound changes over time in intertidal area.

As said, we presume that both the convergence length and intertidal area have changed over time by reclamation works and natural sedimentation.

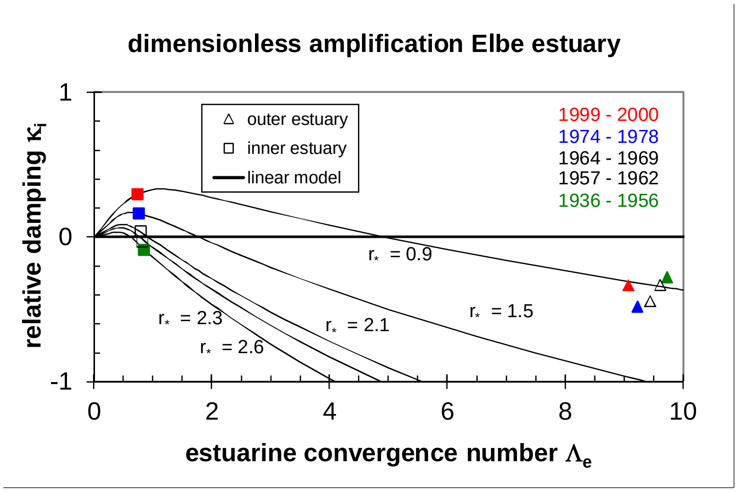

Fig. 4.29: Evolution of dimensionless tidal damping in Elbe River; the five data points and lines for the inner estuary represent the various fairway depths within the five time windows inserted in the graph (e.g. Fig. 4.25).

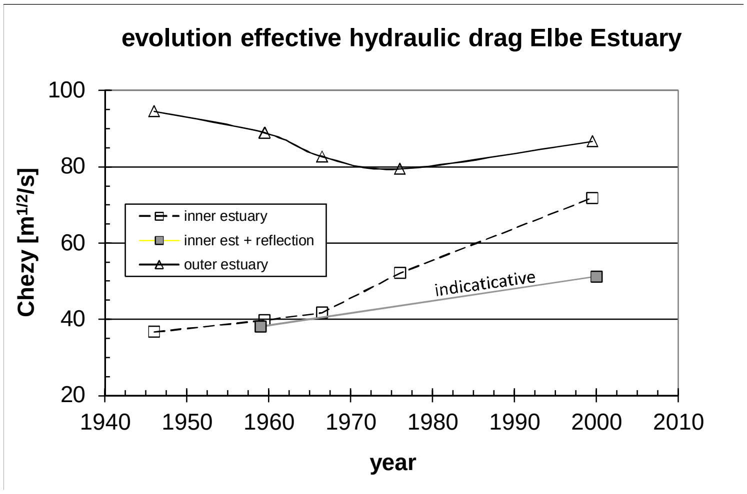

Fig. 4.30: Variation in effective hydraulic drag along the Elbe River as a result of human interventions.

From the dimensionless roughness parameter r_*, a Chézy coefficient C can be established, assuming that the damping in flow velocity is identical to the damping in tidal amplitude (as is assumed in our linear model). Fig. 4.30 shows that in the outer estuary C remains around 80 $\mathrm{m}^{1/2}$/s over time. However, in the inner estuary the results suggest that over time, the river becomes very smooth, up to $C \approx 90$ $\mathrm{m}^{1/2}$/s in the 2000s.

The high Chézy-values in the outer estuary are in agreement with the high SPM-values in this part of the river, and the very muddy intertidal areas (e.g. Fig. 4.31).

Another effect which may have reduced the effective hydraulic drag is the continuous off-topping of the bed forms in the Elbe River by maintenance dredging. The longitudinal profile of the river in the lower right panel of Fig. 4.26 reveals considerable bed forms of a few meter height. Such bed forms were already described by Nasner (1974), reporting dune heights of 1 – 3 m, at lengths of 50 – 100 m, hence fairly steep. Such steep bed forms induce large effective hydraulic drag (e.g. Van Rijn, 1990). These bed forms have decreased by about 1 dm or so, and the reduction in effective hydraulic drag should therefore have been fairly limited.

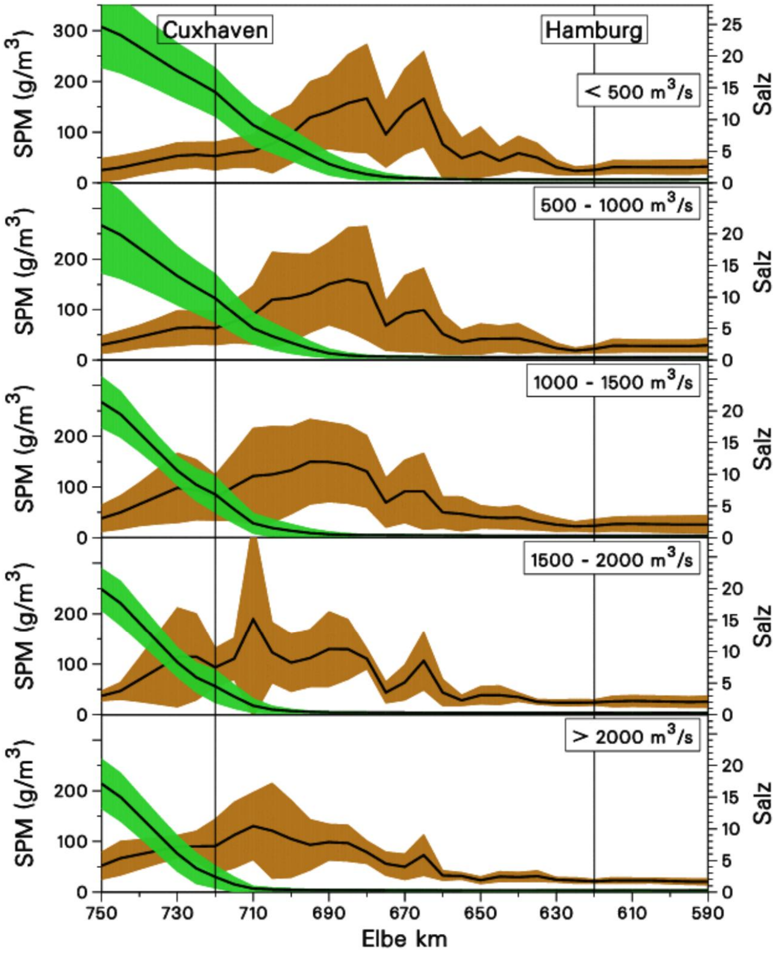

Fig. 4.31: Variation in SPM-concentrations and salinity intrusion as a function of river flow (after Kappenberg and Fanger, 2007). Down-estuary of kmr 670/680, SPM values are high, in agreement with high Chézy-values; up-estuary, SPM-values are low.

Finally, it has to be noted that in our analytical, linear model, the effect of reflections of the tidal wave have not been included. End of the 1950's, the Geesthacht weir was erected, hence arresting the tidal limit at about kmr 585. Furthermore, a distinct step in bed level around the port of Hamburg developed over time, as hardly any deepening took place up-estuary of Hamburg (Boelich and Strotmann, 2008). This is depicted in Fig. 4.27. A zero-order assessment of this step in bed level was made by assuming full reflection at kmr 619 (Hamburg). Furthermore, the analysis of the data suggest that in the course of the 1970s, the convergence of the inner estuary has been decreased by river works. Therefore, we present results for L_b = 30 km and 40 km, e.g. Fig. 4.32. All simulations have been carried out with r = 0.003 m/s (sandy riverbed).

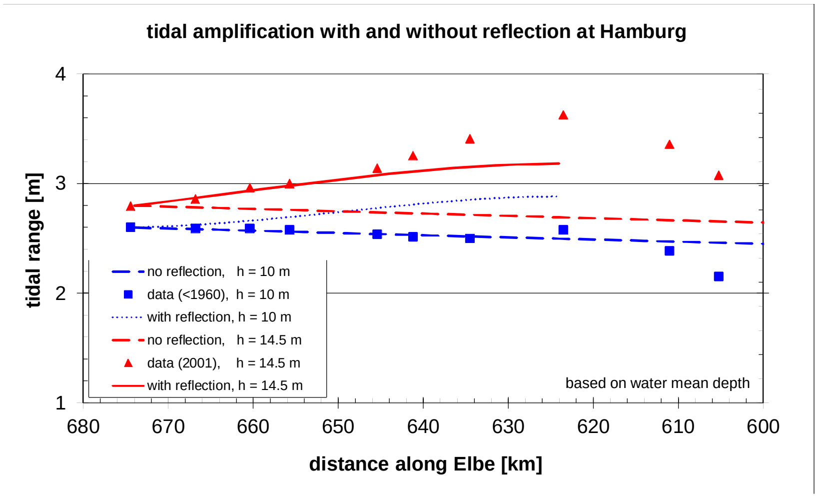

Fig. 4.32: Computation of tidal amplitude for pre-1970 conditions (L_b = 40 km, broken line) and post-1970 conditions (L_b = 30 km, full line).

Therefore, a zero-order assessment of this step in bed level was made by assuming full reflection at km 620 (Hamburg). Furthermore, the analysis of the data suggests that in the course of the 1970s, the convergence of the inner estuary has been increased by river works. Therefore, we present results for L_b = 30 km and 40 km, using the mean depths of Fig. 1, e.g. Fig. 4.27.

The pre-1960 data could only be reproduced assuming an infinitely long river, and a fairly rough bed (r = 0.004). The results in Fig. 4.32 suggest that tidal reflections around kmr 620 did not play a role then. The 2000-data could be reproduced, assuming a very smooth bed, as shown in Fig. 4.30. However, if we presume “sandy” conditions, i.e. r-values not too low, we need to account for reflections of the tide at kmr 620, as shown in Fig. 4.32.

From these observations, we anticipate that the increase in effective bed roughness in the upper estuary (Fig. 4.30) is probably largely overestimated, as part of the amplification should be attributed to reflections. However, it is not likely that full reflection takes place at Hamburg. The increase of Chézy from 38 to 51 $m^{1/2}/s$ can only partly (e.g. for 2 – 5 $m^{1/2}/s$) be explained by the deepening itself. Hence, the indicative increase in C of Fig. 4.30 must be attributed to either a too large simplification of the tidal conditions in the Elbe River, or to decreases in effective hydraulic drag be a reduction in bed forms (e.g. steepness) and/or a small increase in SPM-values. A further elaboration of this hypothesis requires detailed numerical modeling, accounting for the actual changes in bathymetry at great detail.

Next, the travel time of high water between Cuxhafen and Hetlingen (kmr 647, e.g. Fig. 4.33 upper panel) is computed using equ. (17). Computed and measured travel time are compared in Fig. 4.33, showing that the linear model underpredicts the observed travel time by about 10%. Analysis of the sensitivity of the travel time to model parameters showed that the travel time is sensitive in particular to the convergence length, more than to the effective roughness. Hence, this is another indication that the geometrical features of the Elbe are not known sufficiently well.

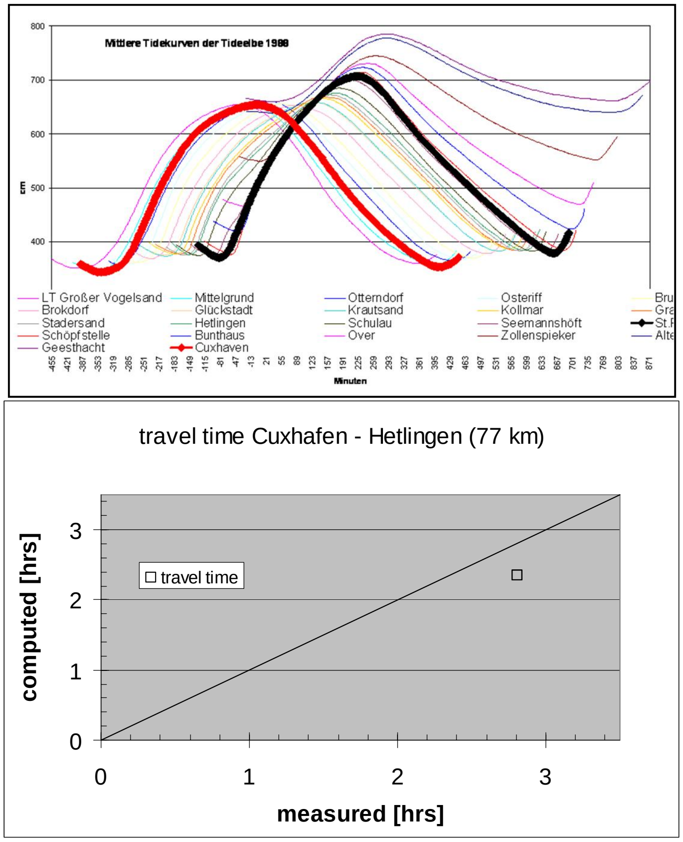

Fig. 4.33: Travel time high water in Elbe River; upper panel: observations in 1988; lower panel: prediction by linear model

Finally, variations in tidal asymmetry have been assessed from variations in the γ-parameter, i.e. the ratio of the wave celerity at high and at low water, in which the actually measured variations in tidal amplitude have been used, in conjunction with the values for river depth h, convergence length L_b, roughness r_* and intertidal area b_*, established and used above. Fig. 4.34 suggests that the outer estuary remained ebb-dominant over time, whereas the inner estuary remained flood dominant over time. These conclusions are more or less sustained with measurements of the current velocity in Fig. 4.35, showing that in the outer estuary, the flow is slightly flood dominant, but in the inner estuary flood-dominance is more pronounced. Note that the underestimation of flood dominance (in the outer estuary) is likely the result of erroneous values (too large) for the intertidal area b_* - see also Boelich and Strotmann (2008).

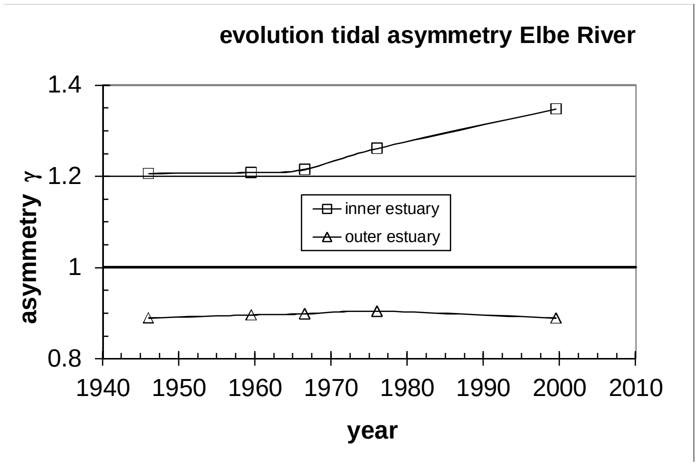

Fig. 4.34: Temporal variations in tidal asymmetry parameter γ in inner and outer estuary.

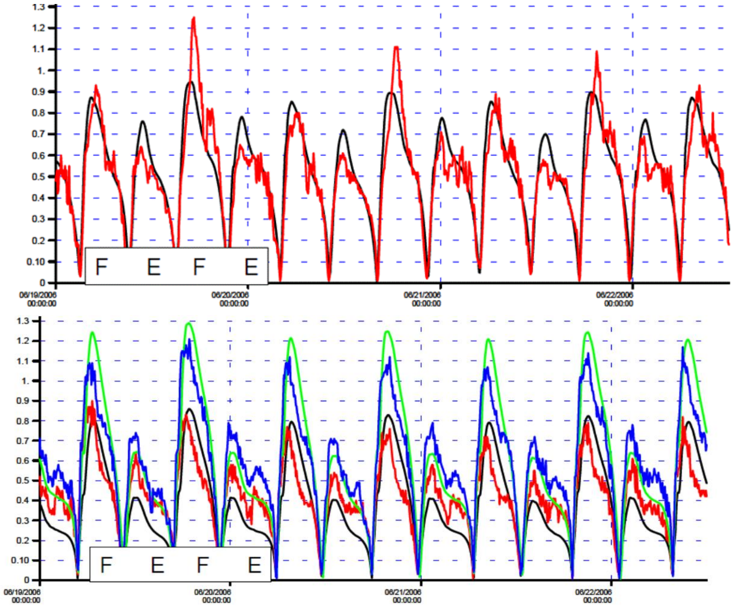

Fig. 4.35: Measured tidal asymmetry along Elbe River; upper panel: near Brunsbuttel; lower panel: near Schulau (after BAW, 2011)

It is to be noted that the flood dominance in the inner estuary follows a subtle interplay from a decrease in γ by increased river depths, and an increase by tidal amplification. This would imply that if the river were sub-divided into more sub-sections, we would expect a larger increase in flood-dominance further upstream, near the port of Hamburg. As the riverine turbidity maximum (RTM) is governed by tidal asymmetry and river-induced flushing, this would imply that:

- the ETM moves upstream with decreasing river flow – indeed it has been observed that dredging needs in the Port of Hamburg increase in years with low river flows (Haar, 1994).
- over time, the ETM would have moved in upstream direction – unfortunately, we have no information to confirm.

Our analysis of the data on the Elbe River suggest that:

1. The tide in the lower estuary (kmr 720 – 670) is largely influenced by a large intertidal area, large convergence length and small effective hydraulic drag. Tidal amplification over time remained relatively small.
2. The analysis with the linear model (infinitely long river) suggests a sharp increase in Chézy coefficient in the inner estuary after 1970, suggesting a sharp increase in SPM in the river. This is, however, not in agreement with the SPM data, which show relatively low SPM-concentrations in this part of the river.
3. The Elbe river depicts a large step in water depth around Hamburg, which becomes more pronounced over time (with deepening of the river). This step should induce reflections of the tidal wave. Our model simulations, however, suggest that this can be only a partial reflection.
4. We have no data on the convergence of the river prior to 1970. However, the analysis with the linear model suggests that the river's convergence has increased (Lb decreased).
5. The analyses indicate that the tidal propagation in the upper estuary is very sensitive to the geometry and bathymetry of the river. This was confirmed by Weilbeer (2013). This sensitivity itself suggest an important effect of reflections of the tidal wave, either at the step in bed level around Hamburg, or otherwise.

However, these conclusions are based on a limited series of data, and further substantiation is possible only upon further analysis. We recommend the following:

- Make harmonic analyses of the historical tidal data at the various tidal stations along the river (analysis should be done on M2 and M4 tidal component).
- Make a proper analysis of the historic development of the river's cross sections, preferably in the form of hypsometric curves.
- Make a detailed analysis of the development of convergence length and intertidal areas.
- Analyze changes in bed forms, in particular variations in the steepness of dunes.
- Analyze the changes in tidal amplitude in relation to geometrical changes along the river, focusing on all sub-sections defined by the existing tidal stations.
- Apply a (one-dimensional) numerical model to study the response of deepening, reclamations, the step in bed level, Geesthacht weir and reduction in effective hydraulic drag in a non-linear model, including possible reflections of the tidal wave.

4.4 The Weser estuary

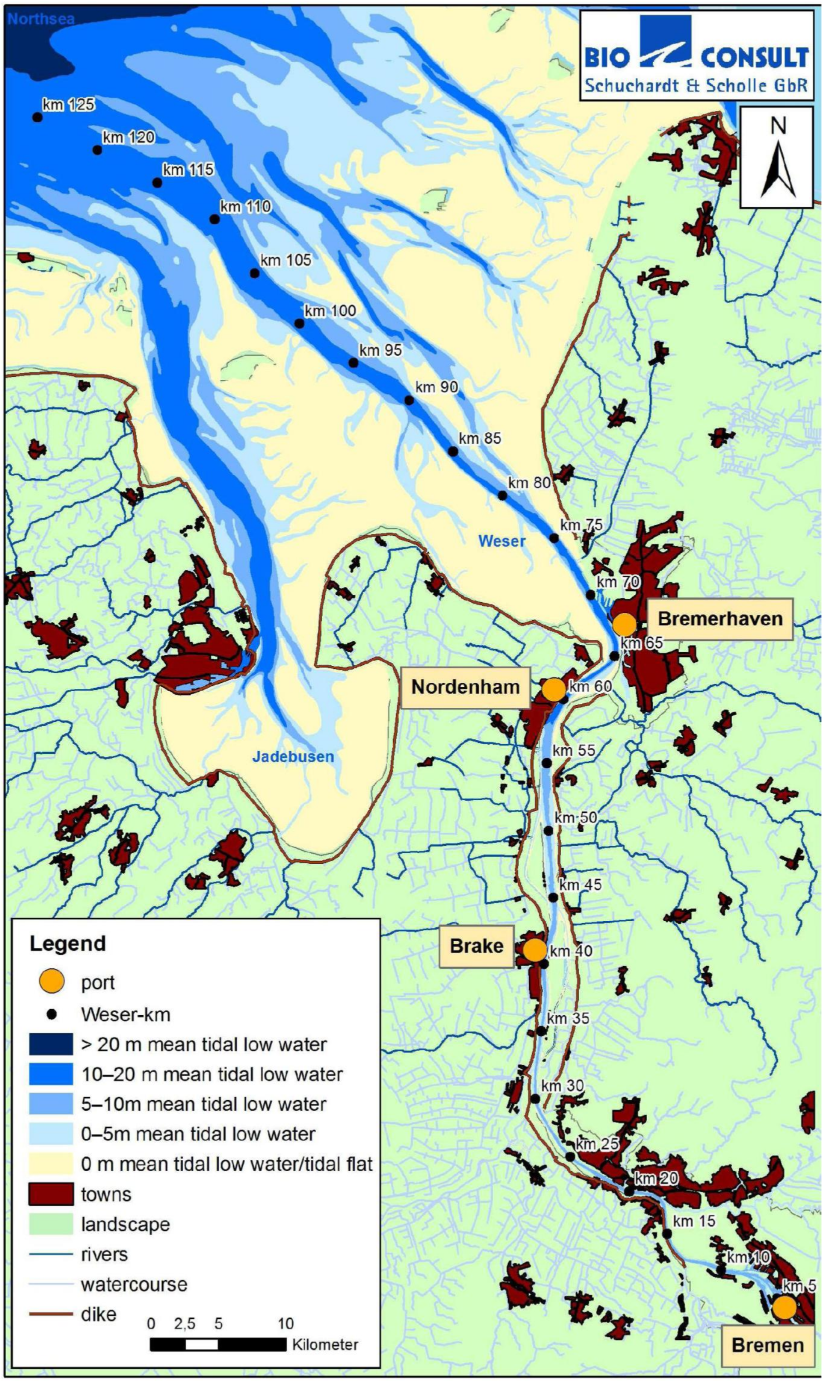

Fig. 4.36: Overview of Weser estuary

We are in the process of acquiring data for the Weser River for an analysis similar to elsewhere in this report. Hence, no results yet, though the enormous deepening of the river in the 20th century suggests problems similar to the other rivers analyzed in Chapter 4 – indeed the graph of Fig. 4. 35 confirms this expectation.

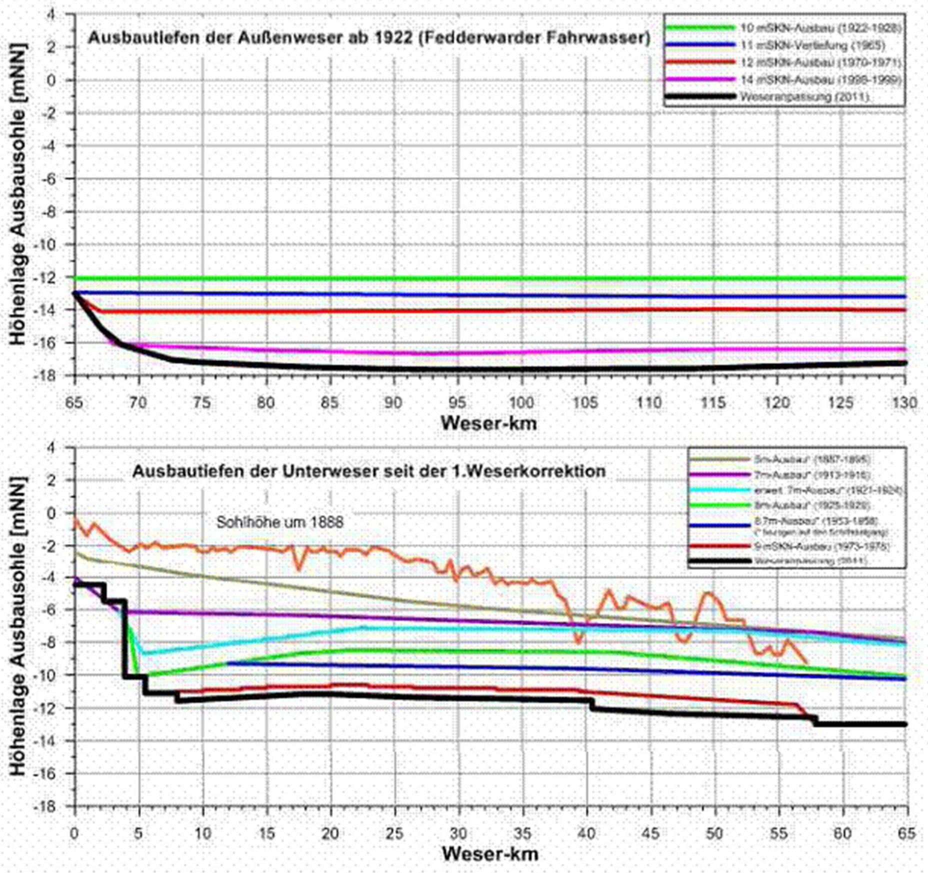

Fig. 4.37: Evolution of water depth along Weser River.

The data are from B. Schuchardt and S. Beilfuss (2012).

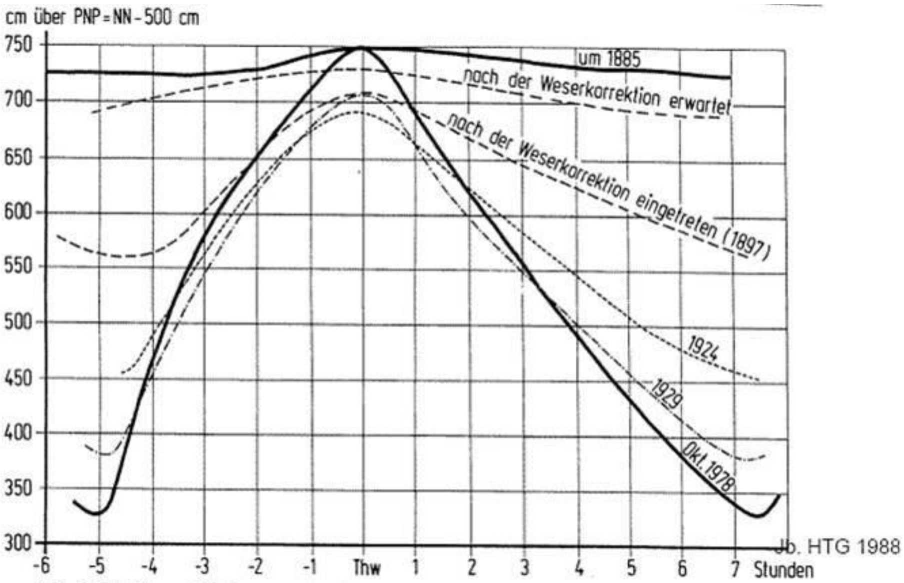

Jb. HTG 1988

Abb. 8. Mittlere Tidekurven der Weser in Bremen nach den Unterweserausbauten

Fig. 4.38: Example of tidal amplification in Bremen over time

Currently, we have no further data available, and we cannot analyze the developments in the Weser River. Yet, the amplifications are so large that we decided to include the results in this report.

4.5 The Upper Sea Scheldt River (Boven Zeeschelde)

Fig. 4.39 shows an overview of the Scheldt estuary from its mouth near Flushing (Vlissingen) to Ghent with indication of the various tidal stations treated in this report (see also Table 4.1, e.g. IMDC, 2012). Further details, including the km-indications are given in Fig. 4.40.

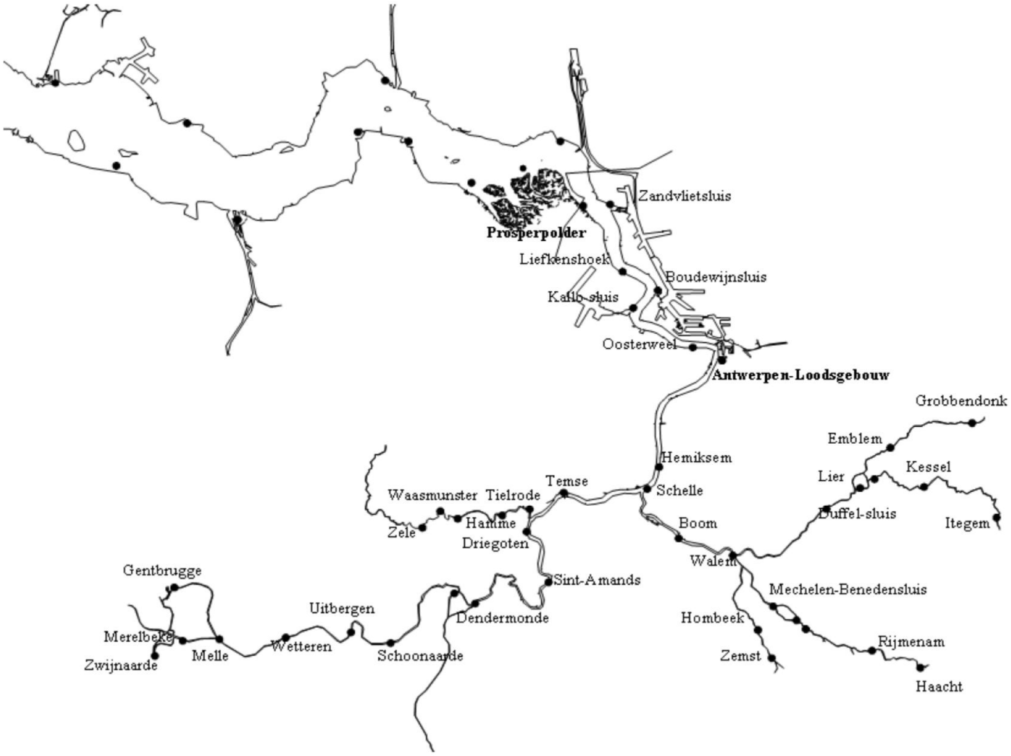

Fig. 4.39: The Scheldt estuary from Flushing to Ghent with the various tidal stations.

Table 4.1: Summary of tidal stations along Sea Scheldt

Name	km from Schelle	km from Vlissingen
Schelle	0	91.2
Temse	7.5	98.7
Tielrode	11.9	103.1
Sint Amands	17.8	108.8
Dendermonde	30.6	121.8
Schoonaarde	41.7	132.6
Uitbergen	47.0	138.2
Wetteren	53.8	145.6
Melle	60.0	150.8

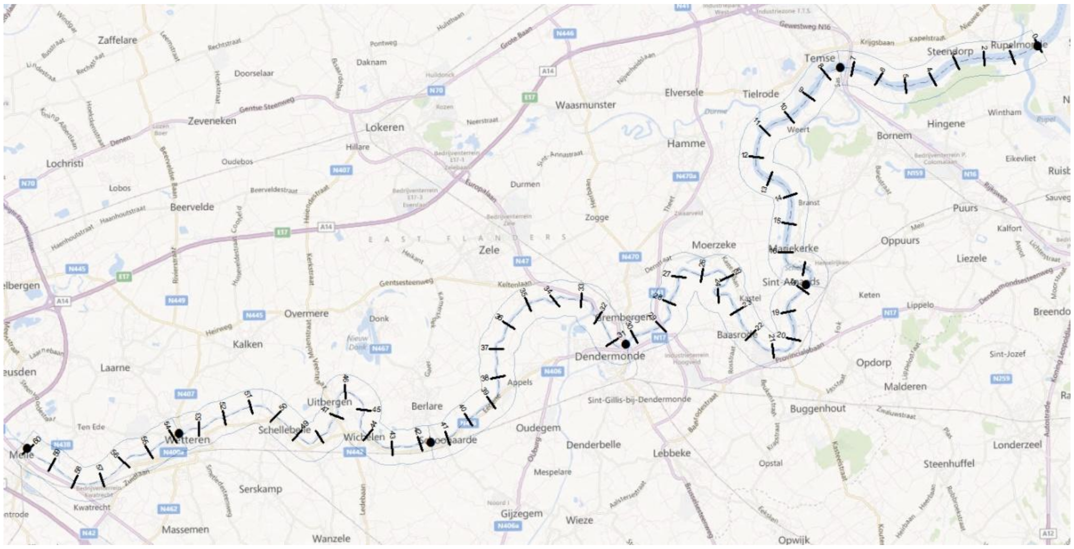

Fig. 4.40: Overview of Upper Sea Scheldt (Boven Zeeschelde) from Schelle (upper right corner) to Melle (lower left corner).

Tidal data for the entire Scheldt estuary are available from before 1900. Kuijper (2012) corrected these data for the 18.6 year cycle, the results of which are shown in Fig. 4.41a. In the following, we focus on the Upper Sea Scheldt, i.e. up-estuary from Schelle. For an analysis of the time evolution of the entire estuary, the reader is referred to Kuijper (2012, Western Scheldt) and Plancke (2012, for Sea Scheldt). To allow further analysis, missing data points have been filled in by interpolation from the available time and spatial series, e.g. Fig. 4.41b.[3)]

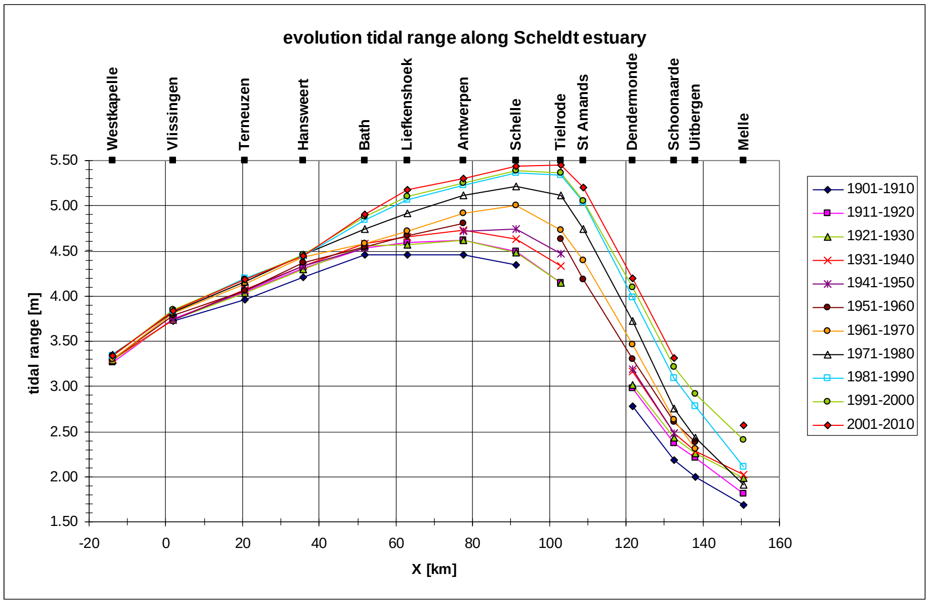

Fig. 4.41a: Evolution of mean tidal range along Scheldt estuary corrected for 18.6 year cycle.

[3)] *Note that no consistent analyses could be made using the original data, obtained by averaging and grouping over decades – clear trends in tidal amplification and reflection could not be obtained.*

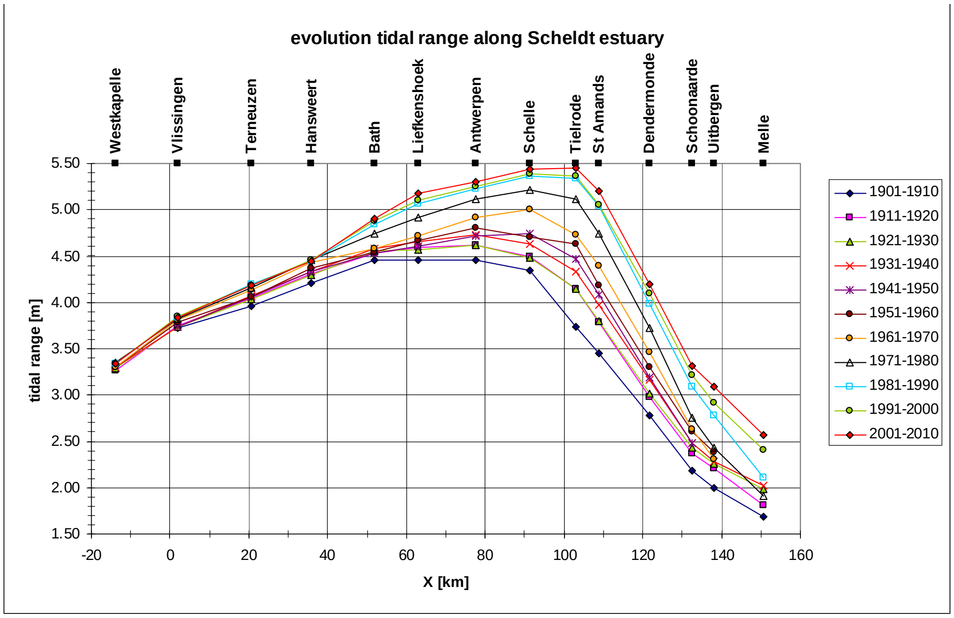

Fig. 4.41b: Same as Fig. 4.41a, but missing data added by interpolation..

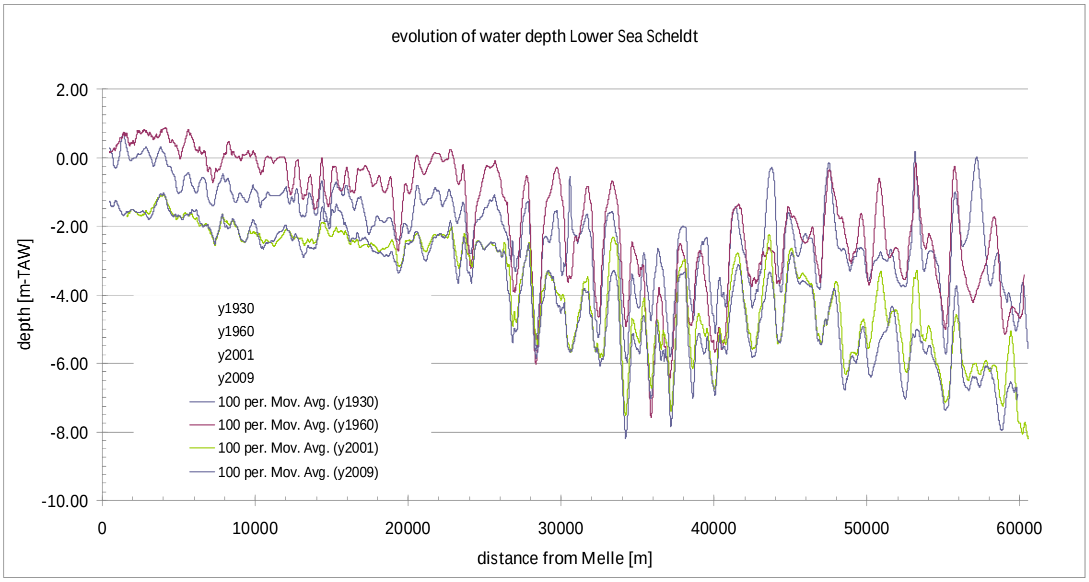

Fig. 4.42: Evolution of water depth Upper Sea Scheldt w.r.t. TAW chart datum .

Note that the tidal range in Fig. 4.41 comprises the difference between long-time mean low and high water – in a next phase of the study, the actual tidal amplitudes should be analyzed.

Van Braeckel et al. (2006) summarize modifications in the Scheldt estuary. The majority of the engineering works in the Upper Sea Scheldt took place before 1900, e.g. rectifications of the river and embanking intertidal areas. In the early 1900s (1900 – 1930) parts of the river were normalized, and later rectifications took place in the Durme. In the 1970s, the river deepened by 1.5 – 2 m, e.g. Fig. 4.42, though no engineering works are reported. Possibly, this deepening was the morphodynamic response to engineering works further down-estuary, such as sand-mining and deepening and widening of Western-Scheldt and/or Lower Sea Scheldt. Also deepening and widening of the Scheldt estuary down-estuary of Antwerp in the second half of the 20th century, and early 21th century had an effect on the tidal evolution, as discussed below (see also Kuijper, 2012).

The evolution of the water depth in the Upper Sea Scheldt is further elaborated in Fig. 4.43 showing the water depth with respect to local mean water level, based on data from IMDC (2012). The water depth in Fig. 4.43 is obtained from dividing the flow-carrying cross section by the width of the river, and then averaging over the river sections in between the tidal stations.

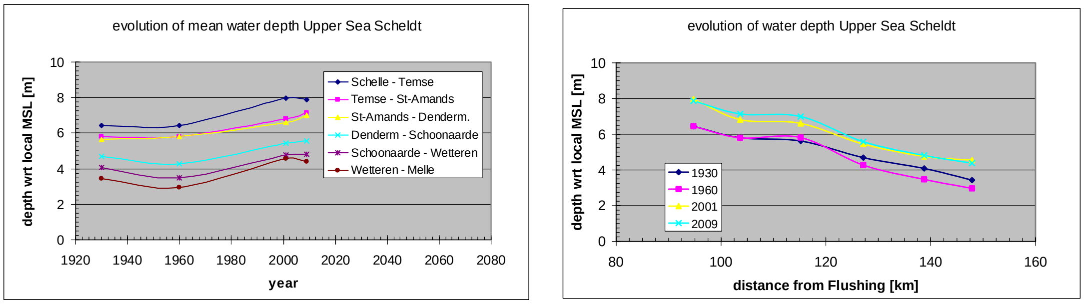

Fig. 4.43: Evolution of mean water depth between the various tidal stations along the Upper Sea Scheldt.

At the head of the estuary, around Ghent, a number of engineering works were carried out between 1950 and 1970. These works consisted of the creation of a new channel of about 4 km length with a shipping lock for access to Ghent. Between around 1960 – 1970 the Upper Sea Scheldt became deeper, and the old northern arm of the Upper Sea Scheldt has silted up largely.

The old Scheldt branch measured about 8.4 km from Melle tidal station to the weir in Ghent, whereas the new branch measures about 7.2 km.

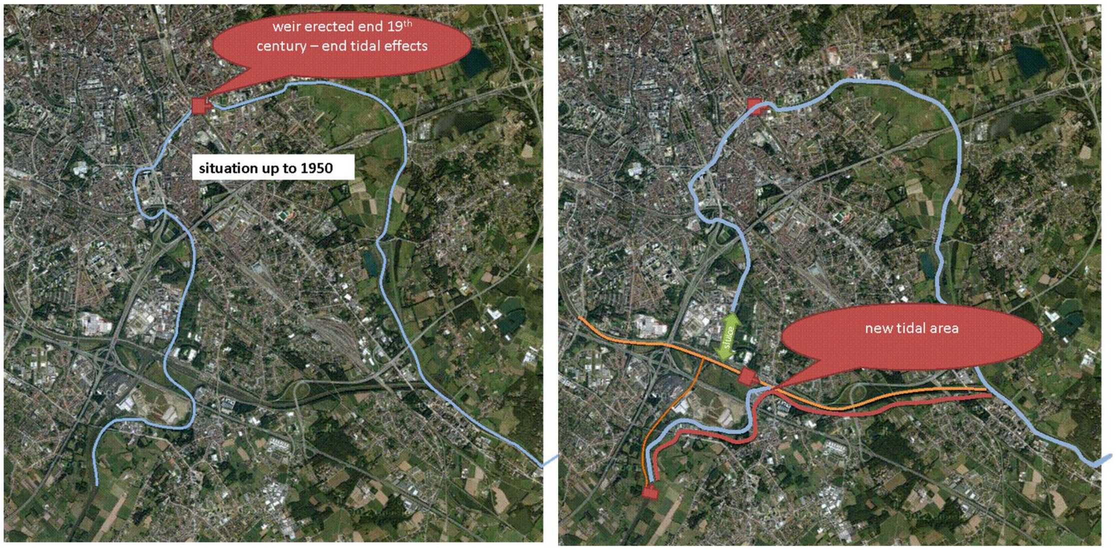

Fig. 4.44: Overview engineering works at head of Upper Sea Scheldt (Meersschaut, pers. com).

The convergence length of the Upper Sea Scheldt is plotted in Fig. 4.45, showing an exponential behavior with a mean value of about 31 km, and little variation since 1930. Note that the river rectifications in the late 19th century must have reduced this convergence length by about 5 km.

Fig. 4.45 suggests a kink in the river's convergence between Dendermonde and Schoonaarde, and the data have therefore been replotted in Fig. 4.46 showing a significant discontinuity in L_b. However, no clear time signal can be identified.

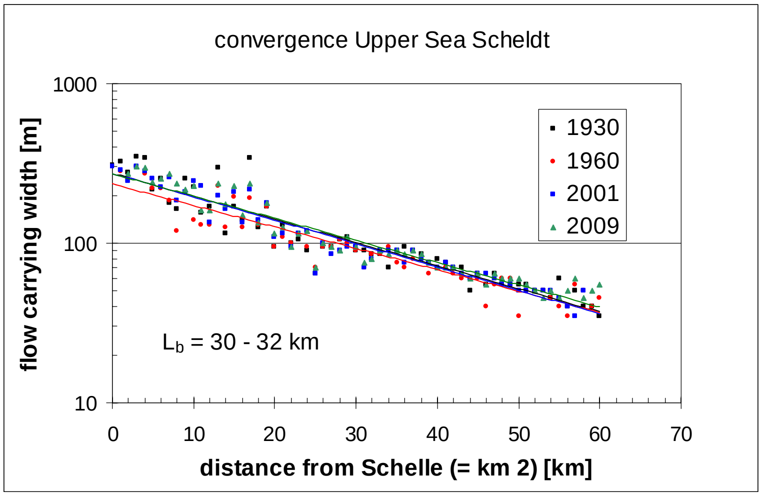

Fig. 4.45: Convergence length of Upper Sea Scheldt shows little variation since 1930.

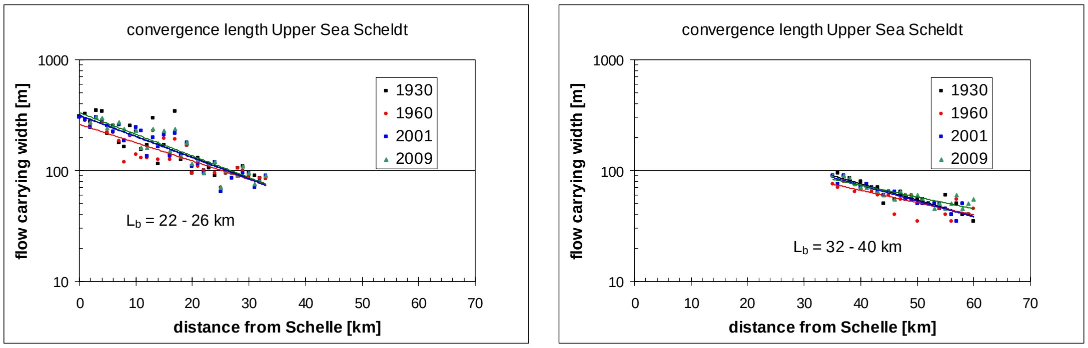

Fig. 4.46: Convergence length of Upper Sea Scheldt for lower part (up to km 34) and upper part (from km 34); km 34 is halfway Dendermonde and Schoonaarde.

Fig. 4.47 presents the total width of the Sea Scheldt River and its flow carrying width, again for the lower and upper reaches. The total width is defined as the width of the river at the edges of its salt marshes. Hence, this total width is expected to be a bit too large, as in our tidal analysis, the mean high water level is relevant (see comment below). From a linear fit, we define a mean value for b_* for the upper and lower reaches.

Fig. 4.47 shows a continuous decrease in b_* since 1850, in particular between 1850 and 1930 in the upper reaches of the river. Note also that in the lower reaches, b_* increases in upstream direction, whereas in the upper reaches b_* decreases in upstream direction (apart from the 1850-data). This difference in trend may have a similar cause as discontinuity in convergence length, discussed above.

It should be noted that, because of its definition with respect to the edges of the salt marshes, the values in b_* in Fig. 4.47 are likely to be an over-estimation of the actual values, which should be related to the river's width at mean high water. Moreover, it is likely that this over-estimation is larger in recent years, because of siltation on intertidal mud flats and subsequent development of vegetation owing to the high suspended sediment concentrations in the river. Visual inspection by the author of this report suggests that in 2012 a large part of intertidal area has been lost in favor of salt marshes.

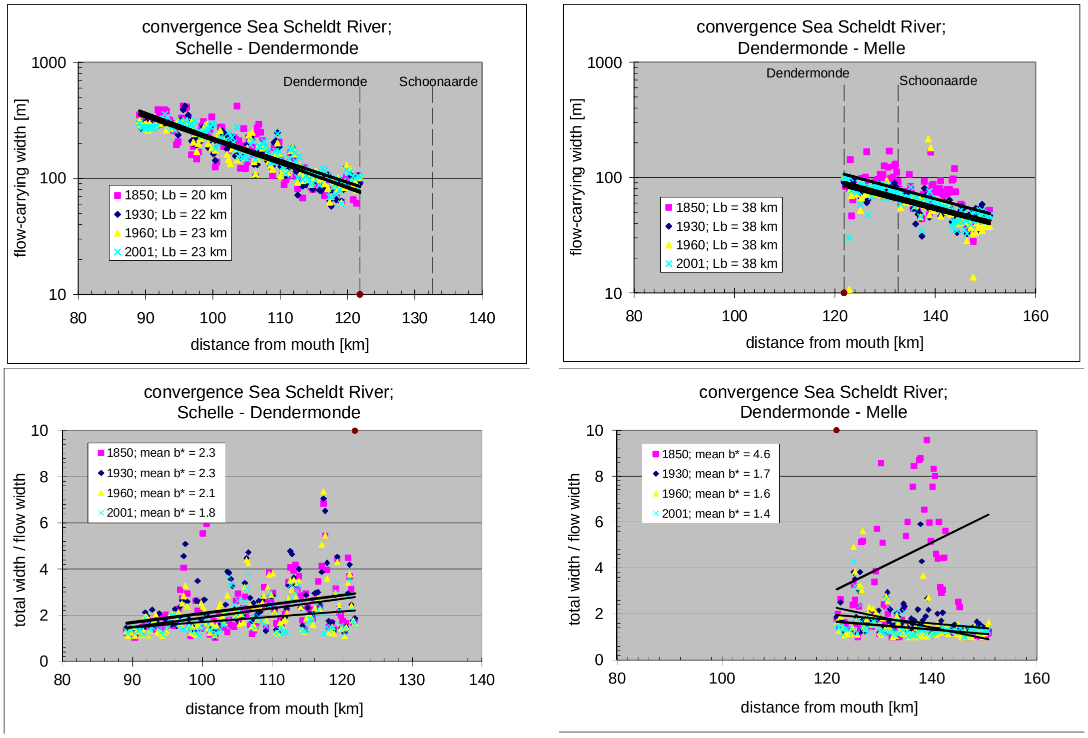

Fig. 4.47: Convergence length of flow carrying width (upper panel) and ratio total width over flow-carrying width (lower panel) of lower reach of Sea Scheldt (Schelle – Dendermonde) and upper reach (Dendermonde – Melle) since 1850.

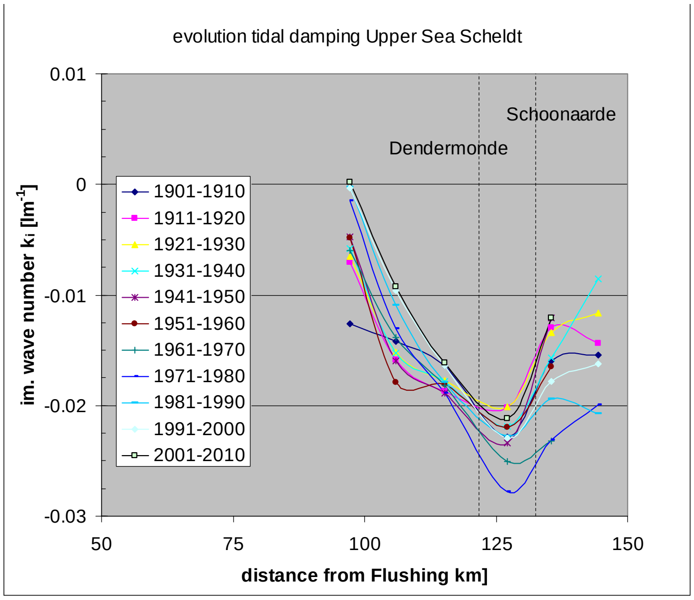

Fig. 4.48: Evolution of imaginary wave number along Upper Sea Scheldt, based on the data of Fig. 4.41b.

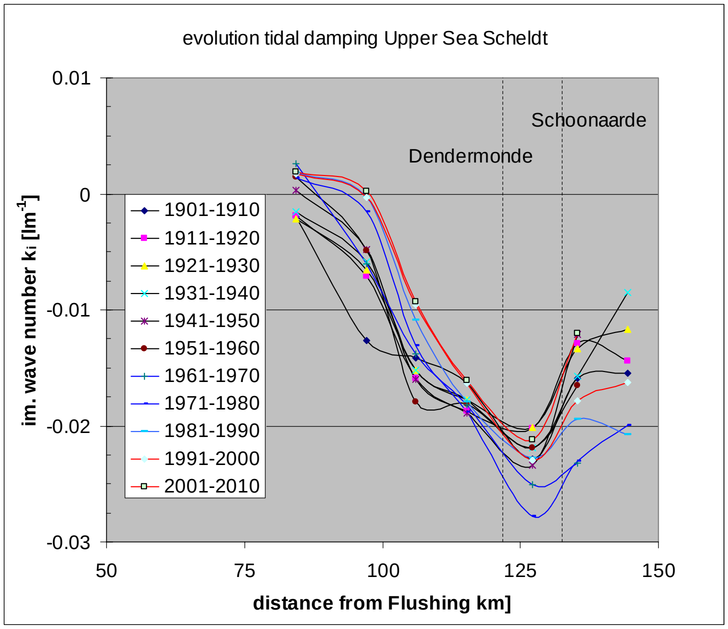

Fig. 4.49: Evolution of the imaginary wave number with time, and grouped for data from before 1960, after 2000, and in between. Time-mean values of data <1960 (black lines) yield $k_{i,old}$.

Fig. 4.48 presents the imaginary wave number as derived from the measured tidal data of Fig. 4.41b, in which missing data points in the original data (e.g. Fig. 4.41a) have been added upon interpolation. Fig. 4.48 shows a number of important trends:

- From Schelle to halfway Dendermonde-Schoonaarde, the damping of the tidal wave increases (k_i more negative), and beyond ~km 125, the damping decreases again.
- In general, the damping along most part of the river has decreased over time.

- Close to Schelle, the tidal wave is no longer damped in the early 21th century.

Fig. 4.43 shows a profound deepening of the Upper Sea Scheldt between 1960 and 2001 (other information suggests that this happened between 1960 and 1970). Therefore, the evolution of the imaginary wave number k_i has been replotted in Fig. 4.49, where the data have been grouped in series before 1960 (black lines), after 2000 (red lines, and in between. Up to Dendermonde/Schoonaarde, k_i has increased with ~0.005 km^{-1}, further up-estuary, the trends are less obvious.

Next, the imaginary wave number before 1960 has been averaged over time, yielding a time-mean variation of k_i with distance, referred to as $k_{i,old}$. Let us next assume that the increase in tidal amplitude at Antwerp is due only to deepening/widening of the Western Scheldt and the Sea Scheldt in the vicinity of Antwerp, i.e. all river stretches down-estuary of Schelle. Then we can "predict" the tidal evolution up-estuary of Antwerp, using the measured evolution of the tidal range at Antwerp, and using $k_{i,old}$. This prognostic tidal evolution is presented in Fig. 4.50, in conjunction with the actual measured evolution, suggesting that the measured amplification from Schelle till Dendermonde/Schoonaarde should be ascribed for about 30% to down-estuary modifications of the Scheldt estuary, and for about 70% to changes in local bathymetry as discussed in Fig 4.43. The anomalous behavior up-estuary of Dendermonde/Schoonaarde is discussed below.

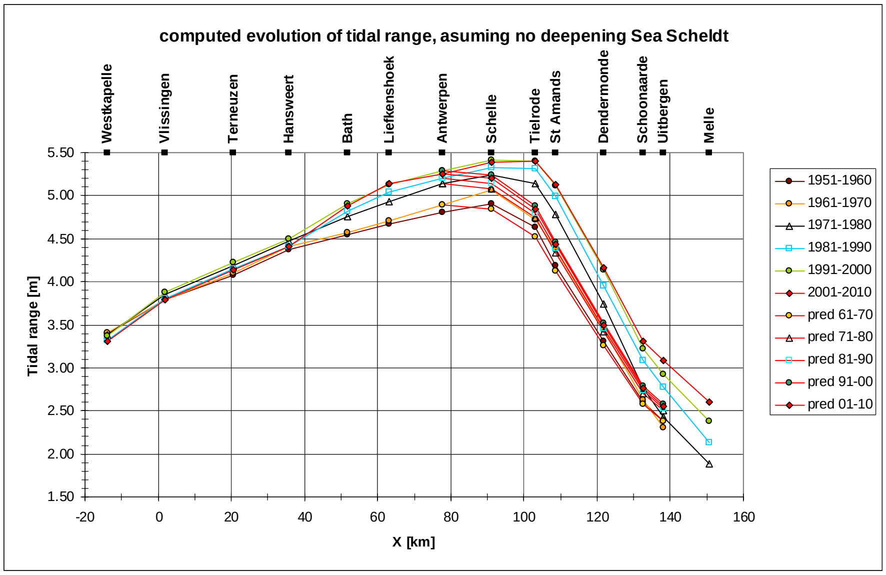

Fig. 4.50: Prognostic tidal evolution along the Upper Sea Scheldt, based on the lower values of the imaginary wave number of Fig. 4.49 (e.g. $k_{i,old}$).

The change in longitudinal trend of the imaginary wave number beyond Dendermonde/Schoonaarde in Fig. 4.49 is remarkable. To explain this trend, we have computed the tidal amplitude over the river beyond Sint Amands without a weir and with a weir 8 km up-estuary of Melle. We have assumed a constant convergence length and a mean depth of 4.5 m. The results are presented in Fig. 4.51 in the form of the difference in imaginary wave number Δk_i between the configuration with and without weir, reproducing the reverse in trend of Fig. 4.49, and an increase by about 0.005 km^{-1}, which is about a factor two too small. Note that these results are not sensitive to the convergence length L_b, but highly sensitive to the water depth – the latter varies considerably over the last part of the river, whereas no information is available on the sections up-estuary of Melle. The results of Fig. 4.51 are therefore only indicative of effect of tidal reflections on the tidal evolution,

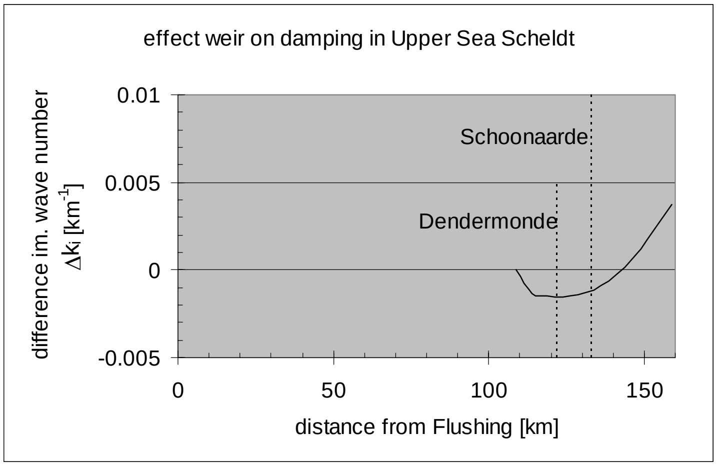

Fig. 4.51: Estimate of effect of weir on tidal damping in upper reaches of Upper Sea Scheldt.

Next, the imaginary wave numbers of Fig. 4.49 are made dimensionless with the convergence length of the Upper Sea Scheldt (e.g. equ. 8), where data up-estuary of Schoonaarde are omitted, as these are affected too much by tidal reflection. The dimensionless damping is plotted against the estuarine convergence number Λ_e in Fig. 4.52, showing a not too systematic trend with time. Data from before the large deepening in the Upper Sea Scheldt (<1960), data beyond 1990 and data in between have been marked with different colors. In particular, the data for the trajectory Dendermonde – Schoonaarde are a bit erratic (results not shown), most likely because of the effects of tidal reflection, and therefore not further included in our analysis.

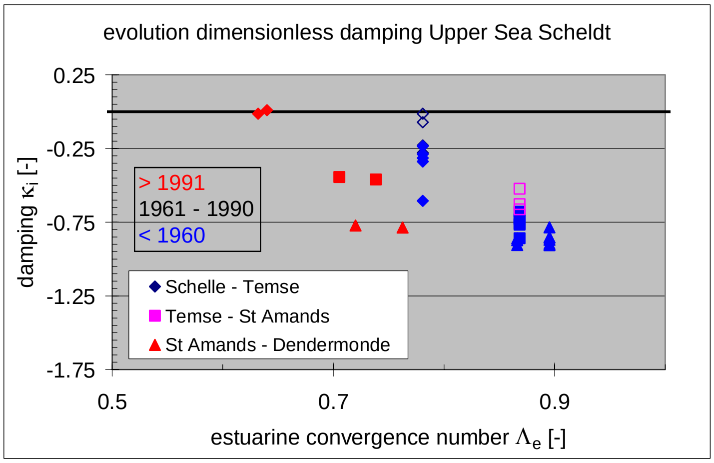

Fig. 4.52: Evolution of dimensionless imaginary wave number κ_i with variations in estuarine convergence number Λ_e.

Next, the linear model for an infinitely long tidal river (equ. 11) is fitted through the data by tuning the roughness parameter r_*, the results of which are presented in Fig. 4.53, showing variations in r_* from 9 to about 3.

To compute the effective hydraulic drag from the fitted r_*-values, we need to make an assumption on the flow velocity in the Upper Sea Scheldt. For this, we have used computational results from the Delft3D model of the Western Scheldt, which show that the velocity amplitudes at Antwerp are about 10% larger than at Flushing, for the current bathymetry. We assume that the tidal velocities at Flushing have not changed much throughout the 20th century, and we assume further that the evolution of the tidal velocities along the Scheldt estuary over time follow the measured variations in tidal range, i.e. can be assessed from the imaginary wave number of Fig. 4.49. Then, by tuning r_* fitting equ. (11) through the dimensionless data, and using the estimated flow velocity and measured water depth, the effective Chézy coefficient can be established. The variation of C with time along the lower part of the Upper Sea Scheldt is presented in Fig. 4.54. All Chézy values are a bit low, which may be attributed to the fact that in the linear model many physical features in the river (bends, bed forms, bank irregularities, local variations in river topography and bathymetry, etc.) are missing. Also, estimates of the flow velocity are rather crude, though errors in this estimate occur only under the root of the solution to C (equ. 8).

Yet Fig. 4.54 suggests that the Chézy coefficient, hence effective hydraulic drag, did not change for the river stretch St Amands – Dendermonde, but increased considerably, in particular over the first part Schelle – Temse. If this reduction in drag would have been caused by high suspended sediment concentrations, this analysis suggests that values in SPM have been large for many decades, which, in conjunction with further deepening (e.g. Fig. 3.3) may explain the increase in C. The anomalous behavior between 1970 – 1990 is not understood, but may be misleading, as topographic/bathymetric data over that period is missing, and had to be manufactured by interpolation from other decades (see also bed level data of Fig. 4.43).

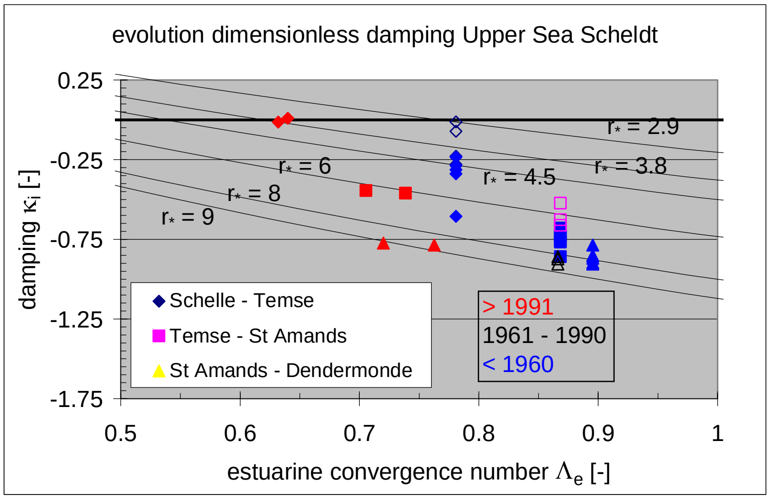

Fig. 4.53: Fits of linear solution trough observations tuning the roughness parameter r_* in the κ_i – Λ_e diagram.

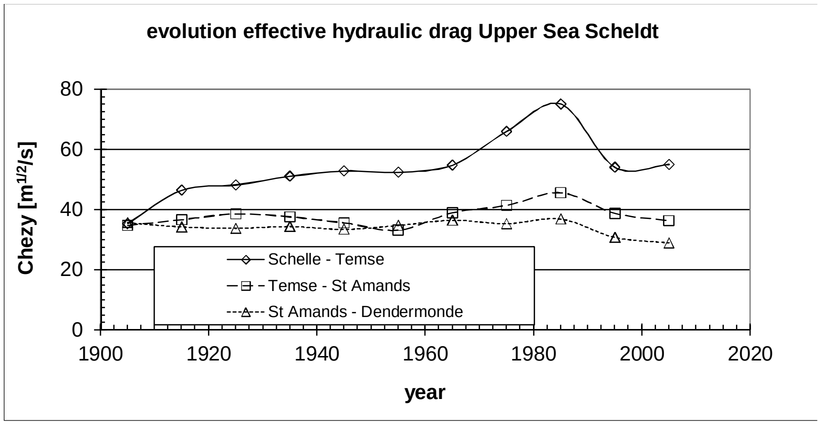

Fig. 4.54: Evolution of effective hydraulic drag (Chézy coefficient) with time,

Fig. 4.55 presents measured data on tidal asymmetry, in the form of the ratio of the period of rising tide and falling tide, showing flood dominance over the entire river, Plancke et al. (2012). It is observed that flood dominance increases in upstream direction, as expected, as water depth decreases in upstream direction. We note that the river fresh water flow is relatively small, hence does only slightly affect the duration of flood and ebb period.

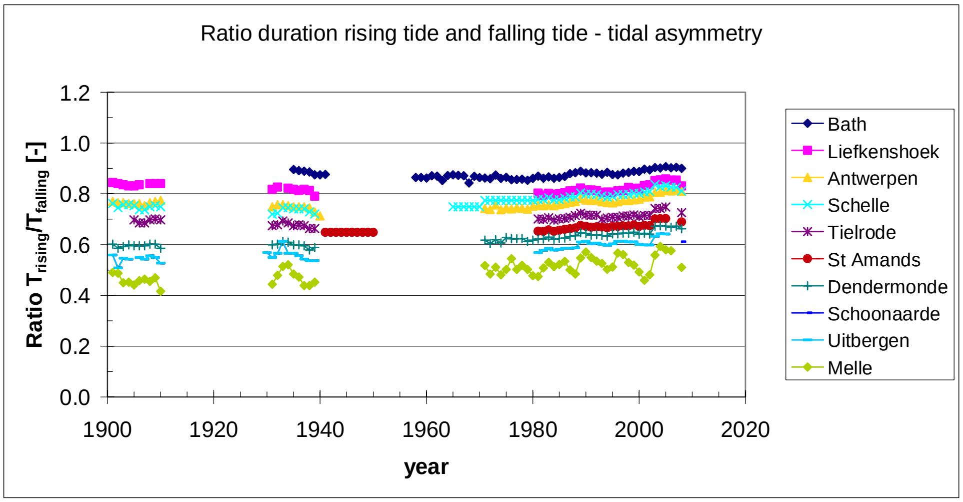

Fig. 4.55: Observed tidal asymmetry in Sea Scheldt.

However, it is remarkable that the asymmetry changes little over time, except may be for Schelle, given the large increase in tidal amplitude. This discrepancy can be explained from two developments:

1. In particular in the upper reaches, the water depth has increased largely in a relative sense. Larger water depth would decrease tidal asymmetry, counteracting the effects of a larger tidal range.
2. Probably more important is the development of tidal asymmetry in the Western Scheldt, e.g. Fig. 4.55, which serves as “boundary conditions” for the Upper Sea Scheldt. Hence, further to local generation of overtides in the Upper Sea Scheldt, tidal asymmetry is “imported” from the down-estuary reaches of the estuary, i.e. the Western Scheldt.

It is beyond the present study to evaluate the evolution of tidal asymmetry in the Western Scheldt, but the behavior of the asymmetry at Hansweert is remarkable, suggesting that its asymmetry tends to re-establish the conditions at the beginning of the 20th century.

5 Summary and conclusions

5.1 Samenvatting met focus op Boven Zeeschelde

Dit rapport beschrijft een analyse van de historische getijontwikkeling in de Boven Zeeschelde om te onderzoeken of de diverse ingrepen in het Schelde-estuarium zouden kunnen leiden tot hypertroebele condities. De rationale voor deze studie ligt in de ontwikkeling van de Eems en Loire rivieren, welke vermoedelijk door uitdiepen en vernauwing zijn verworden tot hyper-geconcentreerde systemen met grote hoeveelheden fluid mud, verticale stratificatie en waterkwaliteitsproblemen (zuurstofloosheid). Deze studie is als volgt opgezet:

1. Data van diverse rivieren zijn verzameld; dit was niet altijd even succesvol, en op het moment van het schrijven van dit rapport waren min of meer betrouwbare data van de Eems, Loire, Elbe en Boven Zeeschelde beschikbaar.
2. Vervolgens is een analytisch model opgesteld op basis waarmee de getijvoortplanting in een getijderivier kan worden berekend.
3. Met dit model is de responsie van menselijke ingrepen (verdieping en vernauwing) op conceptuele wijze geanalyseerd.
4. Het model is daarna gebruikt om de historische ontwikkeling van het getij in de vier bovengenoemde rivieren te analyseren.

In deze sectie worden vooral de conclusies m.b.t. de Boven Zeeschelde samengevat; een meer generieke samenvatting is te vinden in de Engelstalige Summary, waarin de ontwikkeling van de diverse rivieren onderling wordt vergeleken.

In onze analyse wordt impliciet gebruik gemaakt van twee fysische mechanismen.

I. De effectieve hydraulische weerstand in een (getijde)rivier wordt kleiner en de ruwheidslengte wordt groter indien de waterkolom gestratificeerd raakt. Zo’n stratificatie treedt op bij dieptegemiddelde slibconcentraties van ter grootte van enkele 100-en mg/l, mits over een significante lengte van het estuarium. Winterwerp et al. (2009) hebben dit effect semi-analytisch gekwantificeerd. Op basis van dat werk kan worden geconcludeerd dat de toename in Chézy coëfficiënt, voor de rivieren die in dit rapport worden bestudeerd, ongeveer 15 – 30 $m^{1/2}/s$ kan bedragen – deze toename is rechtevenredig met de absolute waterdiepte.

II. In een estuarium/getijderivier kunnen twee troebelingsmaxima (ETM = estuarine troebelingsmaximum) optreden. Het eerste maximum, ETM1, is het klassieke maximum, waarnaar verwezen wordt in alle tekstboeken over estuaria, dat gevormd wordt door een balans tussen stroomafwaarts transport van slib door de rivier en stroomopwaarts transport door estuariene circulatie (door de zout-zoetgradiënt) en mogelijk een beetje getij-asymmetrie. Dit ETM1 treedt op in alle “normale” estuaria, en wordt gevonden in de mond van het estuarium nabij de punt van de zoutindringing.

   Echter, een tweede ETM2 kan bestaan verder bovenstrooms, en wordt gevormd door een balans tussen stroomafwaarts transport van slib door de rivier en stroomopwaarts transport door getij-asymmetrie (zowel in pieksnelheden als verticale menging, i.e. interne asymmetrie).

   Door grote veranderingen (verdiepen, menselijke ingrepen) kan zich dit (tweede) ETM2 ontwikkelen in een rivier die aanvankelijk werd gekenmerkt door een ETM1. Omdat ETM1 en ETM2 worden gedreven door verschillende fysische processen, en beide stabiel zijn, spreken we van een regime-omslag indien zich zo’n tweede ETM2 ontwikkelt. Deze twee regimes zijn in Fig. 5.1 geschetst.

Het analytisch model bestaat uit de analytische oplossing van de eendimensionale ondiep-water vergelijkingen, i.e. de continuïteitsvergelijking en de impulsvergelijking. Deze vergelijkingen zijn gelineariseerd door in de impulsvergelijking de advectieterm te verwaarlozen, en de hydraulische weerstand rechtevenredig met de stroomsnelheid te maken. Ook kan de invloed van rivierafvoer niet worden meegenomen. De oplossing van dit systeem van vergelijkingen bestaat uit het golfgetal als functie van het in dit rapport geïntroduceerde estuariene convergentiegetal en de hydraulische weerstand. Het golfgetal bestaat uit een reëel deel, welke de lengte van de getijgolf voorstelt, en een imaginair deel dat de demping of amplificatie van het getij weergeeft. De vorm (breedte en grootte intergetijdegebied) en diepte van het estuarium worden weergegeven door het estuariene convergentiegetal. Merk op dat verondersteld wordt dat de breedte van de rivier exponentieel afneemt – deze aanname geldt bijna altijd. De oplossing van het analytisch model is geschreven in dimensieloze kentallen, zodat het gedrag van verschillende rivieren onderling vergeleken kan worden. De analytische oplossing beschrijft het gedrag van een ingaande getijgolf en haar reflectie (indien aanwezig). In deze studie wordt het effect van reflecties over het algemeen niet in de analyses meegenomen omdat de vergelijkingen voor een reflecterende golf niet meer analytisch zijn op te lossen in geval van een niet-constante waterdiepte. Indien het bodemprofiel op willekeurige wijze langs de rivier verandert, is ook geen analytische oplossing mogelijk.

Met het analytisch model kan ook de looptijd van de golf door het estuarium en het faseverschil tussen waterstand en stroomsnelheid, alsmede een proxy voor de getij-asymmetrie worden bepaald, alsmede van. In het overgrote deel van de analyses is verondersteld dat de getijderivier oneindig lang is (geen reflecties).

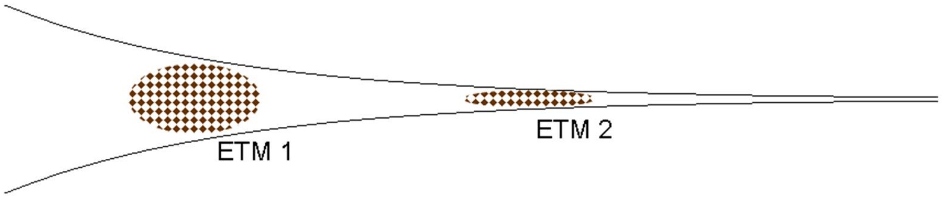

Fig. 5.1: Schets van Estuariene Troebelingsmaxima (ETM); ETM1 wordt gekarakteriseerd door een balans tussen effecten rivierafvoer en estuariene circulatie (en een beetje getij-asymmetrie) en ETM2 door balans tussen effecten rivierafvoer en getij-asymmetrie.

Het analytisch model wordt op twee manieren gebruikt:

I. Veranderingen in getijslag (-amplitude) en getij-asymmetrie worden berekend als functie van hypothetische veranderingen in het areaal intergetijdegebied, de convergentielengte van het estuarium, haar diepte, en de effectieve hydraulische weerstand. Dit levert conceptueel inzicht in het gedrag van een estuarium in responsie op menselijke ingrepen.

II. De waargenomen historische ontwikkeling in getijslag wordt geëvalueerd en gekoppeld aan de historische veranderingen in de vorm van het estuarium:
   - Voor diverse tijdsperiodes wordt voor ieder riviertraject tussen twee getijstations in de demping/amplificatie berekend in de vorm van het (dimensieloze) imaginaire golfgetal.
   - De informatie over de historische ingrepen in de rivieren (verdieping, vernauwing, verlies intergetijdegebied, constructie van een stuw) wordt samengevat in het

estauriene convergentiegetal. Dit getal wordt kleiner bij toenemende convergentie van de rivier, toenemende waterdiepte en afnemende breedte intergetijdegebied.

- De historische ontwikkeling van het imaginaire golfgetal wordt uitgezet tegen de ontwikkeling van het estuariene convergentiegetal. Ieder punt in dat diagram is verkregen uit waarnemingen en vertegenwoordigt een riviertraject over een bepaalde periode.
- Het analytisch model wordt gefit door de bovengenoemde data-punten door de ruwheid in het model te variëren. Aldus wordt de historische verandering in effectieve hydraulische weerstand gereconstrueerd.
- Ten slotte wordt de historische verandering van de getij-asymmetrie geanalyseerd op basis van of het analytisch model, of de actuele waarnemingen.

De responsie van een getijderivier op verdiepen en vernauwen, zoals berekend met het analytisch model, is weergegeven in Fig. 5.2 en 5.3. Verondersteld wordt dat het estuarium oneindig lang is, dat de slibconcentraties aanvankelijk laag zijn, en dat de rivierbodem bestaat uit zand. Bovendien bevindt zich langs de gehele rivier een intergetijdegebied ter grootte van de breedte van het stroomvoerend deel van de rivier. De relatieve getij-amplitude op 60 km van de mond neemt monotoon toe met een verdieping van de rivier, zoals aangegeven met de zwarte lijn in Fig. 5.2.

Indien het intergetijdegebied verdwijnt door bijvoorbeeld bedijkingen of inpolderingen, is de toename in getijslag wat groter – zie de blauwe lijn in Fig. 5.2.

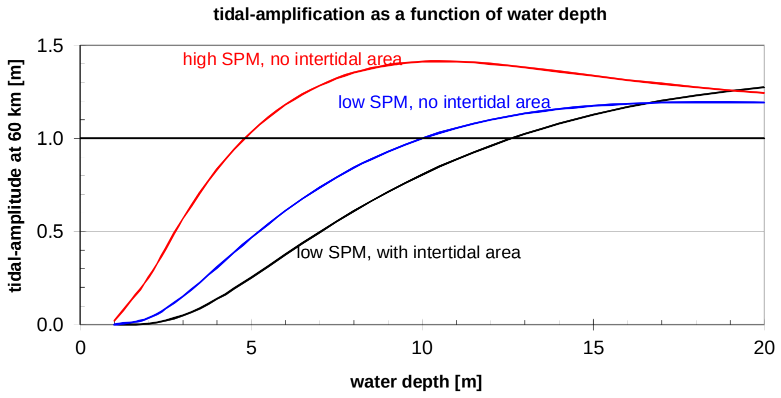

Fig. 5.2: Responsie van getij-amplitude op verdieping als functie van aanwezigheid intergetijdegebied en slib in de waterkolom, c.q. op de bodem.

De belangrijkste responsie van de rivier is echter in Fig. 5.3 weergegeven. Voordat het intergetijdegebied wordt verwijderd, is het getij eb-dominant, d.w.z. dat de getij-gemiddelde slibtransporten zeewaarts gericht zijn (zwarte lijn Fig. 3, een representatieve afstand van de mond – karakteristiek voor het hele estuarium). Merk op dat de effecten van een eventueel extern gegenereerde getij-asymmetrie niet wordt meegenomen. Echter, na verlies van dat intergetijdegebied slaat die richting om, en wordt het systeem vloed-dominant. Dit betekent dat er slib het estuarium in wordt gepompt, dan wel dat slib dat met de rivier wordt afgevoerd in de rivier accumuleert. De condities voor een ETM2 (Fig. 5.1) worden geschapen. Bij toenemende slibconcentratie neemt echter de effectieve hydraulische weerstand af (Chézy coëfficiënt neemt toe), waardoor het getij verder gaat opslingeren (rode lijn in Fig. 5.2), hetgeen weer tot gevolg heeft dat de vloed-dominantie toeneemt (rode lijn in Fig. 5.3). Hierdoor wordt er nog meer slib de rivier in gepompt, en ontstaat een zogenaamde positieve terugkoppeling, of sneeuwbaleffect.

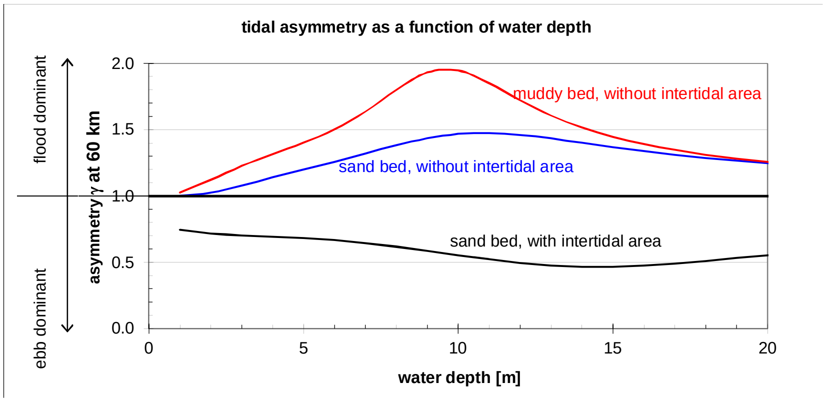

Fig. 5.3: Responsie van getij-asymmetrie(γ-parameter) op verdieping als functie van aanwezigheid intergetijdegebied en slib in de waterkolom, c.q. op de bodem.

Dit sneeuwbaleffect is in Fig. 5.4 geschetst. Opgemerkt wordt dat het verlies in intergetijdegebied dus eigenlijk de veerkracht van de rivier heeft aangetast – met intergetijdegebied slingert het getij ook wel op, maar worden de condities voor ETM2 niet geïnitieerd. Of ETM2 condities daadwerkelijk zullen ontstaan, en de termijn waarop, hangt af van de hoeveelheid slib die beschikbaar is. De tijdsperiode tussen het creëren van de daarvoor “geschikte” condities en de vorming van ETM2 (of hyper troebele rivieren) kan lang zijn, tot decades toe. Het verlies in intergetijde-gebied heeft eigenlijk in heel Europa eind 19^{de}, begin 20^{ste} eeuw plaatsgevonden. De grote verdiepingen werden in de tweede helft van de 20^{ste} eeuw gerealiseerd. Het verlies aan intergetijdegebied beïnvloedt de veerkracht van het estuarium op twee manieren:

1. Verlies aan intergetijdegebied vergroot de getij-amplificatie bij verdiepen en induceert een vloed-dominant systeem (het laatste effect is het belangrijkste),
2. Verlies aan intergetijdegebied verkleint de accomodatieruimte voor slibafzettingen – slib ingebracht in het systeem door de vloeddominantie blijft dan dus in de waterkolom waardoor de effectieve hydraulische weerstand afneemt, en de sneeuwbal in Fig. 4 geïnitieerd kan worden.

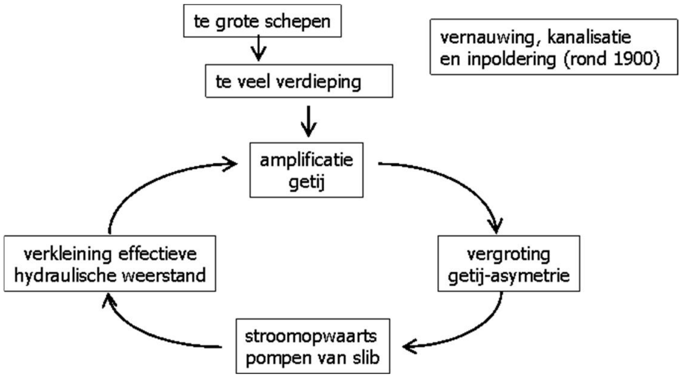

Fig. 5.4: Het sneeuwbaleffect (positieve terugkoppeling. Verdieping na verlies veerkracht kan leiden tot een vicieuze cirkel waarbij meer en meer slib in de rivier accumuleert waardoor getij-amplificatie en getij-asymmetrie sterk toenemen – dit kan leiden tot ETM2 condities.

Merk op dat deze systeemomslag tijd kost – op basis van de data uit de Eems Rivier schatten wij dat hyper-troebele symptomen zichtbaar worden één à twee decennia na het passeren van een omslagpunt.

In het laatste deel van deze samenvatting wordt de ontwikkeling van het getij in de Schelde geanalyseerd, met focus op de Boven Zeeschelde. De belangrijkste ingrepen in het Schelde-estuarium, relevant voor de Boven Zeeschelde, zijn:

- Bedijking, inpolderingen en rechttrekkingen in de Boven Zeeschelde, met name aan het eind van de 19^{de} en begin 20^{ste} eeuw.
- De breedte van de Boven Zeeschelde vernauwt exponentieel naar Gent toe – deze vernauwing is nauwelijks veranderd sinds 1900.
- Verdieping van de Boven Zeeschelde rondom 1960 met 1.5 – 2 m; het is niet met zekerheid bekend wat de oorzaak van deze verdieping is, maar een morfologische responsie op ingrepen benedenstrooms lijkt waarschijnlijk.
- Tot op heden is de bodem van de Boven Zeeschelde nog zeer zandig. Langs de oevers is echter veel slib afgezet, en ook de Durme is vrijwel geheel dichtgeslibd.
- De loop van de rivier rondom Gent is fors veranderd tussen 1950 en 1970. De oude, noordelijke tak (van Melle tot stuw bij Gentbrugge) is in hoge mate dichtgeslibd. Een nieuwe, zuidwaartse tak is gegraven, met een breed, diep stuk naar een grote sluis/stuw in Merelbeke, en een kleine tak naar het zuiden naar de oorspronkelijke rivier, welke na een paar kilometer is afgesloten met een stuw te Zwijnaarde.
- De Westerschelde en Beneden Zeeschelde zijn met name tegen het eind van de 20^{ste} eeuw fors verdiept en verbreed t.b.v. de scheepvaart, terwijl ook zand is onttrokken t.b.v. winning van bouwzand, en delen van het estuarium zijn ingepolderd.

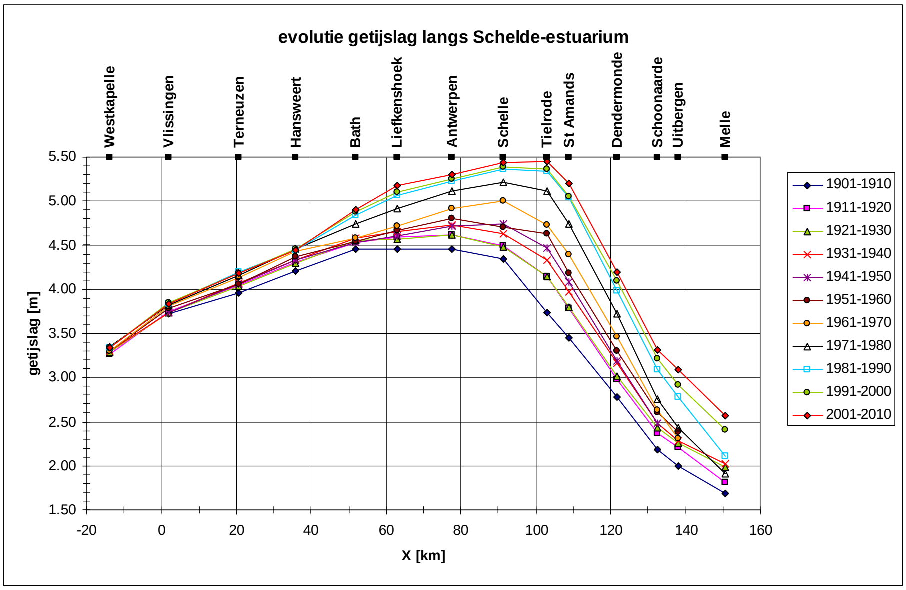

Fig. 5.5: Historische ontwikkeling getijslag langs Schelde-estuarium, gecorrigeerd voor 18.6 jaar cyclus.

De ontwikkeling in getijslag is weergegeven in Fig. 5.5, dat wil zeggen het verschil tussen laag- en hoogwater. Uit deze figuur blijkt dat de getijslag sinds 1900 flink is toegenomen, rondom Tielrode zelfs met meer dan 1.5 m. Uit de analyse in hoofdstuk 4.5 van dit rapport blijkt dat de toename in getijslag in de Boven Zeeschelde (bovenstrooms Schelle) voor ca. 30% is toe te schrijven aan ingrepen benedenstrooms (dus de Westerschelde en Beneden Zeeschelde) en voor ca. 70% door lokale effecten (verdiepingen rond 1960).

Op basis van de data in Fig. 5.5 is de ontwikkeling van de amplificatie/demping van het getij bepaald in de vorm van het imaginaire golfgetal. De resultaten in Fig. 5.6 suggereren dat sinds 1900 het imaginaire golfgetal langs de gehele Boven Zeeschelde minder negatief is geworden, het getij wordt dus minder gedempt. Opmerkelijk is de omkeer in trend vanaf km 125, i.e. vanaf halverwege Dendermonde en Schoonaarde. Analyse met het analytisch model suggereert dat deze omkeer het gevolg is van reflectie(s) van de getijgolf op de bovenstroomse stuwen. Het getij blijft echter gedempt.

Ten slotte is met het analytisch model de verandering in effectieve hydraulische weerstand berekend. De resultaten in Fig. 5.7 laten zien dat in het benedenstroomse deel van de Boven Zeeschelde (Schellle – St Amands) de effectieve Chézy coëfficiënt is toegenomen van ca 40 tot 50 à 60 $m^{1/2}$/s. Dit resultaat dient nog vergeleken te worden met waarnemingen van het slibgehalte in de rivier.

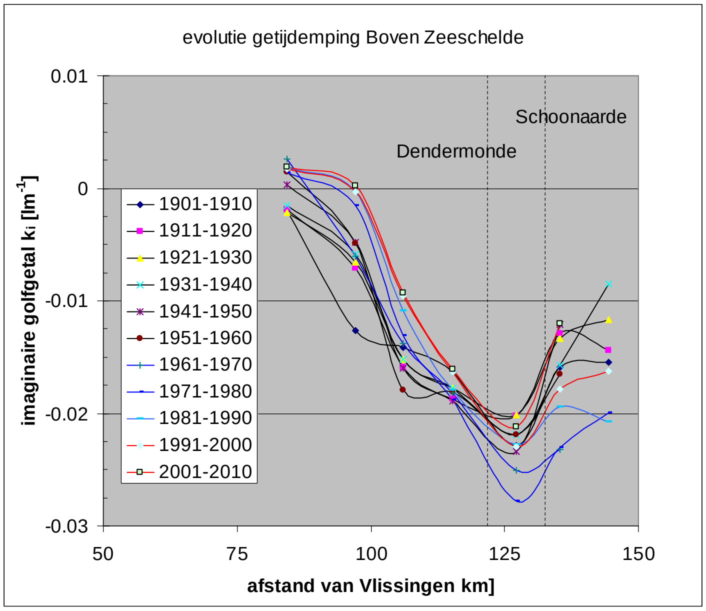

Fig. 5.6: Historische ontwikkeling demping getijgolf langs Schelde-estuarium, gebaseerd op data Fig. 5.5. De demping is gerelateerd aan het imaginaire golfgetal k_i via $a(x) = a_0 \exp\{k_i x\}$, waarin $a(x)$ de getijamplitude op afstand x van locatie 0 is.

De gehele Zeeschelde is vloed-dominant, i.e. de duur van het stijgend water is korter dan die van het dalend water. Deze vloeddominantie neemt toe in stroomopwaartse richting, en is niet veel veranderd sinds 1900.

Met de beschikbare data en het analytisch model kan geen eenduidig antwoord gegeven worden op de vraag of de Boven Zeeschelde zich aan het ontwikkelen is in de richting van een hyper-troebel systeem. Wel is de veerkracht van de Boven Zeeschelde fors afgenomen:

1. Er is vrijwel geen intergetijdegebied meer, en de rivier is over haar gehele lengte vloed-dominant.
2. De accommodatieruimte voor slibafzettingen is fors afgenomen, zodat slibgehaltes in de waterkolom zullen toenemen indien slib de Boven Zeeschelde wordt ingepompt.

Het getij in de Boven Zeeschelde is nog steeds gedempt, maar deze demping neemt af. Fig. 5.7 suggereert dat de effectieve hydraulische weerstand inderdaad is afgenomen, met name na de verdieping rond 1960. Het onregelmatige gedrag van de Chézy coëfficiënt rond 1990 wordt waarschijnlijk veroorzaakt door een onnauwkeurige interpolatie van de dieptegegevens – deze gegevens zijn slechts voor een beperkt aantal jaren beschikbaar.

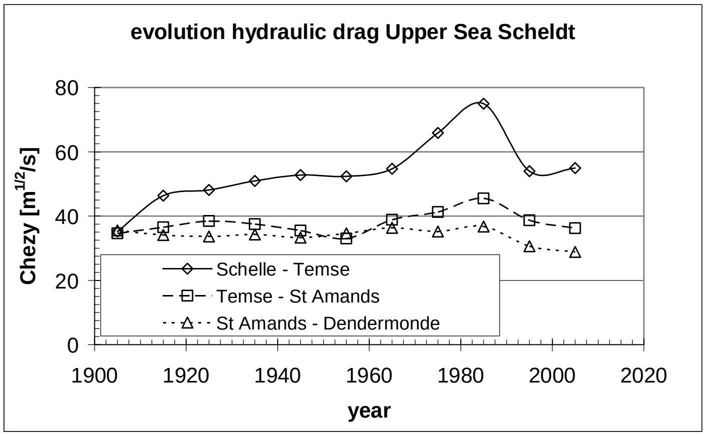

Fig. 5.7: Ontwikkeling effectieve hydraulische weerstand (Chézy coëfficiënt) in Boven Zeeschelde.

Mogelijke mitigerende maatregelen om ongewenste ontwikkelingen af te remmen of te keren bestaan uit:

- Vergroten van de rivierafvoer, waardoor de condities voor ETM2 veranderen,
- Vergroten van de accommodatieruimte zodat ingepompt slib niet in de waterkolom accumuleert,
- Vergroten van het intergetijdegebied om het getij minder vloed-dominant te maken; de benodigde hoeveelheid intergetijdegebied zal moeilijk te realiseren zijn.
- Vergroting van de hydraulische weerstand in het systeem (bijvoorbeeld herstel nu afgesneden bochten),
- Wegbaggeren van huidige slibafzettingen zodat accommodatieruimte wordt vergroot.

Deze maatregelen zijn bedacht op kwalitatieve gronden, en nog op generlei wijze gekwantificeerd, dus hun efficiëntie is onbekend.

5.2 General summary and conclusions

This report describes an analysis of the historical development of the tide in a number of European estuaries in relation to the human interventions (deepening, narrowing, rectifications, ….) carried out during the last century. The rationale behind this study is a fear that the Upper Sea Scheldt (Belgium, river stretch between Schelle and Ghent) may develop into a hyper-turbid system, such as the Ems and Loire rivers. This study is set up as follows:

1. Data of various tidal rivers have been collected. This was not always successful, and at the moment this report was written, more or less reliable/accurate data are available from the Ems, Elbe, Loire and Upper Sea Scheldt.
2. An analytical model has been derived, computing tidal propagation in estuaries.
3. This analytical model was then used to assess in a conceptual way the response of tidal rivers to human interventions.
4. Finally, that model has been used to analyze the measured historical development of the tide in the four rivers mentioned under 1.

This section summarizes the generic findings of this study, comparing the behavior of the various rivers; the conclusions with special focus on the Upper Sea Scheldt (Boven Zeeschelde) are given in the Dutch Summary (Samenvatting) above.

In our analysis, two physical mechanisms are implicitly accounted for:

I. The effective hydraulic drag in a (tidal) river decreases and the friction length increases when the water column becomes stratified. Such stratification occurs at depth-averaged concentrations of fine suspended sediment of a few 100 mg/l. Winterwerp et al. (2009) quantified this effect in a semi-analytical way. This work suggests that the increase in Chézy coefficient, for the rivers treated in this report, would amount to 15 – 30 $\mathrm{m}^{1/2}/\mathrm{s}$ – this increase is linearly proportional with the absolute water depth.

II. In an estuary, two turbidity maxima (ETM, estuarine turbidity maximum) may occur. The first maximum, ETM1, the classic one referred to in all text books on estuaries, is the result of a balance between river-induced flushing and up-estuary transport of fine sediment by estuarine circulation (induced by the longitudinal salinity gradients), and possibly some tidal asymmetry. This ETM1 is found in all “normal” estuaries near the estuary’s mouth at the head of the salinity intrusion.

However, a second may be formed further up-estuary, which is governed by a balance between river-induced flushing and up-estuary transport by tidal asymmetry (both peak velocities and vertical mixing, i.e. internal asymmetry).

As a result of large changes in the river (deepening, human interventions), such a second ETM2 can develop in a river previously characterized by an ETM1. Because ETM1 and ETM2 are driven by different physical processes, and because both ETM’s are fairly stable, we can refer to a regime shift when such a second ETM2 develops. These two regimes are sketched in Fig. 5.8.

The analytical model consists of the analytical solution of the one-dimensional shallow water equations, i.e. continuity and momentum equations, describing the water movement in tidal rivers. Note that the effects of river flow cannot be taken into account. These equations have been linearized by omitting within the momentum equation the advection term, and by making the friction term linear in the velocity. The solution to this set of equations is given in the form of a wave number as a function of the estuarine convergence number, introduced in this report, and the effective hydraulic drag. The wave number consists of a real part, reflecting the tidal wave length, and an imaginary part, reflecting the damping or amplification of the tide in the estuary. The plan form shape of the estuary (e.g. width, intertidal area), and its depth are given by the estuarine convergence number. We assume that the width of the estuary converges in an exponential way, an assumption almost always met in alluvial estuaries. The solution of the analytical model is given in dimensionless numbers allowing mutual comparison of rivers of rather different size. The analytical solution describes the behavior of an incoming tidal wave, and its reflection, if relevant. In this study, the reflected wave is ignored in most cases, as the underlying equations cannot be solved anymore analytically in case of non-constant depths along the river. Note that an analytical solution is not possible either, when the water depth varies arbitrarily along the river.

We also determined the celerity of the tidal wave through the estuary, and the phase difference between water level and flow velocity, as well as a proxy for the tidal asymmetry from the analytical model. In the major part of the work we assume an infinitely long river, unless stated otherwise.

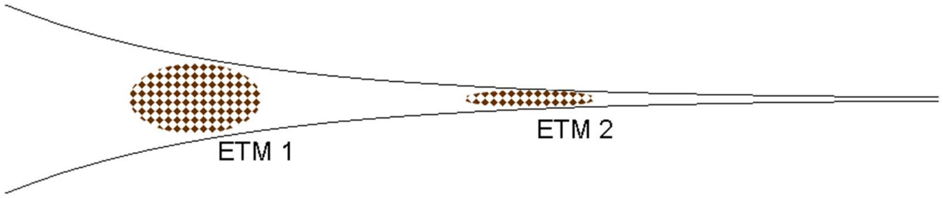

Fig. 5.8: Sketch of Estuarine Turbidity Maximum (ETM); ETM is characterized by a balance between river-induced flushing and estuarine circulation (and some tidal asymmetry), and ETM2 by a balance between the effects of river-induced flushing and tidal asymmetry.

The analytical model is used in two ways:

I. Changes in tidal range (amplitude) and tidal asymmetry are computed as a function of hypothetical changes in the surface of intertidal area, the convergence length of the estuary, its depth, and the effective hydraulic drag. This provides a conceptual picture on the river’s response to deepening and narrowing.

II. The measured historical evolution in tidal range is evaluated and linked to the historical changes in the shape and bathymetry of the estuary:
   - For all time periods available, the damping/amplification of the tide along a stretch of the river, bordered by two neighboring tidal stations, is computed in the form of the (dimensionless) imaginary wave number.
   - The data on historical interventions in the rivers (deepening, narrowing, etc.) are summarized in the estuarine convergence number – this number increases with increasing water depth, increasing convergence of the river’s plan form and decreasing intertidal area.
   - The historical development of the imaginary wave number is plotted against the evolution of the estuarine convergence number. Each data point in that diagram is obtained from actual observations, and represents one river stretch over a specific period of time.
   - The analytical model is fitted through these data points by tuning the roughness parameter of the model. Hence, the historical evolution in effective hydraulic roughness is established.
   - Finally, the historical changes in tidal asymmetry are assessed on the basis of actual observations or with the analytical model.

The response of a tidal river to deepening and narrowing, as computed with the analytical model, is presented in Fig. 5.9 and 5.10. It is assumed that the estuary is infinitely long, than the initial suspended sediment concentrations are low, and that the riverbed is sandy. Furthermore, it is assumed that intertidal areas are present along the entire length of the river – the width of the intertidal area equals the width of the flow-carrying section. The relative tidal amplitude at 60 km from the mouth increases monotonously with depth, as shown by the black line in Fig. 5.9.

Without intertidal area, for instance upon embanking or reclamation, the increase in tidal amplitude is somewhat larger, e.g. the blue line in Fig. 5.9.

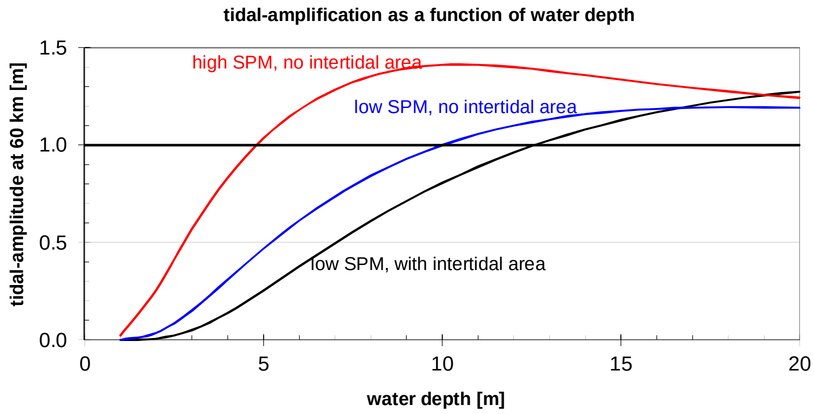

Fig. 5.9: Response of tidal amplitude as function of the presence of an intertidal area and mud in the water column, or on the River bed.

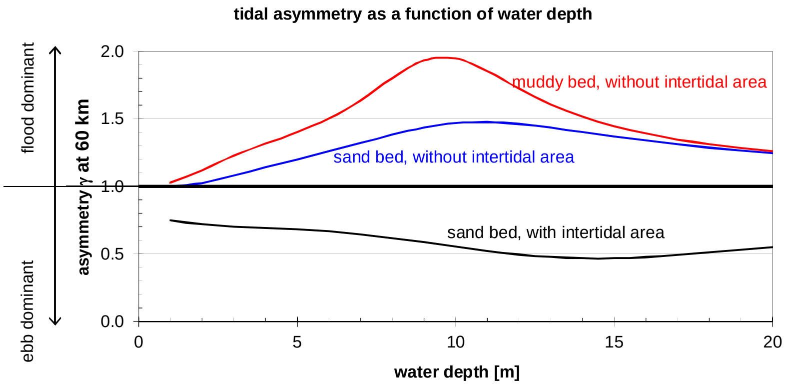

Fig. 5.10: Response of tidal asymmetry (γ-parameter) as function of the presence of an intertidal area and mud in the water column, or on the River bed.

A more important response of the river, however, is presented in Fig. 5.10. With intertidal area, the tide is always ebb-dominant, i.e. time-averaged transports of fine sediment are directed down-estuary (black line Fig. 5.10). Note that we do not address the role of a possibly externally generated tidal asymmetry. After loss of the intertidal area, the system becomes flood-dominant. This implies that mud is pumped into the estuary and/or that riverine mud accumulates within the estuary. Upon deepening, also the flushing capacity of the river decreases. The conditions for an ETM2 (Fig. 5.8) are being created. With increasing suspended sediment concentration the effective hydraulic drag decreases (Chézy coefficient increases), in response of which the tide is further amplified (red line in Fig. 5.9). This then results in an increase in flood-dominance of the system (red line Fig. 5.10), enhancing suspended sediment concentrations and decreasing the effective hydraulic drag further. This positive feed-back loop induces a snowball effect.

This snowball effect is sketched in Fig. 5.11. One could argue that the loss of intertidal area has reduced the resilience of the river – with intertidal area, the tide will be amplified upon deepening of the river, but the system remains ebb-dominant, and the dangerous decrease in hydraulic drag is not initiated, and ETM2 conditions are not generated.

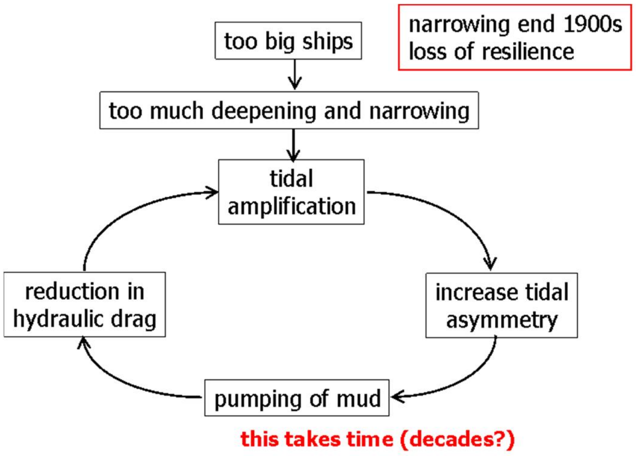

Fig. 5.11: The feed-back loop (snowball effect) for deepening of low-resilient estuaries.

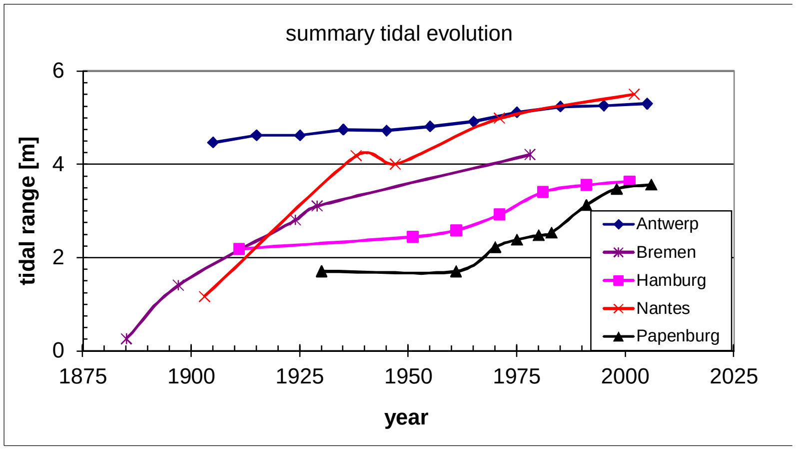

Fig. 5.12: Summary of tidal amplification in the 19th century in a number of European ports.

Whether ETM2 conditions actually will occur, and the time span over which this would happen, is dependent on the amount of fine sediment (mud) available. The time between the creation of “favorable” conditions and the actual occurrence of an ETM2 (hyper-turbid conditions) can be long, up to one to two decades. The loss in intertidal area (loss of resilience) took place mainly in the late 19th and early 20th century throughout Europe, whereas profound deepenings took place in the second half of the 20th century. The loss of intertidal area affects the resilience of the river in two ways:

1. Loss of intertidal area increases the tidal amplitude upon deepening and induces flood-dominant conditions (the latter effect is the more important),
2. Loss of intertidal area causes a loss of accommodation space for the sedimentation of fine sediment – fine sediments brought into the system owing to the river’s flood-dominance

can only remain within the water column, as a result of which the effective hydraulic roughness decreases, and the snowball effect of Fig. 5.11 can be initiated.

In this report the tidal evolution of four rivers has been analyzed, as these are the rivers from which sufficient (historic) data were available. This evolution can be summarized with the evolution of the tidal range at the major ports within these rivers – the accessibility of these ports has been the driving force behind the deepening. The results are presented in Fig. 5.12, showing increases in tidal range varying from 1 to 4 m. Note that all rivers have evolved to tidal conditions known as macro-tidal.

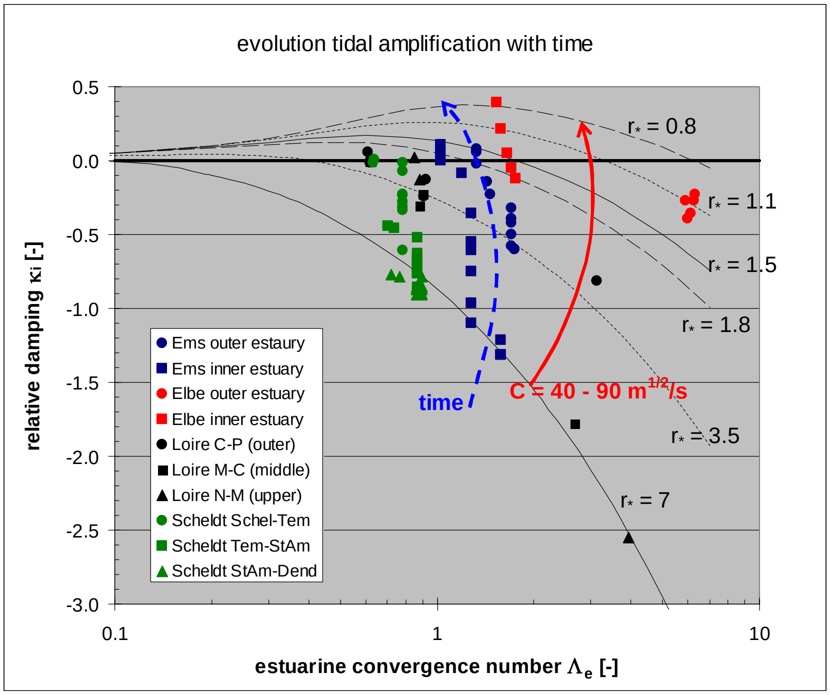

Fig. 5.13: Comparison of historic evolution of dimensionless damping coefficient and estuarine convergence number for four European rivers. Both time and Chézy coefficient follow a diagonal from the lower right to the upper left; $\kappa_i > 0$ *implies amplification of the tide.*

Fig. 5.13 summarizes the calibration of the analytical model by fitting the roughness parameter r_* through the various data points, presented in the dimensionless forms of the relative damping κ_i and the estuarine convergence number Λ_e. All rivers show an increase in r_* with time, i.e. when the rivers are more and more deepened.

This decrease in effective hydraulic drag is further illustrated with the evolution of the computed Chézy coefficient for the four rivers and the various reaches of the river which could be identified. This evolution is presented in Fig. 5.14, showing that the majority of the river reaches have experienced a considerable increase in Chézy coefficient, by about 15 – 30 m$^{1/2}$/s – it is anticipated that the majority of this increase is due to increased levels of suspended sediment concentration. The larger increase has been established for the upper part of the Elbe River. This can be explained by the larger depth of that river, as predicted by the semi-analytical relation on the dependency of the effective hydraulic drag on suspended fine sediment concentrations. The large Chézy-values found for the inner Elbe estuary are not related to high SPM-concentrations – these have not been measured in this part of the river. However, our analysis suggests that the inner Elbe is close to resonance conditions, hence very sensitive to small changes in bathymetry. This resonance cannot be accounted for by the analytical model. Hence the tidal amplification induced by resonance is captured by a very low friction coefficient, which therefore is likely to be erroneous.

It is noted that all rivers show profound flood-dominant conditions – this follows from both the analytical model, as from observations on flow velocities and/or the duration of rising vs falling tide.

The computed increase in Chézy coefficient has been summarized in Fig. 5.15, together with some data made available by prof. Townend (Thames, Mersey and Severn) and data from the Gironde (Villaret et al., 2011) and the Western Scheldt ((Kuijper and Lescinski, 2012). From the red data points we know that the river experiences serious problems with high concentrations of fine sediment, whereas no excess Chézy values have been established for the green points – here the river still behaves “normal”. Fig. 5.15 suggests that a diagonal line can be drawn in that graph representing the tipping point/zone for the establishment of hyper-turbid conditions. However, unless this shift in behavior is further supported by additional data and/or research, the reddish line in Fig. 5.15 remains fairly speculative. Prandle (2003) found a similar decrease in friction factor for muddy systems, but he related the friction coefficient *f* to the mud content of the bed; data in his paper are incomplete to add to the current analysis.

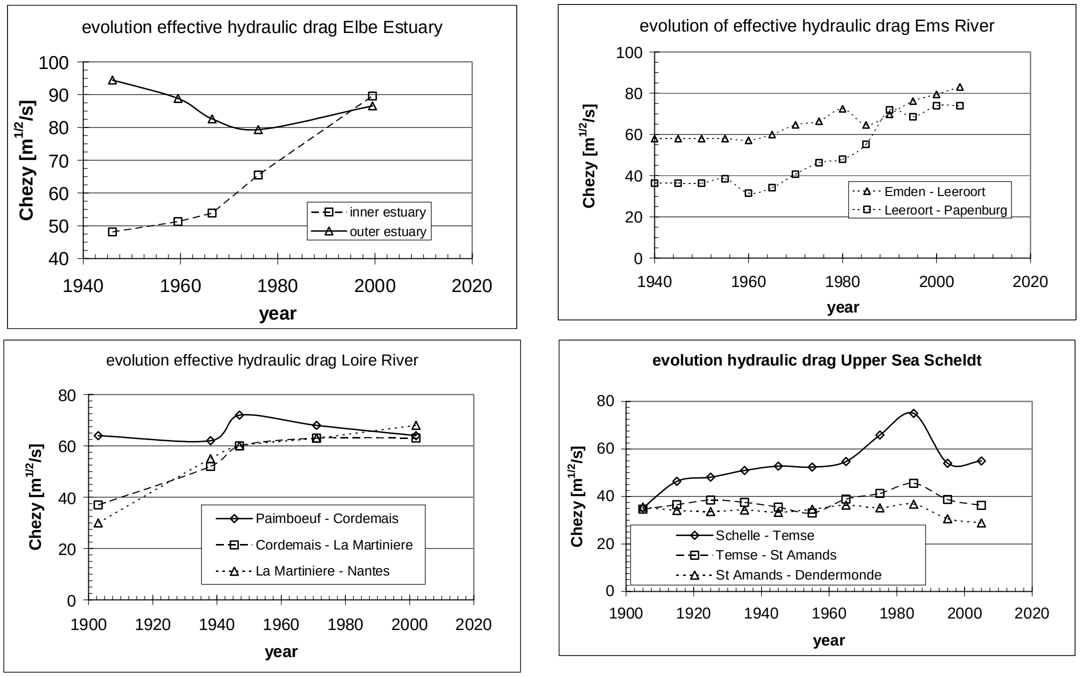

Fig. 5.14: Summary of evolution of computed Chézy coefficient with time for four European rivers.

We have not yet been able to quantify the tipping point for the response of the estuaries to human interventions, e.g. narrowing and deepening. However, a change in effective hydraulic drag may be a useful indicator. This drag can be obtained from an analysis of tidal data, as in this report, or from the use of numerical hydraulic models, in which the (effective) roughness coefficient is tuned in the calibration of the model.

Fig. 5.15 suggests that this is indeed a versatile way forward, but currently we have four data point only, if we assume that the Ems, Loire and Elbe river have passed the tipping point, and the Upper Sea Scheldt not.

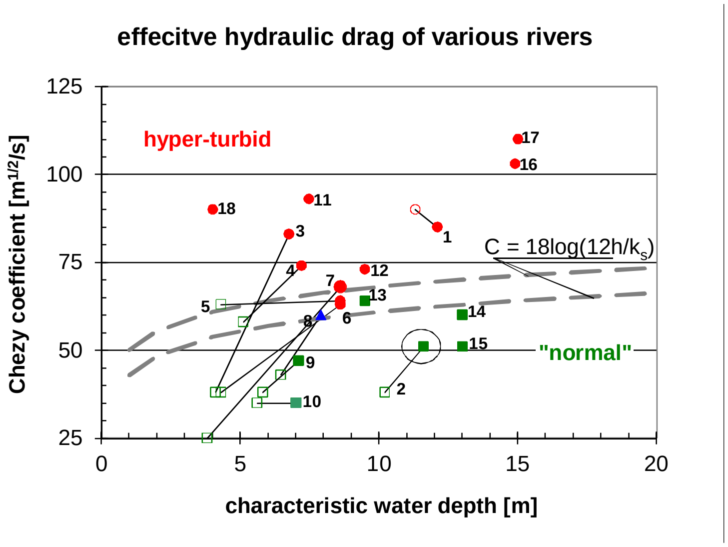

Fig. 5.15: Comparison of effective hydraulic drag in some rivers as a function of water depth. The C-h relation is based on k_s = 2 and 5 cm, arbitrary values. Red symbols depict hyper-turbid conditions, green symbols "normal conditions, and blue symbols possibly transitional systems; open symbols reflect historical data. 1: Elbe-outer; 2: Elbe-inner; 3: Ems/E-L; 4: Ems/L-P; 5: Loire/P-C; 6: Loire/C-laM; 7: Loire/LaM-N; 8: Scheldt/S-T;9: Scheldt/T-StA; 10: Scheldt/StA-D; 11: Thames; 12: Severn-inner; 13: Severn-outer; 14: Western Scheldt; 15: Gironde-outer; 16: Gironde-inner (Villaret et al., 2011); 17: Yangtze estuary; 18: Vilaine (Vested et al., 2013). Note that data on Elbe-inner may be spurious because of tidal reflections, as discussed in Section 4.3.

This argument is further sustained by Table 5.1 in which a series of natural macro-tidal estuaries and heavily engineered systems are given. This table suggests that macro-tidal conditions and abundant availability of fine sediments are necessary conditions for initiation of the regime shifts described above. It seems therefore useful to gather data on the (effective) hydraulic drag of the rivers in Table 5.1, and add these to Fig. 5.15.

A final observation relates to the effects of climate change. With increasing sea level, water depths increase, which induce similar effects as a deepening of the river. However, the major impact is most likely a further squeezing of the river, reducing intertidal areas further, thereby reducing the resilience of the system.

Table 5.1: Comparison of natural, macro-tidal rivers with (very) high suspended sediment concentrations and heavily engineered estuaries. This table suggests that by engineering estuaries too much, their regime is shifted from the left column to the right column.

deepened and narrowed		natural macro-tidal rivers	
Ems (Germany)	+++	Amazon mouth (Brazil)	+++
Elbe (Germany)	++	Alligator River (Australia)	++
Garonne (France)	++	Bay of Fundy (Canada)	+++
Loire (France)	+++	Bay Saint Malo (France)	+++
Ouse (UK)	++	Jiaojiang River (China)	++
Seine (France)	+/++	Mersey (UK)	+++
Trent (UK)	++	Severn River (UK)	+++
Vileine (France)	++		
Weser (Germany)	+/++		
Western Schelde	+		
Upper Sea Scheldt	++		

+++ hyper-turbid conditions
+ “normal” estuarine conditions

6 Recommendations

The analysis of historical data of four rivers with a linear, analytical model has revealed a profound positive feed-back between the tidal properties and suspended fine sediment. This analysis also suggest the existence of a tipping point, beyond which a tidal river evolves more or less autonomously to a hyper-turbid state – such a tipping point could be passed upon extensive engineering works (deepening, narrowing, …) in a tidal river. However, this tipping point could not be quantified, nor was it possible to define indicators identifying the passage of a tipping point. Possibly this tipping point can be identified from a thorough stability analysis of the governing equations. This, however, requires a major study, and for the time being we propose to try and quantify the tipping point in a more empirical way. For that, the following activities are required:

1. Derive actual tidal amplitudes from the tidal data, instead of working with the difference between high and low water. Similarly, derive the historical tidal asymmetry from the data.
2. Collect historical tidal data from more rivers, preferably in a variety of states, i.e. from hyper-turbid to "normal". These data should be analyzed in a way similar to the method followed in the current report. Moreover, the analysis of the Loire can be improved if more accurate data become available.
3. The analysis in the current report should be confronted with (historical) data on suspended sediment concentration and/or maintenance dredging volumes and composition (sand-mud ratio) of the dredged sediments to substantiate the conclusions on mud-induced decreases in effective hydraulic drag.
4. Collect data/numbers from numerical models calibrated to simulate the tidal propagation in large tidal rivers properly. Unexpectedly low values for the effective hydraulic drag may indicate large suspended sediment concentrations. The calibrated values of the roughness values can be added to our diagram on excess Chézy values to substantiate that diagram further.
5. The amplification in some of the rivers in general, and within the upper part of the Elbe river (up to Hamburg) seem to be affected considerably by wave reflections and/or resonance. Because of the large effect of tidal amplification on tidal asymmetry, hence on the fine sediment dynamics, it is recommended to study the reflections of tidal waves in these estuaries further – this is to be done with a numerical model (1D and/or 2Dh) in conjunction with the historical data on the tidal evolution in the rivers.
6. Set up numerical hydrodynamic models of the various rivers – it is anticipated that one-dimensional models (SOBEK) are sufficient for the analyses required:
    - Validate the linear model derived in this report.
    - The effects of longitudinal variations in bathymetry (depth, intertidal area) can be studied in a more realistic way.
    - The effect of the construction of weirs cannot be studied properly with the analytical model, but is easily addressed with a numerical model.
    - The effects of river flow cannot be studied with the analytical model, but is easily addressed with a numerical model.
    - A numerical model will also provide more sound information on the tidal asymmetry, whereas with the analytical model, only a proxy can be established.

    The computational results from the one-dimensional model can be analyzed in the same way as in the current report, tuning the effective roughness coefficient to calibrate the model.
7. Both the analytical and numerical model can be used, assessing the efficiency of mitigating measures, such as those suggested for the Scheldt River.

It is recommended to study the causes of the deepening of the Upper Sea Scheldt in the 1970's – this should be done with a morphodynamic model, including Lower Sea Scheldt, and possibly (part of) the Western Scheldt.

Acknowledgements

This work was carried within the framework of the LTV-project, which is the acronym for Long-Term Vision of Scheldt estuary with respect to Safety, Accessibility and Nature, in which the following sub-projects are integrated: Maintaining fairways Scheldt estuary, Permits for disposal of dredged sediments and the so-called KPP (knowledge of primary processes) program of Rijkswaterstaat. The study was financed by the Flemish “Afdeling Maritieme Toegang” and the Dutch Ministry of Infrastructure and Environment, Rijkswaterstaat, Waterdienst and Directorate Zeeland.

The results in this report are based on a large number of data from a variety of sources. Some data sets were available at Deltares in reports, or in digital form from studies carried out earlier. Other data have been prepared and made available especially for this project. I would like to thank the following people for their support and supply of data: Dr. Alexander van Braeckel (INBO, Brussels), ir. Gijsbert van Holland (IMDC) and ir. Frederik Roose (Flemish Government) for Scheldt data, Dr Frank Kösters (BAW Hamburg) for data on the Ems, Elbe and Weser rivers, dr. Luc Hamm (Sogreah) for data on the Loire, and dr. Harro Heijer, Dr. Frank Köesters and Mr. Jens Jürges (BAW) for data on the Ems, Weser and Elbe river; and Prof. Ian Townend for data on the Thames and Severn estuaries. Furthermore, dr, Holger Weilbeer (BAW) and dr. Jens Kappenberg (Helmholz Centre) were helpful in some discussions on the Elbe and Ems Rivers.

I would like to thank the reviewers dr. Henk Schuttelaars (Delft University of Technology) and prof. dr. Tom de Mulder (University of Ghent, Belgium), and ir. Cees Kuijper for carefully assessing the derivations of the equations.

References

BAW, 2012. Data received from Dr. Frank Koesters and dr. Jens Jürgens on Ems and Elbe.

Boelich M.J. and T. Strotmann, 2008. The Elbe estuary. Source unknown.

Briere, C., J. Crebas, A. Becker and J.C. Winterwerp, 2012. Analyse de la morphologie du chenal de Nantes et étude de sa restauration - Phase 3 : Etude de l'impact d'une intervention à l'amont de Nantes sur les caractéristiques de la marée. Deltares report 1201695 (in French).

Bruens, A.W., J.C. Winterwerp, C. Kranenburg, 2012. “Physical and numerical modeling of the entrainment by a high-concentrated mud suspension”, ASCE, Journal of Hydraulic Engineering, in press, doi:10.1061/(ASCE)HY.1943-7900.0000545.

Chandramohan, P.V., 1989. Density currents and siltation – with particular reference to Cochin. IHE, Master Thesis, Delft, The Netherlands.

Deltares, 2011. Analyse de la morphologie du chenal de Nantes et étude de sa restauration - Phase 1 : Evolutions passées et fonctionnement actuel. Report 1201695-001.

Dankers, P.J.T., J.C. Winterwerp, 2007.“Hindered settling of mud flocs: Theory and validation. Continental Shelf Research, 27, 1893-1907.

Dronkers, J. (1986). Tide-induced residual transport of fine sediments. In Van de Kreeke, J.: Physics of Shallow Estuaries and Bays, 228-244, Springer, Berlin.

Dronkers, J., 2005. Dynamics of coastal systems. Advanced Series on Ocean Engineering – Vol 25. World Scientific.

Dyer, K. R. 1997, Estuaries: a physical introduction. Chichester, England. John Wiley and Sons.

Friedrichs, C., 2010. Barotropic tides in channelized estuaries. in A. Valle Levinson, Contemporary Issues in Estuarine Physics. Cambridge University Press, 27 – 61.

Haar, T., 1994. Wirkung der Stromungsumlenkwand amd Kohlfleet. Strom- und Hafenbau, Hamburg, Gewasserkundlich Studie Nr. 13.

Jay, D.A. and Musiak, J.D., 1996. Internal tide asymmetry in channels: origins and consequences. In: Pattiaratchi C (ed) Mixing processes in estuaries and coastal seas. American and Geophysical Union Coastal and Estuarine Sciences Monograph, 219-258.

Herrling, G., 2007. Changes of the Hydrodynamic Regime due to Historical Pressures on Estuarine Geomorphology; the Example of the Ems-Dollard Estuary. Research project: INTERREG IIIB North Sea project HARBASINS; Work package 4: „Hydro-morphological impacts and pressures“ Lower Saxony Water Management, Coastal Defense and Nature Conservation Agency, Coastal Research station.

IMDC, 2012. Analyse bodemgegevens Boven Zeeschelde. Note I/NO/11387/12.226/VBA.

Kappenberg, J. and H.-U. Fanger, 2007. Sedimenttransportgeschehen in der tidebeeinflussten Elbe, der Deutschen Bucht und in der Nordsee. GKSS-Forschungszentrum Geesthacht GmbH – Geesthacht, Report 2007/20.

Krebs M. and H. Weilbeer, 2005. Ems-Dollart Estuary. Die Küste 74, 252-262.

Kuijper, K. and J. Lescinski, 2012. LTV O&M thema veiligheid (theme safety) – sub project 1: data analyses and hypotheses Western Scheldt. Deltares report 1204405.

Nasner, H., 1974. Uber das Verhalten von Transportkorpern im Tidegebiet. Mitteilungen Franzius Institut, Heft 40. Hannover, Germany.

Kuijper, Kees, Jamie Lescinski, 2012, LTV Veiligheid en Toegankelijkheid. Sub project B: Data analysis Western Scheldt. Report 1204405. Deltares.

Plancke, Y., T. Maximova, S. Ides, P. Peeters, E. Taverniers, F. Mostaert, 2012, Werkgroep O&M - Projectgroep Veiligheid. Sub project 1: Data analysis and hypothesis - Upper Sea Scheldt. Report WL2012R756_05_rev4_0. Flanders Hydraulics Research.

Prandle, D., 2003.` Relationships between Tidal Dynamics and Bathymetry in Strongly Convergent Estuaries. Journal fo Physical Oceanography, 33, pp 2738-2750.

Prandle, D., 2004. How tides and river flows determine estuarine bathymetries. Progress in Oceanography, 61, 1–26.

Postma, H., 1961. Transport and accumulation of suspended matter in the Dutch Wadden Sea. Netherlands Journal of Sea Research 1, 148-190.

Schijf, J.B. and J.C. Schönfeld, 1953. Theoretical considerations on the motion of salt and fresh water. Proceddings Minnesota International Hydraulics Convention. Minnesota.

Schrottke, K. and Bartholomä, A., 2008. Detaillierte Einblicke in die ästuarine Schwebstoffdynamik mittels hochauflösender Hydroakustik. Tagungsband zum Seminar Ultraschall in der Hydrometrie: neue Technik; neuer Nutzen; FgHW / DWA, Koblenz, June 2008, 75-82.

Schuchardt, B. and S. Beilfuss, 2012. Sediment management strategies in the Weser estuary. Bio Consult, report 08.10.2012, prepared for NLWKN Oldenburg.

Sogreah, 2006. Expertise et connaisssance du systeme estuarien de Loire – Tome 1: Analyse historique, Report 1711457R2 (in French).

Talke, S.A., De Swart, H.E. and De Jonge, V.N., 2009. An idealized model and systematic process study on oxygen depletion in highly turbid estuaries. Estuaries and coasts, 32 (4), 602-620.

Van Braeckel, A., Piesschaert, F. en van den Bergh, E., 2006. Historische analyse van de Zeeschelde en haar getijgebonden zijrivieren. 19e eeuw tot heden. INBO report INBO.R.2006.29

Van Rijn, L.C., 1990. Principles of sediment transport in Rivers, Estuaries and Coastal Seas. Aqua Publications.

Van Rijn, L.C., 2011. Comparison hydrodynamics and salinity of tide estuaries; Elbe, Humber, Schelde and Weser. Deltares Report 1203583-000.

Van Straaten, L.M.J.U. and Ph. H. Kuenen, 1958. Tidal action as a cause of clay accumulation. Journal of Sedimentary Petrology, 28 (4) 406-413.

Van Straaten, L.M.J.U. and Ph. H. Kuenen, 1957. Accumulation of fine grained sediments in the Dutch Wadden Sea. Geologie en mijnbouw 19, 329-354.

Villaret, C.,N. Huybrechts, A.G. Davies and O.Way, 2011. Effect of bed roughness prediction on morphodynamic modelling: Application to the Dee estuary (UK) and to the Gironde estuary (France). 34th IAHR World Congress, Brisbane, Australia, pp 1149-1156, ISBN 978-0-85825-868-6,

Vroom, J., H. van den Boogaard and B. van Maren, 2012. Mud dynamics in the Eems-Dollard, research phase 2 – Analysis of existing data. Deltares, report 1205711-001.

Weilbeer H. and M. Klöpper, Bundesanstalt für Wasserbau, 2011. Model Validation and System Studies for Hydrodynamics, Salt and Sediment Transport in the Elbe Estuary - Basic Information for the River Engineering and Sediment Management. Draft Report A39550310069.

Weilbeer, H., 2013. Personal communication.

Winterwerp, J.C., 2001. Stratification effects by cohesive and non-cohesive sediment. Journal of Geophysical Research, 106 (C10) 22559-22574.

Winterwerp, J.C. ,2002. Scaling parameters for high-concentrated mud suspensions. in: Elsevier, Proceedings in Marine Science, No 5; Proceedings of the 6th International Conference on Nearshore and Estuarine Cohesive Sediment Transport, INTERCOH-2000, ed. J.C. Winterwerp & C. Kranenburg, 171-186.

Winterwerp, J.C., Z.B. Wang, T. van der Kaaij, K. Verelst, A.C. Bijsma, Y. Meersschaut, M. Sas, 2006. Secondary currents by weak salinity gradients in estuaries. Ocean Dynamics, 56, 284-294.

Winterwerp, J.C. , 2006. Stratification effects by fine suspended sediment at low, medium and very high concentrations. Geophysical Research, 111 (C05012) 1-11.

Winterwerp, J.C., M. Lely and Qing He, 2009. Sediment-induced buoyancy destruction and drag reduction in estuaries. Ocean Dynamics, 59 (5) 781-791.

Winterwerp, J.C., 2011. Fine sediment transport by tidal asymmetry in the high-concentrated Ems River. Ocean Dynamics, 61 (2-3) 203-216, DOI:10.1007/s10236-010-0332-0.

De eventuele referentie naar het data-analyserapport voor de Beneden-Zeeschelde is:
Wasser- und Schiffahrtverwaltung des Bundes. Zentrales Datenmanagement der WSD Nord - Portal Tideelbe, 1999; see also http://www.portaltideelbe.de/Projekte/FRA1999/-Beweissicherung/Ergebnispraesentation/profile_elbe/index.html.

Nomenclature

symbol	unit	description
A_c	m^2	flow-carrying cross section
a	m	tidal amplitude
a_0	m	tidal amplitude in river mouth
a^+	m	tidal amplitude of incoming wave
a^-	m	tidal amplitude of reflecting wave
b	m	river width
b_c	m	width flow-carrying cross section
b_t	m	total width
b_*	m	dimensionless width (equ. 8)
Δb	m	width intertidal area
C	$m^{1/2}/s$	(effective) Chézy coefficient
C_0	$m^{1/2}/s$	Chézy coefficient for neutral conditions
C_{SPM}	$m^{1/2}/s$	Chézy coefficient induced by suspended fine sediment
c	m/s	wave celerity
c	kg/m^3	mass concentrations suspended sediment
c_D	-	drag coefficient
F	kg/m	total fine sediment transport rate per unit width, integrated over tidal period
F_a	kg/m	F by tidal asymmetry
F_g	kg/m	F by estuarine (gravitational) circulation
F_l	kg/m	F by lag effects (scour lag and settling lag)
F_p	kg/m	F by tidal pumping – in this report referred to as Fa
F_r	kg/m	F by residual flow (river flow and Stokes' rectification)
F_s	kg/m	F by Stokes' drift
F_v	kg/m	F by asymmetry in vertical mixing (internal asymmetry
g	m/s^2	gravitational acceleration
h	m	water depth (mean water level – bed level)
k	m^{-1}	wave number: $k = k_r + i\, k_l$
k_r	m^{-1}	real wave number: $k_r = 2\pi/\lambda$
k_i	m^{-1}	imaginary wave number
L_b	m	estuarine convergence length
L_*	m	non-dimensional estuarine convergence length (equ. 8)
P	kg/ms	production/erosion of fine sediment per unit width
Ri_f	-	flux Richardson number
Ri_*	-	bulk Richardson number
r	m/s	linear friction coefficient
r_*	-	non-dimensional linear friction coefficient (equ. 8)
S	kg/ms	sedimentation of fine sediment per unit width
t		time
T		tidal period
U	m/s	amplitude flow velocity
U_0	m/s	amplitude flow velocity in river mouth
U^+	m/s	amplitude flow velocity of incoming wave

U^-	m/s	amplitude flow velocity of reflecting wave
u	m/s	flow velocity
u_*	m/s	shear velocity
x	m	longitudinal coordinate (positive up-estuary)
β	-	Rouse number
Γ	-	dimensionless parameter in tidal asymmetry proxy (equ. 20a)
γ	-	proxy for tidal asymmetry
η	m	instantaneous water level
κ	-	dimensionless complex wave number: $\kappa = \kappa_r + \mathrm{i}\ \kappa_l$ (equ. 8)
κ_r	-	dimensionless real wave number
κ_i	-	dimensionless imaginary wave number
κ^+	-	dimensionless complex wave number incoming wave
κ^-	-	dimensionless complex wave number reflecting wave
Λ_e	-	(dimensionless) estuarine convergence number (equ. 8)
ℓ	m	length of estuary in case of weir
λ	m	length tidal wave
ω	s^{-1}	tidal frequency: $\omega = 2\pi/T$
ϕ	rad	phase angle between tidal water level and flow velocity

A Ocean dynamics papers

While finalizing this report, also two scientific papers have been drafted, and submitted to Ocean Dynamics. At the time of issuing the overall report of the study, these papers had been reviewed and accepted for publication. As these papers summarize in a more concise way the major findings described in the report, these papers are added as an appendix to this report.

Man-induced regime shifts in small estuaries – I: theory

JOHAN C. WINTERWERP[1,2,*], ZHENG BING WANG[1,2]

1. Deltares (formerly WL|Delft Hydraulics), PO Box, 177, 2600 MH Delft, The Netherlands
2. also: Delft University of Technology, Environmental Fluid Mechanics, PO Box 5048, 2600 GA Delft, The Netherlands

* corresponding author, email: han.winterwerp@deltares.nl

ABSTRACT: This is Part I of two papers on man-induced regime shifts in small, narrow and converging estuaries, with focus on the interaction between effective hydraulic drag, fine sediment import and tidal amplification, induced by river engineering works, e.g. narrowing and deepening. In this part, a simple linear analytical model is derived, solving the linearized shallow water equations in exponentially converging tidal rivers. Distinguishing reflecting and non-reflecting conditions, a non-dimensional dispersion equation is derived which yields the real and imaginary wave numbers as a function of the estuarine convergence number and effective hydraulic drag. The estuarine convergence number describes the major geometrical features of a tidal river, e.g. intertidal area, convergence length and water depth. This model is used in Part II analyzing the historical development of the tide in four rivers.

Part I also presents a conceptual model on the response of tidal rivers to narrowing and deepening. It is argued that, upon the loss of intertidal area, flood-dominant conditions prevail, upon which fine sediments are pumped into the river, reducing its effective hydraulic drag. Then a snowball effect may be initiated, bringing the river into a hyper-turbid state. This state is self-maintaining because of entrainment processes, and favourable from an energetic point of view, and therefore highly stable. We may refer to an alternative steady state.

KEY WORDS: tidal amplification, hydraulic drag, dispersion equation, regime shift, Elbe, Ems, Loire, Scheldt

1. INTRODUCTION

Figure 1 depicts the evolution of the tidal range over roughly the last century in five European ports, which are all situated more than 50 km from the mouth of fairly small and narrow estuaries. It is generally accepted that this large tidal amplification is caused by the ongoing deepening and canalization of these rivers, accommodating ever-larger ships; though the precise mechanisms behind are not yet understood. Of course, the increases in high water levels, and decreases in low water levels form serious problems by themselves, e.g. enhanced flood levels, lowering of ground water table. However, it becomes more and more evident that such deepening and narrowing induce large environmental problems as well. Infamous are the Ems (Germany) and Loire (France) Rivers. Today, both rivers can be characterized as hyper-turbid, with suspended sediment (SPM) concentrations of several 10 g/l, and large-scale occurrences of fluid mud. Strong vertical stratification causes serious water quality problems, and in the Loire the enhanced salinity intrusion hampers fresh water intake for industry and agriculture. The causes of the evolution of Loire and Ems to these hyper-turbid states are not yet fully understood (Talke et al, 2008 & 2009; Chernetsky, 2010; Winterwerp, 2011), though there is consensus that the large amplification of the tidal range must have played an important role.

The aim of this paper is to enhance our understanding on the evolution of the tidal amplification in narrow estuaries in general, and the evolution towards a hyper-turbid state in particular. This is done by analyzing the historical developments of the tide in four rivers, e.g. the Elbe, Ems, Loire and Scheldt (the only rivers for which sufficient detailed data are available). Part II of this paper describes the results of this analysis, which is carried out using a simple analytical model of the tidal propagation in narrow tidal rivers, described in the present Part I of this paper.

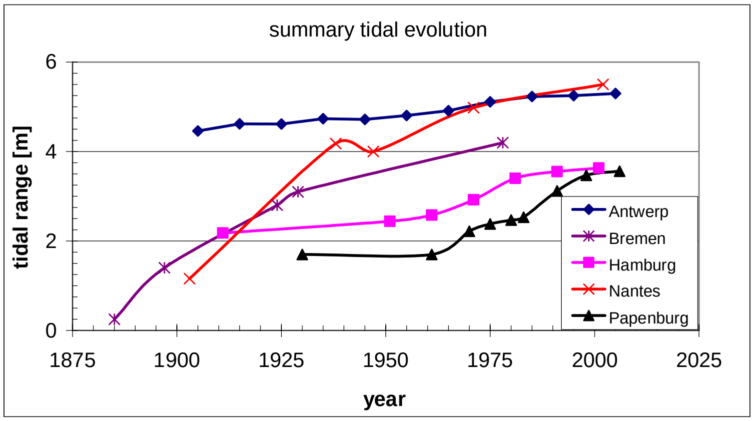

Fig. 1: Tidal evolution in five European ports (Antwerp along Scheldt, Belgium; Bremen along Weser, Germany; Hamburg along Elbe, Germany; Nantes along Loire, France; and Papenburg along Ems, Germany).

The model presented here is certainly not the first analytical approach of the water movement equations. In fact, analytical studies on the behavior of tides in estuaries go back many decades. Hunt (1964) was probably the first to emphasize the important role of channel convergence on tidal propagation – all estuaries treated in the present paper have a converging plan form. However, the first complete description is most likely by Dronkers (1964). Since his pioneering work, many more studies have been published on the analytical solutions of the shallow water equations in estuaries. LeBlond (1978) analyzed the tidal propagation and phase speed in the Frazer and Saint Lawrence Rivers, which were schematized as straight channels with a rectangular cross section. When the friction length is small compared to the tidal wave length, i.e. when friction dominates, the wave equations become diffusive, explaining the observed tidal propagation in these two rivers.

Prandle and Rahman (1980) pursued a systematic study on the effects of channel convergence on tidal propagation in general, and on tidal amplification in response to reflections against a barrier in particular. The channel convergence was modeled through power law functions of both river depth and width, and the friction term was linearized, as in the current study. Through a series of diagrams, the role of estuarine parameters on tidal amplification, such as length, location of the barrier, etc. was studied.

Jay (1991) generalized the solutions even further by studying the tidal wave propagation in channels with converging topography, accounting for intertidal areas, river flow and reflections and including first-order non-linear effects with respect to tidal amplitude, advection and friction. From his general solutions, Jay established three regimes. The first two regimes are characterized by small friction effects, and are described by the “standard solution” of Green’s model. These regimes are referred to as weakly dissipative (Lanzoni and Seminara, 1998). The first regime is governed by strong topographic effects (strong convergence of the estuary), and in the second regime, acceleration effects dominate. When topographic and acceleration effects balance, friction becomes progressively more important, and Jay refers to “critical conditions” (e.g. strongly dissipative, Lanzoni and Seminara, 1998). The wave equations become parabolic, and diffusive in character, contrary to the hyperbolic behavior of frictionless systems.

The effects of channel convergence in rivers with intertidal area were further studied by Friedrichs and Aubrey (1994), a priori assuming that horizontal velocity gradients are small. This assumption was verified for three tidal rivers, e.g. the Delaware, the Thames and the Tamar River. Such conditions are referred to as synchronous, and we will see later in the current paper that these are important in understanding the response of tidal rivers to ongoing deepening. In that case, the water movement equations simplify considerably, revealing a 90^o phase difference between water level and tidal flow. The tide in such synchronous estuaries is not a classical standing wave, as emphasized by many authors. Friedrichs and Aubrey further introduce a proxy for the tidal asymmetry, referred to as γ, which is the ratio of the wave celerity at high and low water. For $\gamma > 1$, the tide is flood-dominant, which was verified for the three rivers above. An excellent summary of this work is given in Friedrichs (2010), presenting approximations of tidal characteristics in estuaries of a wide variety in shapes and bathymetries.

Lanzoni and Seminara (1998) also study the complete, non-linear water movement equations, distinguishing four estuarine regimes, identified by weak and strong dissipation and weak and strong convergence, respectively. Further to this distinction, the water movement equations are scaled in different ways, yielding four different solutions. One conclusion, relevant for the current study, is that for strongly dissipative systems, ebb-dominant conditions would prevail, whereas in weakly dissipative estuaries, the tide is always flood dominant.

Toffolon and Savenije (2011) summarize the work by Savenije (2001) and Toffolon et al. (2006), presenting a complete solution of the linearized water movement equations for narrow estuaries with intertidal area, including the effects of limited length (reflections against a weir). They introduce an iterative procedure accounting for the non-linear effects of friction and relatively large tidal amplitude. In case of a closed-end estuary with non-constant depth, the estuary is divided in sub-sections, and a set of linear equations is obtained with internal boundary conditions at the junction of these sub-sections. Cai et al. (2012) elaborate further on this work by analyzing the effects of a somewhat different friction model.

The model by Van Rijn (2011) is basically similar to that of Toffolon and Savenije (2011), though Van Rijn followed a somewhat different approach. Further to these linear analyses, followed by most other authors, Van Rijn also elaborates an energy approach in which non-linearities are explicitly accounted for, at the cost though of unknown values of phase angle and flow velocity, which have to be derived from the linear model.

All these studies elaborate more or less on the linearized water movement equations. However, for (fine) sediment transport, tidal asymmetry may be an even more important parameter, which however can only be studied when non-linear effects in the equations are accounted for. This has been done for instance by Jay (1991 – though with very little emphasis), Lanzoni and Siminara (1998); Talke et al. (2008), Talke et al. (2009), Chernetsky et al. (2010); Schuttelaars et al. (2012), by maintaining first and/or second order non-linearities in their equations. Speer and Aubrey (1985) and Friedrichs and Aubrey (1988) presented numerical solutions of the water movement equations for an idealized, shallow and long estuary with a non-converging channel and constant, rectangular cross section, but including the non-linear advection and friction terms, and the effects of intertidal area. The results were presented in a series of famous diagrams, indicating when ebb- or flood-dominancy can be expected as a function of the tidal amplitude relative to the water depth, and areal of intertidal area.

In the current papers, we study the evolution of the tide and SPM (suspended particulate matter) concentrations in narrow estuaries with intertidal area, and possibly of limited length (weir) in response to human interventions, e.g. narrowing and deepening by analyzing observed changes in tidal properties. For this purpose we need a simple and transparent model, allowing comparison of the various rivers under consideration, focusing on tidal damping/amplification mainly. The analytical models summarized above are either complete, but not too transparent, or are based on simplifications which prohibit application over the full range of conditions considered in the present papers. Therefore, we derive an alternative solution, which is basically identical to the work by Jay (1991); Toffolon and Savenije (2011); and Van Rijn (2012), but contains three parameters only. This model is derived in Section 4, and then applied to analyze the response of an estuary to narrowing and deepening conceptually in Section 5.

A crucial step in our analysis is the influence of suspended matter (fine sediments) on the effective hydraulic drag in (tidal) rivers, as a result of which the response of a river to narrowing and deepening becomes amplified, as explained in Section 2. This amplification may become so large that the river develops an alternative steady state – the hyper-turbid regime. We refer to a regime shift, which is elaborated upon in the Sections 3 and 6.

In Part II of this paper, the conceptual picture described in the current Part I is applied to the Elbe, Ems, Loire and Scheldt rivers. Historical data on river engineering works and the tidal response to these interventions are analyzed with the analytical model of Part I, discussing the effects of SPM on the effective hydraulic drag, and the effects of tidal reflections against constructions in the river.

2. SUSPENDED MATTER AND EFFECTIVE HYDRAULIC DRAG

In this paper, the effective hydraulic drag in a tidal river is expressed in terms of the Chézy coefficient C, as C relates directly to the logarithmic law of the wall, and we can use $U/u_* = C/\sqrt{g}$, where U = depth-mean flow velocity, u_* = shear velocity, and g = gravitational acceleration. When deepening a river by e.g. dredging, the effective hydraulic drag is known to be affected in two ways, i.e. by the increase in depth itself, where the bed structure (roughness height k_s) remains unchanged, and by off-topping possible bed forms in the river. This can easily be seen from the relation between C and k_s:

$$C = 18 \log\left\{12h/k_s\right\} \tag{1}$$

This relation shows that when the water depth is doubled at constant k_s, C increases by at most 5 m$^{1/2}$/s.
Van Rijn (1984) shows that by reducing bed form heights in tidal rivers, k_s may decrease by a decimetre or so. In that case, equ. (1) shows that again C may increase by about another 5 m$^{1/2}$/s. We show in Part II that such a decrease in bed forms may have taken place in for instance the Elbe River.

However, there is a third mechanism that may reduce the effective hydraulic drag, i.e. stratification effects by suspended matter (Vanoni, 1946; Taylor and Dyer, 1977; Soulsby and Wrainwright, 1987; Villaret and Trowbridge, 1991, to name a few). Vertical stratification by suspended matter reduces the vertical exchange of turbulent momentum, reducing viscous dissipation. In case of fine suspended sediments, these stratification effects are well distributed over the water column (e.g. Soulsby and Wainwright, 1987), and therefore quite effective. Winterwerp et al. (2009) proposed a simple formula for the reduction in hydraulic drag, induced by suspended matter:

$$\frac{\overline{u}}{u_*} \equiv \frac{C_{eff}}{\sqrt{g}} = \frac{C_0}{\sqrt{g}} + \frac{C_{SPM}}{\sqrt{g}} = \frac{C_0}{\sqrt{g}} + 4h\mathbf{Ri}_*\boldsymbol{\beta} \tag{2}$$

where C_0 and C_{SPM} are the Chezy values for sediment-free conditions, and for the sediment-induced effects, with the bulk Richardson number $\mathbf{Ri}_*$ and Rouse number $\boldsymbol{\beta}$ defined as:

$$\mathbf{Ri}_* \equiv \frac{\left(\rho_b - \rho_w\right) gh}{\rho_b u_*^2} \quad \text{and} \quad \boldsymbol{\beta} \equiv \frac{\sigma_T W_s}{\kappa u_*} \tag{3}$$

where ρ_b and ρ_w are the bulk density of the suspension and clear water, respectively, W_s = the effective settling velocity, σ_T = Prandtl-Schmidt number (~0.7 – 1), and κ = von Kármàn constant (~0.4). Relation (2) is depicted in Fig. 2 (after Winterwerp et al. 2009); the various “data points” reflect the results of a large number of numerical simulations.

With increasing SPM concentrations, $\mathbf{Ri}_*$ increases, whereas for larger particles (flocs), $\boldsymbol{\beta}$ increases. Basically, Fig. 2 depicts that with increasing SPM concentrations, C_{eff} increases. For the rivers under consideration in Part II, water depths vary between 5 and 10 m, though the Elbe is considerably deeper. In that case, Chézy values may increase by 15 – 30 m$^{1/2}$/s, considerably more than for the two other mechanisms. It is to be noted that such effects may occur at SPM concentrations as low as several 100 mg/l, provided that these elevated concentrations are found over a substantial length of the river (Winterwerp et al., 2009). In the following, it is hypothesized how this interaction between suspended matter and turbulent flow may initiate a snowball effect, leading to the regime shifts observed in e.g. the Ems and Loire Rivers.

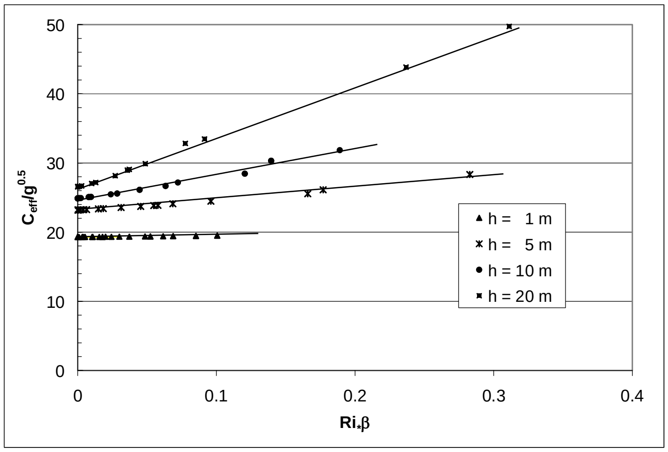

Fig. 2: Increase in effective Chézy coefficient as a function of Richardson and Rouse number, and water depth, based on the semi-analytical approach by Winterwerp et al. (2009).

3. A SECOND ESTUARINE TURBIDITY MAXIMUM – THE HYPER-TURBID STATE

Most estuaries are characterized by elevated SPM (suspended particulate matter) concentrations at the head of the salinity intrusion. This phenomenon is known as the estuary turbidity maximum (ETM). All textbooks on estuarine dynamics explain the mechanisms behind the occurrence of such ETM (e.g. Dyer, 1973), and the general consensus is that this ETM is largely governed by a balance between river-induced flushing and up-estuary transport by estuarine circulation (also known as gravitational circulation). Other, often secondary processes contributing to the dynamics of an ETM are Stokes' drift and its rectification, tidal asymmetry effects, and lag effects (scour and settling lag). In the following we refer to this turbidity maximum found at the head of salinity intrusion as ETM1.

However, under special conditions, processes other than the estuarine circulation may dominate the ETM dynamics, in which case no correlation with salinity intrusion is found. For instance, Brenon and LeHir (1999) studied the processes on the formation of the turbidity maximum in the Seine estuary with the use of a three-dimensional model, comparing model output with observations. From a sensitivity analysis they concluded that in the Seine, the estuarine turbidity maximum at spring is mainly governed by a process referred to as tidal pumping, e.g. the asymmetry in peak tidal velocities.

Lin and Kuo (2001) carried out field measurements in the York River (USA) and found a second ETM, beyond the salinity-driven ETM1. Lin and Kuo argued that this ETM is maintained by tidal asymmetry and lag effects, in conjunction with a large availability of fine sediments in the riverbed.

Chernetsky et al. (2010) discussed the formation of a secondary ETM in the Ems River, well beyond the area of salinity intrusion, which is clearly depicted in Talke et al. (2009). The dynamics of this ETM are governed by tidal asymmetry, in response to ongoing deepening of the river. We refer to this second turbidity maximum as ETM2, and for simplicity in the following argumentations, we define:

- ETM1 is controlled by a balance between river-induced flushing and estuarine circulation, and
- ETM2 is controlled by a balance between river-induced flushing and asymmetry in peak tidal velocities,

in which we are purposely ignoring other effects. This picture is sketched in Fig. 3, showing conceptually that ETM1 and ETM2 can exist together, and that ETM2 is always found up-estuary of ETM1. However, in practice, ETM1 and ETM2 may merge, as in the Ems (Talke et al., 2009).

Winterwerp (2011) postulated a sequence of developments in estuarine dynamics in response to river deepening through which an ETM2 is formed in rivers which are initially characterized by a regime with one ETM1 only. It was argued that, if SPM concentrations become large enough, a self-maintaining alternative regime would evolve with an ETM2, dominated by asymmetries in peak velocities and vertical mixing (internal asymmetry, e.g. Jay and Musiak, 1996), balanced by river-induced flushing.

Hence, a tidal river may be characterized by two alternative steady states, one state (regime) with only one ETM1, and one with an ETM2 (possibly in conjunction with an ETM1 as well). In the following sections, we will argue further how such a regime shift may develop in response to river engineering works. Here we summarize two arguments on the stability of the second regime.

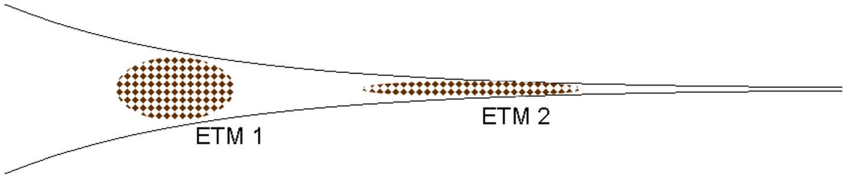

Fig. 3: Cartoon of the turbidity maxima ETM1 and ETM2 in a converging estuary; ETM1 is governed by river-induced flushing and estuarine circulation, whereas ETM2 is governed by river-induced flushing and tidal asymmetry.

The first argument follows from the stability diagram for suspensions of fine sediments in open channel flow, developed by Winterwerp (2001, 2006, e.g. Fig. 4). The horizontal axis of Fig. 4 depicts the volumetric concentration ϕ of the suspended sediment particles, which, for fine sediments, can be large at small mass concentrations because fine sediment flocs contain large amounts of water. The vertical axis depicts the flux Richardson number $\mathbf{Ri_f}$, a measure for the efficiency of vertical mixing, which can be interpreted as the ratio of potential energy required for mixing of fine sediments over the water column, and the kinetic energy available for mixing. Experimental evidence shows that a turbulent flow cannot be stable when $\mathbf{Ri_f}$ exceeds a critical value, reflected by $\mathbf{Ri_{f,cr}}$ (e.g. Turner, 1973; Winterwerp, 2001). Figure 4 shows that at a flow velocity U_2, SPM concentrations may attain values for which $\mathbf{Ri_f} > \mathbf{Ri_{f,cr}}$, upon which the turbulent flow field collapses. In practice, this means that fluid mud is formed.

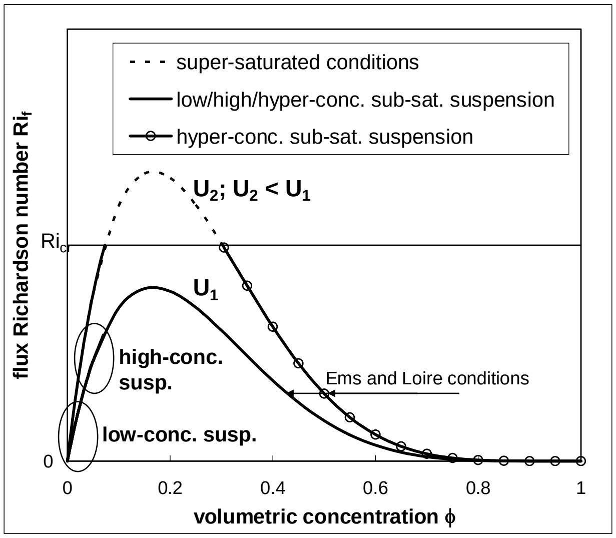

Fig. 4: Stability diagram for fine sediment suspensions showing that a bi-modal behaviour – a particular Richardson number can be obtained at two different SPM concentrations (after Winterwerp. 2006).

At larger flow velocity $U_1 > U_2$, the stability curve is continuous, with two distinctly different branches though. In the left, rising branch, an increase in ϕ implies an increase in $\mathbf{Ri_f}$, hence less favourable conditions from an energetic point of view. In the right, descending branch, an increase in ϕ yields a decrease in **Ri**$_f$, hence energetically more favourable conditions. This branch refers to so-called hyper-concentrated conditions: the turbulent flow "likes" high concentrations, as a further increase in ϕ requires less energy to keep the sediment in suspension. It can be argued that the Ems and Loire Rivers are currently in this hyper-concentrated state (Winterwerp, 2011). The bi-modal behaviour of Fig. 4 is attributed to hindered settling effects – at higher ϕ -values, the effective settling velocity reduces, and less energy is required to keep the particles in suspension (e.g. Winterwerp, 2001; Dankers and Winterwerp, 2007).

It is noted that in case of asymmetries in peak tidal velocity, also vertical mixing becomes asymmetric (mixing scales with velocity squared). For instance, flood conditions may be well-mixed, whereas ebb conditions may be highly stratified (e.g. Winterwerp, 2011).

The last important issue on the hyper-concentrated state of tidal rivers concerns the temporal variation in tidal velocity. Around slack water, the suspension settles, forming fluid mud, which then starts to consolidate. So how does the sediment-water mixture remain fluid? Bruens et al. (2011) suggest that during accelerating flow, water overlying the fluid mud is pumped into the fluid mud by entrainment processes. Hence, twice every tidal cycle, the suspension is more or less entirely mixed over the water column. As consolidation rates scale with the fluid mud thickness squared, consolidation is only important over longer time periods, such as the spring-neap cycle.

In this section, we have argued that when conditions would evolve inducing an ongoing increase in SPM concentrations, a regime shift may occur leading to hyper-concentrated conditions. Such a hyper-turbid regime is extremely stable, as favourable from an energetic point of view. Therefore, a river in this state would be difficult to reverse to its original state, as the "energy barrier" of Fig. 4 has to be overcome (or by-passed).

When the river flow is too small to flush the fine sediments occasionally out of the river, the development of an ETM2 regime is a likely candidate to set a regime shift into motion, as the asymmetries in peak velocity and vertical mixing continue to pump fine sediments up-estuary (or trap riverine sediments). Obviously, also the river's flushing capacity decreases with increasing water depth. In the two following sections, we discuss how engineering works may initiate such events.

4. DISPERSION EQUATION FOR CONVERGING ESTAURIES

Basically, all alluvial estuaries have a more or less funnel-shaped plan form. In the remainder, we limit ourselves to the evolution of the semi-diurnal tide ($T \approx 12.5$ hr) in narrow estuaries (one channel only) with intertidal area and an exponentially converging width: $b_c = b_0 \exp\left\{-x/L_b\right\}$, where b_c = width flow-carrying cross section, b_0 = width flow-carrying cross section in the mouth of the estuary, and L_b = convergence length (typical values between ~20 and ~40 km). Furthermore, we assume a more or less rectangular shape of the flow-carrying cross section, such that $A_c \approx hb_c$, where A_c = area of flow-carrying cross section, and h = tide-mean water depth, and a width of the intertidal area Δb, which is a constant fraction of $b_c(x)$. The total width b_{tot} is the sum of b_c and Δb. This cross section is sketched in Fig. 5.

This configuration is fairly similar to the ones studied by Jay (1991); Lanzoni and Seminara (1998); Friedrichs and Aubrey (1994); Toffolon and Savenije (2011); and Van Rijn (2012). The governing equations for conservation of mass and momentum have been linearized by neglecting the advection term and linearizing the friction term in the momentum equation (see also references above):

$$\begin{aligned} &\left(b_c + \Delta b\right)\frac{\partial \eta}{\partial t} + \frac{\partial A_c u}{\partial x} = 0 \\ &\frac{\partial u}{\partial t} + g\frac{\partial \eta}{\partial x} + \frac{ru}{h} = 0 \end{aligned} \qquad (4)$$

where η = instantaneous water level, u = cross-sectional averaged flow velocity, r = linear friction term $\left(r = 8c_D U/3\pi \ [\mathrm{m/s}]\right)$, c_D = drag coefficient, U = characteristic (maximal velocity), and x and t are longitudinal co-ordinate and time (x = 0 at the estuaries mouth, and $x > 0$ up-estuary). The drag coefficient c_D attains values of 0.001 to 0.003 (corresponding Chézy values of 100 – 60 $\mathrm{m}^{1/2}$/s, as $r \approx gU/C^2$), hence r also varies from around 0.001 to 0.003. In the following, we assume that the fresh water river flow is so small that its effects can be neglected. Finally, further to our linear approach, we also assume that parameters may vary along the estuary, such as the tidal amplitude, but that these variations are relatively small, and that the tidal amplitude is small compared to the water depth.

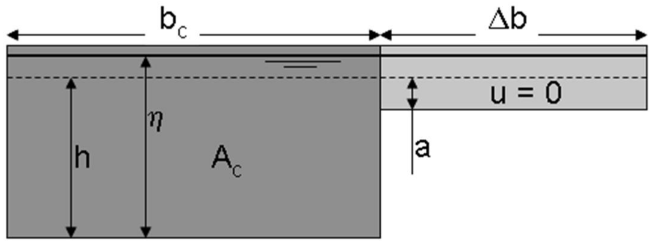

Fig. 5: Schematic cross section of tidal river with flood plain, and definition of parameters used.

If we neglect longitudinal gradients in water depth $\left(\partial h/\partial x\right)$, the continuity and mass balance equation read:

$$\frac{\partial \eta}{\partial t} + \frac{A_c}{b_c + \Delta b}\frac{\partial u}{\partial x} - \frac{A_c}{b_c + \Delta b}\frac{u}{L_b} = 0 \tag{5a}$$

$$\frac{\partial u}{\partial t} + g\frac{\partial \eta}{\partial x} + \frac{ru}{h} = 0 \tag{5b}$$

We assume that the solution to (5) follows a harmonic function:

$$\eta\left(x,t\right) = h + a_0 \exp\left\{i\left(\omega t - kx\right)\right\} \quad \text{and} \quad u\left(x,t\right) = U_0 \exp\left\{i\left(\omega t - kx - \varphi\right)\right\} \tag{6}$$

where a_0 = tidal amplitude at x = 0 (because of our linear approach, a_0 should be much smaller than the water depth h), U_0 = amplitude flow velocity at x = 0, ω = tidal frequency; $\omega = 2\pi/T$; T = tidal period, k = complex wave number; $k = k_r + ik_i$, k_r = real wave number ($k_r = 2\pi/\lambda$), λ = tidal wave length, k_i = imaginary wave number, and φ = phase angle between tide and velocity. Tidal amplification/damping is than defined as $a\left(x\right) = a_0 \exp\left\{k_i x\right\}$.

Next, we substitute (6) into (5a) and (5b), which reads in matrix form:

$$\begin{bmatrix} i\omega & -\left(\frac{A_c}{b_c + \Delta b} ik + \frac{A_c}{b_c + \Delta b}\frac{1}{L_b}\right)\exp\left\{-i\varphi\right\} \\ igk & -\left(i\omega + \frac{r}{h}\right)\exp\left\{-i\varphi\right\} \end{bmatrix} \begin{bmatrix} a_0 \\ U_0 \end{bmatrix} = 0 \tag{7}$$

Requiring the existence of non-trivial solutions, the determinant of equ. (7) should be zero, which yields a dispersion equation implicit in the wave number k:

$$L_b k^2 - ik - \frac{b_c + \Delta b}{ghb_c} L_b \omega^2 \left(1 - i\frac{r}{\omega h}\right) = 0 \quad \text{or} \quad \kappa^2 - 2i\kappa - \Lambda_e \left(1 - ir_*\right) = 0 \tag{8}$$

in which the following dimensionless parameters have been defined:

$$\begin{aligned}
&\kappa = \kappa_r + i\kappa_i = 2kL_b \\
&L_* = \frac{2L_b\omega}{\sqrt{gh}} = \frac{2L_b}{L_g}, \quad \text{where} \quad L_g \equiv \frac{\sqrt{gh}}{\omega} \\
&r_* = \frac{r}{\omega h} = \frac{gU}{\omega h C^2} \\
&b_* = \frac{b_c + \Delta b}{b_c} \\
&\Lambda_e = b_* L_*^2 = \frac{b_c + \Delta b}{b_c} \frac{4L_b^2 \omega^2}{gh} = \frac{4L_b^2\omega^2}{gA_c / b_{tot}}
\end{aligned} \tag{9}$$

Here we introduce the estuarine convergence number Λ_e, through which all geometrical and bathymetrical features of the rivers are accounted for. Λ_e decreases with increasing water depth and river convergence, and with loss of intertidal area. Note that the friction parameter $\hat{\chi}$ introduced by Toffolon and Savenije (2011) is identical to r_*. Another important length scale is the friction length L_r, which follows from the non-linearized momentum equation $L_r = hC^2/g$.

Next, the quadratic dispersion equation (8) is resolved (using MAPLE), yielding the real and imaginary wave number for the tidal propagation in a converging estuary:

$$\kappa_r = \pm\frac{1}{2}\left[2\sqrt{\left(\Lambda_e - 1\right)^2 + \left(\Lambda_e r_*\right)^2} + 2\left(\Lambda_e - 1\right)\right]^{1/2} \tag{10a}$$

and

$$\kappa_i = 1 \mp \frac{1}{2}\left[2\sqrt{\left(\Lambda_e - 1\right)^2 + \left(\Lambda_e r_*\right)^2} - 2\left(\Lambda_e - 1\right)\right]^{1/2} \tag{10b}$$

where the $+/-$ sign represent the incoming wave in equ. (10a) and (10b), respectively, and the $-/+$ sign the reflecting wave. This solution is identical to the solution presented by Jay (1991), Toffolon and Savenije (2011) and Van Rijn (2012). In Part II of this paper it will become clear why we prefer the simple three parameter solution of equ. (10).

Fig. 6 shows the variation of the dimensionless real and imaginary wave number as a function of the estuarine convergence number Λ_e for two values of the dimensionless effective hydraulic drag $r_* = 1$ and 6, characteristic for muddy and sandy beds, respectively. For low Λ_e and r_*, the tide becomes amplified, for sandy beds, characterized by larger roughness, not.

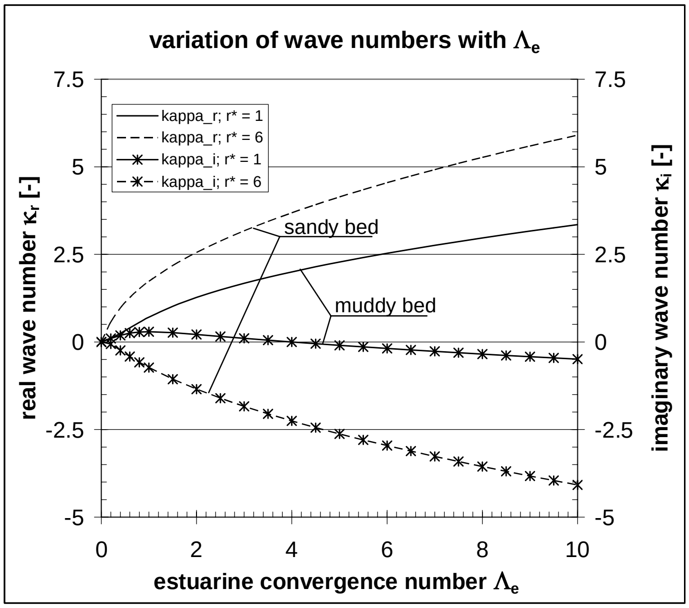

Fig. 6: Variation of dimensionless real and imaginary wave number with estuarine convergence number for incoming wave only (infinitely long estuary; e.g. equ. 10a and 10b).

Let us first analyze the behavior of these solutions for an infinitely long estuary. For a non-converging ($L_b = \infty$), frictionless channel (r = 0), equ. (10) - in dimensional form - converges to the well-known relations $k_r = \omega\sqrt{(b_c + \Delta b)/b_c gh}$ and k_i = 0. For a non-converging channel with friction, we obtain:

$$k_r = \pm\sqrt{\frac{b_*\omega^2}{2gh}}\left[\sqrt{1+r_*^2}+1\right]^{1/2} \quad \text{and} \quad k_i = \mp\sqrt{\frac{b_*\omega^2}{2gh}}\left[\sqrt{1+r_*^2}-1\right]^{1/2} \qquad \text{(11a)}$$

Let us next analyze these solutions for a converging estuary with very high ($r = \infty$) and very low roughness ($r \approx 0$). In the first case the friction term dominates the expression below the square root-sign, in the second case, friction can be neglected. The real and imaginary wave number for a frictionless system read (assuming shallow water, i.e. h not too large)

$$\begin{array}{llll} \kappa_r\big|_{r\downarrow 0} = \sqrt{\Lambda_e - 1} & \text{and} \quad \kappa_i\big|_{r\downarrow 0} = 1 & \text{for} & \Lambda_e \geq 1 \\ \kappa_r\big|_{r\downarrow 0} = 0 & \text{and} \quad \kappa_i\big|_{r\downarrow 0} = 1 - \sqrt{1 - \Lambda_e} & \text{for} & \Lambda_e \leq 1 \end{array} \qquad \text{(11b)}$$

Equ. (11b) shows that for a smooth bed and $\Lambda_e \geq 1$, the tidal wave is amplified with the convergence length $k_i = 1/2L_b$; this is therefore the maximum amplification of the tide according to linear theory; the estuary is said to be in synchronous mode (see below – weakly dissipative, Jay, 1991; Lanzoni and Seminara, 1998).

In case of a rough bed ($r = \infty$), the real and imaginary wave number become (strongly dissipative):

$$\left.k_r\right|_{r\uparrow\infty} = \frac{1}{4L_b}\sqrt{2\Lambda_e r_*} \qquad \text{or} \qquad \left.\kappa_r\right|_{r\uparrow\infty} = \sqrt{\Lambda_e r_* / 2}$$

$$\left.k_i\right|_{r\uparrow\infty} = \frac{1}{2L_b} - \frac{1}{4L_b}\sqrt{2\Lambda_e r_*} \qquad \text{or} \qquad \left.\kappa_i\right|_{r\uparrow\infty} = 1 - \sqrt{\Lambda_e r_* / 2} \tag{11c}$$

From equ. (7) we can derive the velocity amplitude U_0 as a function of a_0:

$$U_0 = \operatorname{mod}\left[\frac{igka_0}{(i + r_*)\,\omega \exp\{-i\varphi\}}\right] = \frac{ga_0}{\omega}\sqrt{\frac{k_r^2 + k_i^2}{r_*^2 + 1}} \tag{12}$$

The phase angle between tidal elevation and velocity follows from substitution of (6) into (5a), elaborating the real part only:

$$i\omega a_0 - i\frac{A_c}{b_c + \Delta b}kU_0 \exp\{-i\varphi\} - \frac{A_c}{b_c + \Delta b}\frac{1}{L_b}U_0 \exp\{-i\varphi\} = 0 \tag{5a′}$$

$$\tan\{\varphi\} = \frac{L_b k_i - 1}{L_b k_r} = \frac{\kappa_i - 2}{\kappa_r} \tag{13a}$$

Note the similarity of (13a) with Van Rijn's Table 1 (2012). Substituting from (11b and 11c) yields the phase angle for a smooth and friction-dominated system (see also Dronkers, 2005 and Friedrichs, 2010):

$$\left.\tan\{\varphi\}\right|_{r\downarrow 0} = -\frac{1}{\sqrt{\Lambda_e - 1}} \quad \text{for } \Lambda_e \geq 1 \quad \text{and} \quad \left.\tan\{\varphi\}\right|_{r\downarrow 0} = \infty; \;\; \varphi = 90^\circ \quad \text{for } \Lambda_e \leq 1$$

$$\left.\tan\{\varphi\}\right|_{r\uparrow\infty} = -\frac{\sqrt{\Lambda_e r_*} + 2}{\sqrt{\Lambda_e r_*}} \approx -1 \quad \text{for all } \Lambda_e \tag{13b}$$

The celerity c of the tidal wave into the estuary is given by:

$$c = \frac{\omega}{k_r} = \frac{2\omega L_b}{\kappa_r} \tag{14a}$$

Substituting from (11a) yields the celerity for a smooth and friction dominated system (e.g. Le Blond, 1978):

$$\left.c\right|_{r\downarrow 0} = \frac{2\omega L_b}{\sqrt{\Lambda_e - 1}} \quad \text{for} \quad \Lambda_e \geq 1 \text{ and } \left.c\right|_{r\downarrow 0} = \infty \quad \text{for} \quad \Lambda_e \leq 1$$

$$\left.c\right|_{r\uparrow\infty} = \frac{4\omega L_b}{\sqrt{2\Lambda_e r_*}} \quad \text{for all } \Lambda_e \tag{14b}$$

The behavior of the tidal wave for frictionless conditions and $\Lambda_e \leq 1$ $\left(\text{i.e. } L_b \leq L_g/2 \text{ for } \Delta b = 0\right)$ needs some further explanation. For these conditions, the wave length and celerity become infinite, whereas the phase angle between water level and velocity becomes 90°. Though these conditions are identical to those of a standing wave, we have to realize we did not prescribe any wave reflections in our boundary conditions. Though this pathological behavior is referred to as super-critical by Toffolon and Saveneije (2011), and was also found by Friedrichs and Aubrey (1994), we do not really understand the physical meaning of these solutions to the equations, and the conditions at which these occur.

Next, we study the propagation and amplification/damping of the tide in an estuary of finite length ℓ (for instance by a weir at $x = \ell$). At the mouth of the estuary we prescribe a simple cosine tide:

$$\eta\left(0,t\right) = h + a_0 \cos\left\{\omega t\right\} \tag{15}$$

in which a_0 = amplitude of the tide in the river mouth. The harmonic solution to equ. (5) than reads:

$$\begin{aligned} &\eta\left(x,t\right) = h + a_0^+ \exp\left\{i\left(\omega t - k^+ x\right)\right\} + a_0^- \exp\left\{i\left(\omega t - k^- x\right)\right\} \quad \text{and} \\ &u\left(x,t\right) = U_0^+ \exp\left\{i\left(\omega t - k^+ x - \varphi\right)\right\} + U_0^- \exp\left\{i\left(\omega t - k^- x - \varphi\right)\right\} \end{aligned} \tag{16a}$$

in which the superscripts $\bullet^+$ and $\bullet^-$ reflect the incoming and reflecting tidal wave. In case of an infinitely long river, equ. (16a) reduces to:

$$\eta\left(x,t\right) = h + a_0 \exp\left\{i\left(\omega t - kx\right)\right\} \quad \text{and} \quad u\left(x,t\right) = U_0 \exp\left\{i\left(\omega t - kx - \varphi\right)\right\} \tag{16b}$$

as in equ. (6). The boundary conditions to the solution of equ. (16a) are given by:

- $x = 0$: $a_0^+ + a_0^- = a_0$; this conditions implies that in the analyses of Part II, the for rivers with a weir, the river should be so long (friction length small) that $a_0 = a_0^+$,
- $x = \ell$: $U = 0$, hence $U^+ = -U^-$.

Further to equ. (5b), the latter implies that

- $x = \ell$: $\partial a^+ / \partial x = -\partial a^- / \partial x$, so that $a_0^+ k^+ \exp\left\{-ik^+\ell\right\} + a_0^- k^- \exp\left\{-ik^-\ell\right\} = 0$.

Hence, we find for the two complex amplitudes of the incoming and reflecting waves a^+ and a^-:

$$a^+ = \frac{k^- \exp\left\{-ik^-\ell\right\} \exp\left\{-ik^+ x\right\}}{k^- \exp\left\{-ik^-\ell\right\} - k^+ \exp\left\{-ik^+\ell\right\}} a_0 \tag{17a}$$

$$a^- = \frac{k^- \exp\left\{-ik^+\ell\right\} \exp\left\{-ik^- x\right\}}{k^+ \exp\left\{-ik^+\ell\right\} - k^- \exp\left\{-ik^-\ell\right\}} a_0 \tag{17b}$$

As $k^- = -k_r + ik_i^- = -k_r + i\left(p+q\right)$ and $k^+ = k_r + ik_i^+ = k_r + i\left(p-q\right)$, where p and q are dummy variables (see Equ. 10), we can re-write (17) as:

$$a_0^+ = \frac{k^- \exp\left\{ik_r\ell\right\}}{k^- \exp\left\{ik_r\ell\right\} - k^+ \exp\left\{-ik_r\ell\right\} \exp\left\{-2q\ell\right\}} a_0 \tag{18a}$$

$$a_0^- = \frac{k^+ \exp\left\{-ik_r\ell\right\} \exp\left\{-2q\ell\right\}}{k^+ \exp\left\{-ik_r\ell\right\} \exp\left\{-2q\ell\right\} - k^- \exp\left\{ik_r\ell\right\}} a_0 \tag{18b}$$

Hence, $\lim_{\ell \to \infty} \left\{ a_0^+ \right\} = a_0$ and $\lim_{\ell \to \infty} \left\{ a_0^- \right\} = 0$, retrieving the simple propagating wave in an infinitely long converging estuary. Furthermore, equ. (17) shows that resonance can occur when:

$$\mathrm{Re}\left[k^+ \exp\left\{ -ik^+\ell \right\} - k^- \exp\left\{ -ik^-\ell \right\} \right] = 0 \;\text{ i.e. }\; \tan\left\{ n\frac{\pi}{2} - k_r^+\ell \right\} = \frac{k_r^+ \exp\left\{ k_i^-\ell \right\} + k_r^+ \exp\left\{ k_i^+\ell \right\}}{k_i^+ \exp\left\{ k_i^+\ell \right\} + k_i^- \exp\left\{ k_i^-\ell \right\}} \qquad (19)$$

As equ. (19) is implicit in ℓ, we cannot determine the conditions for resonance analytically. However, for a straight channel, $k_i^- = -k_i^+$ (e.g. equ. (10b)), $\tan\left\{ k_r\ell \right\} = \infty$, which is the case if $\ell = \lambda/4$, where λ = wave length in a straight frictionless channel, e.g. Dronkers (1964). For a very strong converging channel, e.g. $\lim_{L_b \to 0} k_r = \lim_{L_b \to 0} k_i^+ = \lim_{L_b \to 0} k_i^- = 1$, $\tan\left\{ k_r\ell \right\} = 1$, and $\ell = \lambda/8$. Of course, the wave length in a straight and very converging channel are very much different (in fact if $L_b = 0$, $\lambda = 0$).

The solution to equ. (19) is depicted graphically in Fig. 7 (see also Prandle, 1980). Note that typical values for Λ_e range from a bit smaller than 1 to about 2 (e.g. Part II). The effect of reflections will grow rapidly with decreasing effective hydraulic roughness, as both the tidal amplitude and friction length will than increase.

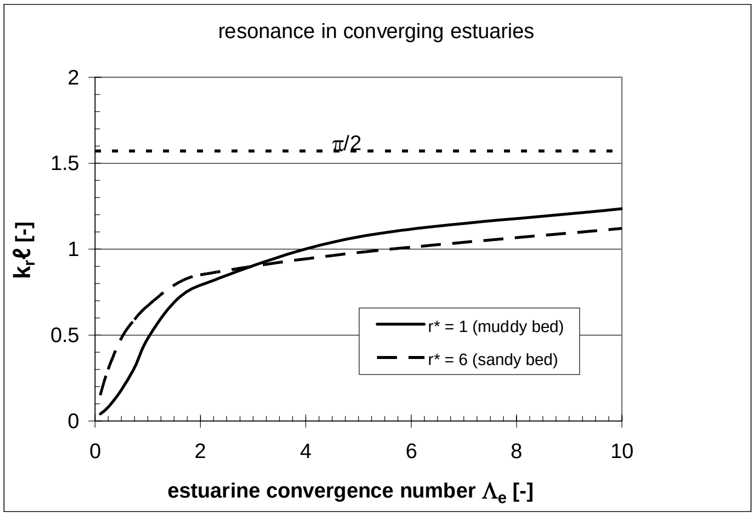

Fig. 7: Conditions for resonance (solution of equ. 19) for a converging estuary as a function of the estuarine convergence number.

Next, we study the dependency of tidal asymmetry on the estuarine bathymetry. Though we prescribe harmonic solutions in a linear model (equ.'s (5) and (16a) with one frequency only), we can derive a proxy for the tidal asymmetry by analyzing the celerity of the tidal wave. In the following, we limit ourselves to infinitely long channels only. Further to Friedrichs (2010) and Dronkers (2005) we define an asymmetry parameter $\gamma = c_{\mathrm{HW}}/c_{\mathrm{LW}}$, where c_{HW} and c_{LW} are the celerity at high water (i.e. $h = h_0 + a$) and low water (i.e. $h = h_0 - a$), respectively:

$$\gamma = \frac{k_{r,LW}}{k_{r,HW}} = \left[\frac{(1+a/h)}{(1-a/h)}\right]^{1/2} \left[\frac{\left[\sqrt{\left(L_*^2-(1-a/h)\right)^2+\left(\frac{L_*^2 r_*}{(1-a/h)}\right)^2}+\left(L_*^2-(1-a/h)\right)\right]}{\left[\sqrt{\left(b_* L_*^2-(1+a/h)\right)^2+\left(\frac{b_* L_*^2 r_*}{(1+a/h)}\right)^2}+\left(b_* L_*^2-(1+a/h)\right)\right]}\right]^{1/2} \tag{20}$$

in which we assume that $\Delta b = 0$ at low water, and the dimensionless parameters have been defined in equ. (9). Note that this proxy is relevant for progressive waves only, and looses its meaning in case of a truly standing wave. Further, for a friction-dominated system we find:

$$\gamma\big|_{r=\infty} = \frac{k_{r,LW}}{k_{r,HW}}\bigg|_{r=\infty} \approx \left[\frac{\dfrac{1}{(1-a/h)}\;\dfrac{1}{(1-a/h)}}{\dfrac{b_*}{(1+a/h)}\;\dfrac{1}{(1+a/h)}}\right]^{1/2} = \frac{1+a/h}{1-a/h}\sqrt{\frac{1}{b_*}} \approx \frac{(1+a/h)^2}{\sqrt{b_*}} \tag{21a}$$

Of course, this solution can be derived directly from the general formulation of wave celerity in a straight prismatic compound channel, e.g. $c=\sqrt{gA_c/b_{tot}}$. For a frictionless system we find four solutions, depending whether L_*^2 and $b_* L_*^2$ are larger or smaller than $(1-a/h)$ or $(1+a/h)$, respectively. We give one solution:

$$\gamma\big|_{r=0} = \frac{k_{r,LW}}{k_{r,HW}}\bigg|_{r=0} \approx \left[\frac{(1+a/h)^2\,\Lambda_e/b_* - (1+a/h)}{\Lambda_e-(1+a/h)}\right]^{1/2} \quad \text{for } L_*^2 \ge (1-a/h) \text{ and } b_* L_*^2 \ge (1+a/h) \tag{21b}$$

In the next section, we study the behavior of these solutions graphically, analyzing the response of an estuary to deepening and narrowing (loosing intertidal area).

5. CONCEPTUAL RESPONSE TO NARROWING AND DEEPENING

In Part II of this paper, we analyze the historical evolution of four rivers, e.g. the Elbe, Ems, Loire and Scheldt Rivers. The length of Ems and Scheldt is restricted by a weir (at Herbrum and Ghent, respectively), hence the tide is likely to be affected by reflections. The depth of the Elbe changes so abruptly beyond Hamburg, that also in the Elbe tidal reflections are to be expected. Hence, ideally, we should use the full analytical solution (equ. 17) to study the tidal properties in these rivers. However, this is not easy, as the depth along these rivers varies considerably, and also the convergence length of two rivers (Elbe and Scheldt) is not constant. Modeling the tide in such inhomogeneous rivers requires division of the river into sub-sections. This is indeed been done in Part II. From a mathematical point of view, accounting for reflections of the tide requires internal boundary conditions between the various sub-sections. This has been elaborated by e.g. Prandle and Rahman (1980); Jay (1991) and Toffolon and Savenije (2011). However, the extensive set of equations lose their clarity, while this clarity was the major reason for developing the current new approach. Therefore, in Part II we analyze these four rivers, assuming infinite length, and we discuss the behavior of the solutions of the previous section for infinitely long rivers as well.

Yet, for the Elbe, Ems and Scheldt, we assess the effects of tidal reflections in a qualitative way, and in the following, we elaborate briefly the behavior of the full solution (equ. 17) by studying that solution graphically. First, we analyze the conditions for resonance in an almost straight channel of 5 m depth, and a weir at 75 km (about ¼ of the undisturbed tidal wave length), as discussed by Dronkers (1964). The results are presented in Fig. 8 for three different friction coefficients; these results are indeed identical to those found by Dronkers (1964). As mentioned, tidal amplification by reflections is expected to grow rapidly with increasing SPM-concentrations, as tidal amplitude and friction length both increase with decreasing hydraulic drag

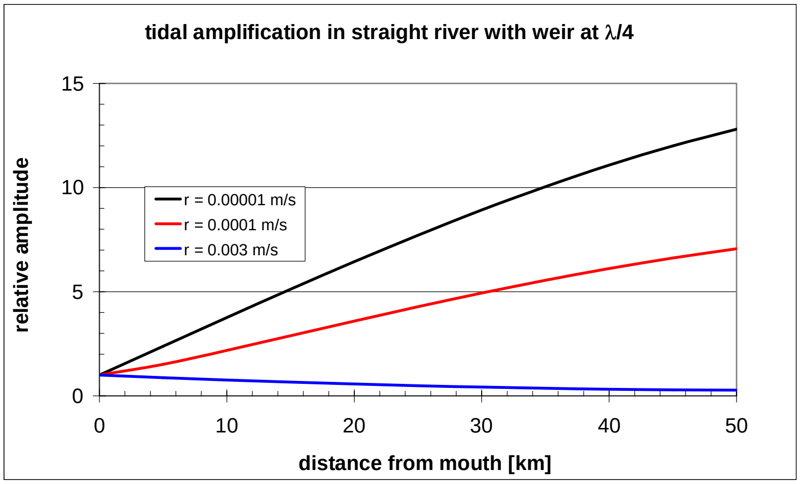

Fig. 8: Amplification of tidal wave in 5 m deep, almost straight estuary (L_b = 50,000 km, λ = 350 km) and weir at ℓ = 75 km; r = 0.000001 m/s yields C ≈ 1000 $m^{1/2}$/s (e.g. almost frictionless); r = 0.0001 m/s yields C ≈ 300 $m^{1/2}$/s and r = 0.003 yields C ≈ 60 $m^{1/2}$/s.

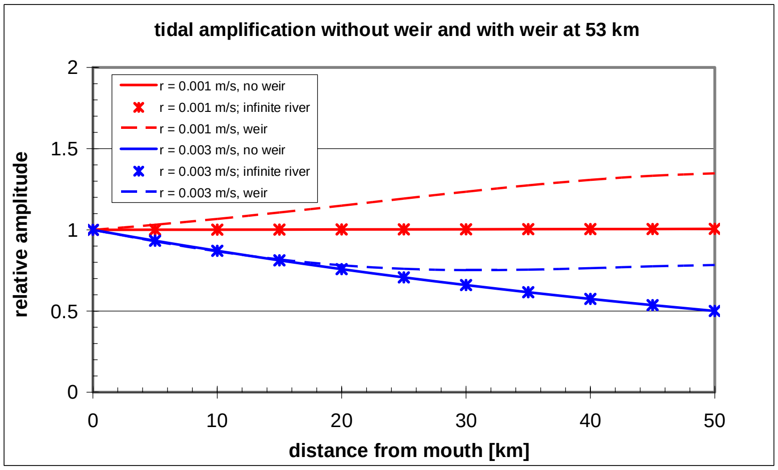

Fig. 9: Amplification of tidal wave in short converging estuary (h = 5 m, L_b = 33 km, ℓ = 53 km); r = 0.001 m/s yields C ≈ 100 $m^{1/2}$/s; r = 0.003 yields C ≈ 60 $m^{1/2}$/s.

Next, we study the effect of river convergence. Fig. 9 presents the computed tidal amplitudes in a 5 m deep converging river (L_b = 33 km, e.g. Ems-conditions) with and without a weir for two values of the friction coefficient, the smaller representative for high SPM conditions and the larger for low SPM concentrations. Though the increase in tidal amplitude is not too different for both cases, the tide in the sandy system remains damped, whereas in the muddy system, the tide becomes amplified.

To check our full solution (e.g. with reflections), we have also plotted the imaginary wave number (10b), which gives directly the relative amplitude in an infinitely long channel, showing exact overlap with equ. (17) for $\ell = \infty$.

In the last part of this section, we discuss the behavior of the solutions of the previous section for an infinitely long channel, assuming a convergence length of 33 km, throughout. Fig. 10 presents the phase difference between the flow velocity and tidal elevation φ (e.g. equ. 13a) as a function of depth, width of intertidal area, and bed friction. Fig. 11 presents the celerity c of the tidal wave into the estuary, using equ. (14a). Because of the rapid increase in c with depth h and inverse friction $1/r$, we have used a logarithmic axis.

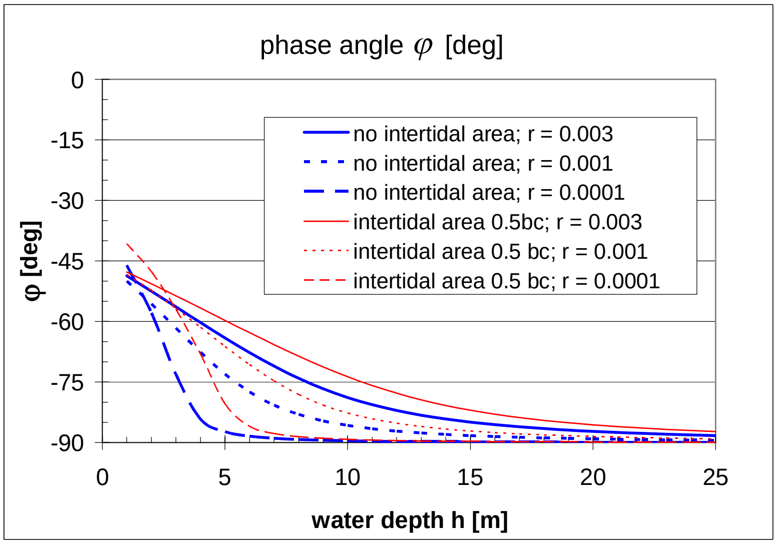

Fig. 10: Phase angle φ between flow velocity and tidal elevation ($\ell = \infty$, L_b = 33 km).

For $\varphi = 90^{\circ}$ (e.g. Fig. 10), high water slack (HWS) occurs at high water (HW), as for standing waves. This condition is met at large water depths, but also at moderate water depths when the hydraulic drag becomes very small. The latter is the case in the presence of pronounced concentration of SPM (several 10 g/l), as in the Ems and Loire Rivers. Fig. 10 shows that c then increases rapidly, and can become so large that high waters along the estuary occur almost simultaneously. For instance, for h = 7 m, and r = 0.001, we find c = 100 m/s (e.g. Fig. 11), and high water at 60 km from the river mouth would occur only 10 minutes after high water at that mouth. Note that a "normal" progressive wave approach $c = \sqrt{gh}$ would yield a travel time of almost 2 hours.

From equ. (5a) we assess that $\varphi = 90^{\circ}$ occurs when $\partial u / \partial x = 0$ (see also Dronkers, 2005 and Friedrichs, 2010), and from equ. (13a), we conclude that $\varphi = 90^{\circ}$ implies $k_r = 0$. The latter is true only for a real standing wave, which implies resonant behavior in the estuary. Note that this solution still represents a progressive wave, even when reflections become important. The first observation also implies large flow velocities over the major part of the estuary. Then, owing to the harmonic solution prescribed (equ. 6), also the tidal amplitude is more or less constant over a large part of the estuary. An estuary with such conditions is called synchronous (e.g. Dronkers, 2005). Examples are the current conditions in the Ems and Loire River (e.g. Part II).

Note that the evolution towards a synchronous estuary is delayed in case of presence of (some) intertidal area, e.g. Fig. 10. However, the celerity decreases with $\Delta b/b_c$ (results not shown), though is not too sensitive to the intertidal area

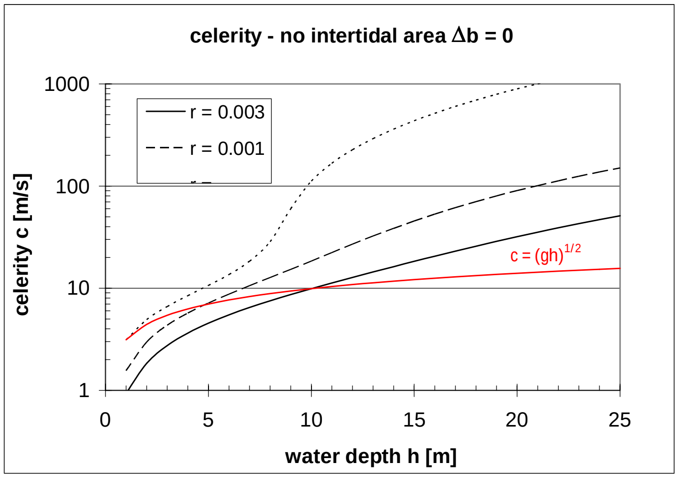

Fig. 11: Celerity of tidal wave ($\ell = \infty$, L_b = 33 km).

Next, we study the conceptual character of the tidal properties in a tidal river in response to deepening as a function of the areal of intertidal area and the effective hydraulic drag, simulating low (r = 0.003 m/s; $C \approx$ 60 $m^{1/2}$/s) and high SPM concentrations (r = 0.001 m/s, $C \approx$ 100 $m^{1/2}$/s). The convergence length is set again at 33 km, and we prescribe a tidal amplitude in the mouth of the river of 1 m to depict the tidal response clearly, though this amplitude is possibly a bit high with respect to our linear assumptions. The intertidal area is set at $\Delta b = b_c$ or $\Delta b = 0$.

First we discuss the situation with low SPM concentrations (r = 0.003 m/s). Figure 11 shows that when the river is deepened, the tidal amplitude increases, as expected. Without intertidal area, the response is a bit stiffer. For large water depth, the amplitude for the case with intertidal area is a bit larger than in the case without intertidal, as in the first case more water enters the river.

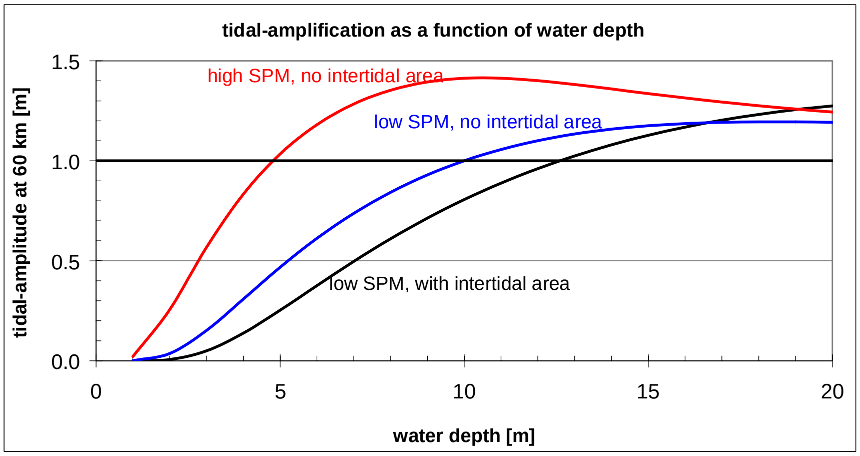

Fig. 12: Response of tidal amplification as a function of water depth, intertidal area and effective hydraulic drag.

Figure 13 shows that the proxy for tidal asymmetry γ changes from ebb dominance for all water depths to flood dominant conditions in case the intertidal area is removed. This observation is not new of course (e.g. Friedrichs and Aubrey, 1988), but the implications for fine sediments have not been elaborated. When the tidal river becomes flood dominant, marine fine sediments are pumped into the river and/or riverine fine sediment are kept within the river. Then, if sufficient fines have accumulated, and are distributed over a considerable length of the river, the effective hydraulic drag is expected to decrease (e.g. Section 3 of this paper). In response to this lower drag (simulated with r = 0.001 m/s), amplification increases further, as depicted in Fig. 12, accompanied by an enhancement of flood-dominance, e.g. Fig. 13. As a result, more fines can accumulate in the river, further decreasing the effective hydraulic drag, setting in motion the snowball effect suggested in the beginning of this paper.

The next section discusses some implications of this picture, and in Part II we analyze historical data to study whether this feed-back can be observed in European rivers.

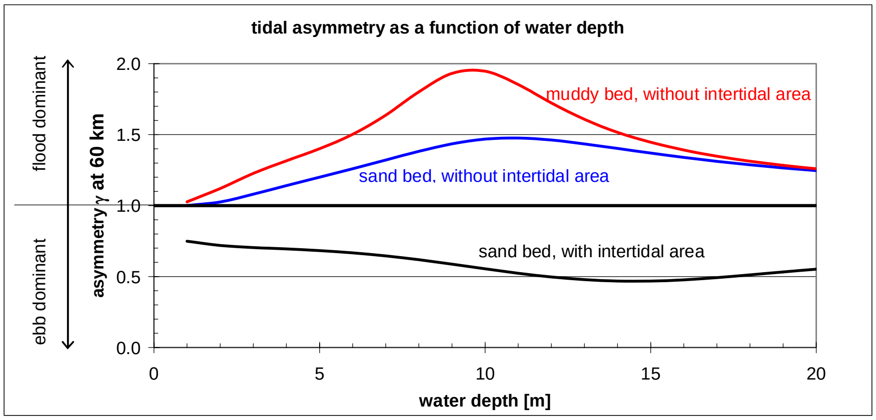

Fig. 13: Response of tidal asymmetry as a function of water depth, intertidal area and effective hydraulic drag.

6. DISCUSSION, SUMMARY AND CONCLUSIONS

This paper presents a conceptual picture on the evolution of a number of “normal” European tidal rivers into a hyper-turbid state in response to narrowing and deepening accommodating ever-larger ships. Part II of this paper describes the actual analysis of the historical data of four European rivers, e.g. the Elbe, Ems, Loire and Scheldt Rivers. In the current Part I, the ingredients required for the analysis and interpretation of the data in Part II are derived and summarized. Our main tool in this is the analytical solution of the linearized water movement equations. Though not new, the solution is formulated in a form that can be used easily to compare the evolution of the various rivers.

Our analysis of the analytical solution itself suggests that, after loss of intertidal area, ongoing deepening may enhance flood dominancy, while decreasing the river’s flushing capacity. As discussed in Part II, loss of intertidal area has been considerably in the 19th century, reclaiming intertidal areas and embanking rivers. Thus, conditions may be induced favourable for the generation of a secondary turbidity maximum, referred to as ETM2. Then, if large amounts of fine sediments would accumulate in the river, the effective hydraulic drag decreases, enhancing the tidal asymmetry further. It is noted that this feed-back may occur already at SPM concentrations of several 100 mg/l (Winterwerp et al., 2009). However, the suspended matter should be spread over a considerable length of the river to induce a measurable reduction in drag. As the accumulation of fines takes time, the time scale for a regime shift towards hyper-turbid conditions is expected to take considerable time after “favourable” conditions for such a regime shift have been established (the tipping point). When SPM concentrations continue to increase, entrainment processes re-fluidize the mud every accelerating tide, preventing consolidation of the sediment-water mixture. Thus, the ETM2 conditions become self maintaining, as the hyper-turbid state is favourable from an energy point of view as well (e.g. Section 2). These ETM2 conditions can therefore be considered as an alternative state in relation to the ETM1 state, common in most “normal” estuaries. This positive feed-back loop is sketched in Fig. 14, depicting the proposed snowball effect leading to hyper-turbid conditions.

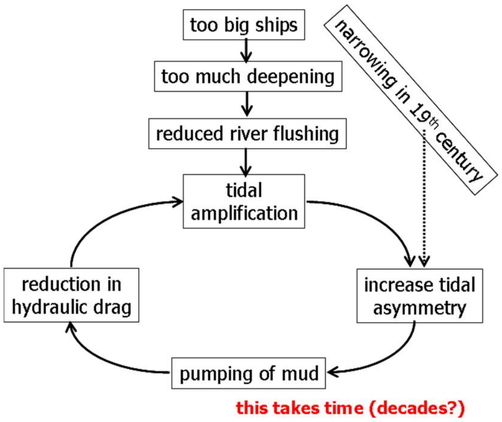

Fig. 14: Conceptual positive feedback loop inducing hyper-concentrated conditions in tidal rivers after intertidal area has been lost, which happened for many rivers in the late 19th century.

As high SPM concentrations in the water column are a necessary condition for the feed-back between tidal amplification and reduction in hydraulic drag, accommodation of fines on intertidal areas may prevent a regime shift in tidal rivers. Thus, intertidal area has two functions:

- With sufficient intertidal area, tidal conditions remain ebb-dominant, preventing the formation of ETM2 conditions. However, a considerable intertidal area is required, estimated at at least 50% of the width of the flow-carrying cross section (see also Friedrichs and Aubrey, 1988).
- Intertidal area can however also accommodate large amounts of fine sediments, preventing their accumulation in the water column. The area required to prevent a regime shift towards hyper-turbid conditions is site-specific, but likely much smaller than the intertidal areas required to affect tidal asymmetry.

It is finally noted that in the current paper three important effects are not being treated (in detail):

- The tidal evolution may be affected by the construction of a weir, limiting the effective length of the river. The reflections of the tidal wave are felt over increasing lengths of the estuary when the effective hydraulic drag decreases. The underlying increase in roughness length is not only the result of a decrease in friction coefficient, but also by the increase in the celerity of the tidal wave.
- Tidal asymmetry in an estuary is not only generated internally, but may also be "imported" from the estuaries environment, for instance a shallow sea in which the estuary flows (e.g. Schuttelaars et al., 2012).
- The effect of river flow with respect to flushing has been discussed (though not quantified); however, river flows can affect the tidal propagation as well, which cannot be elaborated with the linear model in this paper.

In a next phase of this study, we will address these issues, and other non-linear effects with a numerical model, operated in the same sense as the analytical model of this paper, as elaborated upon in Part II of this paper.

ACKNOWLEDGEMENTS

This work was carried within the framework of the LTV-project, which is the acronym for Long-Term Vision of Scheldt estuary with respect to Safety, Accessibility and Nature, in which the following sub-projects are integrated: Maintaining fairways Scheldt estuary, Permits for disposal of dredged sediments and the so-called KPP (knowledge of primary processes) program of Rijkswaterstaat. The study was financed by the Flemish "Afdeling Maritieme Toegang" (Maritime Department) and Rijkswaterstaat, Waterdienst and Directorate Zeeland (the Dutch Ministry of Infrastructure and Environment). The subject of the research in this paper was formulated by Mr. Youri Meersschaut requesting the analysis of the fine sediment dynamics in the Scheldt River. Further we like to thank Mr. Cees Kuijper and dr. Henk Schuttelaars for their many constructive comments and ongoing discussions on this subject, and dr. Tom de Mulder for reviewing a report of this study. We also would like to acknowledge the help of Mr. Marcel Taal in organizing and coordinating our study.

REFERENCES

Brenon, I. and P. LeHir, 1999. Modeling the Turbidity Maximum in the Seine Estuary (France): Identification of Formation Processes. Estuarine, Coastal and Shelf Science, 49: 525–544.

Bruens, A.W., J.C. Winterwerp and C. Kranenburg, 2012. Physical and numerical modeling of the entrainment by a high-concentrated mud suspension. ASCE, Journal of Hydraulic Engineering, 138 (6) 479-490; doi:10.1061/(ASCE)HY.1943-7900.0000545.

Cai, H., H.H.G. Savenije and M. Toffolon, 2012. A new analytical framework for assessing the effects of sea-level rise and dredging on tidal damping in estuaries. Journal of Geophysical Research, 117, C09023, doi:10.1029/2012JC008000.

Chernetsky, A.S., H.M. Schuttelaars and S.A. Talke, 2010. The effect of tidal asymmetry and temporal settling lag on sediment trapping in tidal estuaries. Ocean Dynamics 60:1219–1241, DOI 10.1007/s10236-010-0329-8.

Dankers, P.J.T. and J.C. Winterwerp, 2007. Hindered settling of mud flocs: Theory and validation. Continental Shelf Research, 27: 1893-1907.

Dronkers, J. J., 1964. Tidal Computations in River and Coastal Waters, Elsevier, New York.

Dronkers, J., 2005. Dynamics of coastal systems. Advanced Series on Ocean Engineering – Vol 25. World Scientific.

Dyer, K. R. 1997, Estuaries: a physical introduction. Chichester, England. John Wiley and Sons.

Friedrichs, C.T. and D.G. Aubrey, 1988. Non-linear tidal distortion in shallow well-mixed estuaries: a synthesis. Estuarine, Coastal and Shelf Science, 27: 521-545.

Friedrichs, C. T., and D. G. Aubrey, 1994. Tidal propagation in strongly convergent channels, Journal of Geophysical Research, 99: 3321-3336.

Friedrichs, C. T., 2010. Barotropic tides in channelized estuaries. in Contemporary Issues in Estuarine Physics, edited by A. Valle-Levinson: 27–61, Cambridge Univ. Press, Cambridge, UK.

Hunt, J.N., 1964. Tidal Oscillations in estuaries. Geophysical Journal of the Royal Astronomical Society, 8: 440-455.

Jay, D. A., 1991. Green law revisited: Tidal long-wave propagation in channels with strong topography. Journal of Geophysical Research, 96 (C11) 20,585–20,598.

Jay, D.A. and Musiak, J.D., 1996. Internal tide asymmetry in channels: origins and consequences. In: Pattiaratchi C (ed) Mixing processes in estuaries and coastal seas. American and Geophysical Union Coastal and Estuarine Sciences Monograph, 219-258.

Lanzoni, S., and G. Seminara, 1998. On tide propagation in convergent estuaries, Journal of Geophysical Research, 103(C13) 30,793–30,812.

LeBlond,P . H., 1978. On tidal propagation in shallow rivers. Journal of Geophysical Research, 83: 4717-4721.

Lin J. and A.Y. Kuo, 2001. Downstream turbidity maximum in the York River, Virginia. Estuaries, 24,707–720

Prandle, D., and M. Rahman, 1980. Tidal response in estuaries. Journal of Physical Oceanography, 10: 1552-1573.

Savenije, H. H. G., 2001. A simple analytical expression to describe tidal damping or amplification. Journal of Hydrology, 243 (3–4), 205–215.

Schuttelaars, H.M., V.N. de Jonge and A. Chernetsky, 2012. Improving the predictive power when modeling physical effects of human interventions in estuarine systems. Ocean & Coastal Management, in press; doi:10.1016/j.ocecoaman.2012.05.009.

Soulsby, R.L. and B.L.S.A. Wainwright, 1987. A criterion for the effect of suspended sediment on near-bottom velocity profiles. Journal of Hydraulic Research, 25 (3) 341-356.

Speer,P . E., and D. Aubrey, 1985. A study of non-linear tidal propagation in shallow inlet/estuarine systems I, Theory. Estuarine, Coastal and Shelf Science, 21, 206-240.

Talke, S.A., H.E. de Swart and H.M. Schuttelaars. 2008. An analytical model for the equilibrium distribution of sediment in an estuary. In River, coastal and estuarine morphodynamics, ed. C.M. Dohmen-Janssen and S.J.M.H. Hulscher, 403–412. London: Taylor & Francis.

Talke, S.A., H.E. de Swart, and H.M. Schuttelaars. 2009. Feedback between residual circulations and sediment distribution in highly turbid estuaries: an analytical model. Continental Shelf Research 29: 119–135. doi:10.1016/j.csr.2007.09.002.

Taylor, P.A. and K.R. Dyer, K.R., 1977. Theoretical models of flow near the bed and their implications for sediment transport. The Sea, 6, pp 579-601.

Toffolon, M., G. Vignoli, and M. Tubino, 2006. Relevant parameters and finite amplitude effects in estuarine hydrodynamics. Journal of Geophysical Research, 111, C10014, doi:10.1029/2005JC003104.

Toffolon, M. and H.G. Savenije, 2011. Revisiting linearized one-dimensional tidal propagation. Journal of Geophysical Research, 116, C07007, doi:10.1029/2010JC006616.

Turner, J.S., 1973. Buoyancy effects in fluids. Cambridge University Press.

Vanoni, V.A., 1946. Transportation of suspended sediment by water, ASCE Transactions. 111 (2267) 67-133.

Van Rijn, L.C., 2011. Analytical and numerical analysis of tides and salinities in estuaries; part I: tidal wave propagation in convergent estuaries. Ocean Dynamics, 61: 1719–1741. DOI 10.1007/s10236-011-0453-0

Villaret, C. and J.H. Trowbridge, 1991. Effects of stratification by suspended sediments on turbulent shear flows. Journal of Geophysical Research, 96 (C6) 10659-10680.

Winterwerp, J.C., 2001. Stratification of mud suspensions by buoyancy and flocculation effects, *Journal of Geophysical Research*. 106 (10) 22,559-22,574.

Winterwerp, J.C., M. Lely and Qing He, 2009. Sediment-induced buoyancy destruction and drag reduction in estuaries. Ocean Dynamics, 59 (5) 781-791

Winterwerp, J.C., 2006. Stratification effects by fine suspended sediment at low, medium and very high concentrations. Geophysical Research, 11 (C05012) 1-11.

Winterwerp. J.C., 2011. Fine sediment transport by tidal asymmetry in the high-concentrated Ems River. Ocean Dynamics, 61 (2-3) 203-216, DOI:10.1007/s10236-010-0332-0.

Man-induced regime shifts in small estuaries – II: a comparison of rivers

JOHAN C. WINTERWERP[1,2,*], ZHENG BING WANG[1,2] , ALEXANDER VAN BRAECKEL[3], GIJSBERT VAN HOLLAND[4], FRANK KÖSTERS[5]

3. Deltares (formerly WL|Delft Hydraulics), PO Box, 177, 2600 MH Delft, The Netherlands
4. also: Delft University of Technology, Environmental Fluid Mechanics, PO Box 5048, 2600 GA Delft, The Netherlands
5. Research Institute for Nature and Forest, Kliniekstraat 25, B-1070 Brussels, Belgium
6. IMDC, Coveliersstraat 15, B-2600 Berchem (Antwerp), Belgium
7. Bundesanstalt für Wasserbau, Wedeler Landstr. 157, 22559 Hamburg, Germany

* corresponding author, email: han.winterwerp@deltares.nl

ABSTRACT: This is Part II of two papers on man-induced regime shifts in small, narrow and converging estuaries, with focus on the interaction between effective hydraulic drag, fine sediment import and tidal amplification, induced by river engineering works, e.g. narrowing and deepening. Paper I describes a simple linear analytical model for the tidal movement in narrow, converging estuaries, and a conceptual model on the response of tidal rivers to river engineering works. It is argued that such engineering works may set in motion a snowball effect bringing the river into an alternative steady state.

Part II analyses the historic development in tidal range in four rivers, e.g. the Elbe, Ems, Loire and Scheldt, all in North-West Europe; data are available for many decades, up to a century. We use the analytical model derived in Part I, showing that the effective hydraulic drag in the Ems and Loire have decreased considerably over time, as anticipated in Part I. We did not find evidence that the Upper Sea Scheldt is close to its tipping point towards hyper-turbid conditions, but risks have been identified. In the Elbe, tidal reflections against the profound step in bed level around Hamburg seem to have affected the tidal evolution in the last decades.

It is emphasized that the conceptual picture sketched in these papers is still hypothetical, and needs to be validated, for instance through hind-cast modelling of the evolution of these rivers. This will not be an easy task, as historical data for a proper calibration of the models required are scarce.

KEY WORDS: tidal amplification, hydraulic drag, dispersion equation, regime shift, Elbe, Ems, Loire, Scheldt

1. INTRODUCTION

In many European rivers, tidal ranges have increased dramatically in the course of the 20th century, and some rivers (e.g. Loire and Ems) have evolved into hyper-turbid systems. Though it is recognized that large scale engineering works, such as reclamations, embankments and deepening have caused these tidal amplifications and shifts towards a hyper-turbid state, the underlying mechanisms are not yet fully understood. It is the aim of the present paper to enhance our understanding of these processes. This is done in two papers, analyzing the long-term historic evolution of the tide in four rivers, e.g. the Elbe, Ems, Loire and Scheldt Rivers. This analysis is presented in the current Part II, using the linear analytical model and relevant non-dimensional parameters, derived and discussed in Part I of this paper. In Part I we also hypothesize how a reduction in river-induced flushing and increase in flood dominancy may pump in large amounts of fine sediments (mud), enhancing the effects of river deepening on tidal amplification.

Our methodology is as follows. We collected data on the historical interventions within these four rivers, and on the evolution of the tidal range. Where available, we use the asymmetry from the measured ratio of rising and falling tide. Some data go back to the late 1800s. We are very grateful to a large number of people who have contributed to this data collection. These data have then been elaborated as follows:

15. We have collected and analyzed all available data on historical interventions in the various rivers, starting from the time that the first tidal data are available.
16. The convergence length L_b of the river has been established by plotting the width of the flow-carrying cross-section against length. In some cases, L_b showed a profound kink mid-river, in which case we apply two different values of L_b. Apart for the Elbe and Loire, L_b remained more or less constant over the period over which tidal data are available.
17. When available, the width of the intertidal area was established. If not, an estimate was made on the basis of Google-Earth images – note that in those cases Δb is quite small, and does not contribute too much to the tidal dynamics, hence errors in these are not too important.
18. Water depths were provided in various formats, such as the depth of the river's thalweg. Ideally, the hydraulic radius is to be used, but the mean depth $h = A_c/b_c$ is a good approximation in shallow rivers, which has been used throughout the study.
19. Water depths are generally given with respect to some reference level. The mean water depth had therefore to be corrected for the tidal range, assuming the mean slope is not too large. As a rule of the thumb, we presume that the mean water level is found midway high and low water.
20. The river is subdivided into subsections in between the tidal stations. For each subsection, a characteristic water depth and convergence length are determined.
21. The imaginary wave number k_i is determined from the data for each subsection by dividing the measured tidal ranges of two adjacent tidal stations being Δx apart: $\left(a_2 / a_1 = \exp\left\{ k_i \Delta x \right\} \right)$.
22. When times of bathymetrical and tidal data do not synchronize, either of the two have been interpolated, obtaining a consistent set of synchronous data.
23. Imaginary wave number and bathymetrical data were made dimensionless, obtaining κ_i and Λ_e, as discussed in Part I of this paper.
24. These data points are plotted in a κ_i – Λ_e diagram; every pair of these parameters represents the measured bathymetry and tidal amplification/damping of one subsection of the river for one particular time period. Then, the analytical solution (equ. 10b of Part I) was fitted through these data points by tuning the friction parameter r_*. Note that we assume infinitely long rivers, and do not account for possible reflections against a weir, or otherwise, unless stated otherwise.
25. For some rivers, we studied the effects of tidal reflections in a schematic way; a more thorough approach requires a different model.
26. Step 10 yields the time evolution of r_*, e.g. the change in effective hydraulic drag over time. From r_*, the Chézy coefficient is established, for which the flow velocity is needed. For this, we use the analytical solution given by equ. (12) in Part I.
27. Finally, we determine the tidal asymmetry. In most cases, data on asymmetry are given, and we do not need to use the proxy γ, defined in Part I.
28. For the Elbe and Scheldt rivers, an indicative assessment of the contributions of tidal reflections to the tidal amplifications is made.

This procedure is applied in the chapters 2 through 5 for the Elbe, Ems, Loire and Scheldt Rivers, respectively. The results of these analyses are compared in Chapter 6, where the results are also interpreted with respect to the conceptual picture proposed in Part I.

2. THE ELBE RIVER - GERMANY

The Elbe River originates in the Karkonosze mountains of the Czech Republic and flows through Germany over 630 km passing the city of Hamburg (km 620; largest German seaport) at about 110 km from the mouth at Cuxhaven (km 729, North Sea). At km 588 (Geesthacht), i.e. 32 km up-estuary of Hamburg, a weir was built in 1960. The river downstream of Geesthacht is known as the Tideelbe, and the stretch down-estuary of Hamburg is subject of the study in this section. The mean annual fresh water discharge ranges between 200 to 3600 m^3/s, with a mean value of about 700 m^3/s. The mouth of the estuary is characterized by a narrow deep channel and a very wide tidal flat (Hakensand, Medem Sand, Nordergründe) up to 2 m above LAT (lowest astronomical tide), see also Admiralty Chart No. 3261. The total width of the mouth is about 15 km. The width of the deep channel is in the range of 1500 to 3000 m. The cross-sectional area below LAT of the deep channel at the mouth is in the range of about 20,000 to 40,000 m^2. In this chapter we study the evolution of the Elbe River between km 620 (Hamburg) and km 718 (10 km up-estuary of Cuxhaven), i.e. a river stretch of 98 km; the river widens rapidly down-estuary of km 718.

The following design depths for navigation were implemented (Kappenberg and Fanger, 2007):

- 1936–1950: 10 m (note that these engineering works commenced already at the turn of 19-20th century,
- 1957–1962 11 m
- 1964–1969: 12 m
- 1975–1978: 13.5 m
- 1998–2000: 14.4 m

Note that we do not have data before 1940, though the Portal Tideelbe (e.g. “Veränderungen am Fluss”) states that in 1859 the fairway was deepened to -5.9 m, whereas form 1910 a depth of 8 – 10 m has been maintained. As discussed in the Introduction, this does not mean that the mean depth of the Elbe has increased by 4.4 m since 1936, as the fairway does not cover the entire river’s cross-section, e.g. Fig. 1. Also, since the 1930s some intertidal area was lost as well by embankments and reclamations works, and some tributaries were closed by a sluice or weir. Major reclamations and embankments works were carried mainly in the lower part of the Elbe River in response to the 1962 and 1976 floods. Note that as a result of the fairway deepening, the river bed depicts a step of about 14 m around Hamburg (Kappenberg and Fanger, 2007).

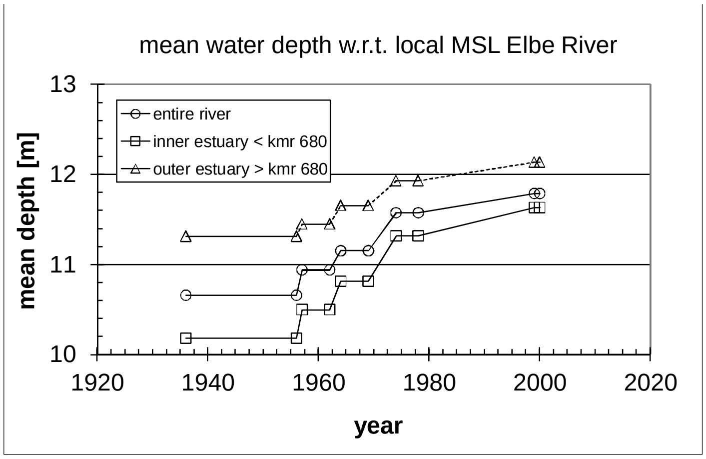

Fig. 1: Variation in mean water depth in inner estuary (km 620 – 680) and outer estuary (km 680 – 718).

Longitudinal bathymetrical data over the period 1995 – 2010 presented by the Portal Tideelbe (1999) show that the riverbed is characterized by bed forms which can be fairly steep with lengths of the order of 100 m, and heights varying from a few dm to about 2 m. However, the data do not clearly depict a substantial change over time in the character of these bed forms. Hence, we may expect not too much change in effective hydraulic drag by reducing bed from heights.

Fig. 2 presents the evolution of the tidal range along the Elbe River, as presented by Weilbeer and Klöpper (2011), based on historical data at 16 stations. Fig. 2 shows that initially, i.e. in the beginning of the century, the tide was damped over the entire estuary. However, after the 1970s, a considerable amplification of the tide up-estuary of km ~680 (between Glückstadt and Freiburg) is observed. Only up-estuary of Hamburg the tide is damped again. This irregular behavior is likely to be attributed to a kink in the convergence of the river around km 680. In the outer estuary, i.e. down-estuary of km 680, a convergence length of 93 km is found, whereas in the inner estuary, L_b = 30 km is found. It is postulated that this fairly uncommon distribution is the result of human interventions, e.g. embanking and reclamation, in particular following the 1962 and 1976 floods. There are indications that the convergence of the inner river was increased in the course of the 1970s (L_b from 40 km to 30 km), though the data are not too accurate. Fig. 2 suggests that the tide penetrates the river up to the weir at Geesthacht since the 1970s.

In the following, we distinguish between the inner and outer estuary, with a transition around km 680. Because of a lack of sufficiently detailed data, we treat the outer and inner estuary as two different, but homogeneous parts of the river. Then, based on the data of Fig. 2, the variation in the imaginary wave number k_i can be assessed for the two river sections.

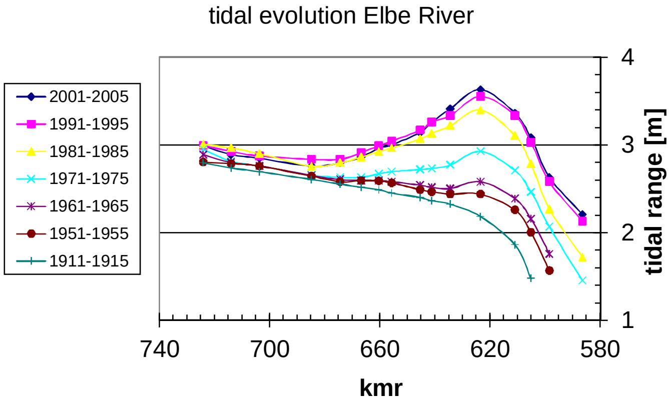

Fig. 2: Evolution of tidal range in the Elbe River (after BAW, 2012); Hamburg is around kmr 620.

Next, tidal and bathymetrical data are made dimensionless, using the definitions of equ. (9) of Part I, and the friction coefficient r_* has been tuned to match the linear analytical model with the observations, assuming an infinitely long river. The results are presented in Fig. 3, showing a profound difference in the behaviour of the outer and inner estuary. Amplification in the outer estuary has not changed too much over time (see also Fig. 2), and the dimensionless friction coefficient r_* does not vary too much. On the contrary, r_* varies largely in the inner estuary, reducing from about 2.6 to 0.9.

The Chézy coefficients established from the various r_* values of Fig. 3 are presented in Fig. 4. The values in the outer estuary are high, and more or less constant over time. On the other hand, in the inner estuary, C is found to increase largely up to values of about 70 $m^{1/2}/s$. As this increase cannot be attributed to a reduction in bed forms, this large increase in C should be attributed to other effects.

The high Chézy-values in the outer estuary are in agreement with the high SPM-values in this part of the river, and the very muddy intertidal areas (e.g. Kappenberg and Fanger, 2007). Weilbeer and Klöpper (2011) needed similar smooth roughness values in a three-dimensional hydrodynamic model to simulate the tidal propagation properly.

However, SPM concentrations are consistently low in the inner estuary, hardly exceeding 50 mg/l (e.g. Kappenberg and Fanger, 2007), suggesting rough bed conditions. These low values are (partly) to be attributed to the sediment management in the river around Hamburg, where large amounts of fines are removed from the system, keeping the harbour basins accessible. Indeed, in this part of the river, Weilbeer and Klöpper (2011) needed larger roughness values to simulate the tidal propagation properly, though they had difficulty in properly simulating tidal amplification and phase with uniform roughness values. So why does the analytical linear model predict such large increases in *C*–values in the inner estuary, while assuming an infinitely long estuary?

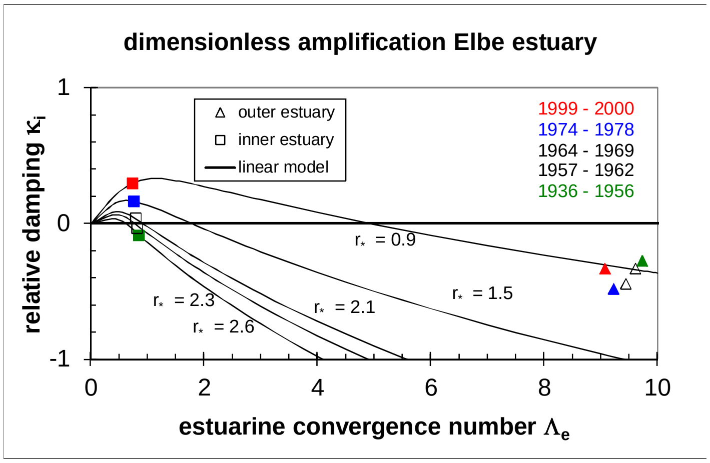

Fig. 3: Dimensionless imaginary wave number κ_i as a function of the estuarine convergence number Λ_e, and fitted solution of the analytical model (infinitely long river) by tuning r_*.

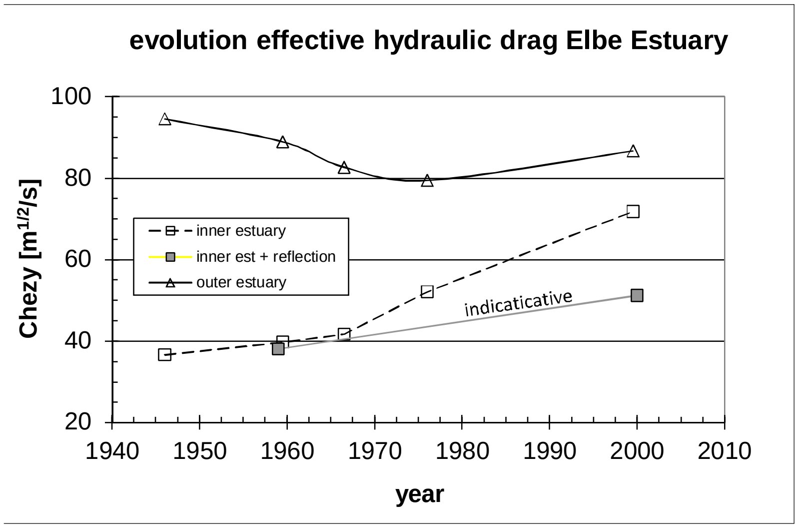

Fig. 4: Evolution of Chézy coefficient with time, based on the r_*-values established from Fig. 3; also indicative results are presented accounting for tidal reflections in the river.

The answer may be found in the large discontinuity in bed level in the Elbe, with a step of about 14 m at km 620 (Kappenberg and Fanger, 2007). This discontinuity is likely to induce reflections, increasing the tidal range, an effect not accounted for in the analysis of Fig. 4. Therefore, a zero-order assessment of this step in bed level was made by assuming full reflection at km 620 (Hamburg). Furthermore, the analysis of the data suggests that in the course of the 1970s, the convergence of the inner estuary has been increased by river works. Therefore, we present results for L_b = 30 km and 40 km, using the mean depths of Fig. 1, e.g. Fig. 5.

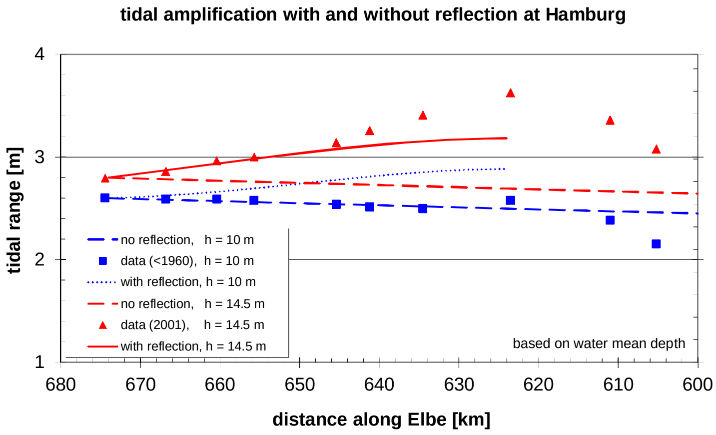

Fig. 5: Computation of tidal amplitude for pre-1970 conditions (L_b = 40 km, r = 0.004 m/s – broken line) and post-1970 conditions (L_b = 30 km, r = 0.003 – full line).

The pre-1960 data could only be reproduced assuming an infinitely long river, and a fairly rough bed (r = 0.004). The results in Fig. 5 suggest that tidal reflections around kmr 620 did not play a role then. The 2000-data could be reproduced, assuming a very smooth bed, as shown in Fig. 4. However, if we presume “sandy” conditions, i.e. r-values not too low, we need to account for reflections of the tide at kmr 620, as shown in Fig. 5.

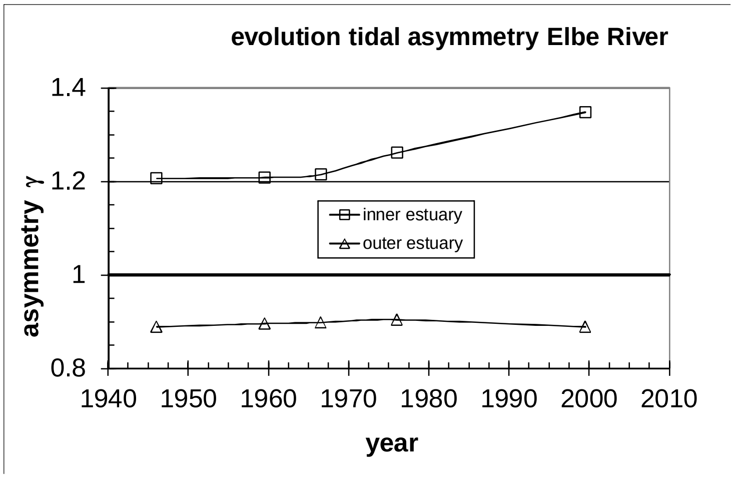

Fig. 6: Evolution of tidal asymmetry, based on the γ-proxy defined in Part I.

From these observations we anticipate that the increase in effective bed roughness in the upper estuary (Fig. 4) is probably largely overestimated, as part of the amplification should be attributed to reflections. However, it is not likely that full reflection takes place at Hamburg. The increase of Chézy from 38 to 51 $m^{1/2}/s$ can only partly (e.g. for 2 – 5 $m^{1/2}/s$) be explained by the deepening itself. Hence, the indicative increase in C of Fig. 4 must be attributed to either a too large simplification of the tidal conditions in the

Elbe River, or to decreases in effective hydraulic drag be a reduction in bed forms (e.g. steepness) and/or a small increase in SPM-values. A further elaboration of this hypothesis requires detailed numerical modeling, accounting for the actual changes in bathymetry at great detail.

Finally, we have computed the proxy γ for the tidal asymmetry (Part I, equ. 19). Fig. 6 shows that the outer estuary seems ebb-dominant, whereas the inner estuary seems to be flood-dominant. This disjunctive behaviour is to be attributed to the considerable intertidal area, still present in the outer estuary. This behaviour is corroborated by BAW (2012) showing that near Hamburg the ratio rising to falling tide amounts to about 3:4, hence profoundly flood-dominant conditions. Apparently, the river flow is (still) so large that large quantities of fine sediment cannot accumulate in the water column up-estuary of the salinity front. In other words, a secondary turbidity maximum (ETM2, e.g. Part I) cannot be formed (e.g. Weilbeer and Klöpper, 2011). This role of the river flow is corroborated by the observations that maintenance dredging requirements in the Port of Hamburg increase with decreasing river flow (Kappenberg and Fanger, 2007).

3. THE EMS RIVER – GERMANY

The Ems River (Unterems) is about 53 km long from the weir at Herbrum to Emden, flowing through Germany. Emden is located more or less at the border between Germany and The Netherlands, but more important, almost at the mouth of the river, where it flows into the wide and shallow Ems-Dollard estuary. This river is renowned for its large suspended sediment concentrations, with values up to 30 – 40 g/l over most of the upper part of the river (e.g. Talke et al., 2009). Though detailed data do not exist, it is believed that the regime shift of this river was set in motion in the early 1990s (De Jonge et al., 2000). These high concentrations are found well beyond the region of salinity intrusion, and move to and fro with the tide. These conditions are characteristic for the secondary estuarine turbidity maximum (ETM2) discussed in Part I of this study. Also profound layers of fluid mud are found, in particular around slack water and neap tide (e.g. Schrottke and Bartholomä, 2008). Currently, the total mass of suspended solids amounts to about 1 Mton, while yearly about 1.5 Mton of solids is removed from the Ems River by dredging. For further details on the river, the reader is referred to Krebs and Weilbeer (2005).

The data of four tidal stations are analyzed in this paper, e.g. Emden (km 53), Leerort (km 28), Papenburg (km 13) and Herbrum (km 0). The Ems River is engineered mainly to serve the Jos L. Meyer Wharfs in Papenburg, i.e. in case cruise ships are to be sailed down-estuary, the Ems River is dredged.

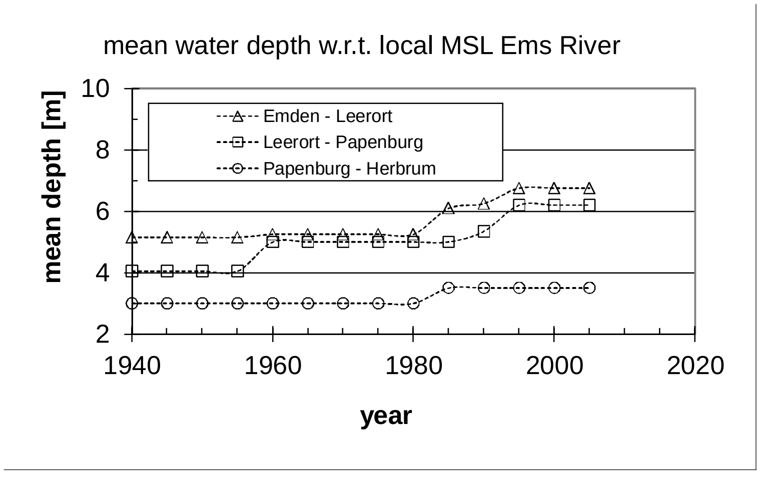

Fig. 7: Evolution of mean design water depths in Ems River for three trajectories (water depth with respect

to mean sea level at Emden).

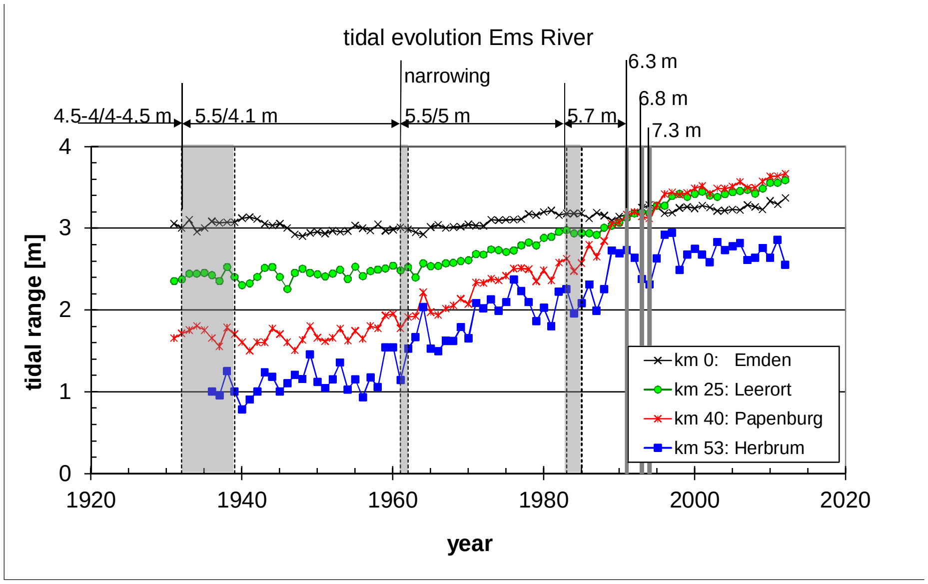

Fig. 8: Evolution of measured mean tidal range in Ems River and summary of interventions – 5.5/4.1 m indicates a design depth of 5.5. m over the Emden-Leerort reach, and 4.5 m over the Leerort-Papenburg reach; design depth Papenburg-Herbum reach was 3 m till 1980, and then 3.5 m (data collected by Vroom et al., 2012).

The Ems River is characterized by a profound tapering. The overall convergence length of the river amounts to about 19 km, whereas for the stretches between Emden – Leerort $L_b \approx 32$ km, Leerort – Papenburg $L_b \approx 27$ km, and Papenburg – Herbrum $L_b \approx 33$ km. In the following, we refer to these three sections as E-L, L-P and P-H. The apparent discrepancy of the overall convergence length and those of three smaller stretches of the river is attributed to some jig-saw patterns in the river's plan form. In our analysis, we used the larger values per sub-section.

An overview of the various interventions in the river was summarized in Vroom et al. (2012), based on information from Rijkswaterstaat and the Bundesanstalt fur Wasserbau (BAW). The evolution in mean water depths for the three stretches E-L, L-P and P-H is presented in Fig. 7, where the target depths have been averaged to obtain mean values for these sections. The river bed is dredged to these design depths only when a big cruise ship has to be conveyed down-river from the Meyer Wharfs – on average this is done once a year.

Around 1961, in the upper part of the river (P-H), groins have been constructed, narrowing the river locally, but no reclamation of intertidal area took place anymore after 1940. At present, the area of intertidal area is virtually zero, and the small areas remaining after embanking of the river have silted up considerably. In our analysis we assume an intertidal area of 10%, which is so small that it does not notably affect the tidal characteristics in the river. There are no indications that the convergence length of the river has changed much over the period of our analyses.

The response of the tidal range to these interventions is presented in Fig. 8, in conjunction with an overview of the human interventions (Vroom et al., 2012)). Fig. 8 suggests that the response of the tidal range to the various interventions is not instantaneous, but takes considerable time to attain equilibrium – Fig. 7 suggests a time scale of at least 1 – 2 decades. We will address this further below. Finally, it is noted that the tidal range at Herbrum (and to a lesser extend Papenburg) becomes highly irregular, which is to be attributed to yearly variations in river flow. In a next phase of the study, we will address the role of river flow further.

From Fig. 8, the imaginary wave number κ_i (amplification factor) was determined. For the trajectory Papenburg-Herbrum, the highly irregular behavior hampers a proper analysis, and we therefore ignore the behavior of the tide along this trajectory. Moreover, this reach must be affected by reflections against Herbrum weir (see below). It is noted that for both reaches, E-L and L-P, the data show that amplification of the tide is observed from 1995 on – before the tidal wave was still damped, though only slightly (see also Fig. 9).

Next, the imaginary wave number is made dimensionless with the convergence length L_b and plotted against the estuarine convergence number Λ_e in Fig. 9. Then the linear solution (equ. 10b, Part I) is fitted through the data by tuning the roughness parameter r_*. Again, we assume an infinitely long estuary, or in other words, we assume that the effects of reflection against the weir at Herbrum down-estuary of Papenburg are small.

Fig. 9 shows a profound evolution in tidal characteristics, time runs diagonally from bottom-right to top-left. It is remarkable that for instance in the period 1960 – 1980 the damping over the reach Leerort-Papenburg decreased considerably, though Λ_e did not change. This is most likely due to slow (morphological) responses of the river to the engineering works, carried out earlier.

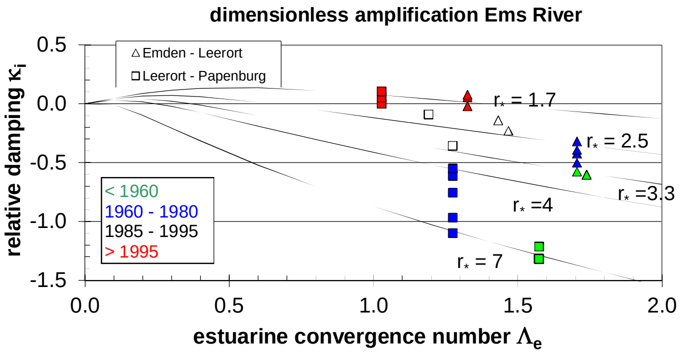

Fig.9: Fits of linear solution to observed data through tuning of roughness parameter in $\kappa_i - \Lambda_e$ diagram.

For a more physical interpretation, the roughness parameter r_* has to be converted to the Chézy coefficient C. For this conversion we use the computed amplitude of the flow velocity (equ. 12, Part I) in conjunction with measured tidal amplitudes.

Fig. 10 suggests that up to the 1960s the Ems River was quite rough, with Chézy values in the E-L reach of about 60 $m^{1/2}/s$, which is typical for a sandy river bed. Further upstream, in the L-P reach, Chézy values as low as 40 $m^{1/2}/s$ are found. We are not certain that these low values are entirely correct, but if so, they may be indicative for steep bed forms (dunes), such as observed for instance in the Elbe and Weser Rivers (e.g. Van Rijn, 1993). The gradual increase in Chézy coefficient between the 1960s and 1980s may than be attributed to a gradual increase in water depth in (morphodynamic) response to earlier engineering works, and/or a decrease in dune heights and steepness owing to ongoing dredging. However, from the 1990's onward, the Ems River became more and more infamous for its very high suspended sediment concentrations with hyper-concentrated values towards the end of the 20th century. Today, suspended sediment concentrations measure several 10 g/l, e.g. Talke et al. (2009). The very large values of C = 80 – 90 $m^{1/2}/s$ can only be explained from the profound buoyancy-induced damping by the large suspended sediment concentrations (e.g. Part I).

As we have ignored the effects of tidal reflections against the weir at Herbrum we expect that the Chézy values, in particular for the trajectory Leerort-Papenburg are a bit over-estimated, and should be lower by a value of about 5 – 10 $m^{1/2}/s$. In particular, we have argued in Part I that the effect of tidal reflections becomes apparent over a larger stretch of the river, owing to an increase in roughness length with reducing hydraulic drag.

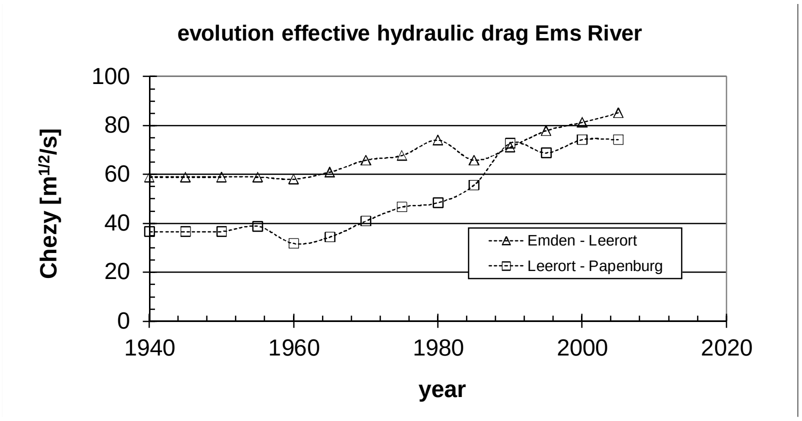

Fig. 10: Evolution of effective hydraulic drag (Chézy coefficient) with time.

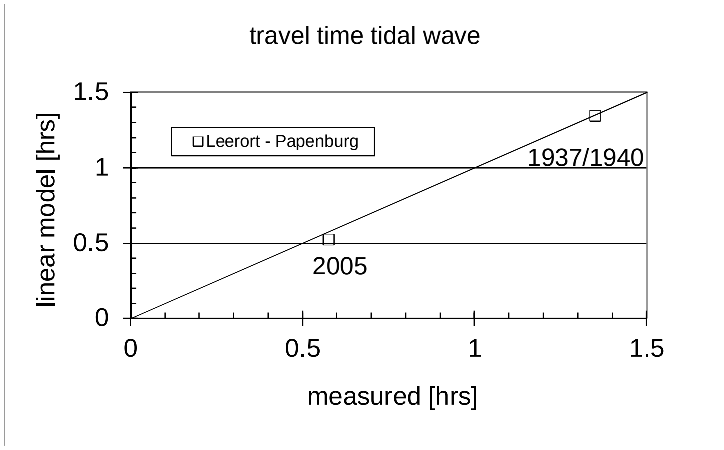

Fig. 11: Measured and computed travel time tidal wave along Ems River in 1940 and 2005 – "measured" data follow from a detailed analysis of the tidal evolution with a three-dimensional numerical model Herrling and Niemeyer (2008).

Next the evolution in celerity along the Ems River is elaborated. We use the results of an analysis by Herrling and Niemeyer (2008) on the tidal propagation (travel time) between Leerort and Papaneburg in the late 1930s and 2006. Using the estuarine convergence number Λ_e, and the roughness parameter r_* obtained from calibration of the linear model against the observed evolution in tidal range, the celerity computed with the linear model (equ. 14a, Part I) can be compared to the numerical results by Herrling and Niemeyer (2008). Fig. 11 shows that the linear model predicts the evolution in travel time very well, though only two points in time are available, of course.

Finally, the asymmetry parameter γ (e.g. equ. 20, Part I) is determined, using the measured values of water depth and tidal amplitude. The results are presented in Fig. 12, showing that over the entire data range, $\gamma >$ 1, i.e. flood dominant conditions prevail, as anticipated in Part I for rivers with little or no intertidal area.

The tidal asymmetry remains almost constant for the E-L trajectory of the river, but γ for the L-P trajectory grows continuously after the deepening of the 1960s, exceeding the asymmetry in the E-L range beyond the 1980s. Also the data suggest a profound flood dominance of the tide, though no information is available on the historic development (Vroom et al., 2012).

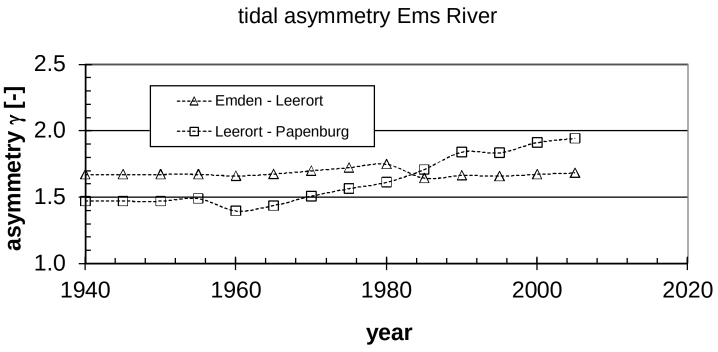

Fig. 12 : Evolution of tidal asymmetry parameter with time.

4. THE LOIRE RIVER – FRANCE

The Loire estuary from St Nazaire to Nantes measures about 53 km. In this paper, we study the development of the tide in the Loire river from Paimboeuf (at km 14), which is located at the transition between the inner and outer estuary, where the estuary converges strongly. Hence, we study a stretch of about 40 km. Mean fresh water flow rates range from 400 – 700 m^3/s, with maxima up to 5000 m^3/s. The data discussed below have been collected in a study by Deltares commissioned by GIP (Briere et al., 2012), summarizing reports by Sogreah (2006), in particular Sogreah's report on the historical development of the Loire River.

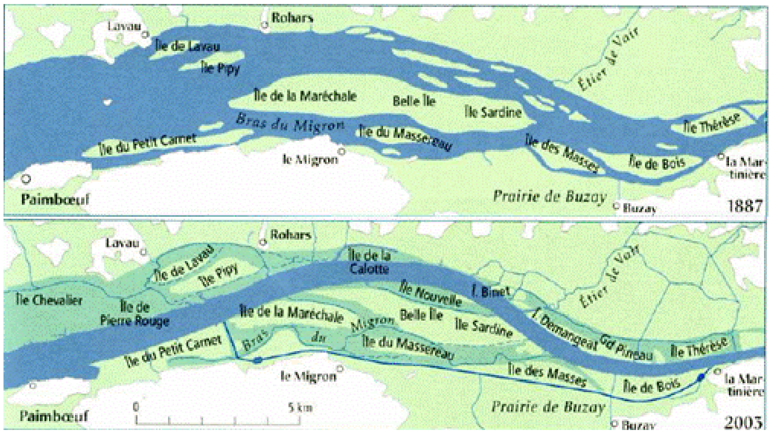

Fig. 13: Canalization of the Loire River in 1903 – 1910.

In the early decades of the 20th century, the Loire River was heavily modified. Fig. 13 shows the canalization of the river up to La Martinière (km 37), realized in the first decade. This canalization took place up to Nantes (km 53), but unfortunately, no maps are available for the section La Martinière-Nantes. The effect on the river's convergence (e.g. L_b) has not been so large; it is estimated that L_b decreased from about 25 – 30 km in the beginning of the 20th century to about 21 km today. However, the intertidal area has decreased considerably from b_* = 2 to about 1.1 at present. Note that between km 32 and 36, the river is very narrow, owing to an array of massive groins in the river's bend.

A decade later, e.g. 1910 – 1920 the so-called Bassin Marée was formed by large-scale extractions of sand from the river upstream of Nantes. We were not able to find detailed data on these withdrawals, but bathymetrical data suggests that the river bed was affected and lowered well beyond Nantes. Up to Nantes, the river is deepened by almost 5 m. However, also many tens km's up-estuary, the river deepened by many meters. It is likely, that this deepening was only partly the direct result of dredging and sand extraction, and that also morphological responses to the large changes in river's plan form contributed to the deepening. For our analysis, though, the actual causes of the bed level changes are not relevant.

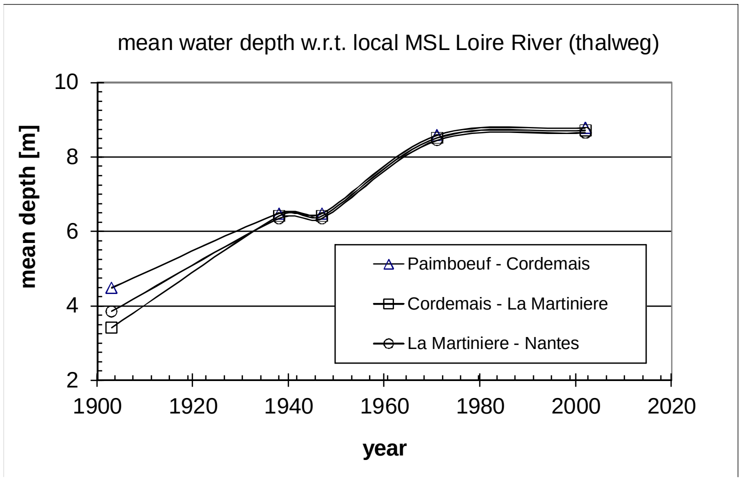

Fig. 14: Evolution of water depth (thalweg) with respect to local mean water level (data convergence: chart datum CM96 is 3.6 m below MSL at St Nazaire).

The evolution in water depth is presented in Fig. 14, showing a profound deepening in the early 20th century, and then again in the 1960's (Sogreah, 2006). As discussed above, the early/mid 1900 deepening may have been the by-product of the significant narrowing of the river in the first decade of the 20th century (Fig. 13) and the subsequent formation of the Bassin Marée, increasing the river's tidal prism. However, we have no further data on these interventions and their implications.

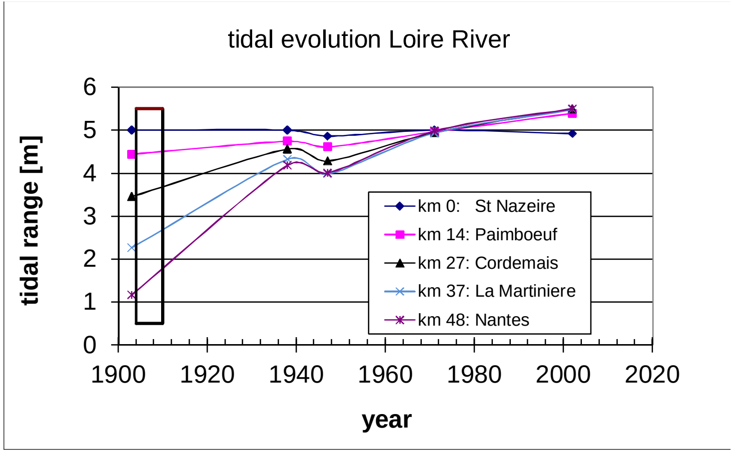

Fig.15: Evolution of the tidal amplitude along the Loire River; the black box represents the period of river narrowing (e.g. Fig. 13). The irregular behavior around 1940 is likely caused by inaccurate data.

The data received concern values of the thalweg with respect to local chart datum CM96, which is about 3.6 m below mean sea level at the mouth of the estuary (St Nazaire). It is estimated that MSL is about 0.3 m higher at Nantes, and the subsequent slope in MSL along the river has been accounted for in Fig. 14. From an analysis of the data of the present bathymetry, it is estimated that the thalweg lies about 1 – 2 m below the mean water depth (cross-section divided by river width), e.g. Deltares (2011). In the following, we assume that the depth of Fig. 14 should be raised by 1 m for the years 1900 – 1947, and with 2 m for the years thereafter – this has been accounted for in the analyses below.

Note that the data of Fig. 14 are neither very accurate, nor complete, so the analysis in this section cannot be too accurate, in particular the developments later in the 20th century – more detailed data have been requested.

The measured evolution in tidal amplitude is presented in Fig. 15, showing huge amplifications of the tide in the first half of the 20th century. Though at a smaller rate, the tidal amplitude continues to increase after the 1950s; at Nantes for instance by 0.7 m. In the following we focus on the inner river (e.g. up-estuary of Paimboeuf) and subdivide the river further to the four tidal stations along the river (Paimboeuf – Cordemais; Cordemais – La Martiniere; La Martiniere – Nantes, e.g. stretches of 13, 10 and 11 km respectively).

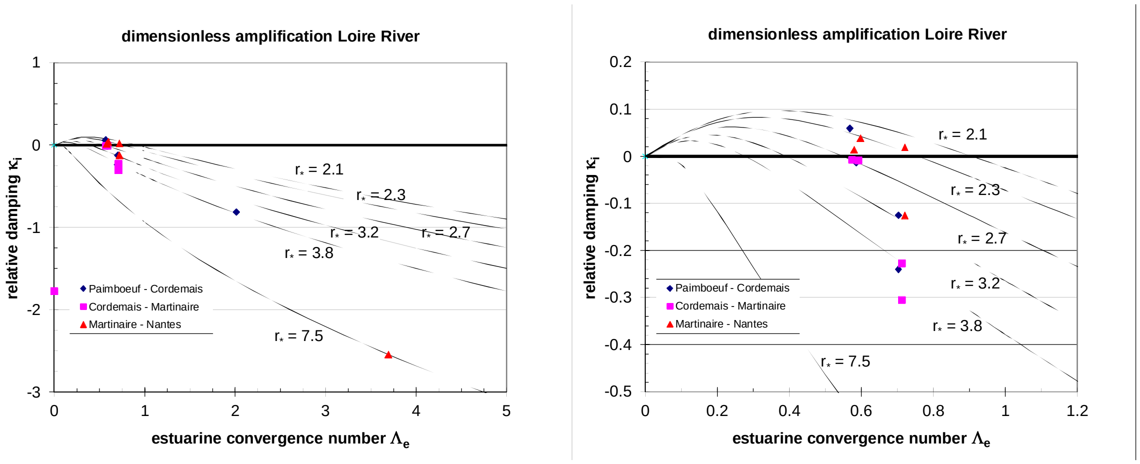

Fig. 16: Tidal amplification as function of estuarine convergence number – Fig. 16a (left panel) contains all data, whereas Fig. 16b (right panel) contains data after 1930 only.

The evolution of the dimensionless imaginary wave number κ_i is established as a function of Λ_e, the results of which are shown in Fig. 16. Huge changes occurred in the early 20th century, no doubt because of the canalization of the river in that period. From 1940 onwards, $\kappa_i \approx 0$, i.e. the tide is no longer damped in the Loire River. Note that the trend is very strong and consistent in the early 20th century, but thereafter becomes a bit erratic. We believe that this is due to inaccuracies in the data, both in the bathymetrical information, and in the tidal data.

Next, the linear model for an infinitely long tidal river (equ. 10b, Part I) is fitted to the measured tidal damping by tuning the effective dimensionless roughness coefficient r_* to the data, e.g. Fig. 16.

From the fitted r_*-values, the effective Chézy coefficient can be obtained, using the observed (corrected) water depths and computed flow velocities (e.g. equ. 12, Part I).

Fig. 17 shows the variation in Chézy coefficient throughout the 20th century for the three river sections in the Loire. The Chézy coefficient in the first part of the estuary (Paimboeuf – Cordemais) has basically remained constant over time at a value between 60 and 70 m$^{1/2}$/s. However, in the upper two sections, the Chézy coefficient has increased from around 30 – 40 m$^{1/2}$/s up to 60 – 70 m$^{1/2}$/s. The major changes took place in the period before 1940, when the estuary was considerably narrowed, and the tidal prism increased by the creation of the Bassin Marée. Note that the higher values are not very high, in particular not for a very muddy system as the Loire – fluid mud is general observed between Cordemais and Nantes (Sogreah, 2007). However, the increase in C is consistent with the results for the Ems River, and with our estimates in Part I, Section 2 of that paper.

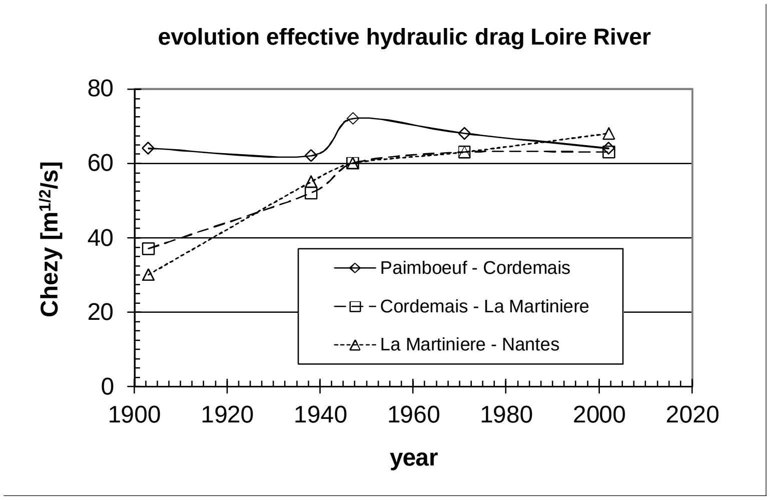

Fig. 17: Evolution of effective hydraulic drag Loire estuary – note that because of low accuracy of the tidal data, the error in this graph is relatively large.

Because of inaccuracies in the available tidal data it is not possible to obtain proper trends in the γ-parameter (proxy for tidal asymmetry) with the analytical model. However, all information reveals that the tide in the Loire has become highly asymmetrical. Whereas the tide at the mouth of the Loire River (observations at Donge, e.g. Sogreah, 2006) is almost symmetrical, near Nantes the tide rises in about 4 hours, and whereas falling tide is about 50% longer. These observations are corroborated by numerical simulations by Sogreah (2006).

Note that the asymmetry in flow velocity is largely affected by the fresh water river flow, which may be large. Hence, the effects of tidal asymmetry (both in peak velocity and internal mixing) may be overruled by the effects of the river flow, inducing ebb dominance, flushing mud from the system. Indeed, Sogreah (2006) reports full flushing of the turbid water (or fluid mud) from the river at prolonged (>12 days) high river flows, e.g. around 2000 m^3/s, conditions which may, however, not occur every year. According to anecdotal information, it takes a few weeks only after such flushing conditions to re-establish hyper-turbid conditions.

5. THE SCHELDT RIVER – BELGIUM

The Scheldt estuary is located in Belgium and The Netherlands, and measures almost 200 km, from its mouth along the North Sea to the weirs/sluices in Ghent. In Belgium, the river is known as the Lower and Upper Sea Scheldt; the Upper Sea Scheldt is fresh. The head of salinity intrusion migrates in the Lower Sea Scheldt with the tide and river flow. Large port developments took place along the Lower Sea Scheldt (Port of Antwerp). The fresh water flow varies between 30 and 300 m^3/s, with a long-term mean of about 120 m^3/s.

Because these large port developments hamper the use of the simple linear analytical model developed in Part I, the focus of this section is on the Upper Sea Scheldt from Schelle (kmr 91.2 from Flushing) to Melle (kmr 150.8 from Flushing). The weir in Ghent lies about 8 km up-estuary of Melle.

Van Braeckel et al. (2006) summarize modifications in the Scheldt estuary. The majority of the engineering works in the Upper Sea Scheldt took place before 1900, e.g. rectifications of the river and embanking intertidal areas. In the early 1900s (1900 – 1930) parts of the river were normalized, and later rectifications took place in the Durme. In the 1970s, the river deepened by 1.5 – 2 m, e.g. Fig. 18, though no major engineering works were carried out in this river section. Probably, this deepening was largely induced by the morphodynamic response to engineering works further down-estuary, such as sand-mining and deepening and widening of the navigation channel in the Western-Scheldt and Lower Sea Scheldt. Also deepening and widening of the navigation channel in the Scheldt estuary down-estuary of Antwerp in the second half of the 20th century, and early 21th century must have had an effect on the tidal evolution, as discussed below (see also Kuijper and Lescinski, 2012).

The evolution of the water depth in the Upper Sea Scheldt is further elaborated in Fig. 18 showing the water depth with respect to local mean water level, based on data from IMDC (2012). The water depth in Fig. 18 is obtained from dividing the flow-carrying cross-sectional area by the width of the river, and then averaging over the river sections in between the tidal stations.

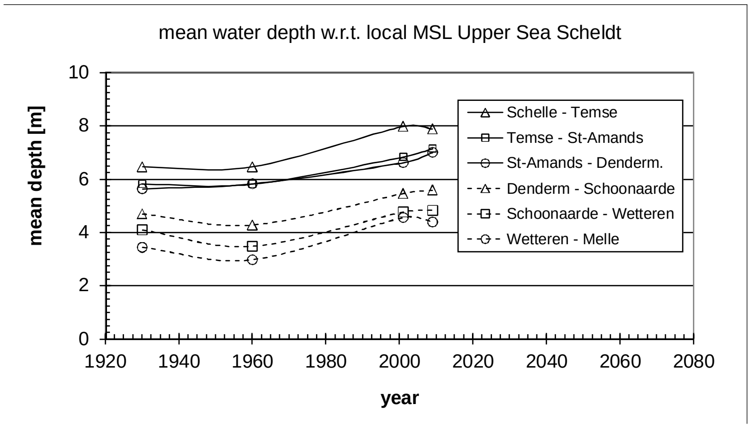

Fig. 18: Evolution of mean water depth between the various tidal stations along the Upper Sea Scheldt.

At the head of the estuary, around Ghent, a number of engineering works were carried out between 1950 and 1970. These works consisted of the creation of a new channel of about 4 km length with a shipping lock for access to Ghent. Between around 1960 – 1970, the Upper Sea Scheldt became deeper, and the old northern arm of the Upper Sea Scheldt has silted up largely. This old Scheldt branch measured about 8.4 km from Melle tidal station to the weir in Ghent, whereas the new branch measures about 7.2 km.

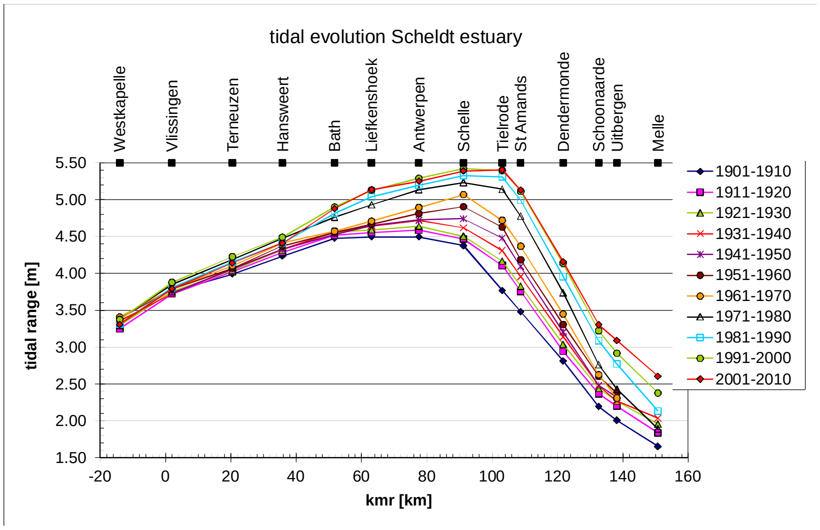

Fig. 19: Evolution of tidal range in Scheldt estuary, corrected for 18.6 year cycle.

The convergence length of the Upper Sea Scheldt depicts a kink around km 124, i.e. between Dendermonde and Schoonaarde. In the lower 32 km of the Upper Sea Scheldt, L_b measures about 24 km, and in the upper 28 km about $L_b = 36$ km, with some variations over time. Note that the river rectifications in the late 19th century must have reduced this convergence length by about 5 km.

The width of the intertidal area shows a continuous decrease since 1850, in particular between 1850 and 1930 in the upper reaches of the river. Today, b_* is small, measuring about 1.1, and has been small over most of the time of our analysis.

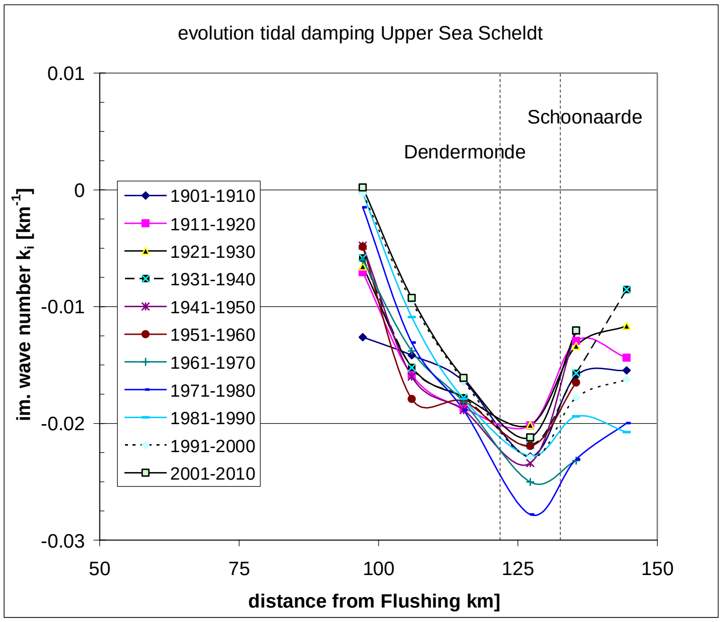

Fig. 20: Evolution of imaginary wave number along Upper Sea Scheldt, based on the data of Fig. 19.

Tidal data for the entire Scheldt estuary are available from before 1900. Kuijper (2012) corrected these data for the 18.6 year cycle, the results of which are shown in Fig. 19. In the following, we focus on the Upper

Sea Scheldt, i.e. up-estuary from Schelle. For an analysis of the time evolution of the entire estuary, the reader is referred to Kuijper (2012, Western Scheldt) and Plancke (2012, for Sea Scheldt).

Fig. 20 presents the imaginary wave number k_i as derived from the measured tidal data of Fig. 19, showing a number of important trends:

- From Schelle to halfway Dendermonde-Schoonaarde, the damping of the tidal wave increases (k_i more negative), and beyond ~km 125, the damping decreases again.
- In general, the damping along most part of the river has decreased over time.
- Close to Schelle, the tidal wave is no longer damped in the early 21th century.

The change in longitudinal trend of the imaginary wave number beyond Dendermonde/Schoonaarde in Fig. 20 is remarkable, and we suspect that this trend is due to reflections of the tidal wave against the weirs around Ghent. To explore this further, we have computed the tidal amplitude along the river beyond Sint Amands without and with a weir 8 km up-estuary of Melle. We have assumed a constant convergence length and a mean depth of 4.5 m. The results are presented in Fig. 21 in the form of the difference in imaginary wave number Δk_i between the configuration with and without weir. Figure 21 shows a difference of about 0.005 km^{-1}, suggesting that the reverse in trend of Fig. 20 can indeed be explained by tidal reflections although the computed increase is about a factor two too small. Note that these results are not sensitive to the convergence length L_b, but highly sensitive to the water depth – the latter varies considerably over the last part of the river, whereas no information is available on the sections up-estuary of Melle. The results of Fig. 21 are therefore only indicative of the effect of tidal reflections on the tidal evolution.

Next, the imaginary wave numbers of Fig. 20 are made dimensionless with the convergence length of the Upper Sea Scheldt (e.g. equ. 9, Part I), where data up-estuary of Schoonaarde are omitted, as these are affected too much by tidal reflection. The dimensionless damping is plotted against the estuarine convergence number Λ_e in Fig. 22, showing the same trend in time, as for the other rivers, i.e. time runs diagonally from the right-lower corner to the left-upper corner. Data from before the large deepening in the Upper Sea Scheldt (<1960), data beyond 1990 and data in between have been marked with different colors. In particular, the data for the trajectory Dendermonde – Schoonaarde are a bit erratic (results not shown), most likely because of the effects of tidal reflection, and therefore not further included in our analysis.

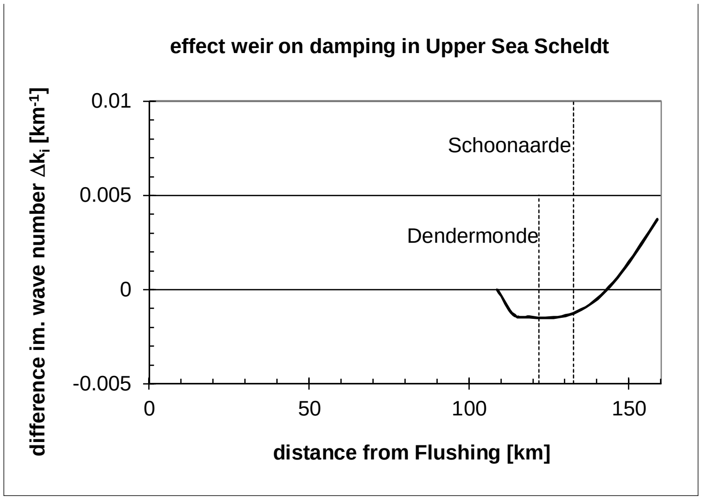

Fig. 21: Estimate of effect of weir on tidal damping in upper reaches of Upper Sea Scheldt.

Next, the linear model for an infinitely long tidal river (equ. 10b, Part I) is fitted through the data by tuning the roughness parameter r_*, the results of which are also presented in Fig. 22, showing reduction in r_* from 9 to about 3.

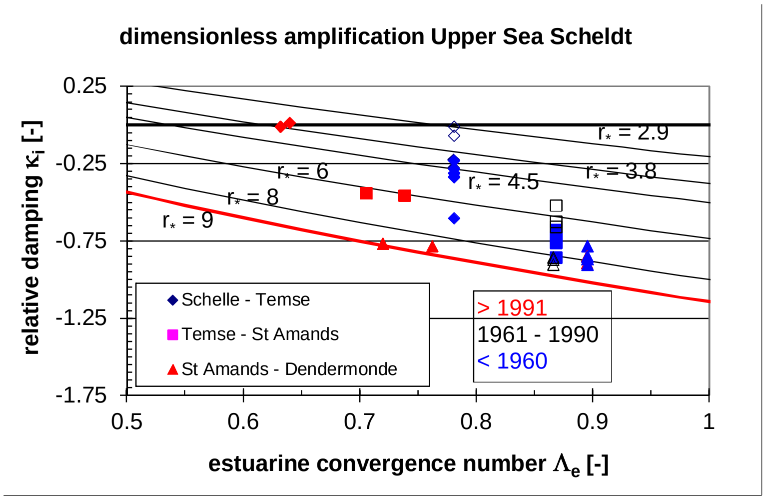

Fig. 22: Fits of linear solution trough observations tuning the roughness parameter r_* *in the* $\kappa_i - \Lambda_e$ *diagram.*

To compute the effective hydraulic drag from the fitted r_*-values, we use again the amplitude of the flow velocity from equ. (12) (Part I), and the measured tidal amplitudes. The computed variation of C with time along the lower part of the Upper Sea Scheldt is presented in Fig. 23. All Chézy values are a bit low, which may be attributed to the fact that in the linear model many physical features in the river (bends, bed forms, bank irregularities, local variations in river topography and bathymetry, etc.) are missing.

Yet, Fig. 23 suggests that the effective hydraulic drag, hence the Chézy coefficient did not change in the river stretch St Amands – Dendermonde, but increased considerably over the first part Schelle – Temse. If this reduction in drag would have been caused by high suspended sediment concentrations, this analysis suggests that values in SPM have been large for many decades, which, in conjunction with the deepening in the 1960s/1970s (e.g. Fig. 18) may explain the increase in C. The anomalous behavior between 1980 – 1990 is not understood, but may be misleading, as topographic/bathymetric data over that period is missing, and had to be created by interpolation of data from other decades (see also bed level data of Fig. 18).

Indeed, SPM values have been reported to be fairly large at about 200 mg/l over a long stretch of the river up to km 100 (Temse). Unfortunately, no historic SPM-data exist, and it therefore not possible to relate the results of Fig. 23 to such data.

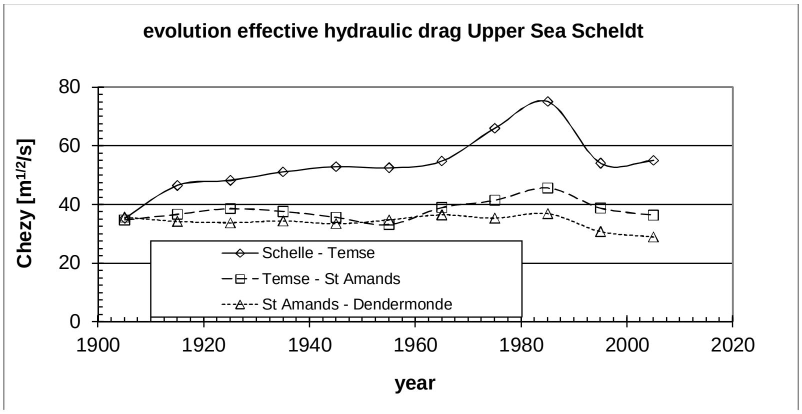

Fig. 23: Evolution of effective hydraulic drag (Chézy coefficient) with time,

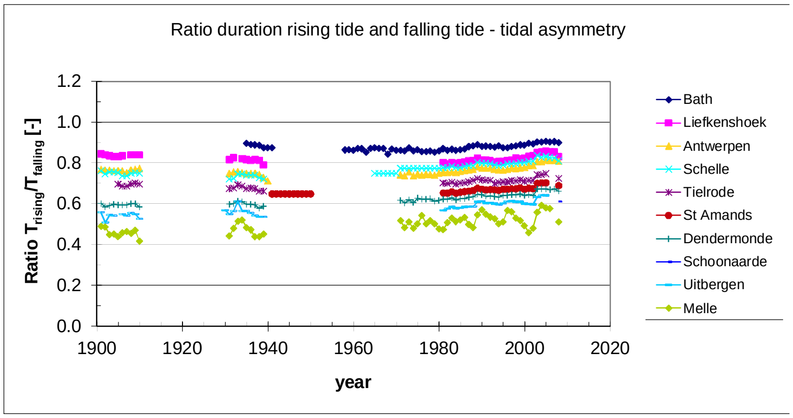

Fig. 24: Observed tidal asymmetry in Sea Scheldt.

Fig. 24 presents measured data on tidal asymmetry, in the form of the ratio of the period of rising tide and falling tide, showing pronounced flood dominance over the entire river (Plancke et al., 2012). It is observed that flood dominance increases in upstream direction, as expected, as water depth decreases in upstream direction. We note that the river's fresh water flow is relatively small, hence does only slightly affect the duration of flood and ebb period.

However, it is remarkable that the asymmetry changes little over time, except may be for Schelle, given the large increase in tidal amplitude. This discrepancy can be explained from two counteracting developments:

3. In particular in the upper reaches, the water depth has increased largely in a relative sense. Larger water depth would decrease tidal asymmetry, counteracting the effects of a larger tidal range.
4. Probably more important is the development of tidal asymmetry in the Western Scheldt, e.g. Fig. 24, which serves as "boundary conditions" for the Upper Sea Scheldt. Hence, further to the local generation of overtides in the Upper Sea Scheldt, tidal asymmetry is "imported" from the down-estuary reaches of the estuary, i.e. the Western Scheldt. Wang et al. (2002) showed that the flood dominance at Bath, the most upstream station in the Western Scheldt, has been decreasing in time.

It is beyond the present study to evaluate the evolution of tidal asymmetry in the Western Scheldt, but the behavior of the asymmetry at Hansweert is remarkable, suggesting that its asymmetry tends to re-establish the conditions at the beginning of the 20th century.

6. DISCUSSION, SUMMARY AND CONCLUSIONS

In the 20th century, many European rivers have experienced large amplification of the tide, often with enormous environmental consequences. In this paper, and the accompanying Part I, we have analyzed the historical development of these amplifications in four tidal rivers with the aim to understand their response to human interferences. This analysis of the data is carried out with a linear analytical model, solving the shallow water equations, e.g. Part I. The tidal amplification in these rivers can be characterized by a dimensionless imaginary wave number κ_i, as a function of the estuarine convergence number Λ_e, and a dimensionless friction coefficient r_* - the latter decreases with decreasing effective hydraulic drag. Λ_e decreases with increasing water depth, decreasing convergence length (increase in tapering) and decreasing intertidal area.

Using these dimensionless numbers, the tidal evolution of estuaries can be compared mutually. The friction coefficient r_* is established by calibration of the analytical model through the data, assuming an infinitely long estuary (e.g. no reflections). The rivers have been divided into sub-sections, following available bathymetrical data and tidal stations. The results of this comparison are presented in Fig. 25, where the temporal evolution runs along a diagonal from the lower-right corner to the upper-left corner. Each data point reflects the tidal amplification in a specific river section over a certain period of time. The analytical model predicts that, within the range of relevant values, e.g. Fig. 25, a decrease in Λ_e induces amplification of the tide (or, more precise, a reduction in the amount of damping), or, in other words, κ_i increases. Further to this response in tidal amplification, the river becomes flood-dominant, at small intertidal area (e.g. Part I). However, the sensitivity of κ_i to variations in Λ_e around $\Lambda_e = 1 – 2$ at small r_* is small (e.g. Fig. 6, Part I). From a practical point of view, this implies that for such conditions it will not be easy to reduce the tidal amplification by interventions in the river.

This analytical picture is corroborated grossly by the data. Fig. 25 shows that all rivers, except the outer Elbe, depict a decrease in r_* while Λ_e decreases as a result of engineering works. The decrease in r_* from 7 to 0.8 implies an increase in Chézy coefficient from about 40 (e.g. a sandy bed with bed forms) to about 90 $m^{1/2}/s$ (e.g. a very muddy environment).

In detail though, the rivers have different stories. The Ems and Lore Rivers are infamous for their very large suspended sediment concentrations (several 10 g/l) and occurrences of fluid mud. From the analyses in Part I, it is hypothesized that both rivers have passed a tipping point, evolving into their current hyper-turbid state following a positive feed-back between tidal amplification, flood dominance and up-estuary transport of fine sediment. At that state, frictional effects are very small because of sediment-induced buoyancy destruction (e.g. Winterwerp, 2001), and the tide becomes highly sensitive to bathymetrical and geometrical changes (e.g. Jay, 1991). At high SPM-values, the hyper-turbid conditions become self-maintaining, as these conditions are favourable from an energy point of view – the river has migrated towards an alternative steady state.

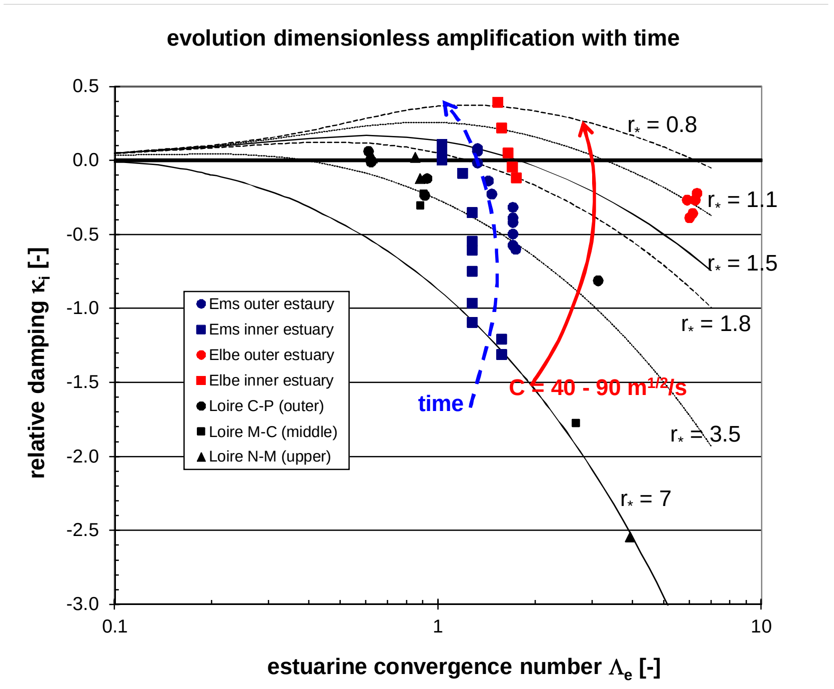

Fig. 25: Comparison of tidal evolution in four European rivers. In the course of time, Λ_e decreased continuously, inducing κ_i to increase. Note that data for the inner Elbe are misleading, as there are indications that the tidal evolution in the Elbe is affected more by reflections, than by high suspended sediment concentrations.

Moreover, the tidal amplification in the Ems is affected by reflections against the weir at Herbrum. The effects of such reflections increase with decreasing effective hydraulic drag, as the friction length increases rapidly.

In Part I it was argued that the tide in estuaries becomes very sensitive to deepening after loss of intertidal area: with that loss, the resilience of the estuaries decreased. This sensitive response is well depicted with the tidal evolution in the Loire upon the large narrowing of the river in the early 20th century.

The tidal range in the Sea Scheldt in the vicinity of Antwerp and the lower part of the Upper Sea Scheldt has increased by about 1 m. In particular, the large amplification in the Upper Sea Scheldt is remarkable, as locally no large-scale engineering works took place in the 20th century. Yet, the river deepened by 1 – 2 m over considerable lengths. We have indications that this deepening likely reflects the morphodynamic response of the estuary to large scale deepening and widening of navigation channel in the river further down-estuary, and the large scale of sand extraction (about 250 Mm^3 of sediment has been removed from the Scheldt estuary since 1955). In the lower part of the Upper Sea Scheldt, e.g. up-estuary of the head of salinity intrusion, SPM values are now increasing to several 100 mg/l, which may explain the decrease in effective hydraulic roughness, established with the linear analytical model. This increase, beyond the salinity intrusion, is likely to be attributed to the strong flood-dominance of the tide, in conjunction with a reduction in flushing capacity of the river.

The tide in the upper 25 km of the Upper Sea Scheldt is affected by reflections of the tidal wave against the structures erected around Ghent. Currently, the riverbed is sandy, and the tide damped. It is anticipated that the tidal amplification in general, and the impact of tidal reflections in particular will increase rapidly if the SPM concentrations in the Upper Sea Scheldt would increase further, as the roughness length L_r reduces with increasing SPM-values. Currently, it cannot be established whether or not the Sea Scheldt is approaching a tipping point towards hyper-turbid conditions.

The plan form of the Elbe has been modified largely, and the fairway was deepened by many meters. In the lower part of the Elbe, SPM-concentrations are quite large, and we established a fairly low effective hydraulic drag, consistent with information from German colleagues. However, SPM-concentrations in the upper part of the Elbe are low, owing to the sediment management around the Port of Hamburg. The strong increase in tidal range in this part of the river is likely to be attributed to (partial) reflections of the tidal wave against the large step in river depth in Hamburg.

The effects of tidal reflections can only be studied qualitatively with the linear analytical model, whereas the effects on (variations in) river flow cannot be studied. Yet, from the data it can be concluded that for instance the tide in the Ems' section between Papenburg and Herbrum is strongly affected by the river flow, even though this flow is quite small. More advanced models, accounting for non-linear effects and detailed bathymetrical features, are required to analyze the effects of tidal reflections and river flow in further detail; this is subject of further work.

In spite of the limitations of the current analyses, and the differences in the details of the temporal evolutions of the various rivers, a number of general conclusions can be drawn from the analytical study in Part I, and the data analysis of Part II of our paper:

1. The observed amplification of the tide in the four rivers cannot be explained from geometrical/bathymetrical changes in these rivers alone.
2. The loss of intertidal area from these tidal rivers has reduced their resilience to further engineering works (e.g. deepening) largely; also accommodation space for suspended fine sediments has been lost. This loss in resilience took place in the late 19th and early 20th century, whereas further engineering works took place in the second half of the 20th century.
3. The interaction of suspensions of fine sediments with the tidal movement may set in motion a positive feed-back loop through a reduction in effective hydraulic drag. Then, large amounts of fine sediments may be pumped into the river owing to their flood-dominance. The alternative, hyper-turbid state towards which the river may develop, is very stable and self-maintaining.
4. In some rivers, the tide is affected by reflections against constructions in the river – such effects become more prominent with decreasing effective hydraulic drag. This is particularly the case for the upper part of the Elbe River.

It is noted that the behavior of the Ems and Loire River is not unique. Other rivers have been largely engineered as well, whereas also a number of more-or less "pristine" rivers (Severn, Yangtze[4)]) are also characterized by hyper-turbid conditions. Fig. 26 summarizes values of Chézy coefficients for a number of rivers (and their sub-sections) as a function of the water depth, depicting the SPM state of these rivers by the color of the symbols. It is well-known that hyper-turbid rivers are characterized by high C-values. Possibly, the evolution of effective hydraulic roughness may indicate whether a river approaches its tipping point at which a positive feed-back loop sets in motion the river's development towards hyper-turbid conditions. The "normal" C-h-k_s relation (Fig. 26) may serve as a reference for this analysis. Further work is required to elaborate on this diagram, and to account for the effects river flow and tidal reflections. The data suggest that the development of hyper-turbid conditions upon passing a tipping point may take one to two decades. The availability of fine sediments is probably a limiting factor in this.

Finally it is emphasized that a full understanding of the tidal evolution in these rivers, in conjunction with the sediment dynamics (SPM-values, morphodynamic response) requires hind-cast simultations of these developments with advanced numerical models, integrating hydrodynamics, morphodynamics and fine sediment transport. Until then, the analyzes presented in this paper remain hypothetical.

[4)] *We realize that the Yangtze is not pristine – however, the high SPM-values occurred well before the various large-scale interventions in the river and its catchment.*

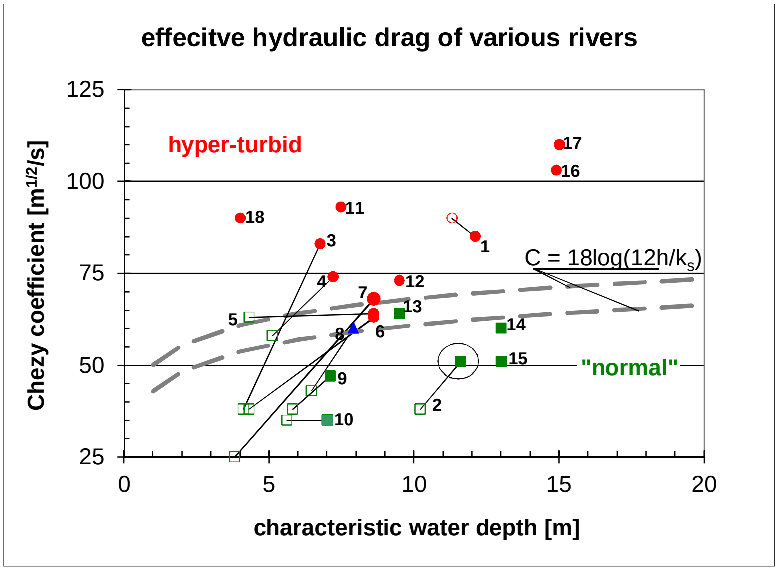

Fig. 26: Comparison of effective hydraulic drag in some rivers as a function of water depth. The C-h *relation is based on* k_s *= 2 and 5 cm, arbitrary values. Red symbols depict hyper-turbid conditions, green symbols "normal" conditions, and blue symbols possibly transitional systems; open symbols reflect historical data.*
1: Elbe-outer; 2: Elbe-inner; 3: Ems/E-L; 4: Ems/L-P; 5: Loire/P-C; 6: Loire/C-laM; 7: Loire/LaM-N; 8: Scheldt/S-T;9: Scheldt/T-StA; 10: Scheldt/StA-D; 11: Thames; 12: Severn-inner; 13: Severn-outer; 14: Western Scheldt; 15: Gironde-outer; 16: Gironde-inner (Villaret et al., 2011); 17: Yangtze estuary; 18: Vilaine (Vested et al., 2013). Note that data on Elbe-inner may be spurious because of tidal reflections, as discussed in Section 2.

ACKNOWLEDGEMENTS

This work was carried within the framework of the LTV-project, which is the acronym for Long-Term Vision of Scheldt estuary with respect to Safety, Accessibility and Nature, in which the following sub-projects are integrated: Maintaining fairways Scheldt estuary, Permits for disposal of dredged sediments and the so-called KPP (knowledge of primary processes) program of Rijkswaterstaat. The study was financed by the Flemish "Afdeling Maritieme Toegang" (Maritime Department) and Rijkswaterstaat, Waterdienst and Directorate Zeeland (the Dutch Ministry of Infrastructure and Environment). The subject of the research in this paper was formulated by Mr. Youri Meersschaut requesting the analysis of the fine sediment dynamics in the Scheldt River. Further we like to thank dr. Henk Schuttelaars for his many constructive comments and ongoing discussions on this subject, and dr. Tom de Mulder for reviewing an earlier report on this study. We also would like to acknowledge the help of Mr. Marcel Taal in organizing and coordinating our study.

The results in this paper are based on a large number of data from a variety of sources. Some data sets were available at Deltares in reports, or in digital form from studies carried out earlier. Other data have been prepared and made available especially for this project. We would like to thank the following people for their support and supply of data: Mr. Frederik Roose (Flemish Government) for Scheldt data, dr. Luc Hamm (Sogreah) for information on the Loire, dr. Harro Heijer and Mr. Jens Jürges (BAW) for data on the Ems, Weser and Elbe river; and Prof. Ian Townend for data on the Thames and Severn estuaries. Furthermore, dr. Holger Weilbeer (BAW) and dr. Jens Kappenberg (Helmholz Centre) were helpful in some discussions on the Elbe and Ems Rivers.

REFERENCES

BAW, 2012. Data received from Dr. Frank Kösters and Jens Jürges on Ems and Elbe.

Briere, C., J. Crebas, A. Becker and J.C. Winterwerp, 2012. Analyse de la morphologie du chenal de Nantes et étude de sa restauration - Phase 3 : Etude de l'impact d'une intervention à l'amont de Nantes sur les caractéristiques de la marée. Deltares report 1201695 (in French).

de Jonge, V.N., 2000. Importance of temporal and spatial scales in applying biological and physical process knowledge in coastal management, an example for the Ems Estuary. Cont. Shelf Res. 20, 1655e1686

Herrling, G. and H.D. Niemeyer, 2008. Comparison of the hydrodynamic regime of 1937 and 2005 in the Ems-Dollard estuary by applying mathematical modeling. Research project: INTERREG IIIB North Sea project HARBASINS; Work package 4: „Hydro-morphological impacts and pressures“Lower Saxony Water Management, Coastal Defense and Nature Conservation Agency, Coastal Research station.

IMDC, 2012. Analyse bodemgegevens Boven Zeeschelde. Note I/NO/11387/12.226/VBA.

Kappenberg, J. and H.-U. Fanger. 2007. Sedimenttransportgeschehen in der tidebeeinflussten Elbe, der Deutschen Bucht und in der Nordsee. GKSS report 2007/20; ISSN 0344-9629.

Krebs M. and H. Weilbeer, 2005. Ems-Dollart Estuary. Die Küste 74, 252-262.

Kuijper, C. and J. Lescinski, 2012, LTV Veiligheid en Toegankelijkheid. Sub project B: Data analysis Western Scheldt. Report 1204405. Deltares.

Plancke, Y., T. Maximova, S. Ides, P. Peeters, E. Taverniers and F. Mostaert, 2012, Werkgroep O&M - Projectgroep Veiligheid. Sub project 1: Data analysis and hypothesis - Upper Sea Scheldt. Report WL2012R756_05_rev4_0. Flanders Hydraulics Research.

Schrottke, K. and A. Bartholomä, 2008. Detaillierte Einblicke in die ästuarine Schwebstoffdynamik mittels hochauflösender Hydroakustik. Tagungsband zum Seminar Ultraschall in der Hydrometrie: neue Technik; neuer Nutzen; FgHW / DWA, Koblenz, June 2008, 75-82.

Sogreah, 2006. Expertise et connaisssance du systeme estuarien de Loire – Tome 1: Analyse historique, Report 1711457R2.

Talke, S.A., H.E. de Swart and V.N. de Jonge, 2009. An idealized model and systematic process study on oxygen depletion in highly turbid estuaries. Estuaries and coasts, 32 (4), 602-620.

Toffolon, M. and H.G. Savenije, 2011. Revisiting linearized one□dimensional tidal propagation. Journal of Geophysical Research, 116, C07007, doi:10.1029/2010JC006616.

Van Braeckel, A., F. Piesschaert and E. van den Bergh, 2006. Historische analyse van de Zeeschelde en haar getijgebon den zijrivieren. 19e eeuw tot heden. INBO report INBO.R.2006.29.

Vested, H.J., C. Tessier and E. Goubert, 2013. Numerical modeling of morphodynamics – Vilaine Estuary. Ocean Dynamics, in press.

Villaret, C., N. Huybrechts, A.G. Davies and O. Way, 2011. Effect of bed roughness prediction on morphodynamic modelling: Application to the Dee estuary (UK) and to the Gironde estuary (France). Proceedings 34th IAHR World Congress - Balance and Uncertainty, Brisbane, Australia: 1149-1156, ISBN 978-0-85825-868-6.

Vroom, J., H. van den Boogaard and B. van Maren, 2012. Mud dynamics in the Eems-Dollard, research phase 2 – Analysis of existing data. Deltares, report 1205711-001.

Weilbeer H. and M. Klöpper, Bundesanstalt für Wasserbau, 2011. Model Validation and System Studies for Hydrodynamics, Salt and Sediment Transport in the Elbe Estuary - Basic Information for the River Engineering and Sediment Management. Draft Report A39550310069.

Wang, Z.B., C. Jeuken, H. Gerritsen., H.J. de Vriend and B.A. Kornman, 2002, Morphology and asymmetry of vertical tide in the Western Scheldt Estuary, Continental Shelf Research, 22 (17) 2599-2609.

Wasser- und Schiffahrtverwaltung des Bundes. Zentrales Datenmanagement der WSD Nord - Portal Tideelbe, 1999; see also http://www.portaltideelbe.de/Projekte/FRA1999/Beweissicherung/-Ergebnispraesentation/-profile_elbe/index.html.